A Theoretical Investigation of Topological Insulator Nanostructures

THÈSE N^{O} 6900 (2016)

PRÉSENTÉE LE 19 FÉVRIER 2016

À LA FACULTÉ DES SCIENCES DE BASE
GROUPE YAZYEV
PROGRAMME DOCTORAL EN PHYSIQUE

ÉCOLE POLYTECHNIQUE FÉDÉRALE DE LAUSANNE

POUR L'OBTENTION DU GRADE DE DOCTEUR ÈS SCIENCES

PAR

Naunidh Singh VIRK

acceptée sur proposition du jury:

Prof. M. Q. Tran, président du jury
Prof. O. Yazyev, directeur de thèse
Dr C. A. Pignedoli, rapporteur
Dr C. Barreteau, rapporteur
Prof. H. Dil, rapporteur

ÉCOLE POLYTECHNIQUE
FÉDÉRALE DE LAUSANNE
Suisse
2016

To my nearest and dearest

Acknowledgements

I would like to initially express my sincere gratitude towards my supervisor Professor Oleg Yazyev. Firstly, for giving me the chance to undertake research within his inaugural group at EPFL. Secondly, I would be lying if I said this journey had been entirely plain sailing, and I am thus extremely grateful for his guidance, unwavering support, professionalism and for having had my best interests at heart through out the duration of the PhD.

Next I would like to extend my thanks to members of our research group. First and foremost, a special mention is due to Gabriel Autès, having played a role in practically all aspects of the work undertaken in this thesis he was a constant pillar of support, and always ready to listen and help no matter how trivial or menial the request. Moreover, this facilitated a nurturing environment which greatly aided my understanding of physical concepts. Similarly, I would also like to thank Hyungjun Lee, who through accommodating discussions helped advance my knowledge, particularly with respect to the work related to the latter parts of the thesis. Having both started our PhDs concurrently, I thank Fernando Gargiulo for being always ready to help, both professionally and personally. Finally, I would like to thank the remaining members of our group Artem, Diego and Vamshi for their insights and input, particularly during group meetings, throughout my tenure here.

On a more practical level I am indebted to Noemi Porta, Tanya Castellino and Anh Eymann for all their effort behind the scenes which more than enable the smooth day to day functioning of our work.

Going slightly further back in time I would also like to take this opportunity to thank my previous Bachelor's supervisor Professor Neil Allan, and especially my Master's supervisors Professor Nicholas Harrison and Dr. Barbara Montanari, without whom I would never have trod down this path.

On a more personal level innumerable lunches and coffee breaks with colleagues and friends at the Institut de Théorie des Phénomènes Physiques have provided a welcome respite from the daily rigours of graduate life. Stretching beyond the confines of academia, I thank all the friends and acquaintances that have made this a unique experience in an astoundingly beautiful corner of the world.

To end, I would like to dedicate this thesis to my family and friends, and in particular my parents, through whose immeasurable support and sacrifice I was provided with every opportunity to arrive at where I am today, to which I will be forever grateful.

Lausanne, January 2016 N. V.

Abstract

The topology of the electron wavefunctions in certain band insulators can give rise to novel topological phases. Materials harbouring such topological phases are termed topological insulators (TI). A gapped bulk electronic spectrum, described by a topological invariant, and gapless boundary modes, tend to characterize the non-trivial topology. This work describes a theoretical investigation of the Z_2 topological insulator phase in Bi_2Se_3 and Bi_2Te_3, and the topological crystalline insulator (TCI) phase in SnTe, subject to nanoscale confinement. Specifically, it details the electronic structure, and properties of low-dimensional nanostructures derived from the bulk topological phase.

For the bismuth chalcogenides, a first principles methodology is applied to compute the energetics of high-index surfaces, followed by an analysis of the electronic properties of corresponding topological surface state charge carriers. Our calculations find several stable terminations of high-index surfaces, which can be realized at different values of the chemical potential of one of constituent elements. For the uniquely defined stoichiometric termination, the Dirac fermion surface states exhibit a strong anisotropy, with a clear dependence of Fermi velocities and spin polarization on the surface orientation. Non-stoichiometric surfaces undergo self-doping effects, which results in the presence of topologically trivial mid-gap states.

These findings guide the construction of Bi_2Se_3 nanostructures of a nanowire (NW) and nanoribbon (NR) morphology. A tight-binding formalism is utilised to study, firstly, the impact of finite-size effects on the electronic spectrum of each nanostructure. Secondly, the effects of confinement on the topological properties of two-dimensional (2D) Dirac fermion surface states. Quantum confinement around each nanostructure perimeter entails the formation of a series of discrete one-dimensional (1D) sub-bands in the bulk gap. An analysis of how the band gap varies as a function of nanostructure dimensions finds that the dependence is highly sensitive to nanostructure morphology. We reveal a clear correspondence between the spin helicity of the 2D surface Dirac cone and the spin properties of the 1D sub-bands. This is exemplified in the real space spin textures of each nanostructure. For the NW morphology, this correspondence gives rise to an energy dependent spin polarization density. Whereas for the NR morphology the presence of two separate surface types results in a more complex relationship.

Finally, via a similar tight-binding formalism, we establish how the crystal-symmetry-dependent topological phases of SnTe (001) thin films are exhibited in lower dimensional nanowires. SnTe (001) thin films, defined by either mirror or glide symmetry, realise distinct

2D TCI phases. As the band dispersion of NWs are characterised by which of these symmetry classes they belong to, we subsequently connect the distinctive NW surface states to the respective parent 2D TCI phase. Lastly, we show that the robust topological protection offered by the mirror symmetry protected 2D TCI phase is manifested in robust surface states of NWs of equivalent symmetry.

Key words: topological Insulator, topological crystalline insulator, Bi_2Se_3, Bi_2Te_3, SnTe, nanostructure, nanowire, nanoribbon, DFT, tight-binding

Résumé

La topologie des fonctions d'ondes des électrons dans certains isolants des bandes peux donner lieu à de nouvelles phases topologiques. Les matériaux dans lesquels se manifestent ces phases sont classifiés isolants topologiques. La topologie non triviale tends à être caractèrisée par un spectre électronique de volume isolant, d'écrit par un invariant topologique, mais comprenant des états de surface métalliques. Ce travail dćrit l'étude théorique des phases d'isolant topologique Z_2 dans les composés Bi_2Se_3 et Bi_2Te_3, ainsi que la phase d'isolant topologique cristallin dans le SnTe. Plus particulièrement, la structure électronique, ainsi que les propriéteés dérivées de la phase topologique de volume de nanostuctures à dimensionalité réduite sont décrite.

Pour les dichalcogènes de bismuthe, une méthodologie à partir de principes premiers est utilisée pour calculer l'énergetique de surfaces à indice élevé, suivie d'une analyse des propriétés électronique des porteurs de charges topologiques de surface correspondants. Nos calculs révèlent plusieurs terminaisons stables de surfaces à indice élevé, qui peuvent être réalisées pour différentes valeurs du potentiel chimique de l'un des éléments constituants. Pour la terminaison stochiométrique définie de manière univoque, les fermions de Dirac de surface sont fortement anisotropiques, avec des vitesses de Fermi et des polarisations de spins dépendants de l'orientation de la surface. Des surfaces non-stochiométriques subissent des effets d'auto-dopage, qui résultent en la présence d'états de mid-gap topologiquement triviaux.

Ces trouvailles guident la construction de nanostructures de Bi_2Se_3 avec une morphologie de nanofils et de nanorubans. Un formalisme de la liaison forte est utilisé pour étudier, dans un premier temps, l'impact d'effets de taille finie sur les propriétés électroniques de chaque nanostructure, et dans un second temps, les effets de confinement sur les propriéteés topologiques de fermions de Dirac de surface bidimensionnels. Le confinement quantique autour de chaque nanostructure mène à la formation d'une série discrète de sous-bandes monodimensionelles dans l'énergie de bande interdite du volume. Une analyse de la variation de l'énergie de bande interdite en fonction des dimensions de la nanostructure fait état d'une dṕendance fortement sensible á la morphologie de la nanostructure. Notre analyse révèle une correspondance claire entre l'hélicité des états de la surface bidimensionelle du cône de Dirac et les propriétés de spin des sous-bandes monodimensionelles. Cette dernière est illustrée par les textures de spins dans l'espace réel de chaque nanostructure. Pour le nanofil, cette correspondance donne lieu à une dépendence de l'énergie de la polarisation locale de spin. En revanche, pour la morphologie de nanoruban, la présence de deux types de surface résulte en une relation plus complexe.

Finalement, avec un formalisme de la liaisons fortes similaire, on établit les phases topopogiques dépendants des symétries cristallines dans des couches minces de SnTe (001) dans des nanofils à basse dimensionalité. Les couches minces de SnTe (001), définies soit par la symétrie de miroir, soit par la symétrie de rf́lexion glissé, réalisent des phases topologiques cristallines bidimensionelles distinctes. Comme la dispersion de bande de nanofils est caractérisée par à laquelle de ces deux classes de symétrie elle appartient, on relie les états de surface distincts aux phases topologiques cristallines 2D parentes respectives. Enfin, on montre que la protection topologique robuste offerte par la phase topologique cristalline de miroir 2D se manifeste par des états de surface robustes des nanorubans de symétrie équivalente.

Mots clés : isolant topologique, isolant topologique cristallin, Bi_2Se_3, Bi_2Te_3, SnTe, nanostructure, nanofil, nanoruban, DFT, liaison forte

Contents

Acknowledgements **v**

Abstract **vii**

Résume **ix**

1 Introduction **1**

1.1 Topological Phases . . . 1

1.1.1 Integer Quantum Hall Effect and the TKNN Invariant . . . 1

1.1.2 Quantum Spin Hall Effect . . . 3

1.1.3 Z$_2$ Invariant-Two dimensions . . . 5

1.1.4 Z_2 Invariant-Three dimensions . . . 7

1.1.5 Mirror Chern Number . . . 9

1.2 Experimental Work on Topological Phases . . . 10

1.2.1 $\mathrm{Bi}_{1-x}\mathrm{Sb}_x$ alloy . . . 11

1.2.2 Topological Electronic Materials . . . 12

1.2.3 Bismtuh Chalcogenides . . . 13

1.2.4 Tin Telluride . . . 15

1.3 Nanostructures of Topological Materials . . . 19

1.3.1 Bismuth Chalcogenides . . . 19

1.3.2 Tin Telluride . . . 24

1.4 Outline . . . 27

2 Methodology **29**

2.1 Density Functional Theory . . . 29

2.1.1 General Formalism . . . 29

2.1.2 First Principles Calculations on Topological Insulator Materials . . . 38

2.2 Tight-Binding Model . . . 42

2.2.1 General Formalism . . . 42

2.2.2 Hopping Integral . . . 45

2.2.3 Spin-Orbit Interaction . . . 47

2.2.4 Tight-Binding Parameters . . . 48

3 High-Index Surfaces of Bismuth Chalcogenide Nanostructures 55
3.1 Energetics 56
3.1.1 Methodology 57
3.1.2 Results 58
3.2 Electronic Structure 62
3.3 Conclusions 68

4 One-Dimensional Nanostructures of Bi_2Se_3 Topological Insulators 73
4.1 Methodology 74
4.2 Results 76
4.2.1 General Model of 1D Nanostructures 76
4.2.2 Nanowires 80
4.2.3 Nanoribbons 86
4.3 Conclusions 91

5 One-dimensional Nanostructures of Topological Crystalline Insulators 93
5.1 Methodology 94
5.2 Results 96
5.2.1 Two-dimensional Thin Films 96
5.2.2 Square Cross-Section Nanowires 101
5.2.3 Rectangular Cross-Section Nanowires 106
5.3 Conclusions 108

6 Outlook 111

Bibliography 127

Curriculum Vitae 129

1 Introduction

The term topological insulator (TI) has become somewhat of a buzzword in condensed-matter physics in recent years. As evident from the name itself, the term implies a refinement of what is traditionally considered an insulator. This refinement stems from the notion of topological equivalence, whereby two insulators are said to be topologically equivalent if one can be transformed into the other upon smoothly altering the Hamiltonian without closing the gap. For a TI, the topology of the electron wavefunction is such that it is not possible to smoothly connect the Hamiltonian with that of an ordinary insulator. Consequently, a key differentiator between such a topologically nontrivial phase and a trivial insulator, is that an interface between the two necessitates the formation of boundary states and closure of the energy gap. This bulk-boundary correspondence is a characteristic feature of TIs, which in 3D manifests in the formation of gapless topological surface states. The distinction between a topologically non-trivial phase and that of a trivial insulator is denoted in their respective topological invariants. As the notion of bulk-boundary correspondence and the definition of a topological invariant are fundamental to topological phases, we call on both when introducing the Z_2 topological insulator and topological crystalline insulator phases below. Beforehand, we briefly summarize the advances that led to their discovery.

1.1 Topological Phases

1.1.1 Integer Quantum Hall Effect and the TKNN Invariant

A cornerstone of the recent surge of developments in topological phases in condensed matter was the discovery of the integer quantum Hall effect (IQHE) [1]. The basis of the IQHE is that when a two-dimensional electron gas is subjected to large magnetic fields, at extremely low temperatures, this leads to a quantization of the electron's cyclotron orbitals, with the energy spectrum transformed into a series of discrete, quantized Landau levels. Moreover, as a result, when the Fermi energy E_F lies in between two Landau levels the Hall conductivity, σ_{xy}, is also quantized:

$$\sigma_{xy} = \upsilon \frac{e^2}{h} \quad (\upsilon = 1, 2, 3, \ldots) \tag{1.1}$$

where υ is an integer number. A subsequent fundamental insight [2], was that the integer υ is of topological origin.

To briefly expand on the notion of topologically distinct phases, a crystalline solid can be described through Bloch theorem [3] by an effective single particle Hamiltonian $H(\boldsymbol{k})$, where, due to translation symmetry, $\boldsymbol{k}$ is the crystal momentum within the irreducible Brillouin zone. The momentum dependence of the eigenvalues, $E_m(\boldsymbol{k})$, corresponding to the eigenstates, or Bloch states, $|\mu_m(\boldsymbol{k})\rangle$, of this Bloch Hamiltonian defines the band structure of the system. If there is a non-zero energy gap separating the occupied valence bands from the unoccupied conduction bands, the system is insulating. Two insulators are said to be topologically equivalent if their respective Hamiltonians can be slowly transformed into one another, whilst maintaining a finite, non-zero energy gap.

A key finding from Ref. [2] was that υ defines a topological invariant, termed the TKNN invariant or Chern number [4], which differentiates the IQHE as a phase topologically distinct, or inequivalent, from that of an ordinary insulator. The TKNN invariant is given by

$$\upsilon = \sum_{m=1}^{N} \frac{1}{2\pi} \int_{BZ} \nabla \times i \langle \mu_m(\boldsymbol{k}) | \nabla | \mu_m(\boldsymbol{k}) \rangle d^2\boldsymbol{k} \tag{1.2}$$

$$= \sum_{m=1}^{N} \frac{1}{2\pi} \int_{BZ} \nabla \times A_m d^2\boldsymbol{k} \tag{1.3}$$

$$= \sum_{m=1}^{N} \frac{1}{2\pi} \int_{BZ} F_m d^2\boldsymbol{k} \tag{1.4}$$

where $A_m = i\langle \mu_m(\boldsymbol{k}) | \nabla | \mu_m(\boldsymbol{k}) \rangle$ is the Berry connection [5], and $F_m = \nabla \times A_m$ the Berry curvature, with the summation over all the occupied Bloch states $|\mu_m(\boldsymbol{k})\rangle$, and with the integral of the Berry curvature being over the Brillouin zone. As Eqn.1.2 is dependent only upon the occupied states, the TKNN invariant is insensitive to small perturbations to the Hamiltonian. Furthermore, as υ_m is restricted to being an integer multiple of 2π, as can be seen from Eqn.1.2, this discrete nature alongside the robustness of the Hamiltonian helps explain the specific quantization of σ_{xy}, and the role of υ as a topological invariant for the integer quantum Hall system.

An interesting question arises when considering what happens at the interface between a topologically trivial system, such as an insulator, or equivalently the vacuum, and a topologically non-trivial system, for example one exhibiting the IQHE. Given the notion of topological equivalence defined above, at such an interface, a change in the topological invariant inherently necessitates the closure of the energy gap, and, subsequently, the presence of conducting states within it. These states have indeed been observed at the IQHE-vacuum interface [6], and are termed edge states, this is further supported by the fact that the states are localised at the edge within a distance approximate to that of the electron cyclotron orbital radius [6]. Thus, one can think of these states as a skipping motion electrons undergo as they rebound off the edge of the interface (Fig.1.1**a**). In a direct manifestation of the bulk topology of the IQHE, these edge states are chiral, in that they propagate in a single direction around the perimeter (i.e. edges) of the interface. Moreover, as there are no available states for backscattering, they are immune to disorder, which is again reflected in the pronounced quantization of the conductivity in the IQHE (Eq.1.1). The notion of edge states, whether chiral or of related properties, are fundamental to topologically non-trivial phases, and will be an important theme in the continued discussion below.

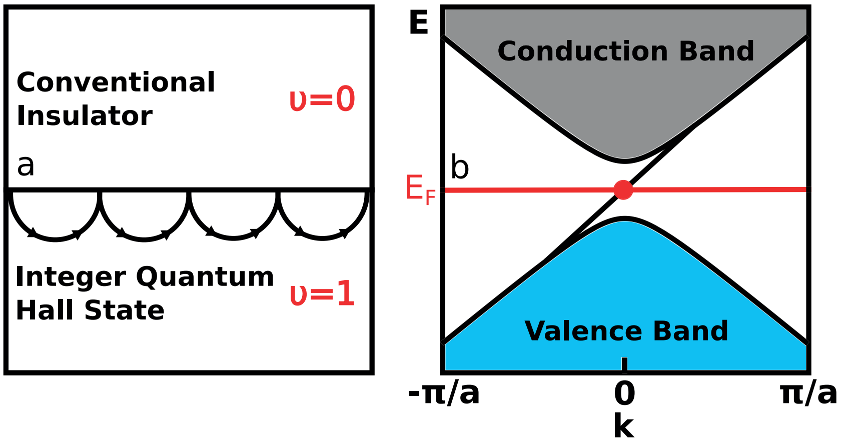

Figure 1.1 – Interface between a conventional insulator and an integer quantum Hall phase gives rise to chiral edge states. **a** Schematic representing edge states as skipping cyclotron orbits. **b** Band structure resulting from solution of the Haldane model in a semi-infinite geometry with a single band connecting the valence to the conduction band.

The chiral edge states of the IQHE can also be modelled explicitly via the Haldane model [7], which is a simple tight-binding model of a graphene lattice under a periodic magnetic field. Solution of this model in a semi-infinite geometry leads to an exact manifestation of the chiral edge modes, with a single band traversing the insulating energy gap, and connecting the valence bands to the conduction bands as is shown in Fig.1.1**b**. . This can be formally stated in the form of the bulk-boundary correspondence [8], which states that regardless of the number of right N_R or left N_L moving edge modes in the insulating gap, the overall difference between the two is strictly dictated by the bulk topology, and is equivalent to the difference in the Chern number across the interface:

$$N_R - N_L = \Delta n. \tag{1.5}$$

1.1.2 Quantum Spin Hall Effect

Accessing the IQHE requires high magnetic fields, extremely low temperatures, and a complex experimental setup, whereby directly manipulating chiral edge states is difficult. Thus, from the perspective of actual applications, taking advantage of the IQHE is somewhat impractical. From a more fundamental standpoint, the necessity of breaking time reversal symmetry via an external magnetic field or through magnetic ordering, raises the question of whether topologically non-trivial phases can also be observed in time reversal symmetric systems.

The spin-orbit interaction offers a novel route to a form of topological protection which is distinct to that governing the IQHE, and lifts the stipulation of broken time reversal symmetry. A simple model through which this non-trivial topology can be illustrated is the Kane-Mele model [9], which was derived from the original Haldane model for the IQHE. The essence of Kane and Mele's proposal, and in direct contrast to Haldane's original, is the preservation of time reversal symmetry and, crucially, the inclusion of spin. In doing so, this leads to a spin-orbit interaction dependent term in the tight-binding Hamiltonian of a graphene lattice, mentioned above; which, due to spin-orbit coupling (SOC), allows the Hamiltonian to be partitioned into two separate parts for spin up and down electrons, respectively. Considered as two isolated entities, each part is equivalent to Haldane's model for the IQHE, and thus, as before, implies the presence of chiral edge states. This is indeed the case, however, the role of the magnetic field in the IQHE is now played by the SOC. As the sign of the SOC switches for opposite spins, therefore each spin has an opposite sign of the Hall conductivity, and thus under an applied electric field the direction of the current will be opposite for each respective spin. Subsequently, considering both spins together, this leads to an overall Hall conductivity of zero, but results in a non-zero spin current $\boldsymbol{J}_s = (\hbar/2e)(\boldsymbol{J}_\uparrow - \boldsymbol{J}_\downarrow)$, defined by a quantized spin Hall conductivity:

$$\sigma^s_{xy} = \frac{e}{2\pi}. \tag{1.6}$$

Moreover, considered together, each chiral edge state combined forms a time reversal symmetric helical pair [10]. Helicity here describes the coupling of an electrons spin to its momentum, where spin up electrons propagate in one direction, whilst spin down electrons propagate in the opposing, with a crossing occurring at specific time reversal invariant momenta (TRIM), as can be seen in Fig.1.2. In two dimensions, this phase is dubbed the "quantum spin hall effect (QSHE)" [9]. The helical nature of the edge states has important implications for transport properties of the quantum spin Hall phase. Ordinarily, a one-dimensional conductor would have spin up and down states propagating in both directions, whereby electrons would be sensitive to Anderson localization, in the presence of weak disorder. Conversely, the helical nature of edge states in the quantum spin Hall phase, means that due to time reversal symmetry there is an absence of scattering matrix elements between time reversal invariant pairs [9]. This essentially means that backscattering is forbidden as it involves flipping the electron spin. Resultantly, edge states are perfectly transmitted across a disordered region, even for strong disorder, contingent on the condition that time reversal symmetry remains unbroken.

The model so far described essentially consists two copies of the IQHE, where the total TKNN invariant is zero, due to time reversal symmetry, as each spin has an independent Chern number $\upsilon_\uparrow = -\upsilon_\downarrow$. However, it has been assumed thus far that the spin is a conserved property, which for any realistic system is not the case. For example, terms stemming from the Rashba effect or from orbital mixing, will lead to spin nonconservation, and as such this model breaks down somewhat. In particular, the quantization of the spin hall conductivity (Eq.1.6) would not be be so exactly defined. Nonetheless, it was subsequently shown [11], remarkably, that the topological protection of the gapless edge states in the quantum spin hall phase, defined by a crossing at a TRIM point, is still present, even when spin nonconserving effects have been accounted for. As the total TKNN invariant is zero, this is suggestive of a novel form of topological protection for time reversal invariant systems, distinguishing the QSHE from that of an ordinary insulator, and distinct to that underlying the IQHE.

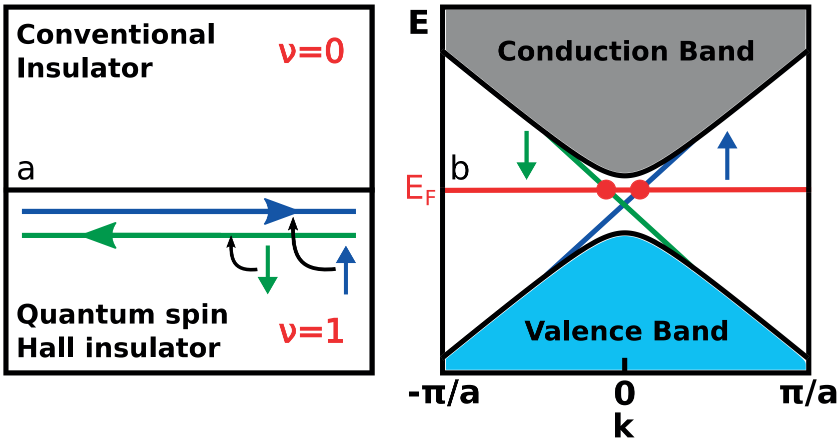

Figure 1.2 – Quantum spin Hall effect gives rise to helical edge states. **a** Schematic representation of the interface between a conventional insulator and a quantum spin Hall insulator. **b** Solution of the Kane-Mele model (see text) of a graphene lattice with spin-orbit interactions accounted for results in helical edge states, where spin up and spin down electrons propagate in opposing directions.

1.1.3 Z_2 Invariant-Two dimensions

Kane and Mele [11] introduced the Z_2 invariant to describe this non-trivial topology, which is underpinned by time reversal symmetry.

Time-reversal invariant systems are described by the time-reversal operator

$$\Theta = e^{i\pi \frac{S_y}{\hbar}} K \tag{1.7}$$

where S_y is the spin operator and K complex conjugation. As $\Theta^2 = -1$ for spin one half particles, Kramer's theorem dictates that, in a periodic system described by Bloch wavefunctions, each Bloch eigenstate at wave vector $\boldsymbol{k}$ is degenerate with a time reversed Bloch state. Thus, an energy band for a state at $+\boldsymbol{k}$ has the same energy as that of a state at $-\boldsymbol{k}$. As a result of the periodicity of the crystal Brillouin zone there exist time-reversal invariant momenta (TRIM) or TRIM points where $+\boldsymbol{k}$ and $-\boldsymbol{k}$ are equivalent, and two-fold degenerate. For a two-dimensional system there are four TRIM points (Fig.1.3**a**) given by

$$\Gamma_{i=(n_1 n_2)} = \frac{1}{2}(n_1 \boldsymbol{b}_1 + n_2 \boldsymbol{b}_2) \tag{1.8}$$

where $n_j = 0, 1$ and $\boldsymbol{b}_{1,2}$ are the reciprocal lattice vectors.

To formally derive the Z_2 invariants [12], a unitary matrix, built from the cell periodic eigenstates $|u_m(\boldsymbol{k})\rangle$ of the Bloch Hamiltonian, can be defined

$$w_{mn}(\boldsymbol{k}) = \langle u_m(\boldsymbol{k})|\Theta|u_n(-\boldsymbol{k})\rangle \tag{1.9}$$

As $w_{mn}(\boldsymbol{k}) = w_{nm}(-\boldsymbol{k})$, and therefore at each TRIM $w_{mn}(\Gamma_i) = w_{nm}(-\Gamma_i)$, this means that $w(\Gamma_i)$ is antisymmetric. Furthermore, since the Pfaffian of an antisymmetric matrix is equal to the square of its determinant, δ_i at each TRIM can be defined such that

$$\delta_i = \frac{\sqrt{\det[w(\Gamma_i)]}}{\mathrm{Pf}[w(\Gamma_i)]} = \pm 1. \tag{1.10}$$

Finally, on the condition that $|u_m(\boldsymbol{k})\rangle$ is continuous, the Z_2 invariant ν is defined

$$(-1)^{\nu} = \prod_{i=1}^{4} \delta_i. \tag{1.11}$$

In two dimensions the single Z_2 invariant differentiates the topologically non-trivial quantum spin Hall phase, $\nu = 1$, also termed a 2D topological insulator (TI), from a trivial two dimensional (2D) insulator, $\nu = 0$.

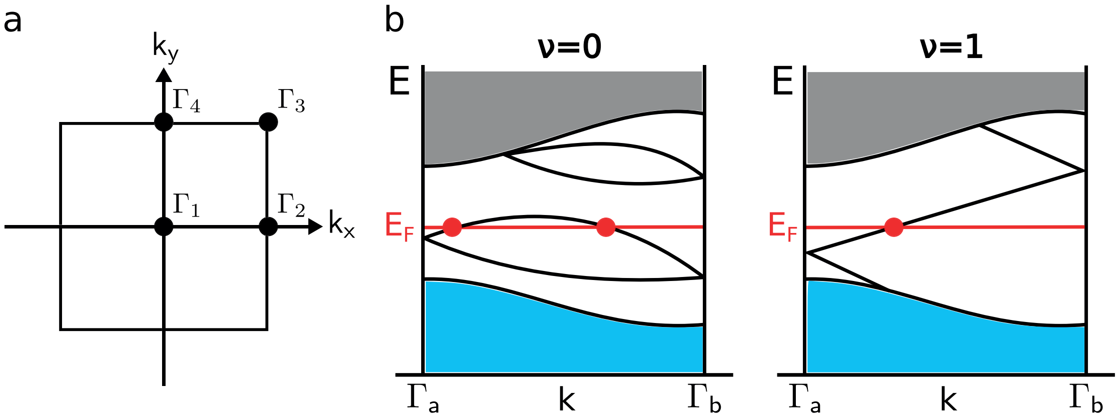

Figure 1.3 – Z_2 invariant in two dimensions. **a** 2D Brillouin zone with four TRIM points. **b** Inspection of the band dispersion between two Kramers degenerate TRIM points at $\Gamma_a = 0$ and $\Gamma_b = \frac{\pi}{a}$ allows topologically trivial (left) and topologically protected edge states (right) to be distinguished. **b** (left) An even number of edge states crossing the Fermi energy E_F indicates a topologically trivial phase. **b** (right) An odd number of edge states crossing E_F indicates a topologically non-trivial phase.

The nature of this Z_2 invariant, can be further clarified by inspecting the band dispersion of the edge states of a 2D time reversal invariant insulator between two TRIM points [8, 13]

(Fig.1.3). Corresponding electronic states are schematically plotted, in Fig.1.3**b**, between TRIM points $\Gamma_\mathrm{a} = 0$ and $\Gamma_\mathrm{b} = \frac{\pi}{a}$. Given the presence of edge states within the bulk insulating gap, what is of interest is how a state at Γ_a connects to that at Γ_b. Accounting for the fact that time reversal symmetry requires that at each TRIM the states are doubly generate, and, moreover, that due to spin-orbit coupling, away from each TRIM point this degeneracy is broken, there are two ways in which they can connect. The first, as shown in Fig.1.3**b**(left), involves a pair of bands connecting each state within the bulk gap, with E_F intersecting the edge states an even number of times. In the second case, as shown in Fig.1.3**b**(right), each state is connected by a single band, with E_F intersecting the bands an odd number of times [13]. In the first case there is no form of topological protection, as the edge states can be pushed out of the gap, and thus it is representative of a topologically trivial phase, as defined by $\nu = 0$ above. Whereas in the second case, this is not possible, with an odd number of crossings indicative of topological protection, and it represents a topologically insulating phase, as defined by $\nu = 1$ above.

1.1.4 Z_2 Invariant-Three dimensions

The term ’topological insulator’ was originally used to describe a topologically non-trivial phase in three dimensions defined by the Z_2 invariant [14]. Deriving it in 3D is an extension of the above methodology, this leads to eight distinct time-reversal invariant momenta:

$$\Gamma_{i=(n_1 n_2 n_3)} = \frac{1}{2}(n_1 \boldsymbol{b}_1 + n_2 \boldsymbol{b}_2 + n_3 \boldsymbol{b}_3) \tag{1.12}$$

for $n_j = 0, 1$, where the three-dimensional Brillouin zone can be seen as a cube with each TRIM point as an individual vertex of that cube. There are consequently four Z_2 topological invariants $\nu_0; (\nu_1 \nu_2 \nu_3)$ [15–17], and 16 distinct topological phases. The four Z_2 invariants in three dimensions can be split into two separately defined classes ν_0 and $(\nu_1 \nu_2 \nu_3)$. The single ν_0 invariant is a product of all eight TRIM points

$$(-1)^{\nu_0} = \prod_{i=1}^{8} \delta_i \tag{1.13}$$

and for $\nu_0 = 1$ defines a "strong" topological insulator. Whilst the three $(\nu_1 \nu_2 \nu_3)$ invariants, defined as

$$(-1)^{\nu_l} = \prod_{n_{j\neq k}=0,1; n_j=1} \delta_{i=(n_1 n_2 n_3)} \quad (l = 1, 2, 3) \tag{1.14}$$

are products of four TRIM points, analogous to the invariant in two dimensional case, and furthermore can be thought of as individual invariants for the symmetrically distinct faces of the cubic Brillouin zone described above. For a $\nu_0 = 0$ invariant, the $(\nu_1 \nu_2 \nu_3)$ invariants can subsequently define two distinguishable phases. The first phase consists of $\nu_l = 0$ for $(l = 1, 2, 3)$, and this denotes a topologically trivial phase, for example a band insulator. The second phase arises when $\nu_l = 1$ for at least one of $(l = 1, 2, 3)$, and denotes a "weak" topological insulator. This can be seen as a series of stacked 2D quantum spin Hall insulators, defined by the 2D Z_2 invariant just described. Importantly, unlike the $\nu_0 = 1$ phase, these phases are not subject to the same topological protection, and the topological distinction of a given "weak" phase is sensitive to disorder.

The presence of inversion symmetry in a crystal structure greatly simplifies the determination of the Z_2 invariant. Specifically, as Bloch states $u_m(\boldsymbol{k})$ at each TRIM are also parity eigenstates with eigenvalues $\xi_j(\Gamma_i) = \pm 1$, thus by taking the product of the parity eigenvalues over Kramer's pairs of occupied bands δ_i can be determined

$$\delta_i = \prod_j \xi_j(\Gamma_i). \tag{1.15}$$

From which the overall Z_2 invariant is defined, as described above.

To further elucidate the nature of these invariants one can inspect the band dispersion of surface states for the 3D crystal [15] (Fig.1.4). For the cubic construction described above, the surface Brillouin zone will consist of four TRIM, which can be labelled $\Gamma_i (i = 1, 2, 3, 4)$. Due to Kramer's degeneracy, the band crossings at each TRIM are two-dimensional Dirac points, whilst away from these crossings the degeneracy is lifted due to spin-orbit coupling. As with the 2D edge states, what again is of interest is the connections between the different TRIM $\Gamma_i (i = 1, 2, 3, 4)$.

In the case of a weak topological insulator, the stacking of 2D quantum spin Hall layers causes the helical edge states to form anisotropic surface states. This is illustrated by an example of the Fermi surface of a possible weak topological insulator in Fig.1.4**a**. In this case there is a surface state band intersecting the Fermi energy between points Γ_1 and Γ_2, and points Γ_3 and Γ_4, where the surface band structure between each of these pairs of points would resemble the connectivity for non-trivial edge states described above. However, unlike the 2D edge states, the surface states of a weak topological insulator are not protected by time reversal symmetry, as, crucially, the surface Fermi arc encloses an even number of TRIM points [13].

In the case of a strong topological insulator, the surface Fermi arc encloses an odd number of TRIM, for example for a single Dirac point, as shown in Fig.1.4**b**, this leads to the Z_2 invariant $\nu_0 = 1$. It should be noted that, unlike in the case of a weak topological insulator, a strong topological insulator is not built or derived from the 2D quantum spin Hall effect. As such, it defines an entirely novel, three-dimensional, topologically non-trivial phase, completely distinct to 2D phases such as the IQHE and the QSHE. A defining feature of a strong topological insulator is the helicity of the surface state. This is directly analogous to the pair of helical edge states of the quantum spin Hall phase, described earlier. As time reversal symmetry dictates that two states at **k** and -**k** have opposite spins, thus, in the case of a strong topological insulator, there is a 2π precession of the spin around Fermi surface, as evident in Fig.1.4**b**. This results in a non-trivial π Berry phase, which is another hallmark of strong TIs [15]. Similarly to the QSH insulator, these surface states are topologically protected by time-reversal symmetry to non-magnetic sources of disorder.

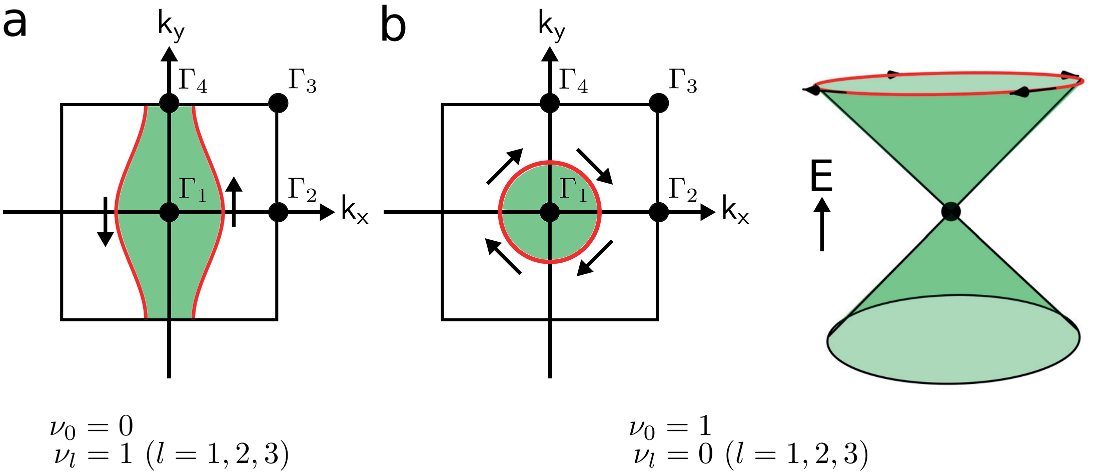

Figure 1.4 – Examples of surface Brillouin zones for a weak (**a**) and strong (**b**) 3D topological insulator, showing the Fermi circles enclosing an even and odd number of Dirac points, respectively. The simplest example of a strong topological insulator is that where the Fermi circle encircles a single Dirac point, giving rise to the surface state dispersion of a single Dirac cone (**b**-right).

1.1.5 Mirror Chern Number

The discovery of Z_2 topological insulators (TIs) sparked a surge of interest in the characterization of distinct phases protected by a non-trivial topology and the associated search for pertinent material systems. Furthermore, it led to a broad classification of topological phases based on the underlying symmetry governing the non-trivial topology [18–20]. For example, in the case of Z_2 TIs the symmetry protected topology stems from time-reversal symmetry (TRS), combined with strong spin-orbit interactions, as explained above. However, this classification was ordered around the presence or absence of non-spatial symmetries, for example that of TRS. Subsequently, the question also arose as to whether there are alternative forms of topological protection, offered by other symmetry classes, such as spatial symmetries. One recent (Fig.1.5) intriguing direction was based on the idea to topologically classify band insulators based on the point-group symmetry of the parent crystal, with topologically non-trivial phases protected by point-group symmetries, termed topological crystalline insulators (TCIs) [21]. In the specific case of a crystal with mirror symmetry, the corresponding topological invariant defining this phase is the mirror Chern number N_m [22].

Mirror symmetry is defined by the mirror operation M which is a product of spatial inversion P and a two-fold rotation C_2 around the axis perpendicular to the plane of rotation. If a mirror plane is defined as $z = 0$, subsequently the mirror operator is given by

$$M(\hat{z}) = PC_2(\hat{z}), \tag{1.16}$$

which takes $z \rightarrow -z$. In the presence of spin-orbit coupling, a C_2 rotation rotates both the spatial and spin coordinates of an electron. Since applying the mirror operation (Eqn.1.16) to an electron wavefunction twice is equivalent to a 2π rotation that changes the sign of a spinor, thus $M^2 = -1$ and eigenvalues of M are either $+i$ or $-i$ [23].

For a periodic crystal where mirror symmetry is preserved, at specific mirror invariant planes Bloch states $|\mu_m(\boldsymbol{k})\rangle$ can be chosen as eigenstates of M. Consequently, this leads to two sets of Bloch eigenstates, $|\mu_{m,\pm i}(\boldsymbol{k})\rangle$, labelled by the distinct mirror eigenvalues $\pm i$. For each set of Bloch eigenstates this allows the definition a corresponding Chern invariant $\upsilon_{\pm i}$. The sum of the Chern invariants

$$\upsilon = \upsilon_{+i} + \upsilon_{-i}, \tag{1.17}$$

is the topological invariant that determines the quantized Hall conductance (Eqn.1.1) [23]. However, the difference

$$N_m = \frac{\upsilon_{+i} - \upsilon_{-i}}{2}, \tag{1.18}$$

defines a novel topological invariant termed the mirror Chern number [22]. For mirror symmetric systems, a nonzero integer value of this invariant signifies a non-trivial topological crystalline insulator phase [24].

1.2 Experimental Work on Topological Phases

From an experimental perspective, realising the QSH phase in graphene is beyond the scope of current experimental ability, stemming from the fact that given how light the element is, its intrinsic SOC is extremely small. Even though attempts have been made to increase this value, through, for example, magnetic doping, these are yet to bear fruit. However, at a similar time to Kane and Mele's [9] original proposal, and in a logical step via the use of heavier elements, the phase was predicted in HgCdTe quantum wells [10], and shortly after also experimentally realised [25].

The experimental signature of the QSH phase in the HgCdTe quantum well structures was given by the measurement of a quantized longitudinal conductance of $2e^2/h$ [25], with the factor of two associtated with the combination of both edge states. However, other properties characteristic of the Z_2 topology, such as the helical spin texture and a Dirac band crossing, are yet to be observed. This is primarily due to the complexity of the experimental setup [25], whereby edge states are probed solely using charge transport measurements, as the interface is buried deep within a heterostructure setup, and moreover measurements have to be made at temperatures on the order of millikelvins.

1.2.1 $\mathbf{Bi}_{1-x}\mathbf{Sb}_x$ alloy

In stark contrast, the experimental conditions required to grow and probe the relevant properties of 3D topological insulators have proved less demanding, relative to their 2D counterparts, investigated thus far, and have hence led to a proliferation of discovered materials. An initial spark was the prediction [13], concurrent to the theoretical classification of the Z_2 invariant in 3D [14, 15, 17], and subsequent experimental realisation of the strong TI phase in a $Bi_{1-x}Sb_x$ alloy [26].

The prediction was based on the reasoning that as both pure Bi and Sb are materials with a finite direct band gap, with inversion symmetry, Eq.1.15 could be used to determine the Z_2 invariants of each. In doing so, Bi was predicted to be topologically trivial, with Z_2 indices (0;000), whilst Sb non-trivial, with indices (1;111), reflected in an inverted band ordering, relative to Bi, at the L TRIM point [13]. Given that pure Bi is a semimetal, the gradual substitution of Bi by Sb, to form the alloy $Bi_{1-x}Sb_x$, leads to some significant changes in electronic structure, as previous band structure studies have shown [27–29]. The two pertinent changes are, firstly, that at $x \approx 0.04$ the ordering of the conduction and valence bands at the L point inverts from that in topologically trivial Bi, to that in topologically non-trivial Sb. Secondly, a transition from a semimetallic to an insulating state is observed for $x \approx 0.07$, with the alloy becoming a direct band gap insulator for $0.09 < x < 0.18$. Finally, there is a reversion back to a semimetallic state for $x > 0.22$, thus reflecting the electronic ordering of pure Sb, which is also a semimetal. Consequently, $Bi_{1-x}Sb_x$ was predicted [13] to be a strong TI in the region of the alloy's phase diagram where an inverted band ordering at the L point is present in unison with the formation of an insulating state, i.e. within the limits of $0.09 < x < 0.22$.

Subsequent experimental work using angle-resolved photoemission spectroscopy (ARPES) confirmed $Bi_{0.09}Sb_{0.91}$ to be a strong TI [26, 30]. Two signature features of the topologically protected phase were identified, namely that the Fermi surface encloses Γ an odd number of times [26], and the presence of a helical spin-texture, via spin-momentum locking, signifying a π Berry phase, was also shown utilising spin resolved ARPES [30]. The confirmation was important in that it signified the first experimental realisation of a 3D TI phase, however, the complex nature of the material's surface spectrum [26] limited its potential as a template for more detailed investigations of topological surface states. Another hindrance also being that the band gap of the alloy has a maximal value of ~ 30 meV [28], depending on the value of x, thereby limiting any applications close to room temperature.

As the major foci of this work are concerned with later generations of 3D TIs, experimental details of $Bi_{1-x}Sb_x$ have only been briefly touched upon. However, it is important to highlight two trends that have become prominent themes in research related to TI materials. Firstly, the utility in applying topological band theory, as briefly described in Sec.1.1.4, in the prediction of novel TI materials. Secondly, given that ARPES maps the momentum distribution of a material's occupied electronic states, from the photoemission of electrons upon incident radiation, it serves as an ideal tool for resolving the surface and bulk electronic bands.

Furthermore, as the technique also allows the resolution of the spin, the intricate relationship between the spin and momentum of TI materials can be probed, therefore allowing the bulk topological order to be identified.

1.2.2 Topological Electronic Materials

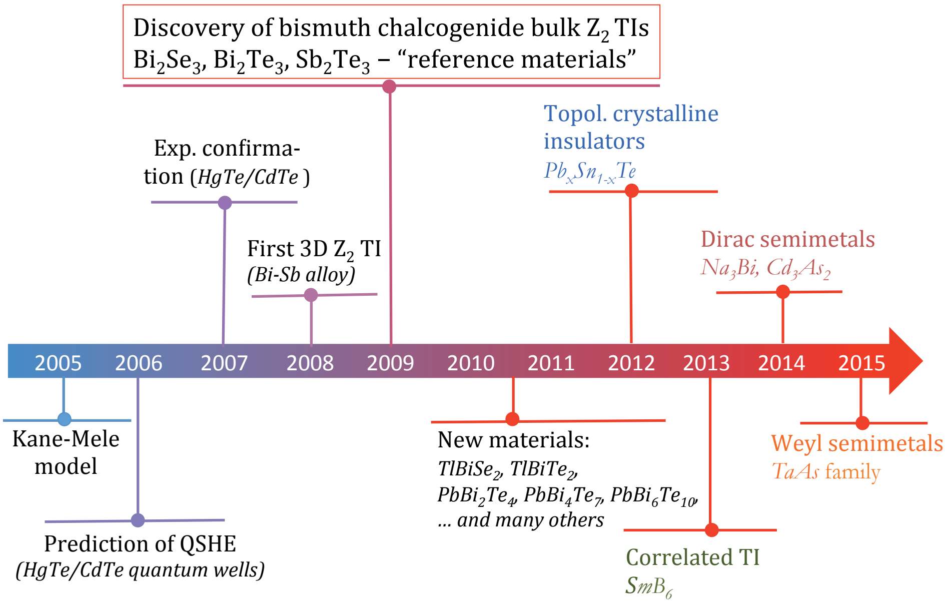
Discovery of bismuth chalcogenide bulk Z2 TIs
Bi2Se3, Bi2Te3, Sb2Te3 – "reference materials"
Topol. crystalline insulators
PbxSn1-xTe
Exp. confirmation (HgTe/CdTe)
First 3D Z2 TI (Bi-Sb alloy)
Dirac semimetals
Na3Bi, Cd3As2
2005
2006
2007
2008
2009
2010
2011
2012
2013
2014
2015
Kane-Mele model
New materials:
TlBiSe2, TlBiTe2, PbBi2Te4, PbBi4Te7, PbBi6Te10, ... and many others
Weyl semimetals
TaAs family
Prediction of QSHE (HgTe/CdTe quantum wells)
Correlated TI
SmB6

Figure 1.5 – Timeline showing various milestones in relation to topologically insulating materials that have been discovered, since the initial publication of the Kane-Mele [9] model in 2005, till the very recent discovery of the Weyl semimetal class [31]. Figure is courtesy of O. Yazyev.

Given the limitations associated with $Bi_{1-x}Sb_x$, described above, this triggered the search for materials with simpler surface states and larger band gaps. Two limiting conditions being that any candidate material must have strong spin-orbit coupling, implying the need of heavy elements, and secondly the presence of a band gap that is of a similar magnitude to the SOC, in order that a SOC induced topological phase can be formed.

This led to the identification of the binary bismtuh chalcogenides, Bi_2Se_3 and Bi_2Te_3, as 3D Z_2 TIs, and for reasons that shall be outlined below, they have come to be seen as prototypical materials defined by that topology. Their discovery also denotes a watershed, that began with the initial classification of the Z_2 invariant by Kane and Mele [9], and led to the subsequent prediction and realisation of materials in both 2D and 3D, as has been described. Moreover, the development of the theoretical methodology and experimental techniques within that period, not only initiated a surge to find other Z_2 TIs, but has also enabled research directions into novel, i.e. non Z_2, forms of topological order. An overview of these developments can be seen in the schematic timeline shown in Fig.1.5. Thus, this also defines the point at which the field of novel topological phases in condensed matter reached a relative level of maturity, and which has subsquently blossomed.

In the context of this thesis, the two system classes under investigation are, firstly, the Z_2 TI phase, primarily in the bismuth chalcogenides, Bi_2Se_3 and Bi_2Te_3. And, secondly, the mirror symmetry protected topologically insulating phase in the topological crystalline insulator SnTe. Thus, what follows is a brief overview of some of the experimental work conducted on the bismuth chalcogenides, as exemplars of strong TIs, and SnTe, that has motivated this work.

1.2.3 Bismtuh Chalcogenides

The bismuth chalcogenides, particularly Bi_2Se_3, are often referred to as reference TI materials. It should be noted that the term reference here, and in wider literature, is with regard to Z_2 TIs. They are the most extensively researched class of TIs, both with respect to the abundance of discovered materials, and their relative maturity in comparison to the other classes, as can be seen in Fig.1.5. This is primarily due to three factors.

The first relates to the simplicity of the topological surface states in Bi_2Se_3. Using the methodology of Fu and Kane [13], defined above, the parity eigenvalues of Bi_2Se_3 and Bi_2Te_3 were determined [32], from which the 3D Z_2 invariants are found to be (1;000). This indicates a non-trivial topological order with a Dirac cone surface state centred around $\boldsymbol{k} = 0$, at $\bar{\Gamma}$ in the surface Brillouin zone, which is shown for the (111) surface in Fig.1.6**a**. In parallel to this was the experimental confirmation, via ARPES [33], that the Bi_2Se_3 surface actually consists of just a single almost idealized Dirac cone, with the complete absence of non-topological surface states, in direct contrast to $Bi_{1-x}Sb_x$. This is evident from the ARPES data displayed in Fig.1.6**b**, which shows the band dispersion of the Bi_2Se_3 (111) surface, along the cuts $\bar{\Gamma} - \bar{\text{M}}$ (Fig.1.6**b** left) and $\bar{\Gamma} - \bar{K}$ (Fig.1.6**b** right) of the surface Brillouin zone (Fig.1.6**a**), with the Dirac cone clearly visible in both. The Z_2 topology was directly confirmed in subsequent work via the measurement of a helical spin texture [34]. This is manifested in a 2π rotation of the spin around the Fermi surface, for example as shown in Fig.1.6**c**, which in turn gives rise to spin filtered surface states, as Fig.1.6**d** displays, where electrons propagating in opposite directions have opposite spins. This spin-momentum locking was directly resolved by measuring the spin polarisation of the surface states along the $\bar{\Gamma} - \bar{\text{M}}$ cut of the (111) surface (Fig.1.6**e** inset)of Bi_2Te_3, as is plotted in Fig.1.6**e**. The spin polarisation is plotted along the y direction, with the x and z components of the spin zero [34], as can be seen the polarisation of the spin flips for $k_x = -k_x$, confirming the Z_2 topological order. Further evidence of the time-reversal protection of the surface states was also given by the observation of the suppression of back scattering from scanning tunneling microscopy/spectroscopy (STM/STS) experiments [35, 36]. Overall, this simplicity makes the topological properties of the material's surface state far more amenable to experimental probing than its counterpart in $Bi_{1-x}Sb_x$.

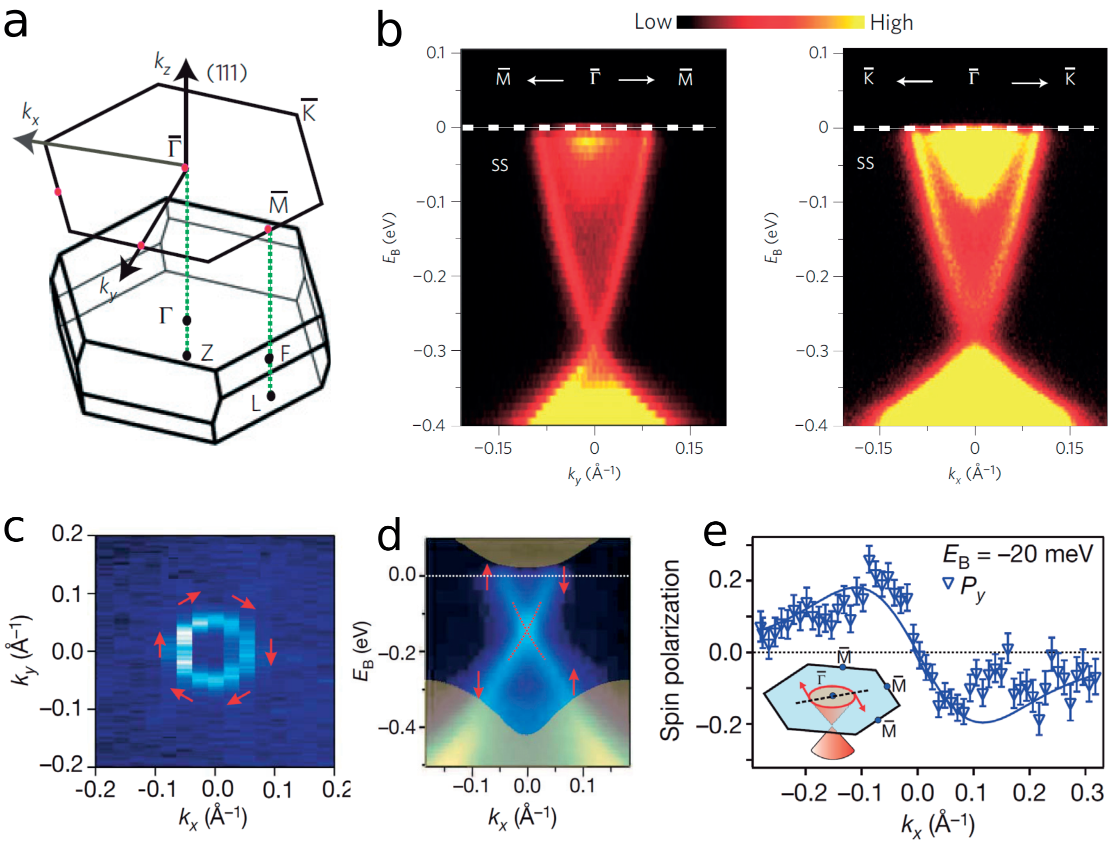

Figure 1.6 – **a** Bi_2Se_3 3D bulk Brillouin zone (BZ), and hexagonal 2D BZ of projected (111) surface. **b** Measured ARPES band dispersion of Bi_2Se_3 (111) surface, with two cuts along $\bar{\Gamma}$-$\bar{M}$ (left) and $\bar{\Gamma}$-$\bar{K}$ (right) in momentum space. ARPES intensity map for Bi_2Te_3, with a cut along k_y, close to the Fermi level (**c**), and with a cut along k_x (**d**). **c** Red arrows show the precession of the spin around the Dirac cone cut. **d** Red arrows showing spin for oppositely propagating states, shaded areas are projections of the bulk bands for Bi_2Te_3 onto the (111) surface. **e** y component of spin-polarization, measured along $\bar{\Gamma}$-$\bar{M}$ at $E_B = -20$ meV, therefore cutting only through surface states. Inset: A schematic of the cut direction. Adapted and reprinted with permission from Ref. [33] (**a**,**b**) and Ref. [34].(**c**,**d**,**e**).

A second reason being that Bi_2Se_3 has a relatively large bulk band gap of ~ 0.3eV [32, 37]. This implies the material's topological properties being robust even up to room temperature, which has important implications for potential applications. Finally, unlike the alloy $Bi_{1-x}Sb_x$, both Bi chalcogenides are of a stoichiometric composition. This allows high purity single crystal growth, facilitating experimental probing, for example in the case of ARPES making it easier to resolve surface states from those of the bulk.

Even though evidence of the Z_2 topology in the bismuth chalcogenides has been provided through surface sensitive techniques such as ARPES and STM/STS, the direct manipulation of the corresponding charge carriers and their associated properties, for example the spin helicity, has proved more difficult. This stems from the fact that in electron transport experiments lacking surface sensitivity, surface charge carriers are masked by contributions from the bulk. The underlying cause seems to be due to, in the case of Bi_2Se_3, n-type doping, either as a result of intrinsic Se vacancies [38–40], or inflicted by exposure to the ambient environment [39, 41, 42]. Various methods have been put forward to deal with this problem, one example being to counter dope the material, for example with Ca [33, 43, 44], however this also introduces additional defects. One particularly efficient strategy to mitigate bulk contributions is to form low-dimensional nanostructures, and, as shall be expanded on below, they also offer an intriguing platform to further investigate topological phenomena unique to these materials.

1.2.4 Tin Telluride

The first TCI material systems were predicted in SnTe and its related alloys Pb_xSn_{1-x}(Te,Se) [24]. In these materials, topologically non-trivial phases, protected by the underlying mirror symmetry of the crystal, give rise to metallic surface states on surfaces where mirror symmetry is preserved. Such non-trivial phases were subsequently experimentally observed, using ARPES, in SnTe [45], $Pb_xSn_{1-x}Se$ [46] and $Pb_xSn_{1-x}Te$ [47].

SnTe crystallizes in the rock-salt structure, see Fig.1.7**a**, and is composed of two interpenetrating FCC lattices, one for each atom type. This results in a FCC bulk Brillouin zone, which is a truncated octahedra with six hexagonal and four rectangular faces. At the centre of each of the four distinct hexagonal faces lie one of the equivalent L TRIM points, as shown in Fig.1.7**b**, which is also where the direct bulk band gap is centred.

The distinct topology of SnTe is rooted in band inversion occurring at the L points. For example, it has long been known that as the Sn concentration in the alloy $Pb_xSn_{1-x}Te$ is increased, thus transitioning from PbTe towards SnTe, the gap at L shuts (x ~ 0.35) and subsequently reopens, signalling a band inversion. This is further supported by more recent first-principles calculations [24, 48–51], whereby the valence (conduction) band at the L point is found to be composed of anion Te (cation Pb) orbitals, as one would expect from an ionic insulator such as PbTe. Conversely, in the case of SnTe the orbital composition is switched, with the valence (conduction) band composed of cation Sn (anion Te) orbitals. The fact that there is band inversion occurring at an even number (four) of TRIM (i.e. L points), results in, as has been discussed, a topologically trivial Z_2 order with invariants (0;000). However, each of the L points lie on planes in momentum space which are invariant to reflection about the {110} mirror planes of the FCC lattice in real space. This can be seen in Fig.1.7**b**, where L_1 and L_2 lie on the $\Gamma L_1 L_2$ plane, and L_3 and L_4 lie on the $\Gamma L_3 L_4$ plane, which are both invariant to reflection about the {110} planes, shown in yellow. Thus, this gives rise to a non-zero mirror Chern number of $N_m = -2$ [24], and defines SnTe as TCI, with a non-trivial topology protected by the mirror symmetry of the crystal.

As with Z_2 TIs, this non-trivial topological order implies the presence of gapless surface states. However, in the case of TCIs protected by mirror symmetry, there is an added stipulation in that as a given crystal surface has a symmetry lower than that of the bulk, only crystal surfaces where mirror symmetry is preserved are expected to harbour metallic states. With

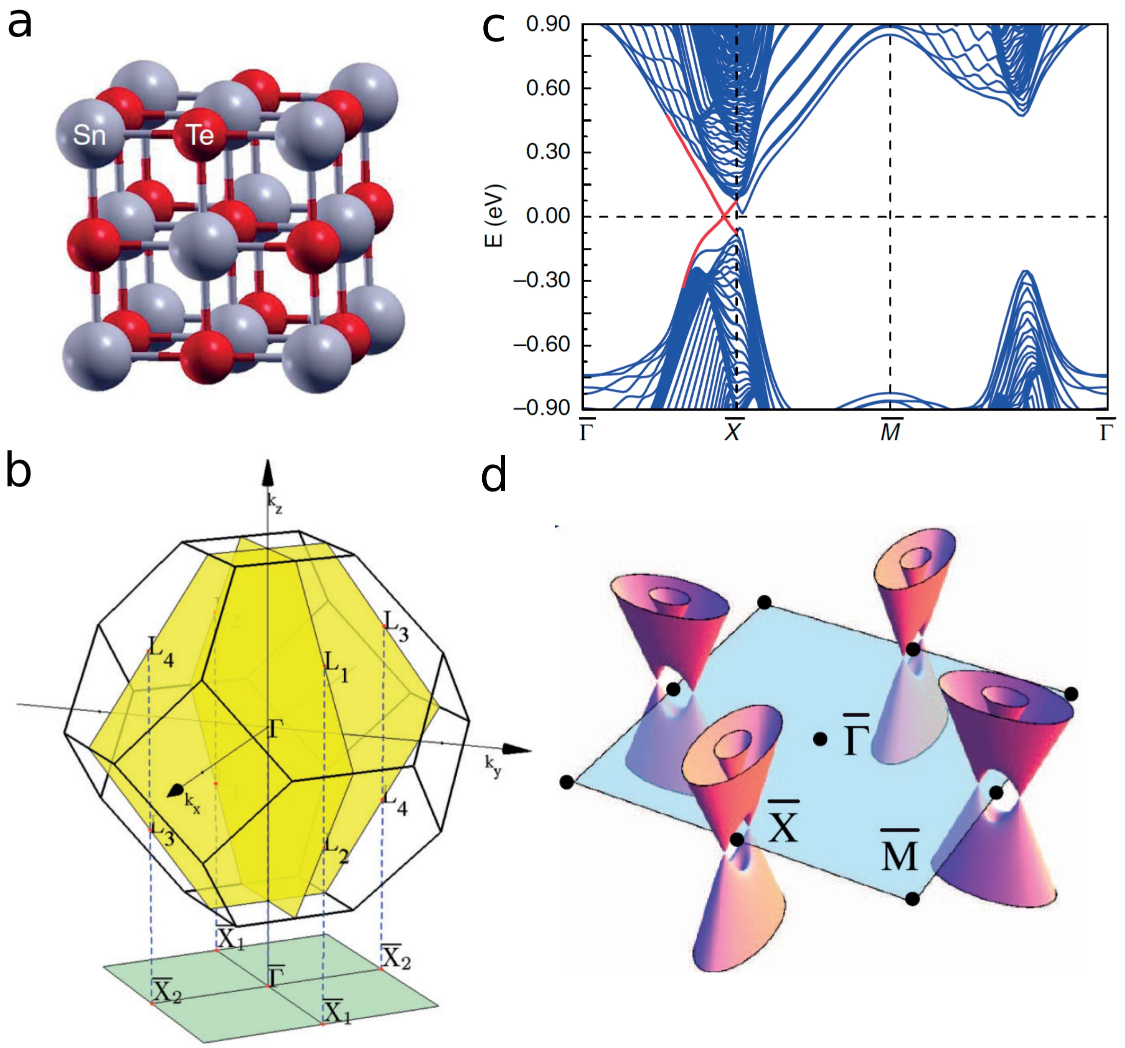

Figure 1.7 – **a** SnTe rock-salt crystal lattice. **b** SnTe face-centred-cubic Brillouin zone (BZ), orientated in direction of the (001) surface, whose 2D (BZ) is shown in green. In the 3D BZ the yellow planes are the {110} mirror planes with respect to the (001) surface. In the green 2D BZ of the (001) surface, the projection of the {110} mirror planes onto the $\bar{\Gamma}\bar{X}$ lines are also shown. **c** SnTe (001) surface band structure. The high symmetry $\bar{M}$ point corresponds to a corner of the 2D rectangular BZ in **b**, as can be seen in **d**. **d** (001) 2D BZ (blue plane), with schematic band structure showing four pairs of double Dirac cone surface states on either side of each $\bar{X}$ point. Adapted and reprinted with permission from Ref. [24] (**a**,**c**), Ref. [52] (**b**) and Ref. [53] (**d**).

respect to SnTe related TCIs specifically, a crystal surface must be symmetric about the {110} mirror planes. Three surfaces where this condition is met are the (001), (110) and (111) surfaces. Focusing on the (001) surface, the projection of the bulk Brillouin zone onto the surface is shown in Fig.1.7**b**. As can be seen, the mirror symmetric plane $\Gamma L_1 L_2$ is projected onto the $\bar{X}_1 - \bar{\Gamma} - \bar{X}_1$ line, with both L_1 and L_2 TRIM projected onto a single $\bar{X}_1$ point, in the surface Brillouin zone. Similarly, $\Gamma L_3 L_4$ is projected onto $\bar{X}_2 - \bar{\Gamma} - \bar{X}_2$, with L_3 and L_4 projected onto the single $\bar{X}_2$ point. This leads to a mirror Chern number of $N_m = -2$ [24], which requires that there should be two Dirac cones, formed from two spin-polarized surface states with opposite mirror eigen values, along each mirror-symmetric line, $\bar{X}_1 - \bar{\Gamma} - \bar{X}_1$ and $\bar{X}_2 - \bar{\Gamma} - \bar{X}_2$, thus giving a total of 4 Dirac points in the surface Brillouin zone. This was initially shown via first-principles band calculations [24], the corresponding band structure is shown in Fig.1.7**c**, where two especially intriguing features of the surface electronic structure were demonstrated. The first relates to the fact that the Dirac points are not located at $\bar{X}_{1,2}$, and are actually symmetrically positioned off that point, at $\bar{\Lambda}_{1,2}$, as can be seen in Fig.1.7**c**, resulting in a double-Dirac cone band structure, where two Dirac points are located either side of each $\bar{X}$, as is shown schematically in Fig.1.7**d**. This is an inherent consequence of the underlying mirror symmetry and related topological protection, as dictated by the mirror Chern number, of the TCI. And moreover results from the projection of two L points onto a single $\bar{X}$. Each $\bar{X}$ point lies on two mirror-invariant lines $\bar{\Gamma} - \bar{X}$ and $\bar{X} - \bar{M}$, as can be gleaned from Fig.1.7**b**. As $\bar{\Gamma} - \bar{X}$ is a projection of a mirror-symmetry invariant plane in the bulk Brillouin zone, whereas $\bar{X} - \bar{M}$ is not, thus the two low energy bands along $\bar{\Gamma} - \bar{X}$ have opposite mirror eigenvalues, whereas those along $\bar{X} - \bar{M}$ have the same [54]. Consequently, this results in a hybridization of the bands along $\bar{X} - \bar{M}$, which due to the mirror symmetry protected topology is forbidden along $\bar{\Gamma} - \bar{X}$, thus resulting in a crossing off $\bar{X}$, and the formation of a Dirac point, on each $\bar{\Gamma} - \bar{X}$ line. It is exactly this physics, specifically two Dirac cones positioned either side of each $\bar{X}$ with the same bands hybridized along $\bar{X} - \bar{M}$, which gives rise to the second intriguing feature of a Lifshitz transition. This describes how the Fermi surface topology varies with energy, at low energies close to the Dirac points, within the bulk band gap, it consists of two disconnected pockets. As the energy increases, the pockets touch each other on the line $\bar{X} - \bar{M}$, and subsequently connect, to form a large electron and small hole pocket, centred on $\bar{X}$, as shown around each $\bar{X}$ point in Fig.1.7**d** [24].

Experimentally, ARPES measurements on the (001) surface of SnTe [45], and related alloys [46, 47], confirmed the non-trivial topological phase described above. It was shown that the surface Brillouin zone consists of four Dirac cones, as represented by the first-principles calculations and ARPES data in Fig.1.8**b**. Furthermore, around each $\bar{X}$ point the presence of the double Dirac cone was also confirmed, as can be seen in Fig.1.8**a**, and more explicitly in Fig.1.8**b**, where one can also observe the linear dispersion associated with each Dirac cone. The helical spin polarization associated with the two Dirac cones in the vicinity of $\bar{X}$ was also measured. Using spin-resolved ARPES, measurements were taken along two cuts along $\bar{X} - \bar{\Gamma} - \bar{X}$, one just below the crossing of the Dirac points, and another further below in energy which cuts through the bulk valence band. Each of these cuts can be seen in Fig.1.8**b**. Spin polarization measurements were taken along each of these cuts, shown in the top part of Fig.1.8**d** for the cut associated with the Dirac cones, and in the lower part of Fig.1.8**d** for the valence band cut. As can be clearly observed, the bands in the former are spin polarized, whilst the states that belong to the valence band show no spin polarization, thereby confirming the helical spin texture. What is particularly interesting is that this provides an almost direct measurement, via spectroscopy, of the mirror Chern number, and confirm these materials as TCIs with a topology protected by the mirror symmetry of the crystal lattice.

Similarly to the bismuth chalcogenides, the non-trivial topological order in SnTe related materials has only been comprehensively shown via surface sensitive techniques, such as ARPES. Moreover, as with Bi_2Se_3 and Se vacancies leading to n-type doping, SnTe, as it is grown, is also heavily doped, in this case p-type doping [55–57] originating from intrinsic Sn vacancies [58]. This is reflected in high bulk carrier densities ranging between 10^{19} to 10^{21} cm^{-3} [58]. However, unlike Bi_2Se_3 which is a layered van der Waals material, and has a natural cleavage plane, whereby thin flakes can be formed via mechanical exfoliation, thus offering one relatively facile method to reduce bulk carrier contributions, in SnTe this is not possible, given its rocksalt crystal structure. As such, direct transport measurements probing the distinct properties of the materials surface states are lacking. One particularly attractive platform, with respect to SnTe, for enhancing contributions from surface states is increasing the surface to volume ratio via nanostructuring. Furthermore, as nanostructuring leads to the formation of different surfaces, given the material's crystal face dependent topological properties, in contrast to Bi_2Se_3, it offers the intriguing possibility to explore the interplay between topological phases belonging to distinct surfaces of a nanostructure, alongside conventional confinement effects. SnTe derived nanostructures shall be discussed in further detail below.

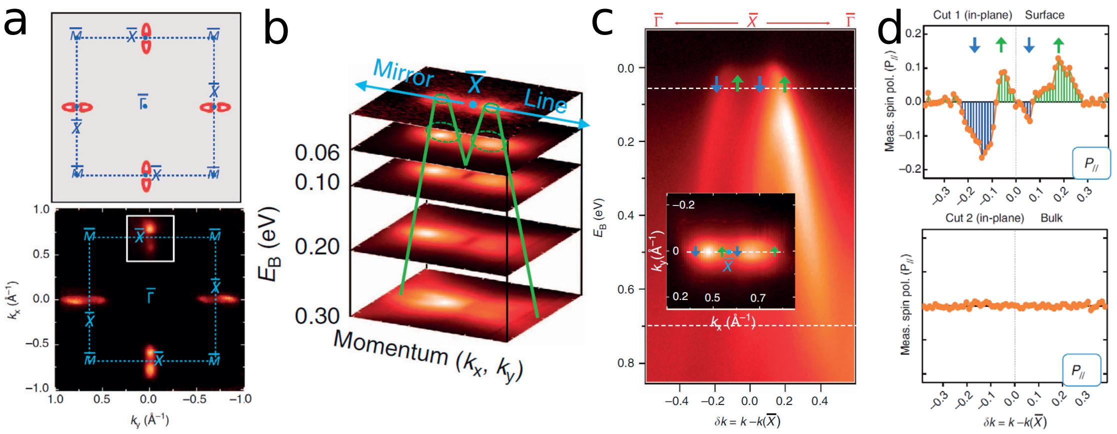

Figure 1.8 – **a** Topologically protected surface states of (001) surface in $Pb_{0.6}Sn_{0.4}Te$. (Top) Surface states calculated from first principles, with the energy cut taken at 0.02 eV below the Dirac point energy, shown in red. (Bottom) Measured ARPES Fermi surface mapping over the surface BZ at an equivalent energy cut. **b** Focusing on a pair of Dirac nodes associated with a single $\bar{X}$ point, for example corresponding to the white square in **a** (bottom). Measured momentum dispersion cuts taken at several energies below the Dirac points, allowing linear Dirac dispersion to be observed. The position of $\bar{X}$ on the mirror symmetric $\bar{\Gamma} - \bar{X} - \bar{\Gamma}$ is also labelled. **c** Measures ARPES momentum dispersion plot along an equivalent mirror symmetry line. Dotted lines represent binding energies (E_B), for which spin resolved measurements were taken, shown in **d**. Dotted line just below Dirac points has $E_B = 0.06$ eV, whilst for dotted line in valence band $E_B = 0.70$ eV. Inset: ARPES iso-energetic contour at $E_B = 0.06$, with blue and green arrows showing measured spin polarization. **d** Measured in-plane spin polarization at $E_B = 0.06$ eV (top), and $E_B = 0.7$ eV (bottom). Adapted and reprinted with permission from Ref. [47].

1.3 Nanostructures of Topological Materials

1.3.1 Bismuth Chalcogenides

An inherent problem associated with bismuth chalcogenide TIs is the difficulty in isolating surface state charge carriers from those of the bulk, as touched upon above. By enlarging the surface to volume ratio, a reduction in the dimensionality of the material is a direct method of enhancing surface contributions.

An immediate and relatively facile way of achieving this enhancement is to take advantage of the weak van der Waals bonding between quintuple layers in this family of materials. This can be accomplished via several different types of mechanical exfoliation, one example being to use the Scotch tape method [59], originally employed to isolate individual graphene flakes from graphite [60], to generate nano flakes. An advantage of the method is its simplicity, however, it is difficult to derive flakes of a consistent shape with smooth edges, and given the nature of the technique it is obviously not scalable. Alternatively, an atomic force microscopy tip has been utilized to exfoliate nanoribbons, possessing smooth surfaces, down to a width of a single quintuple layer [61], but this technique has similar associated problems with respect to scalability. Finally, solution based processing can be used to disperse layers to form nano flakes or films in much larger quantities [62], but again with no direct control over quality or morphology.

A far greater handle over the morphology of nanostructures, alongside the ability to produce them at larger quantities, is available through a series of alternative techniques. Two related mechanisms resulting from chemical vapour deposition (CVD) have been widely harnessed to synthesize single crystal, high quality nanostructures of well defined morphologies. The first is the gold-catalysed vapour-liquid-solid (VLS) mechanism [63, 64], used to grow one-dimensional (1D) nanoribbons and nanowires [65]. The presence of the liquid phase Au particle catalyses the adsorption of vapour phase reagents to supersaturation levels, allowing nucleation to occur, from which crystal growth proceeds from the nucleated seeds at the liquid-solid interface. Distinctive features of the mechanism are that the position of the catalyst dictates the growth direction, which is predominantly unidirectional, whilst its size determines the relative thickness or diameter, of the subsequent nanoribbon or nanowire, respectively. More specifically, in the case of Bi_2Se_3 [65], for example, the material is placed in powdered form at the centre of a tube furnace, where it is evaporated and is subsequently transported, via an Ar gas flow, downstream, where a silicon substrate bearing Au nanoparticles is placed, upon which the interaction with Bi_2Se_3 vapour leads to the aforementioned VLS mechanism, and the formation of crystallized nanostructures. A degree of morphological control is possible based on the position of the substrate and catalyst platform relative to the furnace centre. The placement of the platform closer to the centre, where temperatures are higher, results in the formation of primarily one-dimensional nanoribbons and nanowires. A primary structural differentiator between the two, is that in nanowires growth is parallel to the c axis, i.e. the (001) direction, which is also the direction along which QLs stack (Fig.2.2**a**), which gives rise to rough surfaces along the wire, as can be seen in Fig.1.9**b**. Conversely, in the case of nanoribbons, growth is along an axial direction perpendicular to the *c* axis and (001) direction, which results in smooth top and side surfaces, as can be seen in Fig.1.9**a**. The placement of the substrate platform further from the centre, where temperatures are lower, leads to the formation of solely nanoribbons, with morphologies that are not strictly 1D, for example sawtooth and zig-zag like nanoribbons, as can be seen in Ref. [65]. In the case of nanowires the diameter is defined by the size of the Au catalyst, which is typically ~ 20 nm [66], whilst the length ranges from hundreds of nanometres to tens of micrometres [65]. Nanoribbons have thicknesses ranging from 20 to 100 nm [67], which is again dictated by the size of the Au catalyst, widths vary from 50 nm to tens of micrometers, whilst one dimensional ribbons are ordinarily several micrometers long, however, this can increase to over 100 μm [65]. Also observed in the low temperature region are the presence of hexagonal nanoplates [68], which are distinct to 1D nanoribbons and wires in that their growth on the underlying substrate is accompanied by a complete absence of a Au catalyst nanoparticle, which implies the vapour-solid (VS) mechanism. In contrast to the VLS mechanism, growth is not catalysed by Au nanoparticles, with nucleation occurring directly on the underlying substrate. Defining features of nanoplates are that they tend to be thin, with thickness down to a few QL (where 1QL ~ 1 nm), whilst their lateral dimensions are far greater, on the order of micrometers. Furthermore, their shapes, generally of hexagonal or triangular morphology, with facets at 60°or 120°at the edges, are governed by the underlying symmetry of the crystal lattice [68], an example of a hexagonal nanoplate is shown in Fig.1.9**c**. Both VLS and VS mechanism generate TI nanostructures of a high crystalline quality, and particularly in the case of the VLS mechanism, strain effects, due to the choice of the growth substrate associated with thin-film techniques, such as molecular beam epitaxy (MBE) [69], are avoided as the nanostructures grow off the substrate.

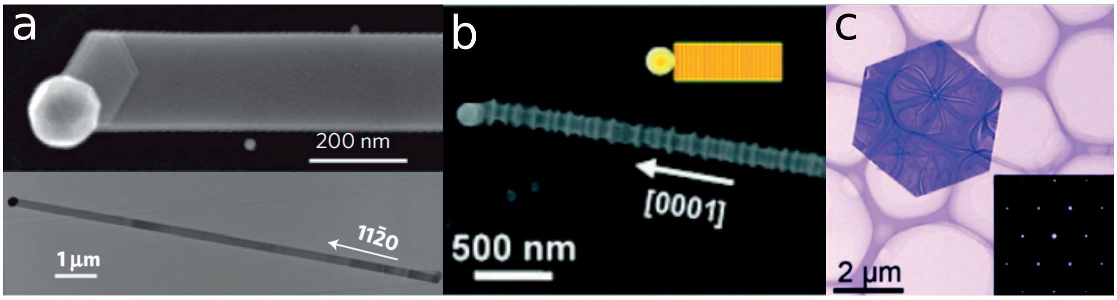

Figure 1.9 – Experimental images of synthesized Bi_2Se_3 nanostructures. **a** (top) Zoomed in transmission electron microscopy (TEM) image of a Bi_2Se_3 nanoribbon, with a Au catalyst nanoparticle at the end. (bottom) Larger scale view showing growth along the $[11\bar{2}0]$ direction. **b** Scanning electron microscopy (SEM) image of a Bi_2Se_3 nanowire grown along the *c* axis parallel to the [0001] direction. **c** TEM image of a hexagonal Bi_2Te_3 nanoplate. The inset is a selected area diffraction pattern taken along the [0001] direction. Adapted and reprinted with permission from Refs. [65, 67, 70], respectively.

Nanoribbons, nanowires, and nanoplates constitute the three primary morphologies of bismuth chalcogenide TI nanostructures. Two other techniques employed to generate them are van der Waals (VDW) epitaxy [71] and chemical synthesis, for example via a solvothermal process. A distinct advantage of VDW epitaxy is that it avoids a problem associated with traditional epitaxial techniques such as MBE, which is constrained by the lattice matching condition between the growth substrate and the epitaxial layer. As bismuth chalcogenides are layered VDW materials, the growth of these materials onto the substrate is governed by weak VDW forces, and consequently the need for the two lattices to match is lifted. This process functions optimally if the substrate is also a layered VDW material, with a chemically inert surface, i.e. in possession of no dangling bonds, one prime example being a mica substrate [72]. VDW epitaxy has been used to controllably grow nanoplates, of both trigonal and hexagonal morphologies, on various substrates, with optimal conditions on mica [72–74], where control over the specific morphology and thickness has been exhibited. One particularly attractive aspect of the method is that it can be slightly modified, in what has been termed selective area VDW epitaxy [72], to allow control over the growth position. Specifically, as growth is locally confined to initial nucleation sites, once these sites are defined this leads to the formation of nanoplate arrays. By confining nucleation sites to specific positions, for example via the use of patterned PMMA films or copper grids as lithography masks, this enables the growth of periodic ordered arrays of nanoplates [72]. This could be a versatile tool in device applications, with potential uses already being explored [74].

Chemical synthesis, in particular via a solvothermal process, is another method to generate TI nanostructures [70, 75, 76]. Given that the reaction conditions in the solvothermal process are relatively non-stringent, for example short reaction times and low temperatures, this allows control of nanostructure morphology. Moreover, a degree of tuning over material properties is also enabled through additional chemical doping [70]. The method has been used to generate high crystalline quality samples of nanoribbons [75] and nanoplates [70, 76].

As has been described one motivating factor in synthesizing bismuth chalcogenide TI nanostructures is to manifest properties of surface states in transport measurements. To this end, given the Dirac dispersion of the charge carriers, and similarly to graphene [60], one signature should be the ambipolar field effect, whereby surface state charge carriers can be tuned smoothly between electrons and holes, with an associated minimum in conductivity as the Fermi level passes through the Dirac point. Even in TI nanostructures, bulk contributions can still overwhelm those from the surface, thus additional tools utilised to isolate surface states are through doping and field-effect gating. Such Fermi level tuning has subsequently allowed the ambipolar field effect and a minimum in conductivity to be detected by measuring a peak in resistance (Fig.1.10**a**-top), a sign change in Hall resistance (Fig.1.10**a**-bottom) and a linear dependence of carrier density at low and high gate voltages [76–80].

Another signature which allows bulk transport to be differentiated from that of the surface is through magnetotransport measurements. Specifically, through magnetoconductance oscillations, i.e. Shubnikov-de Haas (SdH) oscillations, where the conductivity oscillates periodically as a function of the inverse of the applied magnetic field $1/B$, and where the

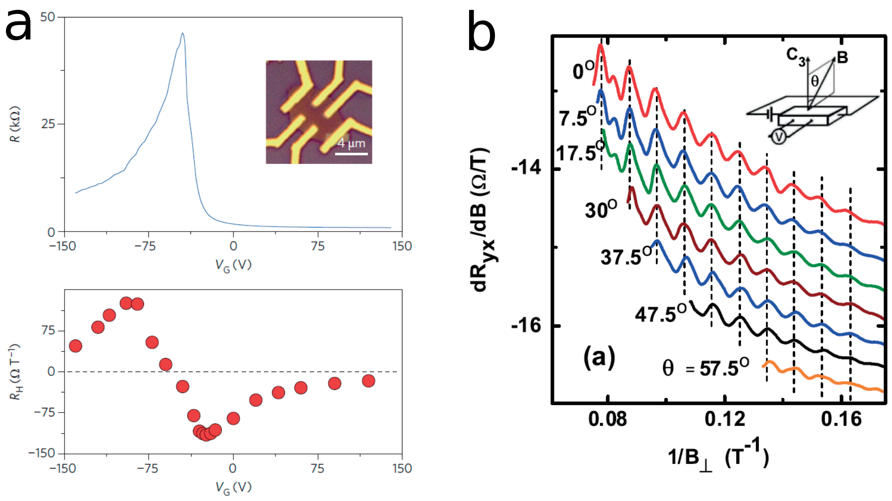

Figure 1.10 – **a** Ambipolar field effect in $Bi_xSb_{1-x}Te_3$ nanoplates. (Top) Dependence of R on gate voltage $V_G \sim 5$ nm thick nanoplate, showing a sharp peak in resistance. Inset: atomic force microscopy (AFM) image of field-effect transistor (FET) measurement device. (bottom) High-field Hall coefficient R_H plotted against V_G for the same nanoplate. Peak at R (top) corresponds to a change in sign in R_H (bottom), at an equivalent V_G. **b** SdH oscillations observed in a 10 nm thick Bi_2Se_3 film, grown by MBE. $\mathrm{d}R_{xy}/\mathrm{d}B$ is plotted as a function of $1/B_\perp$ ($= 1/B\cos\theta$). Adapted and reprinted with permission from Ref. [78] (**a**) and Ref. [81].

oscillatory part of the longitudinal conductivity σ_{xx} is given by [66]:

$$\Delta\sigma_{xx} \sim cos\left[2\pi\left(\frac{F}{B} - \frac{1}{2} + \beta\right)\right] \tag{1.19}$$

where F is the oscillation frequency and β is a phase shift term. In order to determine whether SdH oscillations are of a two dimensional nature, and therefore implying surface origin, the behaviour of the oscillation frequency F as a function of the angle θ, where θ is the tilt angle between the magnetic field direction and the surface normal, can be investigated. Ordinarily, this is accomplished by plotting the resistivity derivative, dR_{xy}/dB, as a function of the inverse of the perpendicular component of the magnetic field, $1/B_\perp$ where $B_\perp = B\cos\theta$ [41]. If F varies as $\sim 1/\cos\theta$, this is a strong indicator of the SdH having a 2D origin [41, 66], as can be seen in experimental data shown in Fig.1.10**b**. Such oscillations have been observed in both bismuth chalcogenide thin films [41, 81, 82] and nanostructures [70, 75, 79].

One final transport signature that shall be discussed is the Aharonov-Bohm (AB) interference, it is of particular interest as it highlights some aspects of the fascinating interplay between the finite size effects and morphology of nanostructures and the topological properties of surface states. For electron waves, following closed trajectories encircling a certain magnetic flux, the effect of the flux is to alter the relative phase of the electron waves, leading to interference, which is termed the Aharonov-Bohm effect [83]. Specifically, the wavefunction of the particles pick up a phase of $2\pi\phi/\phi_0$, solely determined by the magnetic flux ϕ, and where $\phi_0 = h/e$ is the flux quantum. This gives rise to periodic oscillations in magnetoconductance, with the AB effect having a characteristic periodicity of oscillation of flux quantum h/e, which was first observed in 2D metallic rings [84]. An ordinary hollow, metallic cylinder with a conducting surface, which can be seen as a series of infinite 2D rings, threaded through its core by a magnetic flux, also displays such periodic oscillations in magnetoconductance [85]. However, in this case the oscillations now have a periodicity $h/2e$, and are termed Altshuler-Aronov-Spivak (AAS) oscillations [85], and are a result of interference between clockwise and anti-clockwise circulating trajectories around the cylinder, and have been observed in carbon nanotubes [86]. The absence of h/e oscillations in the cylindrical case, stems from the fact that, as h/e oscillations can be thought of as originating from 2D ring slices comprising the cylinder, different ring slices have h/e oscillations of different phases, therefore over the cylinder taken as whole they average out.

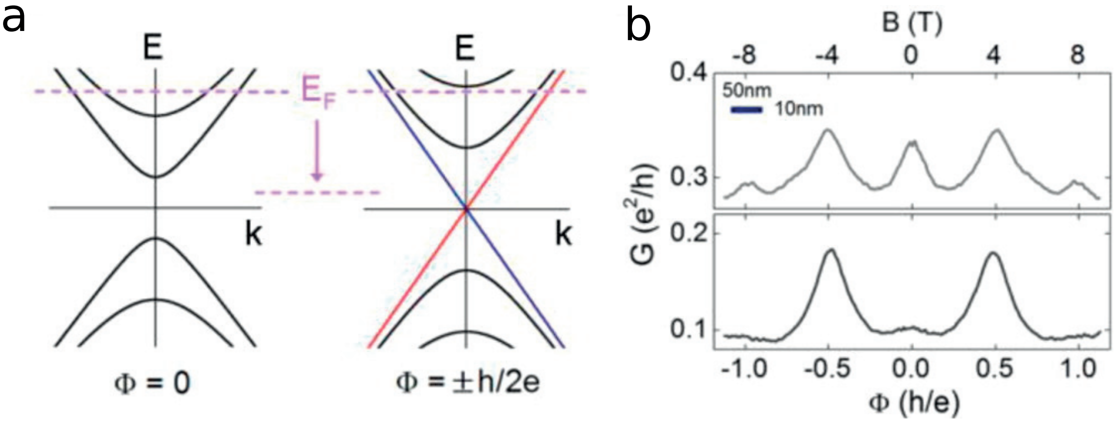

Figure 1.11 – **a** Schematic band structure of a strong TI nanowire showing 1D modes at two flux quantum values of $\phi = 0$ (left) and $\pm h/2e$ (right). **b** Magnetoconductance measurements at V_g = -25 (top), which is representative of the Fermi level cutting through several subands, as can be seen in **a**, and V_g = -45 (bottom), which positions the Fermi level close to the Dirac point, as shown in **a**, and cutting through the single, topologically protected 1D mode. Adapted and reprinted with permission from Ref. [87].

Given topological insulators are insulating in the bulk and conducting on the surface, the unique morphology of the aforementioned TI nanostructures, means they can be seen as hollow metallic cylinders. Initial investigations into the AB effect in TI nanostructures, surprisingly, observed magnetconductance oscillations with a periodicity of h/e [67,75,88]. However, subsequent theoretical [89–91] and experimental works [87] have shown this as a direct consequence of the morphology of the nanostructures and the topological properties of the TI surface states. Specifically, as the electron mean free path is greater than the perimeter of the nanostructure cross section, this leads to momentum quantization and the formation of discrete 1D subbands. Furthermore, spin-momentum locking in TIs results in electrons picking up a π Berry phase, due to the 2π rotation of the spin around the nanostructure perimeter. Combined, both factors result in a band structure, which remains gapped at magnetic flux values of $\phi = 0$. However, when the nanostructures are threaded by specific values of magnetic flux, i.e. at odd half-integers ($\phi = \pm h/2e, \pm 3h/2e, \ldots$), the cancellation of the AB phase and π Berry phase, results in a single, topologically protected, 1D mode. This can be seen in the two schematic band structures displayed in Fig.1.11**a**. Thus, at such specific values of magnetic flux, for example $\phi = 0$ and $\pm h/2e$, if the Fermi level is located close to the Dirac point (Fig.1.11**b**-bottom plot), the conductance should exhibit a minimum at $\phi = 0$ and a maximum at $\pm h/2e$, with an oscillation periodicity of h/e. When the Fermi level is located away from the Dirac point (Fig.1.11**b**-bottom plot) and cuts through more than the single topologically protected mode, a conductance peak is also seen at zero flux $\phi = 0$. This was recently experimentally observed [87, 92], with some representative data shown in Fig.1.11**b**, and is a direct transport based measurement of the helical surface states, and an indirect confirmation of the Berry phase.

1.3.2 Tin Telluride

SnTe is heavily p-type doped, as described above, thus, as with the bismuth chalcogenides, accessing and manipulating surface states directly via bulk transport measurements is difficult. A further complication in the case of SnTe is that it has a cubic, rock-salt crystal structure, and therefore is not a layered vdW material, hence mechanical exfoliation, as a facile method of quickly and simply producing lower dimensional structures, is not possible. Subsequently, lowering the dimensionality of the material by forming thin films and nanostructures offers an attractive platform to enhance surface contributions, again for similar reasons that were detailed above for the bismuth chalcogenides. More interestingly, as the topological protection of the surface states in SnTe, and its related alloys, is due to the mirror symmetry of the crystal, rather than time reversal symmetry, this topological protection is far more sensitive to dimensionality reduction than in the case of strong TIs. As a simple example, in the case of Bi_2Se_3, which is a strong TI with Z_2 invariants (1;000), in theory, the presence of a single Dirac cone centre at Γ is independent of the surface orientation. In the case of TCIs such as SnTe, this is not the case where topological protection is only present on defined surfaces, as has been described. Thus, a key overarching focus of the work related to this section, as shall be highlighted with some examples below, is to further explore how dimensionality reduction impacts upon the mirror symmetry protected topology.

Experimentally, thin films of SnTe and its related alloys have been grown on a variety of substrates, such as Bi_2Te_3 [81], $SrTiO_3$(001) [93] and Si(111) [94], via MBE. Transport measurements for the SnTe (111) surface grown on Bi_2Te_3 [81] revealed SdH oscillations, which were suggestive of Dirac fermion mediated transport. More recent work for (001) thin films of the alloy $Pb_{1-x}Sn_xSe$ grown on $SrTiO_3$(111) [95], have measured the ambipolar field effect, and also the formation of massive Dirac fermions accompanying a gap opening due to surface hybridization, as the thin film approaches the 2D limit. Given the film thickness at which this occurs (~ 10 nm), this is suggestive of a heightened sensitivity to finite-size effects relative to bismuth chalcogenide TIs [95, 96]. Another aspect of the less robust topological protection offered by crystal, relative to time reversal, symmetry in TCIs, is that the surface states are far more amenable to external perturbations, as crystal symmetry can be rather easily broken. This offers a degree of tunability over electronic properties, which could be harnessed for potential device applications. One theoretical study [97] has predicted that a topologically non-trivial phase in SnTe (001) thin films persists down to a thickness of a few atomic layers, with an inverted band band structure at the $\bar{\mathrm{X}}$ points (Fig.1.7), indicating a 2D TCI phase over a wide range of film thicknesses. Moreover, as this 2D TCI is defined by a pair of spin filtered edge states crossing at the non-time-reversal-invariant momenta $\bar{\Lambda}$ (where in the 3D limit the gap approaches zero), the sole form of topological protection is through the mirror symmetry of the crystal. As this mirror symmetry can be broken by an applied electric field, thereby gapping the spin filtered edge states, it was postulated that this edge channel can be thought of as a topological transistor, with spin and charge transport coupled, controllable by an external electric field. More fundamentally, and really highlighting the sensitivity of the mirror symmetry protected topology with respect to dimensionality reduction, was a study which showed that TCI thin films composed of an odd or even number of layers display different topological properties [96]. This stems from symmetry reasons, as odd layers have mirror symmetry, whilst even do not. This shall be discussed in far more detail in the Results section. Intriguingly, it was subsequently predicted that depending on the film thickness (111) thin films of SnTe related TCIs can exhibit the quantum spin Hall phase in a wide range of thicknesses [98, 99], and, furthermore, with this phase tunable under an external electric field [98].

As briefly showcased by some of the examples above, even on transitioning from the bulk to thin films, SnTe TCIs display a rich playground of physics. A further reduction in dimensionality, to form nanostructures, should widen the possibilities yet further. This is based on the reasoning that, firstly, only specific surfaces of SnTe TCIs harbour topologically non-trivial phases, with the phase on each surface distinct, as dictated by its crystal symmetry. Thus, as nanostructures can display multiple surfaces, the interplay between different surfaces could give rise to interesting topological phenomena. Secondly, as nanostructures tend be of a well defined morphology and given their dimensions, this should not only give rise to interference-type effects, for example AB oscillations described above, but also the combination of quantum confinement combined with the mirror symmetry protected topology of different surfaces, is also likely to lead to novel physics. Finally, taking each of these factors individually, or in unison, alongside the amenability of the mirror symmetry protected topology to a variety of perturbations, could enable a wide degree of tunability over any observed phenomena.

The predominant synthesis method for SnTe TCI nanostructures, thus far, has been CVD growth via the (Au catalysed) VLS and VS mechanisms [100, 102–104], described above. Several distinct morphologies are observed, as a consequence of the growth mechanism and the underlying cubic symmetry. Broadly, these fall into four categories: nanowires, nanoribbons, nanoplates and nanocubes, examples of which can be seen in Fig.1.12. For all nanostructure morphologies, two surfaces tend to dominate, the $\{100\}$ and the $\{111\}$ surfaces [100, 102]. The $\{100\}$ surfaces are calculated to be more energetically favourable, and are observed at higher growth conditions, whilst $\{111\}$ surfaces, are calculated to be energetically less favourable, and are observed at lower growth temperatures and in a Te rich environment [100, 102]. In terms of

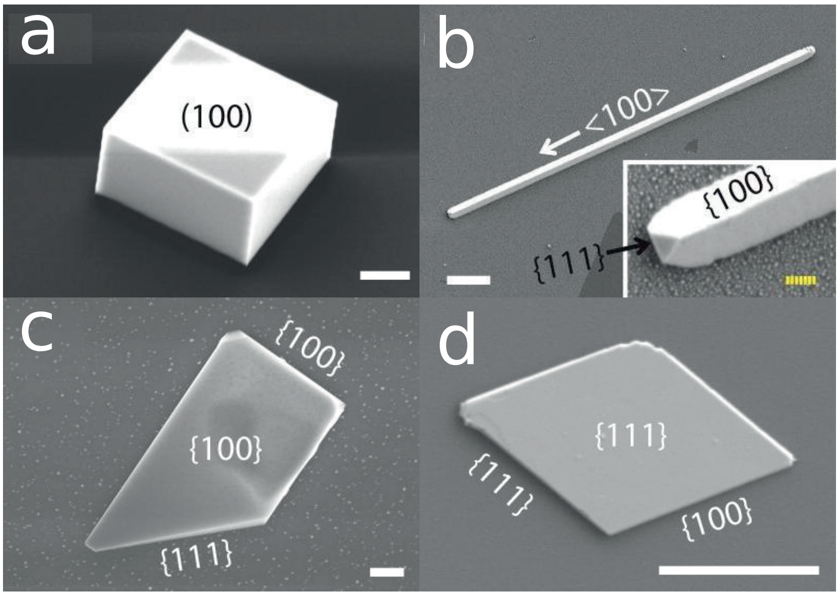

Figure 1.12 – TEM (**a**,**c**,**d**) and SEM images (**b**) of experimentally synthesized SnTe nanostructures. **a** {100} nanocube. **b** {100} nanowire showing a perfectly square cross section. **c** {100} nanoplate. **d** {111} nanoplate. Scale bars in **a**,**c** and **d** are 2 μm and 100 nm in **d**, for the inset in **b** the scale bar corresponding to the dashed yellow line is 200 nm. Facets are marked on each structure. Adapted and reprinted with permission from Ref. [100] (**a**,**c**,**d**) and Ref. [101] (**b**).

actual morphologies, nanocubes are observed in the absence of an Au catalyst, indicating VS growth, at high temperatures all surfaces of the cube are {100} planes, an example is shown in Fig.1.12**a**. At lower temperatures and in a Te rich environment {100} planes dominate, as can be seen in Ref. [102]. The cubic structure clearly stems from the underlying cubic symmetry of the crystal. In the presence of a Au catalyst, indicating VLS growth, at high temperatures, cubic nanowires are formed with a constant cross section, and where each surface again corresponds to a {100} plane, an example is shown in Fig.1.12**b**. At lower temperatures, in a Te rich environment, zig-zag nanowires are formed, showing both {111} and {100} surfaces, with {111} surface dominant, as can be seen in Ref. [102]. Two distinct morphologies of nanoplates and nanoribbons are observed, with top (and bottom) surfaces corresponding to either {100}, observed at high temperature, or {111}, observed at low temperature, surfaces [100]. For {100} nanoplates, side facets occur at angles of 45°, 90°or 135°, implying the presence of {100} or {111} planes as side surfaces, an example is shown in Fig.1.12**c**. For {111} nanoplates, side facets occur at angles of 30°, 60°or 120°, again implying {100} or {111} planes as side surfaces, an example is shown in Fig.1.12**d**. Nanoribbons can just be seen as a thinner version of nanoplates, with the same information pertaining to side surfaces. Examples of a {100} and {111} nanoplate are shown in Figs.1.12**c**,**d**, respectively. For both nanoplates and nanoribbons, the presence of a Au catalyst is observed, indicating VLS growth, however, the fact that the nanoplates and nanoribbons tend to be wider than the catalyst particle, implies additional growth via the VS mechanism [100]. Overall, the observed morphologies tend to be high quality, single crystalline nanostructures, with clean surface terminations, important for potential applications.

Taking into account the relative nascency of the field, transport measurements on TCIs nanostructures are lacking, however, a few have been performed [100, 101, 105, 106]. For example, AB and SdH oscillations have been observed in SnTe cubic nanowires [105]. But given that mirror symmetry protected topology is less robust, relative to Z_2 time reversal protection, particularly with respect to surface orientation, and that the nanowires in Ref. [105] have surfaces which do not all correspond to those showing a topologically protected phase, the observed AB oscillations are probably not a definitive signature of topological surface states protected by mirror symmetry. Other transport experiments, include the observation of weak antilocalization in $Pb_xSn_{1-x}Te$ $\{100\}$ cubic nanowires, when the Sn content (x) reaches $x \sim 0.38$, suggesting a topological phase transition from trivial to non-trivial [106].

1.4 Outline

The purpose of the above was to initially provide a brief and select overview of developments that culminated in the discovery of the Z_2 topological insulator (TI) phase in Bi_2Se_3 and Bi_2Te_3, and the topological crystalline insulator (TCI) phase in SnTe. Given the challenges associated with directly accessing and manipulating topological surface states (TSS) in the respective bulk crystals, we highlighted the unique solutions offered by nanostructuring. Furthermore, it was also touched upon how confinement of TSS may give rise to novel phenomena. From a general perspective, it is also worth mentioning that the continued shrinking of solid state devices imply that nanostructures are likely to play a prominent role in device based applications that seek to harness the properties of TSS. In light of these factors, this work theoretically investigates how nanoscale confinement in the Z_2 TIs Bi_2Se_3 and Bi_2Te_3, and the TCI SnTe, impacts upon electronic structure and properties derived from the bulk topological phase

The remainder of this work is outlined as follows. The proceeding Chapter 2, presents the foundational concepts of the computational methods employed, primarily density functional theory (DFT) and the tight-binding (TB) approximation. A more specific discussion regarding the application of first-principles DFT calculations to investigate topologically insulating phases is also given, alongside a description of the Bi_2Se_3, Bi_2Te_3 and SnTe TB parameters utilised. The hexagonal symmetry and QL stacking of the bismuth chalcogenides entail that nanostructures inevitably expose surfaces other than the (001). As such, Chapter 3 presents our work on the high-index facets of Bi_2Se_3 and Bi_2Te_3. Chapter 4 serves as a natural extension, and describes our work on realistic Bi_2Se_3 nanostructures. A particular focus is paid to how the band dispersion and spin helicity of the 2D surface Dirac cone is exhibited in the electronic spectra of 1D nanowires and nanoribbons. The simpler cubic crystal structure and the mirror-symmetry-dependent topology of SnTe results in a rich interplay between the non-trivial topology and the underlying crystal structure. Thus, finally, Chapter 5 concerns our work on the manifestation of the crystal-symmetry-dependent 2D TCI phases of SnTe (001) thin films in nanowires of related symmetry.

2 Methodology

2.1 Density Functional Theory

2.1.1 General Formalism

For realistic systems, comprised of interacting electron and nuclei, electronic structure theory involves the solution of the many-body Schrödinger equation, given by

$$\hat{H}\Psi = E\Psi \tag{2.1}$$

$$\hat{H} = -\sum_i \frac{\hbar^2}{2m_e}\nabla^2_{\boldsymbol{r}_i} - \sum_I \frac{\hbar^2}{2M_I}\nabla^2_{\boldsymbol{R}_I} + \frac{1}{2}\sum_{i\neq j}\frac{e^2}{|\boldsymbol{r}_i - \boldsymbol{r}_j|} + \frac{1}{2}\sum_{I\neq J}\frac{Z_I Z_J e^2}{|\boldsymbol{R}_I - \boldsymbol{R}_J|} - \sum_{i,I}\frac{Z_I e^2}{|\boldsymbol{r}_i - \boldsymbol{R}_I|} \tag{2.2}$$

where $\hbar$ corresponds to the reduced Planck constant, electrons are denoted by a lower case subscript with mass m_e, whilst nuclei are labelled with upper case subscripts, with the Ith nucleus, having a mass M_I and atomic number Z_I. Application of the Born-Oppenheimer approximation [107] further simplifies the Hamiltonian in equation (2.2) to

$$\hat{H} = -\sum_i \frac{\hbar^2}{2m_e}\nabla^2_{\boldsymbol{r}_i} + \frac{1}{2}\sum_{i\neq j}\frac{e^2}{|\boldsymbol{r}_i - \boldsymbol{r}_j|} + \sum_i V_{ext}(\boldsymbol{r}_i) + E_{II} \tag{2.3}$$

where the external potential, V_{ext}, of the nuclei on the electrons is

$$V_{ext}(\boldsymbol{r}) = -\sum_I \frac{Z_I e^2}{|\boldsymbol{r} - \boldsymbol{R}_I|} \tag{2.4}$$

and E_{II} is the classical electrostatic interaction between two nuclei.

A central premise of DFT is reducing the significant complexity in solving Eq.2.1, by reformulating the complex interacting many-electron problem, described by the Hamiltonian in Eq.2.3, as a far simpler non-interacting single-electron problem. This stems from the two underpinning tenets of the theorem, defined by Hohenberg and Kohn [108]:

- **Theorem I:** For any system of interacting electrons in an external potential $V_{ext}(\boldsymbol{r})$, the potential is determined uniquely, aside from an additive constant, by the ground state electron density $n_0(\boldsymbol{r})$.

Since knowledge of the external potential, $V_{ext}(\boldsymbol{r})$, completely defines the Hamiltonian (Eq.2.3), up to a constant shift, which in turn completely defines the many-body wavefunctions, all the ground state properties of a system are thus, in principle, determined by $n_0(\boldsymbol{r})$.

- **Theorem II:** For all densities $n(\boldsymbol{r})$ that are ground state densities to some external potential $V_{ext}(\boldsymbol{r})$, such that $\int n(\boldsymbol{r})d\boldsymbol{r} = N$ where N is number of electrons in the system, a functional for the energy $E[n]$ in terms of the density $n(\boldsymbol{r})$ can be defined, which holds for any potential $V_{ext}(\boldsymbol{r})$. The form of this functional is given by

  $$E[n] = F[n] + \int V_{ext}(\boldsymbol{r})n(\boldsymbol{r})d\boldsymbol{r} + E_{II} \tag{2.5}$$

  and for a given external potential $V_{ext}(\boldsymbol{r})$, the global minimum of $E[n]$ at the exact ground state density $n_0(\boldsymbol{r})$ corresponds to the exact ground state energy.

The universal functional $F[n]$, where

$$F[n] = T[n] + E_{int}[n] \tag{2.6}$$

defines the internal kinetic and potential energies, respectively, of an interacting electron system. The universality of $F[n]$ stems from the fact that $T[n]$ and $E_{int}[n]$ are functionals of just the density, furthermore that the functional is independent of the external potential $V_{ext}(\boldsymbol{r})$. If the form of $F[n]$ was known, the minimization of Eq.2.5 with respect to the density, would yield the exact ground state density and energy. Theorem II subsequently amounts to the variational principle for the ground state energy in terms of the electron density. More generally, the existence of $F[n]$ means that instead of dealing with a many-electron wavefunction comprised of $3N$ variables, the problem is greatly reduced to dealing with the three dimensional electron density.

The most commonly used practical implementation of DFT is that devised by Kohn and Sham [109], which rests upon the assumption that the exact ground state density of an interacting electron system can be represented by a fictitious system of non-interacting electrons. A primary step in this implementation is to define an auxiliary Hamiltonian

$$\hat{H}_{aux} = -\frac{1}{2}\nabla^2 + V_{KS}(\boldsymbol{r}) \tag{2.7}$$

which describes a system of N non-interacting electrons, where the ground state has one electron in each of the N orbitals $\psi_i(\boldsymbol{r})$ with lowest energy eigenvalues ϵ_i. The density of this auxiliary system is constructed from summing the squares of the orbitals $\psi_i(\boldsymbol{r})$:

$$n(\boldsymbol{r}) = \sum_{i=1}^{N} |\psi_i(\boldsymbol{r})|^2 \tag{2.8}$$

In dealing with electrons described by single orbital wavefunctions $\psi_i(\boldsymbol{r})$, a defining principal of the Kohn-Sham formulation is to split the internal energies of the interacting electron system in Eq.2.6 into an independent electron kinetic energy T_{KS}

$$T_{KS}[n] = -\frac{\hbar^2}{2m_e} \sum_i \langle \psi_i | \nabla^2 | \psi_i \rangle \tag{2.9}$$

and Hartree energy E_H

$$E_H[n] = \frac{e^2}{2} \int \frac{n(\boldsymbol{r})n(\boldsymbol{r'})}{|\boldsymbol{r}-\boldsymbol{r'}|} d\boldsymbol{r}\, d\boldsymbol{r'} \tag{2.10}$$

and a third term, the exchange-correlation functional $E_{xc}[n]$. Consequently, the energy functional for a many-electron system, given in Eq.2.5, can be redefined as

$$E[n] = T_{KS}[n] + E_H[n] + \int V_{ext}(\boldsymbol{r}) n(\boldsymbol{r}) d\boldsymbol{r} + E_{II} + E_{xc}. \tag{2.11}$$

All the complex many-body interactions are now confined to the exchange-correlation functional, $E_{xc}[n]$, which contains the non-classical electron interaction energy and the kinetic energy difference between the interacting and non-interacting systems

$$E_{xc}[n] = F[n] - T_{KS}[n] - E_H[n]. \tag{2.12}$$

Thus far the Kohn-Sham formalism is exact in that if the form of the universal functional E_{xc} were known, then the exact ground state energy could be found using the density. The density itself is constructed from the single orbital wavefunctions $\psi_i(\boldsymbol{r})$ (Eq.2.8), equations for which are determined via the application of the variational principle, that is the minimization of the energy functional $E[n]$ (Eq.2.11) with respect to the variations of the orbitals $\psi_i(\boldsymbol{r})$, subject to the orthonormal constraint that $\langle \psi_i | \psi_j \rangle = \delta_{i,j}$, which results in the one electron Kohn-Sham equation:

$$H_{KS}\psi_i(\boldsymbol{r}) = \left[-\frac{\hbar^2}{2m_e}\nabla^2 + V_{ext}(\boldsymbol{r}) + e^2 \int \frac{n(\boldsymbol{r'})}{|\boldsymbol{r}-\boldsymbol{r'}|} d\boldsymbol{r} + \frac{\delta E_{xc}}{\delta n(\boldsymbol{r})} \right] \psi_i(\boldsymbol{r}) = \epsilon_i \psi_i(\boldsymbol{r}). \tag{2.13}$$

Subsequently, the effective potentials constituting the Kohn-Sham potential in Eq.2.7 are

$$V_{KS}(\boldsymbol{r}) = V_{ext}(\boldsymbol{r}) + V_H(\boldsymbol{r}) + V_{xc}(\boldsymbol{r}) \tag{2.14}$$

where the Hartree, $V_H(\boldsymbol{r})$, and exchange-correlation potential, $V_{xc}(\boldsymbol{r})$, respectively, are:

$$V_H(\boldsymbol{r}) = e^2 \int \frac{n(\boldsymbol{r'})}{|\boldsymbol{r} - \boldsymbol{r'}|} d\boldsymbol{r} \tag{2.15}$$

$$V_{xc}(\boldsymbol{r}) = \frac{\delta E_{xc}}{\delta n(\boldsymbol{r})} \tag{2.16}$$

As the Kohn-Sham potential $V_{KS}(\boldsymbol{r})$ is dependent on the density, it is necessary to solve the Kohn-Sham equation self-consistently. An initial guess for the density is made after which Eq.2.13 is solved to generate a set of orbitals, $\psi_i(\boldsymbol{r})$, from which a new density is found. The iteration of this process is continued until the input and output densities are equivalent i.e. self-consistency has been achieved.

As touched upon above, if the form of the functional $E_{xc}[n]$ were known, solving the equations of the independent-electron Kohn-Sham formalism would yield the exact ground state density and energy of the interacting electron system. However, the form of this functional is unknown, and thus approximations for $E_{xc}[n]$ are needed.

Exchange Correlation Functionals

In the practical application of DFT two dominant and widely adopted approximations to the exchange-correlational functional $E_{xc}[n]$ are the local-density approximation (LDA) [109] and the generalized gradient approximation (GGA) [110].

A significant consequence of the Kohn-Sham formalism in partitioning the Kohn-Sham potential into the independent-electron kinetic and long-range Hartree terms, Eq.2.14, is that the exchange-correlation functional $E_{xc}[n]$ can be approximated as a local function of the density $n(\boldsymbol{r})$. This informs the basis of the LDA, as it assumes that the local exchange correlation energy per electron $\varepsilon_{xc}(n(\boldsymbol{r}))$ is the same as that in a homogeneous electron gas $\varepsilon_{xc}^{hom}(n(\boldsymbol{r}))$ with an equivalent density, with the overall exchange-correlation energy, $E_{xc}[n]$, an integral over all space

$$E_{xc}^{LDA}[n] = \int \varepsilon_{xc}^{hom}(n(\boldsymbol{r}))n(\boldsymbol{r})d\boldsymbol{r} \tag{2.17}$$

In the case of the homogeneous electron gas, the dependence of the exchange-correlation energy, $\varepsilon_{xc}^{hom}(n)$, on the density has been calculated to an extremely high degree of accuracy using quantum Monte Carlo methods by Ceperly and Alder [111], a widely employed parametrisation of which includes that of Perdew and Zunger [112]. Despite its apparent simplicity the LDA has been reliably applied to predict a variety of properties, such as bonding interactions (mainly covalent, ionic and metallic), vibrational frequencies and elastic moduli in atomic, molecular and solid systems.

The GGA is an energy functional that improves on the LDA due to its dependence on both the density and its gradient

$$E_{xc}[n]^{GGA} = \int \varepsilon_{xc}^{hom}(n, \nabla n) n(\boldsymbol{r}) d\boldsymbol{r}. \tag{2.18}$$

A much used parametrisation, which has also been employed in this work, is that of Perdew-Burke-Ernzerhof [113].

Plane Wave Expansion and Pseudopotentials

A primary step in the practical solution of the Kohn-Sham equations is defining an appropriate basis set in which to expand the Kohn-Sham wavefunctions.

For periodic systems, based on Bloch's theorem [3], a natural choice is to use a planewave basis set, which is a complete and unbiased basis. Thus, each Kohn-Sham wavefunction can be expanded as a linear combination of plane waves:

$$\psi_{n\boldsymbol{k}}(\boldsymbol{r}) = \sum_{G} C_{n\boldsymbol{k}}(\boldsymbol{G}) e^{i(\boldsymbol{k}+\boldsymbol{G})\cdot\boldsymbol{r}} \tag{2.19}$$

where n refers to the band index, $\boldsymbol{k}$ the crystal momentum, and $\mathbf{G}$ the reciprocal lattice vectors, defined as

$$\boldsymbol{G} = m_1\boldsymbol{b}_1 + m_2\boldsymbol{b}_2 + m_3\boldsymbol{b}_3 \tag{2.20}$$

with primitive lattice vectors $\boldsymbol{b}_i$ and integers m_i, for $i = 1, 2, 3$. For a given $\boldsymbol{k}$, subsequently, Bloch's theorem (i.e. via Eqn.2.19) dictates that the size of the planewave basis set over which the electron wavefunctions are expanded is infinite, as the sum in Eqn.2.19 runs over the periodic repetitions of the reciprocal lattice vectors $\boldsymbol{G}$. However, in practical applications a kinetic energy cutoff is introduced whereby plane waves possesing a kinetic energy higher than that cutoff are omitted, thus giving a truncated, finite planewave basis set.

Consequently, with the electron wavefunctions described in terms of a plane wave basis set, the Kohn-Sham equations can be expressed as [114]

$$\sum_{\boldsymbol{G}'} \left[\frac{\hbar}{2m_e} |\boldsymbol{k}+\boldsymbol{G}|^2 \delta_{\boldsymbol{G}\boldsymbol{G}'} + V_{ext}(\boldsymbol{G}-\boldsymbol{G}') + V_H(\boldsymbol{G}-\boldsymbol{G}') + V_{xc}(\boldsymbol{G}-\boldsymbol{G}') \right] C_{n\boldsymbol{k}}(\boldsymbol{G}') = \epsilon_{n\boldsymbol{k}} C_{n\boldsymbol{k}}(\boldsymbol{G}). \tag{2.21}$$

Solving Eqn.2.21, involves diagonalizing the Hamiltonian matrix, whose elements are given by the terms in brackets, with the kinetic energy term diagonal. Moreover, the potential terms are represented by their Fourier components, in the form:

$$V(\boldsymbol{G}-\boldsymbol{G}') = \frac{1}{\Omega_{cell}} \int_{\Omega_{cell}} V(\boldsymbol{r}) e^{-i(\boldsymbol{G}-\boldsymbol{G})\cdot\boldsymbol{r}} d^3r. \tag{2.22}$$

where Ω_{cell} is the unit cell volume. The size of the matrix in Eqn.2.21 is dictated by the choice of the aforementioned cutoff energy for the kinetic energy, $(\frac{\hbar}{2m_e})|\boldsymbol{k}+\boldsymbol{G}|^2$. However, generally, regardless of the choice, the size is impractically large when systems are described in terms of both valence and core electrons. A method of overcoming such a problem is through the use of the pseudopotential approximation [115–117].

The basic premise of the pseudopotential approximation is that given the core electrons in a solid provide a negligible contribution to bonding and, consequently, the majority of physical properties, this chemical inertness enables them to be effectively ignored in describing the electron wavefunctions. This enormously reduces the size of the planewave basis set used to describe a given system. The use of pseudopotentials also avoids an additional complexity, in that the size of the basis can still be prohibitively large, in order that the oscillatory behaviour, associated with the valence electron wavefunctions within the core region, is fully captured.

A widely used implementation of the pseudopotential approximation are norm-conserving pseudopotentials [118], which are derived from first principles and have the following desirable properties:

1. For a given "reference" atomic configuration, calculated pseudo eigenvalues concur with real eigenvalues i.e. those determined from an all-electron calculation;

2. After defining a "core radius" r_c, below which the electron wavefunction shall be modified, beyond this radius the real (i.e. all-electron) and pseudo wavefunctions should be equivalent

3. Within the core radius, i.e. from 0 to r_c, the integral of both real and pseudo charge densities should agree, this defines norm-conservation

4. The logarithmic derivatives of the real and pseudo wavefunctions, and their first energy derivatives, agree for $r > r_c$.

Property 4, implied by the norm-conservation condition i.e. property 3, means that the real and pseudo wavefunctions have the same scattering phase shift around the reference energies, which along with property 3 ensure that the pseudopotential for an atom is transferable across different chemical environments.

A standard procedure for creating a pseudopotential is as follows; firstly, an all-electron calculation is performed for a "reference" atomic configuration. Subsequently, the calculated all-electron wavefunction is used to generate a pseudo wavefunction, according to the properties defined above, and ensuring that within the core region the pseudo wavefunction is nodeless. Following which, inversion of the Schrödinger equation leads to screened pseudopotentials for each angular momentum l, and unscreened potentials, via the subtraction of the Hartree and exchange-correlation potentials. Thus, giving transferable bare or ionic pseudopotentials to be used outside of their original reference atomic configurations.

Normconserving pseudopotentials are a form of ionic pseudopotential, where each angular momentum l is treated by a different potential. Therefore, they can be thought of as semilocal, that is local in radial variables r, but non-local in angular variables θ and ψ. Subsequently, the pseudopotential, written in operator form, can be expressed as

$$\hat{V}_{ps}^{ion} = \sum_l |l\rangle V_l^{ion}(r)\langle l|, \tag{2.23}$$

where $|l\rangle$ are the spherical harmonics, and V_l^{ion} the pseudopotential for angular momentum l, and $|l\rangle\langle l|$ an angular momentum projection operator. Based on this semilocal nature, the total ionic pseudopotential can be further split into a long-ranged (l-independent), local part, $V_{loc}(r)$, and a short-ranged (l-dependent), semilocal part, $\Delta V_l(r)$:

$$\hat{V}_{ps}^{ion} = V_{loc}(r) + \sum_l |l\rangle \Delta V_l(r)\langle l| \tag{2.24}$$

where $V_{loc}(r)$ is chosen such $\Delta V_l(r)$ vanishes outside the core regions [117]. Having so defined the total ionic pseudopotential, the external potential, V_{ext} in Eqn.2.21, describing the electron-ion interaction, can be expressed, for a single atom, in momentum space as:

$$V_{ps}^{ion}(\boldsymbol{k}+\boldsymbol{G},\boldsymbol{k}+\boldsymbol{G}') = S(\boldsymbol{G}-\boldsymbol{G}')\left[V_{loc}(\boldsymbol{G}-\boldsymbol{G}') + \sum_l \Delta V_l(\boldsymbol{k}+\boldsymbol{G},\boldsymbol{k}+\boldsymbol{G}')\right], \tag{2.25}$$

where the first term corresponds to the structure factor, and the second term in brackets the form factors. The structure factor is given by [119, 120]

$$S(\boldsymbol{G}-\boldsymbol{G}') = \frac{\Omega_{at}}{\Omega_{cell}} \sum_j e^{-i(\boldsymbol{G}-\boldsymbol{G}')\cdot \boldsymbol{t}^j} \tag{2.26}$$

with Ω_{cell} the unit-cell volume and Ω_{at} the volume per atom, respectively, and $\boldsymbol{t}^j$ a basis vector. The form factor, i.e. the Fourier component, for the local pseudopotential [119, 120] is

$$V_{loc}(\boldsymbol{G}-\boldsymbol{G}') = \frac{1}{\Omega_{at}} \int_{allspace} e^{-i(\boldsymbol{G}-\boldsymbol{G}')\cdot \boldsymbol{r}} V_{loc}(r) d^3r \tag{2.27}$$

and for the semilocal pseudpotential [119, 120],

$$\Delta V_l(\boldsymbol{k}+\boldsymbol{G},\boldsymbol{k}+\boldsymbol{G}') = \frac{1}{\Omega_{at}} \int_{allspace} e^{-i(\boldsymbol{k}+\boldsymbol{G})\cdot \boldsymbol{r}} \Delta V_l(r)|l\rangle\langle l| e^{i(\boldsymbol{k}+\boldsymbol{G}')\cdot \boldsymbol{r}} d^3r \tag{2.28}$$

$$= \frac{4\pi(2l+1)}{\Omega at} P_l(\cos\gamma) \times \int_0^\infty j_l(|\boldsymbol{k}+\boldsymbol{G}|r) j_l(|\boldsymbol{k}+\boldsymbol{G}'|r) \Delta V_l(r) r^2 dr \tag{2.29}$$

where P_l is a Legendre polynomial, j_l a spherical Bessel function, and $\cos\gamma = (\boldsymbol{k}+\boldsymbol{G})\cdot(\boldsymbol{k}+\boldsymbol{G}')/(|\boldsymbol{k}+\boldsymbol{G}||\boldsymbol{k}+\boldsymbol{G}'|)$.

A widely implemented procedure of generating norm-conserving pseudopotentials, that are particularly robust and have a high transferability, is that of Trouiller and Martins [121]. A drawback of norm-conserving pseudpotentials, particularly with respect to first-row and transition metal elements, is that they tend to require a small cutoff radius R_c, in order to adequately describe the high-frequency components in the core region. For such cases the pseudopotential is described as being hard. A method for reducing the consequent size of the plane-wave basis, and associated computational expense, is to use a larger R_c, whilst retaining transferability, to generate softer pseudopotentials, such as the ultrasoft pseudpotentials [122].

Spin Orbit Interaction

Given that several of the systems pertaining to this work contain heavy elements, it is of interest to briefly discuss the inclusion of relativistic effects in DFT calculations. Of the two relativistic effects, which include scalar-relativistic effects (SR) related to the mass-velocity and Darwin terms, and the spin-obit interaction (SOI), the latter is of particular importance. This is evinced by the fact that a fundamental factor in the formation of topologically insulating phases in Z_2 TIs is a result of band inversion, stemming from spin-orbit coupling. Since the origins of relativistic effects are due to interactions occurring well within the core region of an atom, close to the nucleus, the pseudopotential approximation can be naturally extended to include them [123, 124].

One method of achieving this [123] is based on the assumption that as that outside of the core region the major component of a valence electron wavefunction of a heavy atom, described via the Dirac radial equations, is independent of that of the minor component, it can be expressed via a non-relativistic Schrödinger equation. In doing so, the previously described method of inverting the Schrödinger equation can be applied to the major component of an all-electron Dirac wavefunction, to generate norm-conserving pseudopotentials which include relativistic effects up to the order of α^2, where α ($\approx 1/137$) is the fine-structure constant. This methodology also ensures that effects associated with the orthogonality constraints of core electrons, within the core region, are adequately described [124].

More specifically, the methodology involves, firstly, and similarly to non-relativistic pseudopotentials, performing an ab initio DFT all-electron calculation for a reference atomic configuration. However, one now solves the Dirac equations to generate two j-dependent fully relativistic pseudopotentials for each $l > 0$, $V_{l+1/2}$ and $V_{l-1/2}$, and one for $l = 0$, $V_{l+1/2}$. Subsequently, for each l, using a Schrödinger type equation, the pseudopotentials for V_j, with $j = l + 1/2$ or $j = l - 1/2$, are recalculated, such that, up to the order of α^2, the eigenfunctions and eigenvalues match that of the original Dirac equation, beyond the chose cut-off radii R_c [123].

In order to highlight the impact, particularly with respect to heavy atoms, of including relativistic corrections in the pseudopotential approximation, Troullier-Martins norm-conserving pseudopotentials [121] were generated for two representative, light and heavy, elements. Thus, shown in Fig.2.1 are calculated atomic energy levels and pseudopotentials, for carbon (C) and bismuth (Bi), respectively. Calculations were performed using the APE code [125], with the GGA (PBE) functional [113] used to describe the exchange-correlation energy.

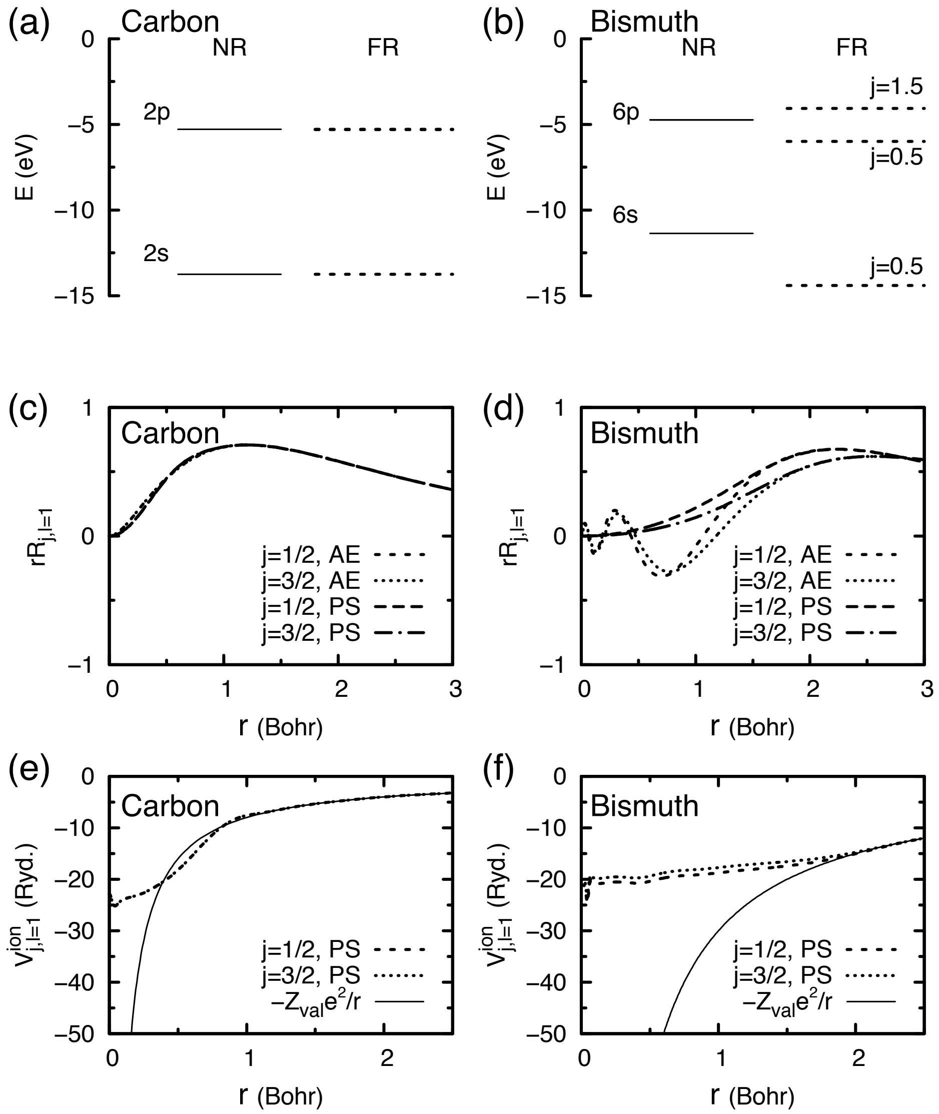

Figure 2.1 – Comparison of fully-relativistic pseudopotentials of carbon (C) and bismuth (Bi)atoms. One-atom energy levels for valence p orbitals of **a** C and **b** Bi without (NR) and with relativistic (FR) effects. Radial all-electron (AE) and pseudo (PS) wave functions for valence p orbitals of **c** C and **d** Bi. Fully-relativistic j-dependent semilocal pseudopotentials for valence p orbitals of **e** C and **d** Bi. Ionic potentials are denoted with solid lines.

As Fig.2.1**a** shows, unsurprisingly, relativistic effects have a negligible effect on the energy levels of the low atomic weight ($z = 6$) C atom, with a SOI splitting of 0.012 eV for the C $2p$ orbitals. Conversely, for the far heavier Bi atom ($Z = 83$), the splitting is substantially larger, with a splitting of 1.9 eV between the $j = 3/2$ and $j = 1/2$ levels, as can be seen in Fig.2.1**b**. This is further evidenced in a comparison of the radial all-electron and pseudo wavefunctions, and also the fully-relativistic pseudopotentials, shown in Figs.2.1**c**,**d** and Figs.2.1**e**,**f**, respectively.

From the fully-relativistic j-dependent semilocal pseudopotentials, described, one can define j-averaged, l-dependent semilocal pseudopotentials

$$V_l^{SR} = \frac{1}{2l+1}\left[(l+1)V_{l+1/2} + lV_{l-1/2}\right] \tag{2.30}$$

and

$$V_l^{SO} = \frac{2}{2l+1}\left[V_{l+1/2} - V_{l-1/2}\right], \tag{2.31}$$

where V_l^{SR} includes only scalar relativistic effects, whilst V_l^{SO} contains information concerning the SOI. Utilising solely the pseudopotential defined by Eqn.2.30 in Eqn.2.23, would allow ab initio calculations with SR effects described. To also include the SOI, it is necessary for an additional term to be added to the KS Hamiltonian

$$\hat{H}^{\mathrm{SO}} = \sum_{l,s} |ls\rangle V_l^{\mathrm{SO}}(r)\boldsymbol{L}\cdot\boldsymbol{S}\langle ls|, \tag{2.32}$$

where $|ls\rangle\langle ls|$ is the projector on the tensor product $L \otimes S$ of functions of a given angular momentum times the spin space [126, 127], and $\boldsymbol{L}$ ($\boldsymbol{S}$) is the orbital (spin) angular momentum operator.

2.1.2 First Principles Calculations on Topological Insulator Materials

Z_2 Topological Insulators: Bi_2Se_3 and Bi_2Te_3

A catalyst which sparked a great deal of interest in the field of topological insulators was the discovery of binary bismtuh chalcogenides, Bi_2Se_3 and Bi_2Te_3, as Z_2 topological insulators [32, 33, 128, 129], with a topological phase belonging to the (1;000) class. This is due to the fact that their topological properties were the first to be amenable to extensive experimental investigation, and also have potential for device applications. This primarily stems from three factors, the first being the relatively simple Dirac fermion surface state of both materials defined by a single Dirac cone, and in particular in the case of Bi_2Se_3 having a near idealized conical dispersion. Secondly, their stoichiometric nature implies that the materials can be synthesized to a high-degree of purity. Finally, their relatively large bulk band gaps could be important for potential device applications. As such, these factors served as an initial inspiration in further investigating these materials.

As a primary starting point the bulk electronic structures of Bi_2Se_3 and Bi_2Te_3 were investigated using first principles density functional theory calculations. With a particular focus being to elucidate the effects of spin-orbit coupling (SOC) in giving rise to band inversion and, consequently, a topologically nontrivial phase.

First principles calculations were performed within the DFT framework, employing the generalized gradient approximation (GGA), specifically the PBE parametrisation [113], to the exchange-correlation functional. Spin-orbit effects were treated self-consistently using fully relativistic norm-conserving pseudopotentials [118], within the two component wavefunction formalism [130–132]. Plane-wave kinetic energy cutoffs were set at 50 and 70 Ry for Bi_2Se_3 and Bi_2Te_3, respectively. The Brillouin zone was sampled with a $8 \times 8 \times 8$ Monkhorst-Pack grid of $\boldsymbol{k}$ points [133]. Convergence of the total energy, with regard to wave function cutoffs and the number of $\boldsymbol{k}$ points, was ensured. Calculations were performed through the PWSCF plane-wave pseudopotential code of the Quantum-ESPRESSO distribution [134]. Experimental crystal structures of bulk Bi_2Se_3 and Bi_2Te_3 were utilized [135].

Bi_2Se_3 and Bi_2Te_3 crystallize in the rhombohedral crystal structure with the space group $D^5_{3d}(R\bar{3}m)$, and are layered materials where each layer is a covalently bonded quintuple layer (QL), as shown in Fig.2.2**a**. Each quintuple layer consists of two Bi atoms (Bi in Fig.2.2**a**), two equivalent Se atoms (Se1 in Fig.2.2**a**) and a third Se atom (Se2 in Fig.2.2**a**) which functions as the inversion centre. Each atomic plane also comprises a triangular lattice, with the trigonal axis parallel to the z axis, meaning that stacking along that direction is -A-B-C-A-B-C- as shown in Figs.2.2**a**,**b**. Interlayer bonding is due to van der Waals interactions, and is far weaker than the covalent intralayer bonding, resulting in a natural cleavage plane between QLs.

In order to observe the effects of SOC on the topological properties of Bi_2Se_3 and Bi_2Te_3, their band structures, computed with and without the inclusion of SOC, are shown in Fig.2.3**a** and Fig.2.3**b**, respectively. The effects of SOC are most evident in the region close to the Fermi level at the Γ point. As can be observed, the inclusion of SOC results in a significant anti-crossing feature between the lowest unoccupied and highest occupied bands at the Γ point, which is indicative of a band inversion. Moreover, as the valence and conduction bands in question are of opposite parity, this confirms the formation of a topologically non-trivial phase, which belongs to the (1;000) class. For Bi_2Se_3 the band gap is predicted to be around 0.3 eV, which concurs well with experimental values [33]. Conversely, for Bi_2Te_3 the band gap calculated using DFT, via the LDA functional, is underestimated with a value of 0.09 eV [136]. However, the same work using GW calculations found a value close to that of 0.17 eV determined experimentally [136].

A more physical intuition of the band inversion occurring at Γ can be gained by observing the evolution of the atomic orbitals under the effects of the relevant interactions, namely chemical bonding, crystal-field splitting and SOC, into the valence and conduction bands. Subsequently, focusing on Bi_2Se_3, the states of interest are those closest to the Fermi level, which are derived from the valence orbitals. As Bi has a valence electron configuration of $6s^2 6p^3$ and Se $4s^2 4p^4$, these correspond to p orbitals. Looking at the schematic energy level diagram in Fig.2.3**c**, in section I chemical bonding leads to hybridization of Bi and Se atomic orbitals, with level repulsion pushing the hybridized Bi and Se states up and down, respectively. As a result of inversion symmetry each state in Fig.2.3**c** is labelled with its respective + or − parity. In section II the crystal field effect breaks the degeneracy of the p orbitals, splitting p_z from the degenerate p_x and p_y. Consequently, the conduction and valence band states closest to the Fermi level are derived from p_z orbitals of Bi and Se, respectively, and are of opposite

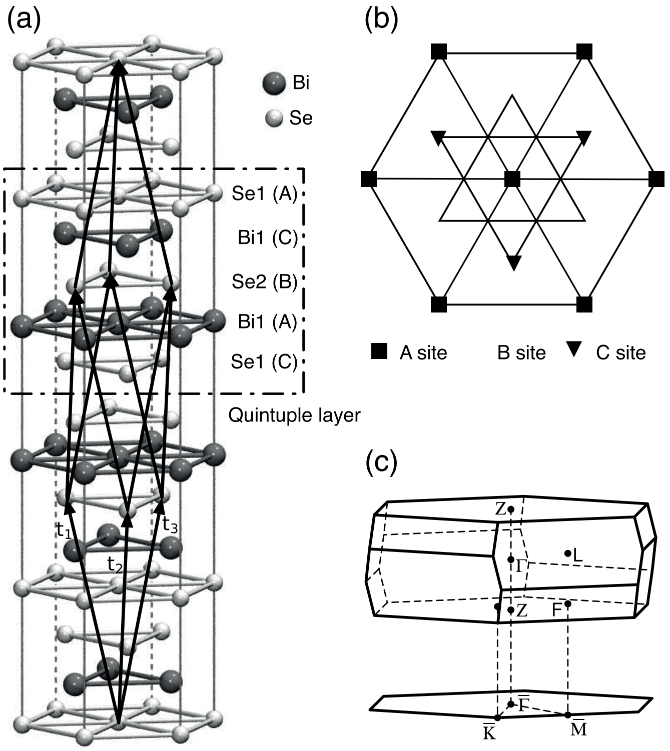

Figure 2.2 – **a** Bulk crystal structure of Bi_2Se_3 with Bi and Se atoms shown in dark and light, respectively. A quintuple layer (QL) unit is indicated by the dot-dashed rectangle with constituent atoms labelled according to the stacking sequence. Primitive lattice vectors $\mathbf{t}_i$ (i=1,2,3) are indicated with arrows. **b** Top view of the crystalline lattice along the (111) (trigonal) direction. **c** Brillouin zone (BZ) of bulk Bi_2Se_3 and its projection onto the two-dimensional (2D) BZ of the (111) surface. Filled dots locate the high-symmetry **k** points.

parity. Finally, as SOC couples spin and orbital angular momenta this leads to a further level repulsion, pushing the Bi p_z derived states, $|p1_z^+\rangle$, down and the Se p_z derived, $|p2_z^-\rangle$, states up. Given that the atomic SOC constant for Bi is large, where $\lambda_{SO} = 1.25$ eV [137], this is of a sufficient magnitude to invert the Bi $|p1_z^+\rangle$ states with respect to the Se $|p2_z^-\rangle$ states, as shown in section III. Moreover, as both states are of opposite parity this results in the formation of the topologically insulating phase. Qualitatively the same analysis just described could be equally applied to Bi_2Te_3, as is evident from the energy level diagram shown in Fig.2.3**d**.

Bulk electronic structure calculations, as detailed above, allow the confirmation of Bi_2Se_3 and Bi_2Te_3 as Z_2 TIs. Subsequently, one would like to determine the presence of the topologically protected surface states. One method of investigating surfaces, using first principles DFT calculations, is via the formation of slab models [138]. The basic premise of such models being to create two-dimensional systems of small enough sizes to be treated computationally, yet of large enough size that each surface is decoupled from the other by a sufficient thickness of bulk material. With the objective to avoid, as far as possible, any unwanted finite-size effects, specifically through the overlap of the respective surface state

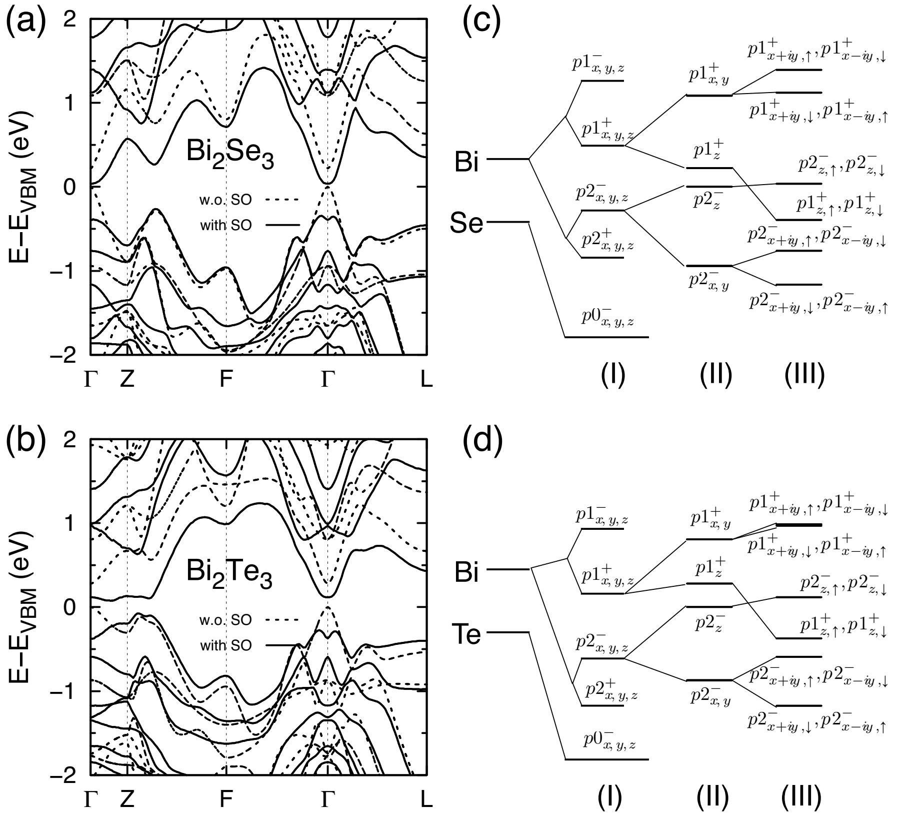

Figure 2.3 – Electronic band structures of **a** Bi_2Se_3 and **b** Bi_2Te_3 obtained using DFT calculations. Solid and dashed lines correspond to the band structures calculated with and without SOI, respectively. The zero of energy is set to the valence band top without the SOI. Schematic energy-level diagrams at the Brillouin zone center (Γ) for **c** Bi_2Se_3 and **d** Bi_2Te_3. The effects of chemical bonding (I), the crystal-field splitting (II) and the spin-orbit interaction (III) are distinguished. Except for (II) and (III) the level positions are arbitrary.

wavefunctions. Previous works employing such models have shown that bismuth chalcogenide slabs of a few QLs are of adequate thickness to properly describe the topological surface states [139].

As mentioned above, the layered crystal structure of bismuth chalcogenide TIs leads to a natural cleavage plane, due to the relatively weak van der Waals interactions between QLs. Cleavage along this plane exposes the stoichiometric (111) orientated surface. Thus, two-dimensional slab models, of defined QL thickness (where 1QL ≈ 1 nm thick), were constructed from complete QL units. Calculated band structures for 5 QL thick slab models are shown in Figs.2.4**a**,**b** for Bi_2Se_3 and Bi_2Te_3, respectively. Each material's slab band structure is superimposed with its bulk band structure projected onto the surface Brillouin zone. The relationship between the bulk and surface Brillouin zones are shown in Fig.2.2**d**. The presence of the Dirac cone, within the semiconducting bulk band gap, is evident at the Γ point in both band structures. The position of the Dirac cone within the bulk gap confirms that the comprising bands are surface-localized states. Given the nature of the slab model construction and the presence of two surfaces each band is subsequently twofold degenerate. For both Bi_2Se_3 and Bi_2Te_3 the energy of the Dirac point lies below that of the bulk valence band maximum. In both cases the dispersion of the Dirac is highly asymmetric, however the electron-hole asymmetry is more pronounced with respect to Bi_2Te_3, which agrees qualitatively with experimental observations [34, 128]. Both band structures also show that slabs of 5 QL are thick enough to avoid any hybridization of topological states localized at opposite surfaces, as in extremely thin slabs this can significantly modify the Dirac cone band dispersion and result in a gap opening. Previous DFT calculations have shown that slab models should be of at least 3 QL and 4 QL thickness for Bi_2Se_3 and Bi_2Te_3, respectively, to ensure the convergence of the surface-state band dispersion [139].

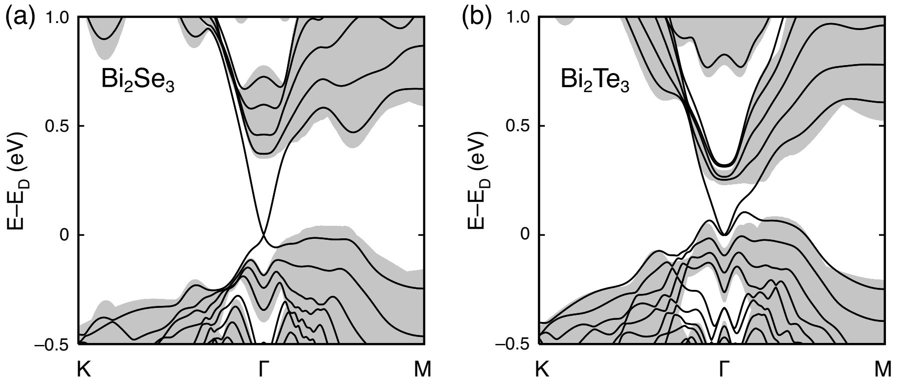

Figure 2.4 – Band structures of the 5 QL slabs of **a** Bi_2Se_3 and **b** Bi_2Te_3 (lines) shown together with the projected band structure of bulk materials (shaded areas). The emergence of Dirac fermion states within the bulk band gap is clearly observed upon confinement. The energies are given with respect to the Dirac point of the topologically protected surface states. Figure reproduced with permission from Ref. [139], 2010 ©American Physical Society.

2.2 Tight-Binding Model

2.2.1 General Formalism

A disadvantage of using ab initio techniques, for example as in the formulation above described with respect to DFT, is that the computational cost becomes prohibitively expensive as the size of a system increases. Tight-binding, as a semi-empirical method, allows much larger systems to be treated. Furthermore, as the quantum mechanical nature of bonding is preserved, much of the interesting physics unique to topological insulators, particularly with respect to the various focus points of this work, is retained. Subsequently, what follows is a general description of the tight-binding method, followed by a comparison of reference calculations between DFT and tight-binding, upon which confidence in its utility in describing certain topological insulator systems was based.

The underlying principle of the tight-binding method, as formulated by Slater and Koster [140], is to replace the exact many-body Hamiltonian operator, given in Eq.2.1 or in

Bra-ket notation $\hat{H}\Psi = E|\Psi\rangle$, with a parametrized Hamiltonian matrix.

In doing so a primary starting point is the use of a localised basis in a single electron picture. This stems from the assumption that as a crystal is made up of atoms, the effective potential seen by an electron within the crystal can be approximated as the sum of isolated, neutral atomic potentials. For a unit cell with lattice vectors $\boldsymbol{R}$ composed of N_{at} atoms i, at atomic positions τ_i (i.e to describe unit cells of two or more atoms), this effective potential can be written

$$V(\boldsymbol{r}) = \sum_{i=1}^{N_{at}} V_i^{at}(\boldsymbol{r} - \boldsymbol{R} - \boldsymbol{\tau_i}) = \sum_{i=1}^{N_{at}} \hat{V}_i^{at}. \tag{2.33}$$

Subsequently, the single electron Schrödinger equation is

$$(\hat{T} + V(\boldsymbol{r}))\Psi(\boldsymbol{r}) = E\Psi(\boldsymbol{r}), \tag{2.34}$$

where $\hat{T}$ is the kinetic energy operator.

An underpinning factor in such a construction is that each atom is comprised of atomic orbitals $\phi_{i\alpha}$ which satisfy the single atom Schrödinger equation

$$(\hat{T} + \hat{V}_i^{at})\phi_{i\alpha} = \epsilon_{i\alpha}^{at}\phi_{i\alpha}, \tag{2.35}$$

the index α denotes an atomic orbital, specifically the angular symmetry of the real orbitals, which for systems of interest to this work are primarily $s, p_x, p_y, pz, d_{xy}, d_{yz}, d_{xz}, d_{x^2-y^2}, d_{z^2}$, and runs from $\alpha = 1, \ldots, N_{orb}$. For the descriptions below Roman characters $(i, j, \ldots)$ refer to atomic sites and Greek letters to atomic orbitals $(\alpha, \beta, \ldots)$

This to lead to a foundational premise of the tight-binding method, in that the wave-functions $|\Psi\rangle$ corresponding to Eq.2.34 can be expanded as a linear combination of atomic orbitals

$$\Psi(\boldsymbol{r}) = \sum_{i\alpha} C_{i\alpha}\phi_{i\alpha}(\boldsymbol{r}) \tag{2.36}$$

which on introducing the Dirac notation $\phi_{i\alpha}(\boldsymbol{r} - \boldsymbol{R} - \boldsymbol{\tau_i}) = \langle \boldsymbol{r}|i\alpha\rangle$, can be rewritten

$$|\Psi\rangle = \sum_{i\alpha} C_{i\alpha}|i\alpha\rangle \tag{2.37}$$

As the systems of interest to this work are each composed of atomic orbitals which construct an orthogonal basis, the overlap of two orbitals on separate atomic sites as described by the overlap matrix

$$S_{i\alpha j\beta} = \langle i\alpha|i\beta\rangle = \delta_{ij}\delta_{\alpha\beta} \tag{2.38}$$

simply reduces to the identity matrix, and as such is omitted from further description below.

Having defined a localised atomic basis, the matrix elements corresponding to the crystal Hamiltonian in Eq.2.34 are given by

$$H_{i\alpha j\beta} = \langle i\alpha|\hat{H}|j\beta\rangle = \langle i\alpha|\hat{T} + \sum_{i=1}^{N_{at}} \hat{V}_i^{at}|j\beta\rangle \tag{2.39}$$

This leads to two distinct sets of terms. The first being the intra-atomic terms, where $i = j$

$$H_{i\alpha i\beta} = \langle i\alpha|\hat{T} + \hat{V}_i|i\beta\rangle + \langle i\alpha|\sum_{j\neq i} \hat{V}_j^{at}|i\beta\rangle \tag{2.40}$$

$$= \epsilon_{i\alpha}^{at}\delta_{\alpha\beta} + \langle i\alpha|\sum_{j\neq i} \hat{V}_j^{at}|i\beta\rangle. \tag{2.41}$$

where the first term is simply the atomic orbital energy level and corresponds to the eigenvalue of the atomic Hamiltonian defined in Eq.2.35. For an atom comprising s,p and d orbitals, there would thus be three distinct levels ϵ_s^{at}, ϵ_p^{at}, ϵ_d^{at} for each type of orbital. The second term relates to the crystal field, and is neglected. The intra-atomic terms compose the diagonal elements of the Hamiltonian matrix.

The off-diagonal or inter-atomic terms, where $i \neq j$ are given by

$$H_{i\alpha j\beta} = \langle i\alpha|\sum_{k} \hat{V}_k^{at}|j\beta\rangle \tag{2.42}$$

These terms can correspond to two-centre integrals, i.e. where $i = k$, or three-centre integrals, i.e. where $i \neq j \neq k$. Given that the wavefunctions $|i\alpha\rangle$, $|j\beta\rangle$ and the potential V_k rapidly decay as one moves away from the respective sites, and that parametrised matrix elements shall be utilised, the contribution of the three-centre integrals are of a much smaller magnitude, and are consequently neglected. This leaves the two-centre or commonly termed hopping integrals

$$H_{i\alpha j\beta} = \langle i\alpha|\hat{V}_i^{at}|j\beta\rangle = t_{ij}^{\alpha\beta} \tag{2.43}$$

The hopping integrals $t_{ij}^{\alpha\beta}$ represent the interaction between orbitals on two atomic sites i and j. The term hopping deriving from the fact that physically they can be thought of as the ability of an electron to "hop" between neighbouring sites and decay rapidly with the distance between two sites. They are a fundamental component of the Slater-Koster tight-binding method, as in that approach the integrals are replaced with a series of parameters which depend solely on the distance between the two atomic sites and the type, specifically the symmetry, of the orbitals under consideration. The nature of this parametrisation shall be described in further detail in the following section.

For a crystal lattice with periodically repeated unit with lattice vector **R**, containing atoms i with orbitals α at sites τ_i, due to the translational invariance of the crystal the eigenfunctions defined in Eq.2.37 can be written in the form of a Bloch sum

$$|\Psi_{i\alpha}(\boldsymbol{k})\rangle = \frac{1}{\sqrt{N}}\sum_{\boldsymbol{R}} e^{i\boldsymbol{k}\cdot(\boldsymbol{R}+\tau_i)}|i\alpha\rangle \tag{2.44}$$

where N is the number of primitive unit cells in the crystal and $\boldsymbol{k}$ is a reciprocal lattice vector. Subsequently, eigenfunctions of the crystal Hamiltonian can be constructed as a linear combination of the Bloch sums

$$|\Psi^{(n)}(\boldsymbol{k})\rangle = \sum_{i\alpha} C^{n}_{i\alpha}(\boldsymbol{k})|\Psi_{i\alpha}(\boldsymbol{k})\rangle, \tag{2.45}$$

with the n dictating the band index, where $n = 1,\ldots,N^{at}N^{orb}$. Thus, there exists a simple relation between the expansion coefficients for $|\Psi^{(n)}(\boldsymbol{k})\rangle$ and $|\Psi^{(n)}(\boldsymbol{r})\rangle$

$$C^{n'}_{i\alpha}(\boldsymbol{r}) = \frac{1}{\sqrt{N}} e^{i\boldsymbol{k}\cdot(\boldsymbol{R}+\tau_i)} C^{n}_{i\alpha}(\boldsymbol{k}) \tag{2.46}$$

Finally, the Hamiltonian matrix is given by

$$H_{i\alpha j\beta} = \langle\Psi_{i\alpha}(\boldsymbol{k})|H|\Psi_{i\alpha}(\boldsymbol{k})\rangle \tag{2.47}$$

$$= \sum_{\boldsymbol{R}} e^{i\boldsymbol{k}\cdot(\boldsymbol{R}+\tau_j-\tau_i)}\langle 0 i\alpha|H|\boldsymbol{R} j\beta\rangle \tag{2.48}$$

where the atomic site i has been located at the origin (i.e. $\boldsymbol{r}-(\boldsymbol{R}+\boldsymbol{\tau_i}) = 0$).

Finally, defining the Schrödinger equation for a periodic crystal, in the tight-binding basis, in terms of the wavefunctions given in Eq.2.45 results in the following matrix equation

$$\boldsymbol{H}(\boldsymbol{k})\Psi^{(n)}(\boldsymbol{k}) = E^{(n)}(\boldsymbol{k})\Psi^{(n)}(\boldsymbol{k}) \tag{2.49}$$

where $\boldsymbol{H}(\boldsymbol{k})$ is the Hamiltonian matrix just described in Eq.2.48. Diagonalizing this matrix, of size $N^{at}N^{orb} \times N^{at}N^{orb}$, allows Eq.2.49 to be solved for each $\boldsymbol{k}$ in the irreducible Brillouin zone. Plotting the resulting eigenvalues $E^{(n)}(\boldsymbol{k})$ as a function of the crystal momentum $\boldsymbol{k}$ leads to the band structure of the crystal.

2.2.2 Hopping Integral

As touched upon above, the overlap integrals, $t^{\alpha\beta}_{ij}$, are solely dependent on the distance between two atomic sites (i.e. the vector $\boldsymbol{R}_{ij}$), and the symmetry of the orbitals under consideration, therefore $t^{\alpha\beta}_{ij} = t_{\alpha\beta}(\boldsymbol{R}_{ij})$.

There are two defining components of the overlap integrals, the first of these are termed the Slater Koster parameters [140]. In deriving these parameters it is assumed that the vector $\boldsymbol{R}_{ij}$ connects the nucleus of the atom i, on which the orbital α resides, to that of atom j, on which the orbital β resides. The orbitals α and β can be described in terms of radial functions multiplied by spherical harmonics, thus for α

$$\phi_{i\alpha} = \phi_{i(\alpha=nlm)}(\boldsymbol{r}) = R_{nl}(r)Y_l^m(\theta,\varphi), \tag{2.50}$$

and β

$$\phi_{i\beta} = \phi_{i(\beta=nlm)}(\boldsymbol{r}) = R_{n'l'}(r)Y_{l'}^{m'}(\theta',\varphi). \tag{2.51}$$

Following this description of the atomic orbitals, a spherical coordinate system is constructed whereby $\boldsymbol{R}_{ij}$ is parallel to the z axis, with origins at each atom, and with the angular form of α given by $Y_l^m(\theta,\varphi)$ and β by $Y_{l'}^{m'}(\theta',\varphi)$. Subsequently, the only non-zero overlap integrals are those for which $m' = m$, for which the corresponding parameters are labelled $V_{ll'm}$. The indices l and l' denote the $s, p, d, \ldots$ form of each atomic orbital for $l = 0, 1, 2$, respectively, whilst m denotes the angular momentum of the orbitals about the overlap axis between the two orbitals and is labelled σ, π, δ for $m = 0, 1, 2$, respectively.This leads to a set of ten parameters, which can be grouped according to the symmetry dictated by m, that is in terms of σ ($V_{ss\sigma}$, $V_{sp\sigma}$, $V_{sd\sigma}$, $V_{pp\sigma}$, $V_{pd\sigma}$, $V_{dd\sigma}$), π ($V_{pp\pi}$, $V_{pd\pi}$, $V_{dd\pi}$) or δ ($V_{dd\delta}$). A linear combination of the spherical harmonics of these parameters can be taken to generate real angular functions.

After deriving these symmetrically irreducible parameters the second component of the overlap integral relates to their form when the geometry of a system is arbitrarily defined. Specifically, if the vector $\boldsymbol{R}_{ij}$ now lies in a Cartesian x, y, z coordinate system, and is simply the displacement vector between the two orbital sites, the overlap integral $t_{ij}^{\alpha\beta}$ must be expressed as a linear combination of the irreducible parameters, orientated along the rotated axes, described above. This is accomplished using the direction cosines of the vector $\boldsymbol{R}_{ij}$, i.e.

$$\frac{\boldsymbol{R_{ij}}}{|\boldsymbol{R_{ij}}|} = (l, m, n). \tag{2.52}$$

Thus, for example for overlapping s and p_x orbitals, the s orbital is invariant, whilst the p_x orbital is transformed to a linear combination of the σ orbital given by parameter $V_{sp\sigma}$, and a π orbital. However, there exists no $sp\pi$ contribution to the overlap integral as the m values are not equivalent for the s and p_x orbitals, as described above. Consequently, the overall overlap integral for t_{ij}^{s,p_x} is $lV_{sp\sigma}$. In the case of the overlap of two p orbitals, for example p_x and p_z, the overlap integral $t_{ij}^{p_x,p_z}$ is expressed in terms of $V_{pp\sigma}$ and $V_{pp\pi}$ and the relevant direction cosines. The corresponding expression for $t_{ij}^{p_x,p_z}$ overlap integrals, and those for the remaining combinations of s and p orbitals, are given in Table.2.1.

A complete table describing not only combinations of s and p but also those of d orbitals can be found in the original paper of Slater and Koster [140]. In the practical application of the Slater Koster tight-binding method when defining overlap integrals for pairs of neighbouring sites it is useful to introduce a cutoff radius R_c, for an interatomic distance above which the overlap integral is set to zero. This is a reasonable approximation, since as the distance between two atomic sites increases, their interaction, defined by the hopping integral, rapidly diminishes, and in general one can assume an exponential dependence.

Table 2.1 – Slater and Koster interatomic matrix elements describing overlap integral between orbitals α and β on two atomic sites i and j, expressed as functions of the direction cosines l, m, n of the vector $\boldsymbol{R}_{ij}$ between them.

Matrix Element	**Expression**
$t_{ij}^{s,s}$	$V_{ss\sigma}$
t_{ij}^{s,p_x}	$lV_{sp\sigma}$
$t_{ij}^{p_x,p_x}$	$l^2V_{pp\sigma}+(1-l^2)V_{pp\pi}$
$t_{ij}^{p_x,p_y}$	$lmV_{pp\sigma}-lmV_{pp\pi}$
$t_{ij}^{p_x,p_z}$	$lnV_{pp\sigma}-lnV_{pp\pi}$

2.2.3 Spin-Orbit Interaction

Spin-orbit coupling is the interaction between the spin of a particle and its orbital angular momentum. It is a relativistic effect which can be derived from the Dirac equation. With respect to electrons, its effects, which become increasingly prominent as the velocity of an electron approaches the speed of light, are more pronounced for core electrons and also for valence electrons of heavy elements. Given that bismuth is a heavy element, SOC plays a significant role in the formation of a topologically insulating phase in the bismuth chalcogenides as it is the underlying cause of the band inversion at Γ, as touched upon above.

The spin-orbit interaction of an isolated atom, where the potential is approximated by a spherical potential, is given by:

$$\hat{H}_{SO}=\xi(\boldsymbol{r})\boldsymbol{L}\cdot\boldsymbol{S} \tag{2.53}$$

where

$$\xi(\boldsymbol{r})=\frac{1}{2m^2c^2r}\frac{1}{r}\frac{dV}{dr} \tag{2.54}$$

and $\boldsymbol{L}=\boldsymbol{r}\wedge\boldsymbol{p}$ and $\boldsymbol{S}=\frac{\hbar}{2}\boldsymbol{\sigma}$ are the orbital and spin momentum operators, respectively. The matrix elements of $\hat{H}_{SO}$, for a periodic crystal system modelled as a sum of atomic-like potentials, as detailed in the tight-binding formalism above, with a basis of atomic spin orbitals $|\alpha\sigma\rangle$ (where σ denotes the spin), are:

$$\hat{H}^{SO}_{i\alpha\sigma j\beta\sigma'}=\langle i\alpha\sigma|\hat{H}_{SO}|j\beta\sigma'\rangle \tag{2.55}$$

This expression can be further simplified by partitioning the orbitals into their radial and angular components, as in Eqs.2.50,2.51, thus giving:

$$\hat{H}^{SO}_{i\alpha\sigma j\beta\sigma'}=\xi_{i\alpha\beta}\langle\hat{\alpha}\sigma|\boldsymbol{L}\cdot\boldsymbol{S}|\hat{\beta}\sigma'\rangle\delta_{ij} \tag{2.56}$$

where

$$\xi_{i\alpha} = \int_0^\infty R_{i\alpha}^2(r)\xi(r)r^2 dr, \quad (\alpha = p\ or\ d) \tag{2.57}$$

and

$$\langle \hat{\alpha}\sigma | \boldsymbol{L}\cdot\boldsymbol{S} | \hat{\beta}\sigma' \rangle = \int_0^{2\pi}\int_0^{\pi} Y_\alpha(\theta,\varphi)\boldsymbol{L}\cdot\boldsymbol{S}Y_\beta(\theta,\varphi)sin(\theta)d\theta d\varphi. \tag{2.58}$$

As $\xi(r)$ is localised near $r = 0$, only onsite, diagonal elements of $\hat{H}^{SO}$ are retained. Furthermore, as the orbital angular momentum operator $\boldsymbol{L}$ only couples orbitals with same l value (i.e. s, p, d), and given that the SOC contribution for s orbitals is zero as $l = 0$, only two spin-orbit coupling coefficients are required, in a spd basis, to describe spin orbit effects in the tight-binding method. Specifically, these are ξ_p or ξ_d, for p and d orbitals, respectively.

Consequently, the effects of spin-orbit coupling can be included in the tight-binding model described earlier by adding the matrix H^{SO} (Eq.2.56) to the on site intra-atomic part of the crystal Hamiltonian, given in Eq.2.41, which results in:

$$H_{i\alpha\sigma,j\beta\sigma'} = H^0_{i\alpha\sigma,j\beta\sigma'} + \xi_{i\alpha\beta}\langle \hat{\alpha}\sigma | \boldsymbol{L}\cdot\boldsymbol{S} | \hat{\beta}\sigma' \rangle \tag{2.59}$$

2.2.4 Tight-Binding Parameters

The Hamiltonian of a system in the tight-binding basis is completely determined by onsite energies ϵ_α^{at} and the hopping integrals $t_{ij}^{\alpha\beta} = t_{\alpha\beta}(\boldsymbol{R}_{ij})$. One method of practically determining these parameters is to fit them to ab initio calculations. For example, for a given crystal structure with a defined lattice constant, one can fit the parameters such that select eigenvalues from the bands computed from ab initio calculations match those determined via the parametrised tight-binding method. This is precisely how the parameters utilised in tight-binding calculations performed in this work were determined. Below follows a description of the parametrisation scheme used in the case of the two system classes for which tight-binding calculations were performed. The first is that of the bismuth chalcogenides, with a particular focus on Bi_2Se_3 as a representative system, the second being tin telluride.

As the valence electrons for both bismuth $(6_s, 6_{p_{x,y,z}})$ and selenium $(4_s, 4_{p_{x,y,z}})$ belong to s and p orbitals, a sp basis was utilised for the tight-binding method, with four orbitals in the basis s, p_x, p_y, p_z for each spin orientation.

A cutoff radius R_c was set such that tight-binding parameters between atom pairs can be categorized into three sets. The first set accounts for interactions between atomic pairs in neighbouring atomic layers. Within this set, parameters were defined for Bi-Se(1) atoms within the same quintuple layer, Bi-Se(2) atoms within the same quintuple layer and for

Se(1)-Se(1) atoms in neighbouring quintuple layers. The second set accounts for interactions between atomic pairs within the same atomic layers. Thus, parameters were defined for Bi-Bi, Se(1)-Se(1) and Se(2)-Se(2) atomic pairs. Finally, the last set accounts for interactions between atomic pairs which were in next-nearest atomic layers, which have been termed second-neighbour layers. Parameters in this set were defined for Se(1)-Se(2), Bi-Bi and Bi-Se(1) atomic pairs.

The Bi_2Se_3 tight-binding parameters utilised in this study were taken from a work by Kobayashi [141]. The parameters were determined by fitting bulk band structures to density functional theory calculations, details of which are included in Ref. [141]. The parameters were fitted such that the dispersion of the highest valence and lowest conduction bands on the Γ-Z and half of the Z-F line (i.e the half closest to the Z TRIM point), within the bulk Brillouin zone, reproduced that of the DFT calculation. The respective high symmetry points can be seen in the Brillouin zone shown in Fig.2.2, and the relevant Bi_2Se_3 bulk band dispersions just described in the band structure shown in Fig.2.3. With the primary reasoning being that the valence band maximum and the conduction band minimum are found close to these lines. Numerical values for the tight-binding parameters are given in Table.2.2.

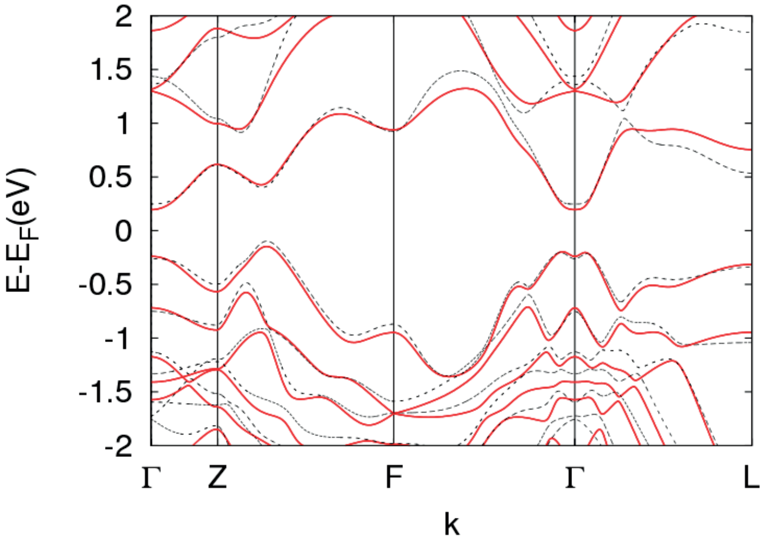

Figure 2.5 – Bulk band structure of Bi_2Se_3. Solid and dotted lines represent results from tight-binding and DFT methods, respectively.

A comparison of the bulk Bi_2Se_3 band structure, computed using DFT according to the method described in Section.2.1.2 and shown in Fig.2.3, and that computed using the tight-binding method, with the parameters given in Table.2.2, is shown in Fig.2.5. It should be noted that in both band structures the effects of SOC have been accounted for.

As Fig.2.5 shows, the correspondence between the two band structures is good. This holds especially true for the bands closest to the Fermi energy, and at the Γ point, which from the perspective of investigating topological properties of surface states is of particular importance.

In contrast to the bismuth chalcogenides a *spd* basis was used to describe SnTe, with nine orbitals in the basis s, p_x, p_y, p_z, d_{xz}, d_{yz}, d_{zx}, $d_{x^2-y^2}$, d_{z^2} for each spin orientation. Due to its simple rocksalt crystal structure, a single set of tight-binding parameters are defined for nearest neighbour Sn and Te atoms. The parameters were taken from a work by Lent et al [142]. The parameters were obtained by fitting the eigenvalues of the bands at the high symmetry Γ, X and L points in the Brillouin zone (Fig.1.7**b**) to ab initio calculations. Further details of the fitting procedure can be found in Ref [142]. Numerical values for the tight-binding parameters are given in Table.2.4. A comparison of the bulk SnTe band structure, computed using DFT according to the method described in Section.2.1.2, and that computed using the tight-binding method, with the parameters given in Table.2.3, is shown in Fig.2.6.

Looking at Fig.2.6 the agreement between the two band structures, particularly for the bands closest to the Fermi energy, is generally quite good. Importantly, the fit is best at the fitted high symmetry points, and, as shall be described later, the parameters reproduce the crucial band inversion at the L point, which signifies the topologically non trivial properties of the material.

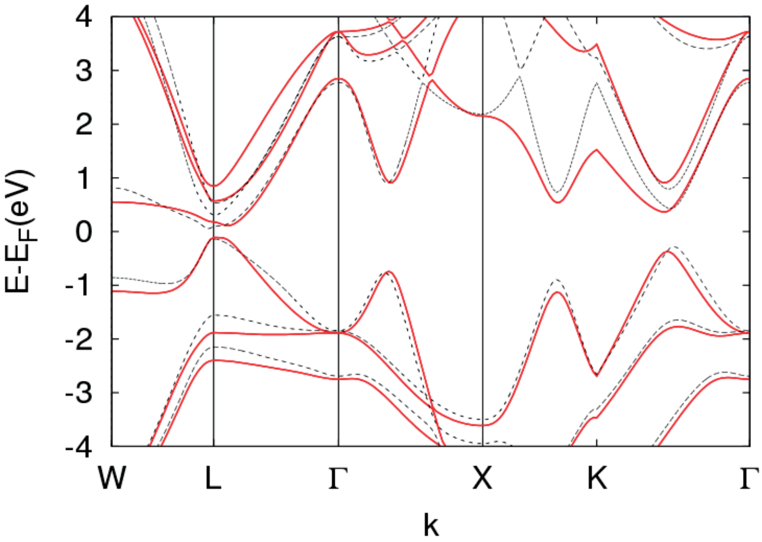

Figure 2.6 – Bulk band structure of SnTe. Solid and dotted lines represent results from tight-binding and DFT methods, respectively.

Table 2.2 – Tight-binding parameters for Bi_2Se_3 Energies are given in eV.

Onsite	**Bi**	**Se(1)**	**Se(2)**
ϵ_s	-10.7629	-10.9210	-13.1410
ϵ_p	0.2607	-1.5097	-1.1893
ξ_p	1.3777	0.2131	0.2421
Nearest-Neighbour Layer	**Bi-Se(1)**	**Bi-Se(2)**	**Se(1)-Se(1)**
$ss\sigma$	-0.6770	-0.2410	-0.3326
$sp\sigma$	2.0774	-0.2012	-0.0150
$ps\sigma$	-0.4792	-0.0193	0.0150
$pp\sigma$	2.0595	2.0325	0.9449
$pp\pi$	-0.4432	-0.5320	-0.1050
Intralayer	**Bi-Bi**	**Se(1)-Se(1)**	**Se(2)-Se(2)**
$ss\sigma$	0.2212	-0.0640	-0.0878
$sp\sigma$	-0.3067	0.2833	-0.2660
$pp\sigma$	0.3203	0.3047	-0.1486
$pp\pi$	-0.0510	-0.0035	-0.0590
Second-Neighbour Layer	**Bi-Bi**	**Bi-Se(1)**	**Se(1)-Se(2)**
$ss\sigma$	-0.0567	0.0333	0.0229
$sp\sigma$	-0.2147	-0.0047	-0.0318
$ps\sigma$	0.2147	0.2503	-0.0778
$pp\sigma$	0.1227	-0.1101	-0.0852
$pp\pi$	-0.0108	0.1015	0.0120

Table 2.3 – Tight-binding parameters for Bi_2Te_3. Energies are given in eV.

Onsite	**Bi**	**Te(1)**	**Te(2)**
ϵ_s	-9.9967	-10.4977	-10.8744
ϵ_p	-0.3774	-1.5684	-1.0189
ξ_p	1.284	0.4861	0.5213
Nearest-Neighbour Layer	**Bi-Te(1)**	**Bi-Te(2)**	**Te(1)-Te(1)**
$ss\sigma$	-0.5815	-0.3734	-0.2926
$sp\sigma$	1.9027	-0.5901	-0.1142
$ps\sigma$	-0.6636	-0.6020	0.1142
$pp\sigma$	1.9956	1.9354	1.1364
$pp\pi$	-0.4868	-0.5084	-0.1792
Intralayer	**Bi-Bi**	**Te(1)-Te(1)**	**Te(2)-Te(2)**
$ss\sigma$	-0.0132	0.0484	0.0771
$sp\sigma$	-0.3312	0.0961	-0.0256
$pp\sigma$	0.1986	0.3243	0.0286
$pp\pi$	-0.0299	0.0399	-0.0927
Second-Neighbour Layer	**Bi-Bi**	**Bi-Te(1)**	**Te(1)-Te(2)**
$ss\sigma$	-0.0912	0.0496	0.0807
$sp\sigma$	-0.0592	-0.0369	-0.0659
$ps\sigma$	0.0592	-0.0184	-0.0572
$pp\sigma$	-0.0614	-0.1993	-0.0390
$pp\pi$	0.0584	0.0828	0.0571

Table 2.4 – Tight-binding parameters for SnTe. Energies are given in eV.

Onsite	**Sn**	**Te**
ϵ_s	-6.578	-12.067
ϵ_p	1.659	-0.267
ϵ_d	8.38	7.73
ξ_p	0.592	0.564
Nearest-Neighbour	**Sn-Te**	
$ss\sigma$	-0.510	
$sp\sigma$	0.949	
$ps\sigma$	-0.198	
$pp\sigma$	2.218	
$pp\pi$	-0.446	
$pd\sigma$	-1.11	
$dp\sigma$	0.624	
$pd\pi$	-1.67	
$dp\pi$	0.766	
$dd\sigma$	-1.72	
$dd\pi$	0.618	

3 High-Index Surfaces of Bismuth Chalcogenide Nanostructures

As has been discussed above, bismuth chalcogenide nanostructures are an attractive platform from which to investigate topological properties of Z_2 TIs. Their high surface-to-volume ratio enhances surface contributions, compensating for the overriding contribution from the bulk, due to doping effects, and thereby providing access to transport measurements of topologically protected surface states. The distinct morphologies of nanostructures, combined with the confinement of topological charge carriers to reduced dimensions, also offers new perspectives on interesting phenomena such as the Aharonov-Bohm effect, and, moreover, is expected to give rise to novel physics.

Bismuth chalcogenides are layered van der Waals (vdW) materials, composed of covalently bonded quintuple layers (QL) held together by weak vdW interactions (Fig.3.1). Thus, there exists a natural cleavage plane, along which lies two equivalent orientations of low energy surfaces, (0001) and (000$\bar{1}$). Thus far, the vast majority of investigations of the surface states of bismuth chalcogenide TIs have focused on the low-energy (0001) surfaces. However, it should be appreciated that any bismuth chalcogenide nanostructure of dimensionality lower than two has to exhibit surfaces with orientations other than the two aforementioned. The properties of topologically protected charge carriers at any such surface are dependent on its crystallographic orientation, atomic structure and chemical composition. Furthermore, the overall properties of a TI nanostructure are defined by the relative presence of different facets on the nanostructure's surface, which is in turn determined by their respective surface energies (i.e. of a given facet).

Fully realizing the potential of bismuth chalcogenide nanostructures for exploring the fundamental physics of TIs, and for their use in any device applications, necessitates a clear understanding of how structure and morphology impact upon electronic properties. Consequently, this chapter details a systematic first-principles investigation of high-index surfaces of Bi_2Se_3 and Bi_2Te_3. The first part involves looking at the energetics of such surfaces, from which the structure and chemical composition of stable surfaces are determined. Finally, based on these results, the electronic properties of corresponding topological surface-state charge carriers, and their dependence on surface orientation and local chemical composition, are explored.

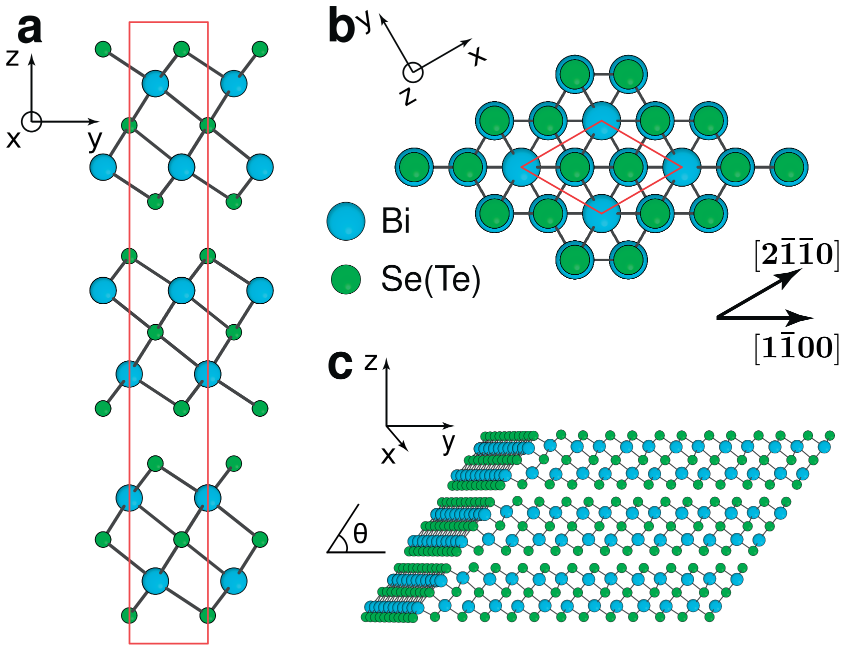

Figure 3.1 – Atomic structure of bulk bismuth chalcogenides and their high-index surfaces. **a**, **b** Crystal structure of bulk Bi2Se3 and Bi2Te3 viewed along the *a* and *c* axes, respectively. The hexagonal unit cell is shown using red lines. High-symmetry crystallographic directions [2$\bar{1}\bar{1}$0] and [1$\bar{1}$00] are indicated in panel **b**. **c** Two-dimensional slab model illustrating the structure of an exemplar high-index surface (left facet). The structures of high-index surfaces of layered bismuth chalcogenides are defined by a stacking angle θ and by the QL termination. The example shown corresponds to $\theta = 57.7°$ and the stoichiometric QL termination (configuration I).

3.1 Energetics

The electronic structure of a material's surface is dictated by the atomic structure of stable configurations of that surface. For layered materials, such as Bi_2Se_3 and Bi_2Te_3, the surface structure is defined by, firstly, how individual QLs terminate, and, secondly, by their orientation with respect to the surface plane, which can be described in terms of the angle θ, as shown in Fig.3.1**c**. In this definition, $\theta = 0°$ corresponds to the degenerate case of the low-energy (0001) surface, for which no QL termination takes place.

As such, the surface energy E (expressed in eV/Å^2) can, to a relatively high degree of accuracy, be related to the termination energy of individual quintuple layers ϵ (expressed in eV/Å) via:

$$E \simeq \frac{3}{c \sin\theta}\epsilon, \tag{3.1}$$

where c is a lattice constant of the hexagonal unit cell of the bismuth chalcogenides, whose values are listed in Table.3.1. Thus, $c/3$ is the QL thickness, with a value of 9.546 Å for Bi_2Se_3, and 10.162 Å for Bi_2Te_3. As this chapter will involve reference to the hexagonal unit cell of bismuth chalcogenides, correspondingly, crystallographic planes and lattice directions will be given in the four-index Miller-Bravais notation below. It should be noted that the approximation in Eqn.3.1 stems from describing the formation energy of a 2D surface in terms of the termination energy of a single 1D QL. In doing so, therefore, a term related to the loss of van der Waal's energy on stacking QLs to form the 2D surface is omitted. Nonetheless, given that the relative magnitude of vdW interactions is small, and that the leading term to the overall surface energy is the QL termination energy, this is considered to be an appropriate approximation.

Another important consideration is that QL terminations can have different local stoichiometries, either Bi-rich or Se(Te)-rich, and as such their relative stabilities are dependent upon the chemical potential of one of the constituent elements, μ_{Bi} or equivalently μ_{Se} (μ_{Te}). The chemical potential reflects experimental conditions under which the nanostructure is grown, and, importantly, as it varies this may result in the formation of a variety of stable surface structures. For example, the facets of differing stoichiometry belonging to different bismuth chalcogenide nanostructures, whose controlled growth is offered by various techniques, such as CVD based methods that were discussed in the Introduction. Hence, given that it should be possible to tailor the structure of high-index surfaces by changing the experimental conditions, this effectively translates into control over the electronic properties of topologically protected states hosted by these surfaces.

3.1.1 Methodology

The energies of QL terminations were systematically investigated by means of DFT calculations, carried out on a large number of single QL models in a nanoribbon configuration.

First principles calculations were performed within the DFT framework, employing the generalized gradient approximation (GGA) to the exchange-correlation functional [113]. Spin-orbit effects were treated self-consistently using fully relativistic norm-conserving pseudopotentials [127] within the two-component wavefunction formalism. A plane-wave kinetic energy cutoff of 35 Ry has been employed for the wave functions. All single QL nanoribbon models used to determine the QL termination energy were relaxed until the maximum force on a given atom was less than 0.025 eV/Å. A Monkhorst-Pack k-point mesh of $4 \times 2 \times 1$ was utilised for Brillouin zone integration [133]. Calculations were implemented through the PWSCF plane-wave pseudopotential code of the Quantum-ESPRESSO distribution [134].

Quintuple layer termination energies were calculated using single QL nanoribbon models of 5.4 nm and 5.7 nm width for Bi_2Se_3 and Bi_2Te_3, respectively. In total, over 60 different termination structures were considered, as is evident from the grey lines in Figs.3.2**a**,**b**. Two distinct orientations of QL edge terminations were investigated, the first having the QL edge orientated along the $[2\bar{1}\bar{1}0]$ crystallographic direction, whereas the other having the QL edge orientated along the $[1\bar{1}00]$ direction. The relationship between each high-symmetry crystallographic direction is shown schematically in Fig.3.1**b**, with an example of a QL termination edge orientated along the $[2\bar{1}\bar{1}0]$ direction corresponding to one of the QLs in Fig.3.1**c**. As the structure of the nanoribbon configurations were derived from the hexagonal unit cell of the bismuth chalcogenides, the corresponding lattice constants are shown in Table.3.1. The lattice constant c of the hexagonal unit cell is taken from experimental data [143]. The lattice constant a of the hexagonal unit cell is an optimised value, determined by manually altering the value of a in the bulk hexagonal unit cell, whilst fixing c to experiment [143], until a minimum in total energy was reached.

Table 3.1 – Lattice parameters of the hexagonal unit cell of Bi_2Se_3 and Bi_2Te_3.

System	a (Å)	c (Å)
Bi_2Se_3	4.178	28.638
Bi_2Te_3	4.403	30.486

Finally, the overall energy $G(\mu_{Bi})$ of a QL termination, calculated as a function of the chemical potential of Bi, μ_{Bi}, per unit length of the edge termination, is given by

$$G(\mu_{Bi}) = \epsilon_{Bi_2X_3} - \frac{N_{Bi}}{2L}\mu_{Bi}, \tag{3.2}$$

with the QL termination energy, $\epsilon_{Bi_2X_3}$, defined as

$$\epsilon_{Bi_2X_3} = \frac{1}{2L}(E_{model} - N_{Bi_2X_3}E_{Bi_2X_3} - N_{Bi}E_{Bi}), \tag{3.3}$$

and where X corresponds to Se (Te). E_{model}, $E_{Bi_2X_3}$ and E_{Bi} are the computed DFT total energies of the nanoribbon model, an isolated two-dimensional QL per Bi2Se$_3$ (Bi2Te$_3$) unit, and a Bi atom in its bulk elemental crystal (i.e. the reference chemical potential $\mu_{Bi} = 0$ eV corresponds to bulk elemental bismuth), respectively. N_{Bi} refers to the number of excess Bi atoms in the model relative to a stoichiometric system (i.e. with Bi:X = 2:3), whilst $N_{Bi_2X_3}$ is the number of stoichiometric Bi_2X_3 units. L is the periodicity of the nanoribbon model, equal to the lattice constant a of hexagonal unit cell, given in Table.3.1, in the case of the QL edge orientated along the $[2\bar{1}\bar{1}0]$ direction, and to $L = \sqrt{3}a$ in the case of the QL edge orientated along the $[1\bar{1}00]$ direction. The $[2\bar{1}\bar{1}0]$ and $[1\bar{1}00]$ lattice directions are labelled in reference to the hexagonal unit cell in Fig.3.1**b**

3.1.2 Results

The calculated overall energies of QL terminations, $G(\mu_{Bi})$, for Bi_2Se_3 and Bi_2Te_3 are plotted in Fig.3.2**a** and Fig.3.2**b**, respectively. Given that $\mu_{Bi} = 0$ eV corresponds to bulk elemental bismuth, the range of μ_{Bi} values, for which $G(\mu_{Bi})$ is plotted, is somewhat arbitrarily chosen in reference to this. As can be inferred from Eq.3.2, the dependence of $G(\mu_{Bi})$ is linear, with

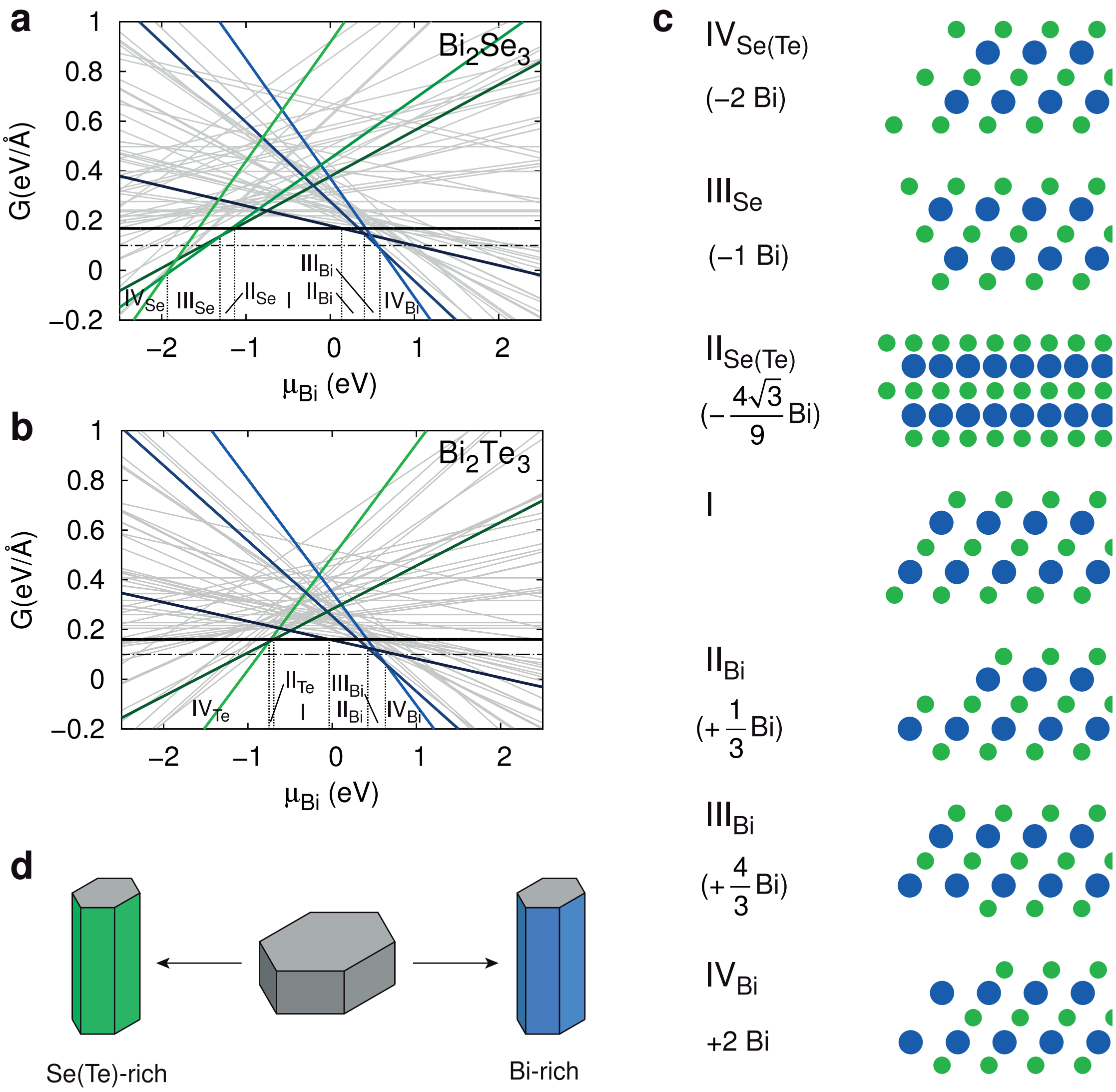

Figure 3.2 – Structure and energetics of QL terminations. **a**, **b** Overall termination energies, $G(\mu_{Bi})$, of Bi_2Se_3 and Bi_2Te_3 QLs, respectively, calculated for a large number of structural models. Coloured lines indicate termination structures showing regions of stability in certain ranges of chemical potential μ_{Bi}. **c** Atomic structures of stable QL terminations. Unrelaxed structures are shown for clarity. For non-stoichiometric terminations, the deviations from the nominal ratio Bi:X=2:3 (in Bi atoms per lattice constant a) are given in parentheses. **d** Schematic illustration showing that at moderate values of μ_{Bi} calculations predict the formation of nanoplates, whilst at extreme positive and negative values of μ_{Bi} the formation of nanowires is predicted, where the dominating surfaces are either Bi or Se(Te)-rich, respectively.

the gradient indicating the local deviation from the stoichiometric ratio Bi:X=2:3, at a given QL edge. QL terminations that were computed to show regions of stability, that is having the lowest value of $G(\mu_{Bi})$ within a certain range of μ_{Bi}, are indicated by thicker, coloured lines. In the case of Bi_2Se_3, seven such configurations were found, one of which was stoichiometric (labelled I in Fig.3.2**a**), three of which have an increased number of Se atoms (II_{Se}, III_{Se} and IV_{Se} in Fig.3.2**a**, and three an increased number of Bi atoms (II_{Bi}, III_{Bi} and IV_{Bi}

in Fig.3.2**a**), relative to the nominal stoichiometric ratio. Atomic structures for each stable configuration are schematically shown in Fig.3.2**c**. The sole stoichiometric termination, I, has a zero gradient, as expected from Eq.3.2, and is characterized by $G = 0.169$ eV/ Å. Moreover, it shows a particularly broad region of stability, within a range of moderate chemical potential values. As a consequence of their varying deviations from ideal stoichiometry, as indicated in Fig.3.2**c**, several distinct non-stoichiometric terminations also become energetically stable. The majority of the stable non-stoichiometric terminations are orientated along the $[2\bar{1}\bar{1}0]$ direction, with just the II_{Se} configuration orientated along the $[1\bar{1}00]$ direction. This implies that high-index surfaces formed by the $[2\bar{1}\bar{1}0]$ QL terminations are preferred from a thermodynamic perspective. However, an observation of a surface formed by the $[1\bar{1}00]$ QL termination, unambiguously points to the structure and stoichiometry of the II_{Se} configuration.

All the stable configurations of Bi_2Se_3 and Bi_2Te_3 QL terminations were structurally relaxed, and these are schematically shown in Fig.3.3. Evident is that, firstly, the stoichiometric termination I shows hardly any structural relaxation. Secondly, that the non-stoichiometric configurations with the largest deviations from the stoichiometric ratio, IV_{Bi} and $\mathrm{IV}_{Se(Te)}$, can be interpreted as the stoichiometric edge configuration I capped by elemental Bi and Se(Te), respectively. Particularly in the case of Bi_2Se_3, this reflects the expected tendency towards the onset of phase segregation into Bi_2Se_3 and elemental Bi and Se, respectively, at extreme values of chemical potential μ_{Bi}. In the case of Bi_2Te_3, the trends discussed above are more or less the same, with very similar structures of stable configurations and their associated energies (Fig.3.2**b**). One pertinent example being, that the stoichiometric configuration I, defined by $G = 0.161$ eV/ Å, is also predicted to be stable across a broad range of μ_{Bi} values. However, one primary difference is that no QL termination analogous to that of III_{Se} (Fig.3.2**c**) is predicted to be stable, and is subsequently not present on the Bi_2Te_3 phase diagram (Fig.3.2**b**).

Knowledge of surface energies E (Eq.3.1) for different crystallographic orientations of the surface allows one to deduce the equilibrium crystal shape, i.e. the shape that minimizes the interfacial free energy, by means of the Wulff construction [144]. Specifically, it defines the magnitude of a unit vector $\hat{\boldsymbol{n}}$ normal to a given crystal facet i, and connecting that facet to a common origin, as equivalent to the surface free energy of that facet $E_i(\hat{\boldsymbol{n}})$. This can be described by the relationship

$$h_i = \lambda E_i \tag{3.4}$$

where h_i is the perpendicular distance from the origin to a crystal facet i, defined by its crystallographic orientation $\{hkl\}$, E_i is the orientation dependent surface free energy, and λ is a constant that accounts for volume [145, 146]. This can be translated into a geometrical construction, whereby crystal facets are represented by planes drawn perpendicular to each unit vector $\hat{\boldsymbol{n}}$. Subsequently, the equilbrium crystal shape is that delineated by the inner envelope of relevant planes. Thus, the Wulff construction enables the contributions of different facets to the overall surface of a nanostructure to be determined.

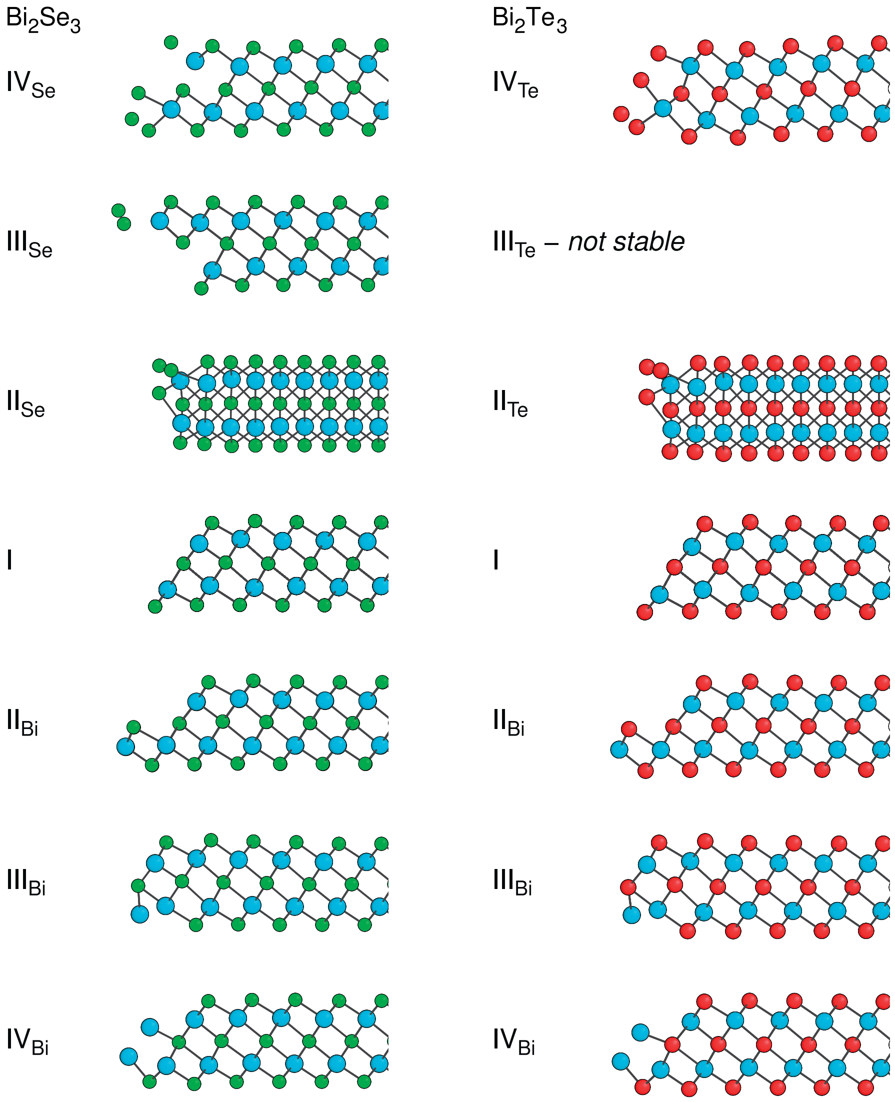

Figure 3.3 – Atomic structures of QL terminations of bismuth chalcogenide topological insulators. Relaxed atomic structures of Bi_2Se_3 (left) and Bi_2Te_3 (right) stoichiometric and non-stoichiometric QL terminations showing regions of stability (see Fig.3.2).

The surface energies of high-index facets can be deduced from the QL termination energies, as discussed above, however, this is not the case for the (0001) orientation, as it is of vdW origin. Nonetheless, the (0001) surface energy can be derived from two recent investigations [147, 148]. For example, in Ref. [147] calculations on a large number of layered systems lead to the derivation of a universal interlayer binding energy of $E_{Bind} = 0.02$ eV/Å^2. Given that the binding energy can be thought of as equivalent to the cleavage energy, and as cleaving a material leads to the formation of two surfaces, subsequently, the surface energy in this case is simply half the cleavage energy, and the (0001) surface energy can be estimated as $E_{vdW} = 0.01$ eV/Å^2. This value can be compared with the energies of high-index surfaces (Figs.3.2**a**,**b**) for $\theta = 90°$ (Eqn.3.1) by plotting $\epsilon_{equiv} = E_{vdW}c/3$, which is shown by the dashed lines in Figs.3.2**a**,**b**. Evident is that in the range of chemical potentials where the most stable QL termination is the stoichiometric configuration I, the low-energy (0001) surface is more thermodynamically favourable, and will be dominant. Consequently, if thermodynamic equilibrium conditions of nanoparticle growth are assumed, within this range of chemical potential values the Wulff construction implies the formation of nanoplatelet or nanoribbon morphology, with top and bottom facets being the (0001) and $(000\bar{1})$ low energy surfaces, whilst pertaining side surfaces would have a stoichiometric composition with QL terminations corresponding to configuration I. This is shown schematically in the middle of the cartoon in Fig.3.2**d**, with such morphologies having also been widely observed in experimental works [65, 68, 70, 149], as was discussed in the Introduction. For chemical potential values corresponding to Bi-rich or Se(Te)-rich conditions, i.e. at larger positive or negative values of chemical potential, respectively, the energies of stable non-stoichiometric surfaces are calculated to be lower than those of the stoichiometric (0001) and configuration I surfaces. This, conversely, implies the nanowire morphology [65, 87] for nanostructures grown under such conditions, with the surface dominated by the non-stoichiometric configurations and orientated along the (0001) direction. Such hexagonal cross-section nanowires are schematically displayed on the right and left hand side of Fig.3.2**d**, and have been directly observed experimentally [150], with non-hexagonal wires of similar configurations also having been widely synthesized [65], as an example shows in Fig.1.9 of the Introduction.

3.2 Electronic Structure

From a general perspective, our above results pertaining to the energetics of high-index surfaces point to the possibility of tailoring the morphology, composition and properties of bismuth chalcogenide nanostructures by controlling growth conditions. As detailed in the Introduction, a primary interest in investigating topological insulator nanostructures, is to study the effects of dimensionality reduction and confinement on the topologically protected properties of surface states (SS). In the specific case of bismuth chalcogenides, a distinct consequence of the Z_2 protected topology for strong TIs, which are defined by the invariants (1;000), is the presence of a single Dirac point on any given crystalline facet [15]. This stems from the fact that the $\nu_0 = 1$ invariant, which is the differentiator of a strong TI, is independent of the choice of reciprocal lattice vectors, as can be gleaned from the description of said invariant in the Introduction. In light of this, after determining the energetics of high-index surfaces, the electronic structure and associated properties related to the topological protection of states at these surfaces, particularly with respect to the stoichiometric configurations, were explored.

As has been discussed, the atomic-scale structure of high-index surfaces is determined by the crystallographic orientation of the surface and the termination of individual QLs. Subsequently, an initial focus was on the first degree of freedom, i.e. investigating the effects of varying the surface orientation, with respect to the stoichiometric termination I (Fig.3.2**c**), given its stability in a wide range of moderate values of chemical potential, for both Bi_2Se_3 and Bi_2Te_3 (Figs.3.2**a**,**b**). Calculations on the electronic structure of high-index surfaces were per-

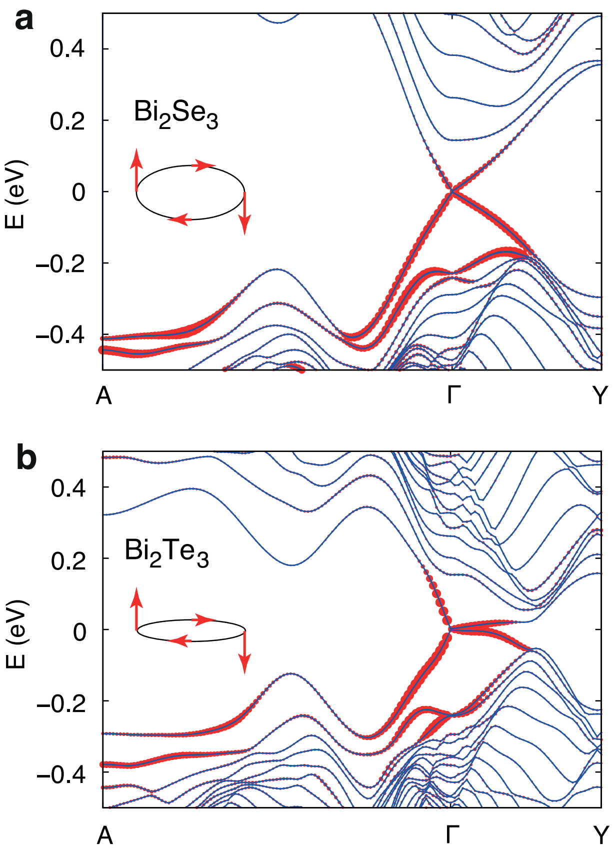

Figure 3.4 – Band structures of stoichiometric high-index slab models of Bi_2Se_3 and Bi_2Te_3. First-principles band structures of slab models of stoichiometric (configuration I) high-index surfaces of **a** Bi_2Se_3 and **b** Bi_2Te_3. The atomic structure of the surfaces is shown in Fig.3.1**c** and corresponds to $\theta = 57°$ and $\theta = 58°$ for Bi_2Se_3 and Bi_2Te_3, respectively. Points A and Y correspond to the Brillouin zone boundaries along directions defined by reciprocal lattice vectors associated with the real-space unit vectors of the surface. The size of red symbols reflects the magnitude of the inverse participation ratio (IPR). Schematic drawings of the constant energy contours depicting the helicity of electron charge carriers are shown in the insets.

formed using two-dimensional slab models of the same thickness as the width of nanoribbon models, as described in the Methodology part of the Energetics section above. The methodology pertaining to the computational details of the first principles calculations was also the same as was described earlier. Lattice constants of slab configurations were calculated assuming bulk lattice constants as well as the stacking order of bulk crystals, as described in relation to Table.3.1 in the Methodology of the Energetics section. Correspondingly, calculations on two-dimensional slab models were perfomed such that the interior part reproduces the bulk crystal structure. An example of one such slab model, of 3 QL thickness, is shown in Fig.3.1**c**, and corresponds to $\theta = 57°$ and $\theta = 58°$ for Bi_2Se_3 and Bi_2Te_3, respectively. In this particular surface configuration, atomic planes along which the QLs are terminated almost coincide with the surface place. Figs.3.4**a**,**b** show the electronic band structures of Bi_2Se_3 and Bi_2Te_3 slabs with such surface terminations, respectively.

For the the k-point path along which the band structures in Fig.3.4 are plotted, Γ-A and Γ-Y are orientated along the reciprocal lattice vectors associated with the real-space lattice vectors of the surface. Specifically, Γ-A is a momentum direction in the 2D Brillouin zone which runs parallel to the periodicity of the surface, i.e. along the QL planes, which can be labelled x', and as can be seen in Fig.3.1**c**, whilst the Γ-Y momentum direction, which can be labelled y', runs orthogonal to that direction within the surface plane. Looking at the actual band structures, as Fig.3.4 shows, both plots display a single Dirac cone centred around the Γ point, characteristic of the topologically protected surface states in strong TIs such as the bismuth chalcogenides, as described above.

A further quantitative confirmation of the surface localised origin of the Dirac cone states can be gained through calculation of the inverse participation ratio (IPR). For a given eigenstate i at crystal momentum **k**, with wavefunction $\psi_{i\boldsymbol{k}}$, if the probability of finding a particle at position **r** is given by $|\psi_{i\boldsymbol{k}}(\boldsymbol{r})|^2$, the IPR is

$$\mathrm{IPR}_{i,k} = \int |\psi_{i\boldsymbol{k}}(\boldsymbol{r})|^4 d\boldsymbol{r}. \tag{3.5}$$

The IPR represents the relative localisation of a given eigenstate, the larger its magnitude the more localised an eigenstate. Subsequently, as both band structures in Fig.3.4 show, the localised character of surface states is confirmed, as one would expect from their topological properties. It may be not strictly evident from Fig.3.4, but each band structure also shows the presence of a gap opening at the Dirac point, with a magnitude of 3 meV and 4 meV for the Bi_2Se_3 and Bi_2Te_3 slab models, respectively. This gap is a result of hybridization between surface states localised at opposite surfaces of the slab, stemming from the finite thickness of the slab models utilised. As the decay length of the surface states into the bulk is on the same order of magnitude as the slab thickness, this leads to spatial overlap of the wavefunctions of each respective slab surface, and consequently a gap opening [139, 151–154].

Perhaps the most interesting observation from the computed band structures in Fig.3.4 is the significant anisotropy, i.e. an orientation-dependent band dispersion of surface-localized Dirac fermion states. As can be seen in Fig.3.4, the dispersion of the SS bands along the Γ-A is steeper than that along Γ-Y, for both Bi_2Se_3 and Bi_2Te_3. This observation agrees well with previous calculations performed on this surface [155] for Bi_2Se_3, and is further confirmed by the experimental observation of an elliptical Fermi surface from ARPES measurements [156] on the same material. Incidentally, this is the only high-index surface of Bi_2Se_3 addressed theoretically, thus far, and, moreover, is the only case of a high-index surface that was investigated experimentally, using samples of Bi_2Se_3 epitaxially grown on an InP(001) substrate [156, 157]. The degree of Dirac fermion anisotropy can be quantified by calculating the Fermi velocities v_F, along each respective momenta direction. Fermi velocities were calculated as the gradient of the linear band dispersion around the Dirac point using

$$v_F = \frac{\nabla_E}{\nabla_{\boldsymbol{k}}\hbar}, \tag{3.6}$$

where $\nabla_{\boldsymbol{k}}$ is the difference in momenta between two k points, in units of m^{-1}, ∇_E is the corresponding energy difference in eV, and $\hbar$ is the reduced Planck constant. Consequently, the degree of anisotropy, quantified as the ratio of Fermi velocities for the momenta along x' direction (i.e. along the QL planes, see Fig.3.1**c**) and along y' direction (perpendicular to x'), $v_F^{x'}/v_F^{y'} = 2.07$, in the case of $\mathrm{Bi_2Se_3}$, agrees well with $v_F^{x'}/v_F^{y'} \sim 2$, observed in the ARPES measurements of Ref. [156]. Intriguingly, the same surface configuration of $\mathrm{Bi_2Te_3}$ shows an even more pronounced anisotropy of the Dirac fermion surface states, with a practically flat band dispersion for the momenta along y' direction (Fig.3.1**c**).

Following the investigation of the above surface configuration, θ was subsequently varied within the range $25° < \theta < 155°$, to generate a series of alternative surface configurations, whose electronic structures were investigated. The atomic structure of three representative surface configurations are shown in Fig.3.5**a**. For all studied surface orientations the band structures feature an anisotropic Dirac cone at the Γ point, but the degree of anisotropy varies across the investigated range of θ. In order to quantify and compare the degree of this anisotropy, between different surface configurations, as before, Fermi velocities were computed above the Dirac point energy and for momenta along x' and y' as a function of surface orientation θ, as shown in Fig.3.5**b** for both $\mathrm{Bi_2Se_3}$ and $\mathrm{Bi_2Te_3}$. The dashed horizontal lines in Fig.3.5**b** also display calculated Fermi velocities for the (0001) surface for $\mathrm{Bi_2Se_3}$ ($v_F \sim 4.8 \times 10^5 \mathrm{m/s}$) and $\mathrm{Bi_2Te_3}$ ($v_F \sim 4.6 \times 10^5 \mathrm{m/s}$). Subsequently, based on the above discussion and on closer inspection of Fig.3.5**b**, one can notice the following systematic trends. Firstly, in the plotted range of surface orientations (i.e. $25° < \theta < 155°$), Fermi velocities of the topological surface state bands of high-index surfaces are generally lower than that for the (0001) surface for both bismuth chalcogenides. Secondly, the largest anisotropies are achieved around $\theta = \frac{\pi}{2}$, which corresponds to QL planes orientated perpendicular to the surface, as is somewhat evident from the atomic structure shown in the middle of Fig.3.5**a**. Thirdly, with respect to $\mathrm{Bi_2Se_3}$, the value of $v_F^{x'}/v_F^{y'}$ does not exceed 2.5, however in the case of $\mathrm{Bi_2Te_3}$, the surface state band is practically dispersionless along y', in a broad range of θ values, and as such results in much larger anisotropies. Another point of interest worth mentioning is that the limits of $\theta = 0°$ and $\theta = 180°$ should correspond to the (0001) surface, and as such as θ approaches one of these limits one would expect $v_F^{x'}$ to approach that of the (0001) surface. Looking at Fig.3.5**b**, this seems to be happening for $\mathrm{Bi_2Se_3}$ as θ approaches 0°. However, as θ approaches 180° for $\mathrm{Bi_2Se_3}$, and for $\mathrm{Bi_2Te_3}$ generally, this is not the case. One conjecture for this behaviour not being manifested is based on the finite thickness of slab models utilised in the calculations. Specifically, as θ approaches these limits the congruent stacking of one QL over another is disrupted.

As was described in the Introduction, characteristic features of topological surface states are their spin properties, with a hallmark feature of the bismuth chalcogenide (0001) surfaces being their helical spin-textures (e.g. Fig.1.6). In light of this, we investigated spin textures of the high-index surfaces discussed in the preceding paragraph by analysing the momentum

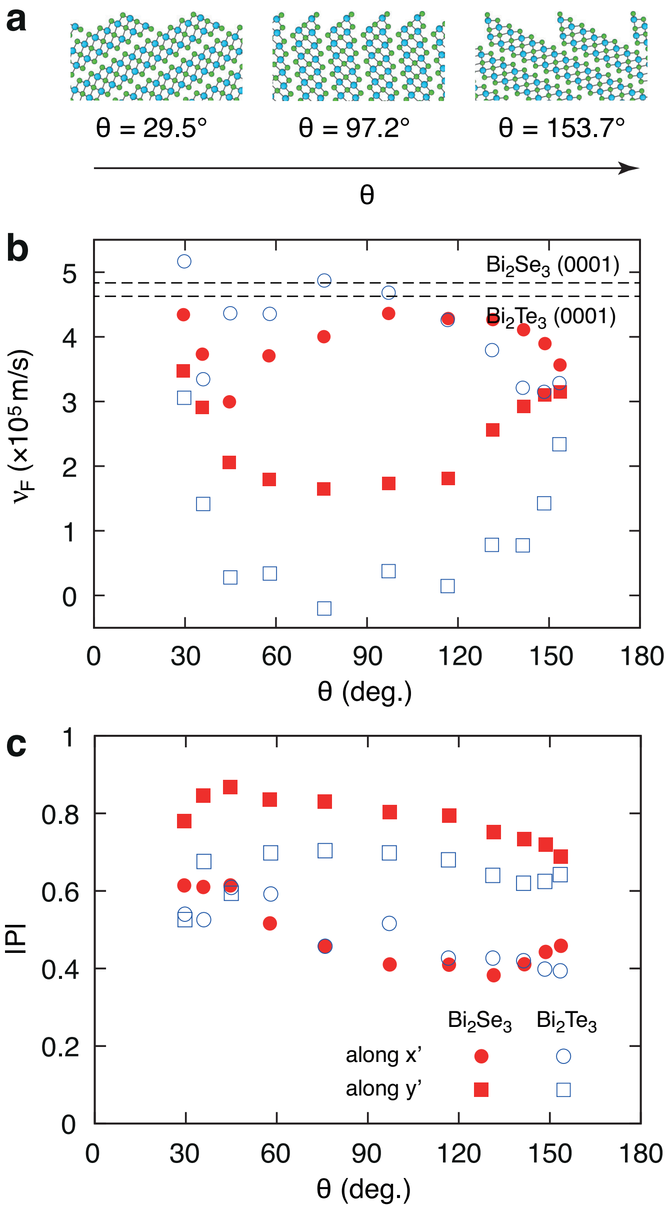

Figure 3.5 – Dependence of the band dispersion of topologically protected states on the surface orientation. **a** Atomic structures of three high-index stoichiometric surfaces of bismuth chalcogenides corresponding to $\theta = 29.5°$, $\theta = 97.2°$ and $\theta = 153.7°$ **b** Fermi velocities v_F and **c** absolute values of spin polarization **P** of electron surface-state charge carriers with momenta along x' and y' directions as a function of surface orientation θ. Values of the Fermi velocity v_F for the (0001) surfaces of Bi_2Se_3 and Bi_2Te_3 are indicated by dashed lines in panel **b**.

dependence of the expectation value of spin operators

$$\langle S_\alpha(\boldsymbol{k})\rangle = \frac{\hbar}{2}\langle \psi(\boldsymbol{k})|\sigma_\alpha|\psi(\boldsymbol{k})\rangle \quad (\alpha = x, y, z) \tag{3.7}$$

where $\psi(\boldsymbol{k})$ are the two-component spinor wavefunctions, and σ_α the Pauli matrices. For all investigated models of high-index stoichiometric surfaces calculations confirm spin-momentum locking of the Dirac fermion surfaces states, with a clockwise direction of rotation of the electron spin above the Dirac point observed. For example, schematic diagrams in the insets of Figs.3.4**a**,**b** display the constant energy contours for both bismuth chalcogenides, for the surface pertaining to $\theta = 57°$, depicting the spin-momentum locking of charge carriers. This picture is consistent with the spin texture of topolgical surface states at the (0001) surface [139], as can be seen, in the case of Bi_2Se_3, by comparing the inset of Fig.3.4**a** with that of the experimental data shown in Fig.1.6. It is of interest that model theory results of Refs. [158–160] predict the breaking of spin-momentum locking and the absence of helical SS on surfaces other than the (0001) and $(000\bar{1})$, i.e. for $\theta \neq 0, \pi$, which they base on symmetry arguments concerning the bulk Hamiltonian in their models.

The momenta-dependent anisotropy of SS charge carriers, that was evident through calculation of the Fermi velocities, also manifests itself in the spin properties of the bismuth chalcogenides, specifically in the magnitude of the spin-polarization vector, given by

$$\boldsymbol{P}(\boldsymbol{k}) = \frac{2}{\hbar}\boldsymbol{S}(\boldsymbol{k}). \tag{3.8}$$

It should be noted that regardless of the surface under consideration, this value is always reduced with respect to the nominal value of 1, due to the strong spin-orbit entanglement in bismuth chalcogenide TIs [139]. Furthermore, its value for both Bi_2Se_3 and Bi_2Te_3 (0001) surfaces is ~ 0.6 [139]. The magnitude of the spin-polarization vector $\mathbf{P}$, for surface state charge carriers above the Dirac point, is plotted as a function of the surface orientation angle θ, for Bi_2Se_3 and Bi_2Te_3, in Fig.3.5**c**. As the figure shows, the magnitude of the spin-polarization vector $\mathbf{P}$ is always lower along the x' direction, whilst along the y' direction, $|\mathbf{P}|$ is lower for Bi_2Te_3 in comparison to Bi_2Se_3. Consistent with the result for Fermi velocities, is that the largest degree of anisotropy occurs around $\theta = \frac{\pi}{2}$. This is of paritcular interest, as the model theory investigations described earlier [158–160] predict that at $\theta = \frac{\pi}{2}$ the spin texture collapses to a single dimension along the x' direction, leading to a complete suppression of spin polarization for momenta oriented along this direction. This is also indicative of the breaking of spin-momentum locking at $\theta \neq 0, \pi$ that these works predict. In the first-principles calculations described here, however, such a vanishing spin polarization is not observed, nonetheless, its magnitude for momenta along the x' direction reaches its minimum down to 0.4 for both chalcogenide materials, at this θ value.

The final part of this chapter focuses on a discussion of the electronic structure of high-index surfaces defined by non-stoichiometric termination of QLs. These surfaces are derived from the non-stochiometric QL edge terminations which show regions of stability in Fig.3.1**a**, and whose relaxed atomic configurations are shown in Fig.3.3, as discussed earlier. Slab models for the non-stoichiometric surfaces were constructed as those for the stoichiometric surfaces described above, whereby the atomic configuration of a given QL termination in the slab corresponds to the relaxed configurations shown in Fig.3.3**c**, and where the interior part reproduces the bulk crystal structure. The θ value for the slab models was $\theta = 57°$, such that atomic planes coincide with the surface plane, as was the case for the initial part of the above discussion in relation to the stoichiometric high-index surface with $\theta = 57°$, and as Fig.3.1**c** highlighted.

The models of non-stoichiometric surfaces are found to reveal generally more complex band structures. The computed band structures of the non-stoichiometric surface models are shown in Fig.3.6 and Fig.3.7, for Se(Te)-rich and Bi-rich surfaces, respectively. In particular, in addition to the topologically protected crossing within the band gap, we observe the presence of topologically trivial mid-gap states and self-doping, i.e. charge transfer between the surface and bulk-like states that leads to the shift of the Fermi level into the valence and conduction bands. Both effects can be considered as detrimental to the observation of topological surfaces states in TI nanostructures. This can be illustrated by looking at representative examples of a Se-rich and Bi-rich surface. Firstly, looking at the band structure of a Se-rich surface, for example that corresponding to the III_{Se} QL termination of Bi_2Se_3 in Fig.3.6, topologically trivial states with a high band dispersion are observed crossing the band gap and strongly hybridizing with the topologically protected states. Secondly, looking at the band structure of a Bi-rich surface, for example that corresponding to the III_{Bi} QL termination of Bi_2Se_3 in Fig.3.7, it is evident that the Fermi level appears shifted into the conduction band, i.e. n-type doping of the bulk-like states is observed. Concurrently, the Dirac point of the topological surface-state band at the Γ point appears to be immersed in the valence band. Furthermore, the change in the position of the Dirac point at Γ pulls another topologically protected crossing at the time-reversal invariant momentum point Y into the bulk band gap. A similar reorganization of the band dispersion of the topological surface states, upon changing the surface structure, has been predicted for a model bulk topological insulator [161].

With respect to the remaining non-stoichiometric high-index surfaces, general trends are that, firstly, all Bi-rich surfaces, i.e. for both Bi_2Se_3 and Bi_2Te_3, tend to be n-type doped, as is evident from Fig.3.7. Secondly, the presence of trivial mid-gap states is observed for both chalcogen and Bi-rich surfaces in the extreme limits of chemical potential $G(\mu_{Bi})$. Specifically, this refers to the Se(Te) rich surfaces $\mathrm{IV}_{Se(Te)}$ and $\mathrm{III}_{Se(Te)}$, and the Bi-rich surfaces IV_{Bi}, for both Bi_2Se_3 and Bi_2Te_3.

3.3 Conclusions

In summary, in this chapter an investigation, based on first-principles calculations, into the atomic structure and electronic properties of high-index surfaces in nanostructures of bismuth chalcogenide topological insulators, Bi_2Se_3 and Bi_2Te_3, was described. Our results predict that several possible quintuple layer terminations of different stoichiometric compositions can be realized, depending on experimental conditions. Both the stoichiometry of the surface and its crystallographic orientation significantly affect the electronic properties of topologically protected surface states, particularly the anisotropy of their Dirac fermion band dispersion and the degree of spin polarization. Moreover, these properties are shown to display clear dependence on the surface configuration. Through this understanding, one can gain a greater degree of control over the properties of nanostructures of topological insulators, aiming at prospective technological applications of these novel materials.

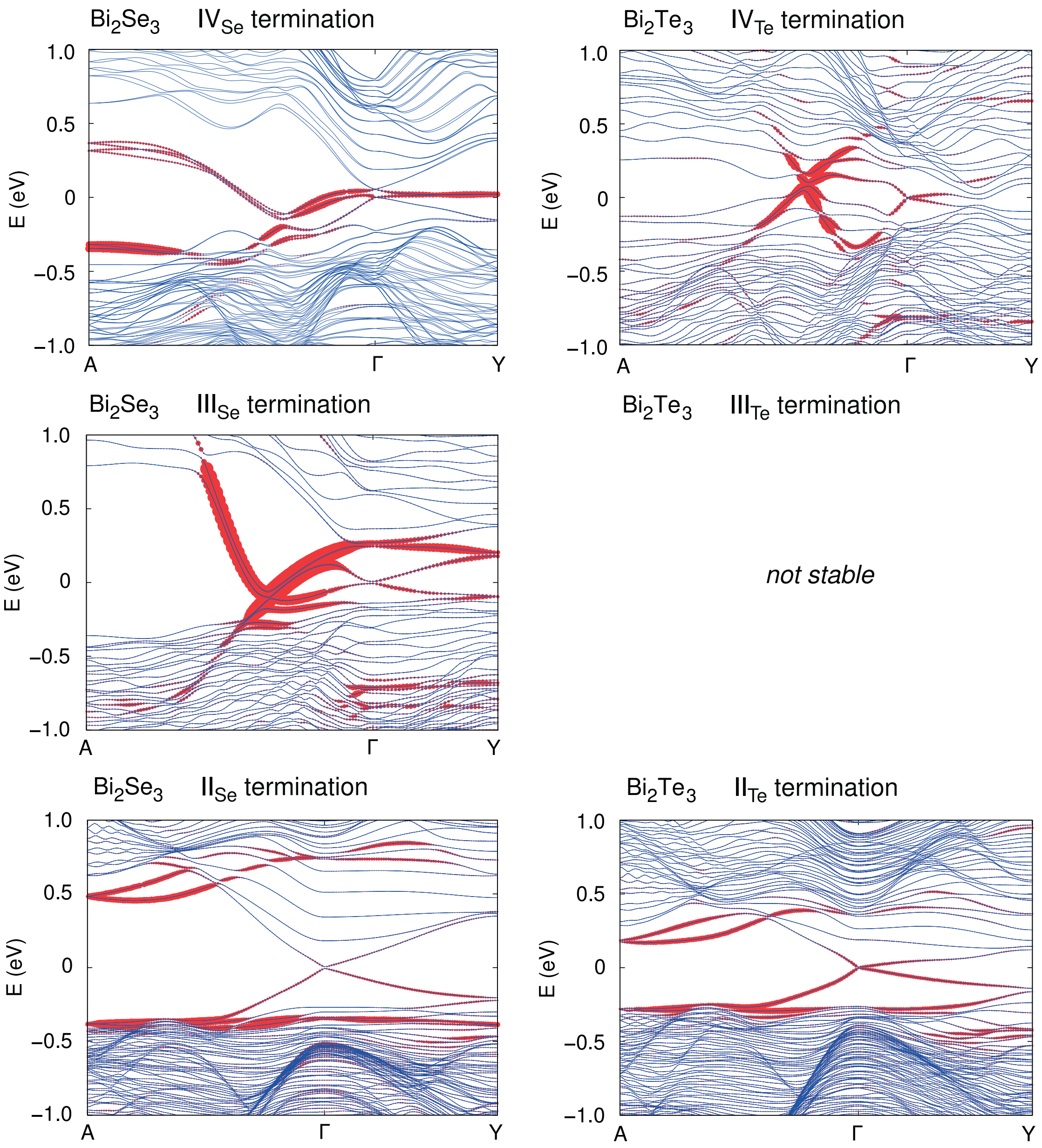

Figure 3.6 – Band structures of Se and Te-rich high-index slab models. First-principles band structures of slab models of Se-rich (left) and Te-rich (right) high-index surfaces of Bi_2Se_3 and Bi_2Te_3, respectively, at $\theta = 57.7°$. Points A and Y correspond to the Brillouin zone boundaries along directions defined by reciprocal lattice vectors associated with the real-space unit vectors of the surface. The size of red symbols reflects the magnitude of the inverse participation ratio (IPR).

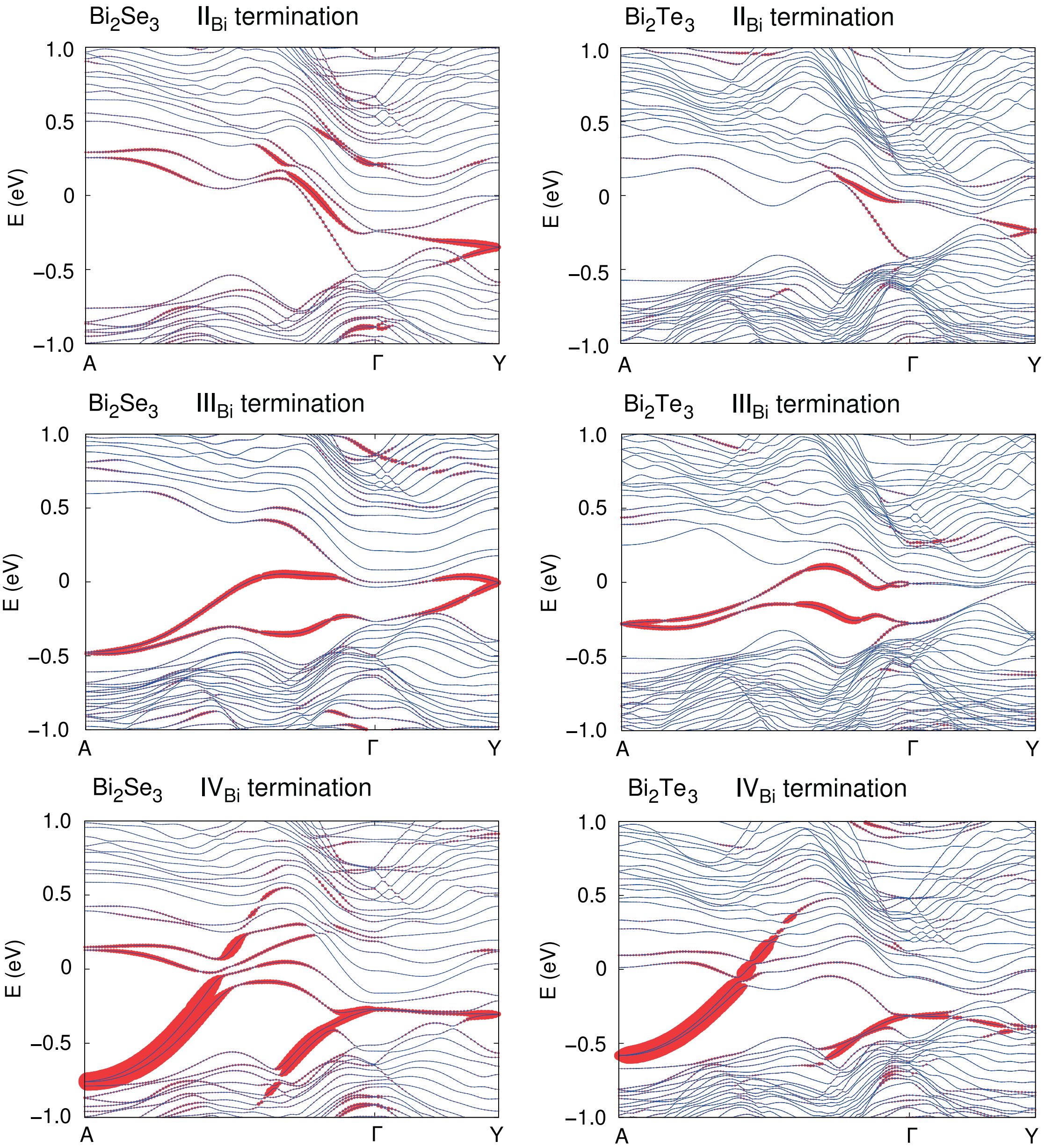

Figure 3.7 – Band structures of Bi-rich high-index slab models. First-principles band structures of slab models of Bi-rich high-index surfaces of Bi_2Se_3 and Bi_2Te_3 at $\theta = 57.7°$. Points A and Y correspond to the Brillouin zone boundaries along directions defined by reciprocal lattice vectors associated with the real-space unit vectors of the surface. The size of red symbols reflects the magnitude of the inverse participation ratio (IPR).

4 One-Dimensional Nanostructures of Bi_2Se_3 Topological Insulators

A single Dirac-cone characterizes the surface states (SS) of three-dimensional (3D) Z_2 topological insulators (TI), such as Bi_2Se_3 and related materials [32–34, 128]. A hallmark feature which results from the Z_2 topology is the helical spin polarization, whereby SS are spin non-degenerate and the electron spin is locked perpendicular to momentum [8, 66, 162], as was explained in the Introduction. Low-dimensional Bi_2Se_3 nanostructures [65, 67, 68, 72, 150, 163] enable the measurement and manipulation of the TI SS spin helicity, as exemplified by the recent observation of the Aharonov-Bohm (AB) effect [87, 92]. Consequently, Bi_2Se_3 nanostructures show promise in harnessing the helical properties of TI SS for applications in future electronic technologies such as spintronics [164–166] and topological quantum computing [167].

However, a detailed understanding of nanostructure morphology and finite-size effects on the electronic structure and topological properties of SS is still required. The morphology and dimensionality of nanostructures entail that surfaces other than the widely investigated (0001) are exposed. Hence, as a primary step it is necessary to have a detailed understanding of these high-index surfaces. This was the purpose of the previous chapter, where we determined the structure and chemical composition of stable surfaces, and found the SS band dispersion and spin texture to depend on surface orientation and local chemical composition. Those results guide the work described in this chapter, where we theoretically investigate models of 1D Bi_2Se_3 nanostructures, via a tight-binding model.

Commonly observed morphologies of Bi_2Se_3 nanostructures [65, 67, 68, 72, 150, 163], including nanowires, nanoribbons and nanoplates, were discussed in the Introduction. In this chapter we focus on, and construct, two distinct morphologies: a hexagonal nanowire (NW) and a nanoribbon (NR). The construction is guided by the finding from the previous chapter that the stoichiometric edge termination I is the most stable for the widest range of chemical potential values (Fig.3.2), and is in accordance with experiments [68, 150]. This is described in further detail below. The use of the term nanostructure in this chapter will collectively refer to both of these morphologies. Tight-binding calculations are used to investigate how finite-size effects and dimensionality reduction affect the electronic structure and SS topological properties, such as the spin helicity. The dependence of the surface state gap on nanostructure size is determined from band structure calculations. The effects of dimensionality reduction on the spin helicity are explored as a result of transitioning from a Dirac cone associated with a 2D surface, to quantized 1D sub-bands associated with a nanostructure.

4.1 Methodology

Tight-binding (TB) calculations were performed on two distinct Bi_2Se_3 morphologies: a hexagonal nanowire and a nanoribbon (Fig.4.1). The specific formalism of the tight-binding approximation utilised was described in the Methodology chapter, where Table.2.2 lists the Bi_2Se_3 TB parameters. Below, as we will be referring to the hexagonal unit cell of Bi_2Se_3 (Fig.3.1**a**), correspondingly, crystallographic orientations will be given in the four-index notation. The choice of the TB method was imposed by size of the NW and NR systems under investigation, where the largest NW and NR supercells contain ~ 7005 and ~ 2160 atoms, respectively. The use of alternative, first principles methods such as DFT would be prohibitively expensive or simply not possible. One potential issue with the TB model utilised is that surface and edge potential effects are not accounted for. However, all the NR systems being investigated have surfaces which either correspond to the (0001) surface, or are defined by a stoichiometric edge termination, where previous work using first principles calculations has shown that little to no edge reconstruction takes place, as discussed in the preceding chapter. Consequently, we believe that the exclusion of these effects in the TB model does not impact upon any conclusions that can be drawn from our results.

For hexagonal nanowires (Fig.4.1**a,b**), the axial direction of the NW is the [0001] direction i.e. c in Fig.4.1**a**. This is parallel to the direction along which QLs stack (Fig.4.1**b**), and is also the experimental growth direction of synthesized Bi_2Se_3 NWs [65, 150]. Each QL in the NW is defined by six hexagonal edges (Fig.4.1**a**). Our work on Bi_2Se_3 high-index surfaces elucidated that the most stable QL edge termination at a wide range of realistic chemical potential values was the QL edge termination I (see previous chapter and Fig.3.2). Consequently, the hexagonal NWs were constructed such that the edge termination at each QL hexagonal edge was termination I. A perspective view of two hexagonal NW edge surfaces is shown in Fig.4.1**b**. Band structure calculations were performed on NW supercells derived from the bulk hexagonal unit cell, with the nature of QL stacking ensuring that bulk crystal structure is preserved. In total six different NW models were considered, where the perimeter of the NW, P_{NW}, varied between 8.2 nm $\leq P_{NW} \leq$ 30.4 nm. The perimeter is the length enclosing the hexagonal cross-sectional area of the NW, which is shown in Fig.4.1**a**. The direction of periodicity for all NWs is parallel to the c direction of the Bi_2Se_3 bulk hexagonal unit cell (z in Fig.3.1**a**). Hence, the periodicity of all NW models corresponds to the c lattice parameter of the hexagonal unit cell and ~ 28.65 Å, the value is equivalent to that in Ref. [141], i.e. from where the TB parameters were taken.

For nanoribbons (Fig.4.1**c,d**), the axial direction of the NR is the $[11\bar{2}0]$ direction, which

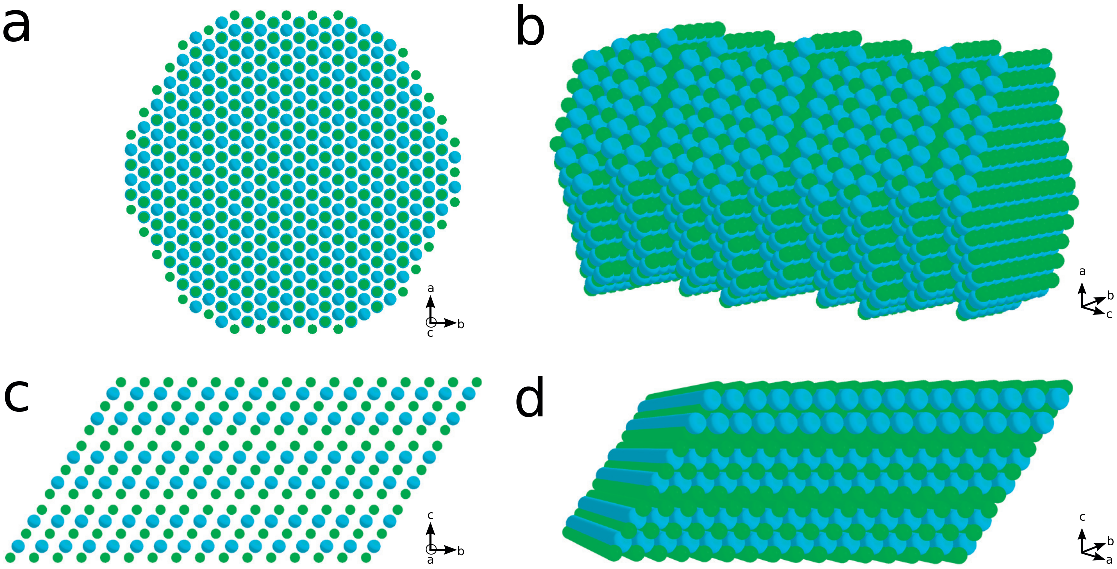

Figure 4.1 – Atomistic models of a Bi_2Se_3 hexagonal nanowire (perimeter ~ 30 nm) and nanoribbon (perimeter ~ 19 nm). **a** Profile showing cross-sectional area of the NW, *ab* plane corresponds to the (0001) facet. **b** Perspective showing QL stacking along the NW axis, i.e. along *c*. **c** Profile showing cross-sectional area of the NR, *cb* plane corresponds to the $(2\bar{1}\bar{1}0)$ facet, and NR axis is parallel to the *a* direction. **d** Perspective showing axial direction of NR axis along *a*. In all plots blue spheres correspond to Bi atoms, whilst green spheres to Se.

corresponds to *a* in Fig.4.1**c**. This is orthogonal to the *c* direction along which QLs stack along, and is also the commonly observed experimental growth direction of Bi_2Se_3 NRs [65, 150]. The constructed NR models have two distinct structural degrees of freedom. The first being the thickness, which is dictated by the number of QLs stacked parallel to *c* (Fig.4.1**c**), and thus defines the vertical dimension of the NR. The second being the width, which defines the dimension orthogonal to the thickness, and is dictated by the width of a given QL parallel to *b* (Fig.4.1**c**). An example of a 3QL thick and ~ 6 nm wide NR is shown in Fig.4.1**c,d**. For a given QL in a NR, the two equivalent edges run parallel to *a*, where the QL edge termination is again I (Fig.3.2), for the same reasons as outlined above for NWs. Subsequently, the NR models exhibit two different sets of facets. One being the equivalent top and bottom (0001) facets, aligned parallel to *a* (Fig.4.1**c**). In the 2D limit this facet corresponds to the extensively studied (0001) surface, which was described in the Introductory chapter (Fig.1.6). The other set being the equivalent side facets, aligned in the orthogonal direction, parallel to the $(10\bar{1}0)$ surface. NR models are constructed such that atomic planes along which QLs terminate practically coincide with the side facet plane. This is evident from the perspective picture in Fig.4.1**d**. In the 2D limit this facet is analogous to that of the Bi_2Se_3 high-index surface with the QL edge termination I and a side surface angle of $\theta \sim 57°$, described in the previous chapter (Fig.3.1**c**). Importantly, this is the only high-index surface that, to our knowledge, has been investigated theoretically, by work we have done (see Fig.3.1**c** and Fig.3.4**a**) that was discussed in the previous chapter, and in Ref. [155], and also then experimentally realized [156]. The width of NRs varied between ~6 nm–19 nm. For each width, band structure calculations were performed on NR supercells where the thickness was also varied between 5QL–9QL (~5 nm–9 nm). In summary, twenty five different NR models were considered, where the range of NR perimeters, P_{NR}, was 23.8 nm $\leq P_{NR} \leq$ 59.2 nm. The perimeter for NRs is the length enclosing the NR cross-sectional area, which is shown in Fig.4.1**c**. The direction of periodicity for NRs is parallel to the a direction of the Bi_2Se_3 bulk hexagonal unit cell (x in Fig.3.1**a**) Thus, the periodicity of all NR models is equivalent to the a lattice parameter of the hexagonal unit cell and ~ 4.11 Å, and again this value is equivalent to that in Ref. [141], as this is where the TB parameters were derived from.

4.2 Results

4.2.1 General Model of 1D Nanostructures

We begin with a general discussion of how dimensionality reduction and finite-size impact upon the electronic structure of a 1D Bi_2Se_3 nanostructure, with a particular focus on how the spin helicity of the 2D Dirac cone is manifested in the quantized 1D sub-bands of a nanostructure.

A two-dimensional Bi_2Se_3 surface can be described by orthogonal momenta directions $k_\parallel$ and $k_\perp$. The Z_2 topology entails that the electronic spectrum of such a surface is characterised by a conical band dispersion (Fig.1.6). Subsequently, the question arises as to how this spectrum is altered on forming a 1D nanostructure. Given the 1D periodicity, $k_\parallel$ can be thought of as the momentum parallel to the axial direction of the nanostructure. This is parallel to the c and a directions for NWs (Fig.4.1**a**) and NRs (Fig.4.1**c**), respectively, as described above. Since $k_\perp$ is the momentum in the direction normal to $k_\parallel$, on transitioning to 1D this consequently becomes the circumferential momentum around the nanostructure perimeter. The dimensions of the nanostructures under investigation are such that the magnitude of the perimeter is markedly smaller than that of the electron mean free path [42, 168]. Thus, surface electrons are subjected to quantum confined circular boundary conditions around the perimeter and $k_\perp$ is quantized.

Alongside the quantization of $k_\perp$, spin-momentum locking of the surface Dirac cone has a major influence over the dispersion of the electronic spectrum of a 1D nanostructure. The spin helicity results in an an electron picking up a π Berry phase due to the 2π rotation of the electron spin around the perimeter. If an applied magnetic flux Φ is threaded through the nanostructure core, an electron acquires an additional phase of $2\pi\Phi/\Phi_0$, where $\Phi_0 = h/e$ is the magnetic flux quantum, as was touched upon in the Introduction.

Taking these factors into consideration, the dispersion of the 1D sub-bands can be described by the following expression

$$E(k_\parallel) = \pm\hbar v_F \sqrt{k_\parallel^2 + k_\perp^2}, \tag{4.1}$$

where $\hbar$ is the reduced Planck's constant and v_F the Fermi velocity. The quantized values of $k_\perp$ are given by

$$k_\perp = \frac{2\pi(l + \frac{1}{2} - \Phi/\Phi_0)}{P}, \tag{4.2}$$

Thus

$$E(l, k_\parallel, \Phi) = \pm\hbar v_F \sqrt{k_\parallel^2 + \frac{[2\pi(l + \frac{1}{2} - \Phi/\Phi_0)]^2}{P^2}}. \tag{4.3}$$

where $l = (0, \pm1, \pm2, \ldots)$ is the angular momentum quantum number, the half integer term $(\frac{1}{2})$ stems from the π Berry phase, and P is the nanostructure perimeter. Subsequently, we can also define a half integer angular momentum

$$n = (l + \frac{1}{2}) = (\pm\frac{1}{2}, \pm\frac{3}{2}, \pm\frac{5}{2}, \ldots) \tag{4.4}$$

The quantized values of $k_\perp$ (Eqn.4.2) can be seen as distinct cuts across the 2D surface Dirac cone (Fig.4.2**a**). In the absence of an applied magnetic flux, i.e. for $\Phi = 0$, the electronic spectrum of a 1D nanostructure (Fig.4.2**b**) remains gapped, due to the half integer shift from the π Berry phase in Eqn.4.3. Consequently, the electronic spectrum is characterised by a series of doubly degenerate discrete 1D sub-bands, which can be labelled by the half integer angular momentum $n = (\pm\frac{1}{2}, \pm\frac{3}{2}, \ldots)$ (Eqn.4.4), and have a dispersion described by Eqn.4.3. An example of such a band structure is drawn in Fig.4.2**b**. The band gap can be derived from Eqn.4.3 at $k_\parallel = 0$, and is given by the energy difference between the lowest and highest energy conducting and valence sub-bands, respectively, for $n = \pm1/2$

$$E_g = \hbar v_F \frac{\pi}{P}. \tag{4.5}$$

Spin-momentum locking of the 2D surface Dirac cone is demonstrated by the helicity of the spin-polarization vector, $\boldsymbol{P}(\boldsymbol{k})$, along the constant energy contours encircling the Dirac point, with

$$\boldsymbol{P}(\boldsymbol{k}) = \left(\frac{2}{\hbar}\right) \times \left[\left\langle S_x(\boldsymbol{k}), S_y(\boldsymbol{k}), S_z(\boldsymbol{k})\right\rangle\right], \tag{4.6}$$

and the expectation value of the spin operators given by

$$\left\langle S_\alpha(\boldsymbol{k})\right\rangle = \left(\frac{\hbar}{2}\right)\left\langle \psi(\boldsymbol{k})|\sigma_\alpha|\psi(\boldsymbol{k})\right\rangle \quad (\alpha = x, y, z), \tag{4.7}$$

where $\psi(\boldsymbol{k})$ are the two-component spinor wave functions, and σ_α the corresponding Pauli matrices. For a 2D surface, defined by momenta $k_\parallel$ and $k_\perp$, spin-momentum locking is evinced by the spin-polarization vector pointing along the orthogonal $(\boldsymbol{k} \times \boldsymbol{z})$ direction [34,139,169,170].

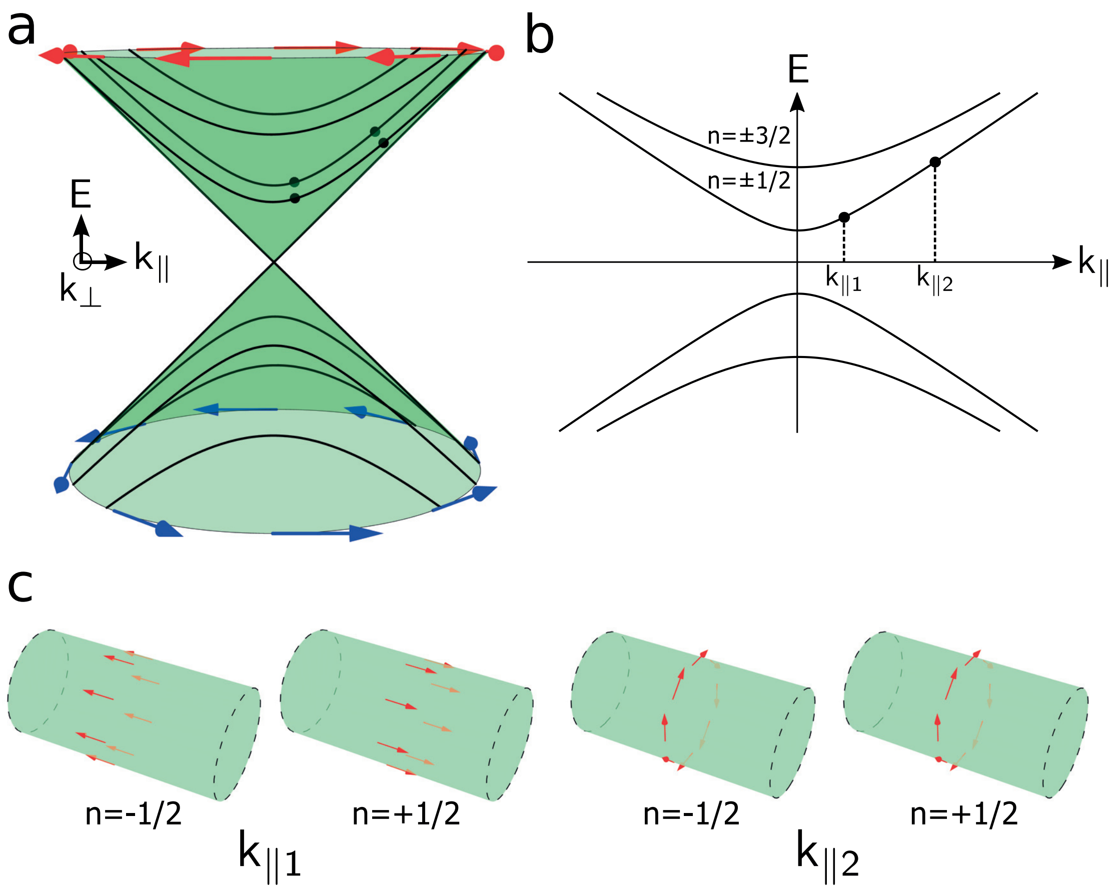

Figure 4.2 – Correspondence between the spin helicity of the Bi_2Se_3 2D surface Dirac cone and the quantized 1D sub-bands of a 1D nanostructure. **a** Schematic of the 2D surface Dirac cone showing quantized 1D sub-bands as distinct cuts through the conical dispersion. Red and blue arrows around the conduction and valence band constant energy contours show a left and right handed helicity, respectively. **b** Schematic band structure of a 1D nanostructure, where the dispersion is described by Eqn.4.3. The horizontal $k_{\parallel}$ axis is the momentum along the nanostructure axis. Each sub-band in the spectrum is doubly degenerate and is labelled by its respective half integer angular momentum n (Eqn.4.4). $k_{\parallel 1}$ and $k_{\parallel 2}$ denote momenta for pairs of degenerate $n = \pm\frac{1}{2}$ states close to Γ and the Brillouin zone boundary, respectively. **c** Schematic of spin textures in 1D nanostructures for $n = \pm\frac{1}{2}$ states at $k_{\parallel 1}$ and $k_{\parallel 2}$. For $n = \pm\frac{1}{2}$ degenerate states only the $S^n_{\parallel}$ component switches direction. Close to the origin at $k_{\parallel 1}$, the $S^n_{\parallel}$ component is significant and the $S^n_{\perp}$ component negligible, therefore the spin texture aligns along the NW axis. Close to the Brillouin zone boundary at $k_{\parallel 2}$, the $S^n_{\perp}$ component is significant and the $S^n_{\parallel}$ component negligible, therefore the spin texture is aligned in the tangent plane to axis and follows the perimeter. The handedness of the spin texture is equivalent for both $n = \pm\frac{1}{2}$ states.

This gives rise to a helicity that is left handed for the conduction band, and right handed for the valence band, represented by the red and blue arrows encircling the constant energy contours in Fig.4.2**a**, respectively. A point that was touched upon in the previous chapter and that is important to reiterate, is that it is possible for the magnitude of $\boldsymbol{P}(\boldsymbol{k})$ to be reduced from a maximum value of 1 (i.e. 100% spin polarization) due to the strong spin-orbit interactions present in Bi_2Se_3 [139]. This is indeed the case for the Bi_2Se_3 (0001) surface, where the magnitude of spin polarization is determined to be ~ 0.5 – 0.6 [139]. Moreover, a reduced value was also found from our work on different surface orientations of a high-index surface characterized by the stoichiometric QL edge termination I, as was discussed in reference to Fig.3.5 in the previous chapter. Given that each hexagonal edge of a NW QL (Fig.4.1**a,b**) is characterized by the same stoichiometric edge termination I, the latter point is of particular relevance to this chapter.

The manifestation of spin-momentum locking in 1D nanostructures can be analysed through the real-space local spin density $\boldsymbol{S}_i$, which is computed from the expectation value of the spin operators projected onto atomic sites $\boldsymbol{r}_i$. At a particular $k_\parallel$ and energy E, a state can be labelled by the half integer angular momentum n of the respective sub-band, subsequently the momentum-resolved local spin density for a given state is

$$\boldsymbol{S}_i^n\left(k_\parallel, \boldsymbol{r}_i\right) = \left(\frac{\hbar}{2}\right)\left\langle \psi\left(k_\parallel\right)\middle|\sigma_\alpha \otimes P_i\middle|\psi\left(k_\parallel\right)\right\rangle \quad (\alpha = x, y, z), \tag{4.8}$$

where P_i is a projector onto atom i, and is defined $P_i = \sum_{\lambda\sigma} |i\lambda\sigma\rangle\langle i\lambda\sigma|$, with λ the orbital index and σ the spin.

Given the electronic spectrum of a 1D nanostructure (Fig.4.2**b**), for the degenerate pair of lowest energy sub-bands we can define a pair of degenerate states, labelled by their respective $n = \pm\frac{1}{2}$ values, at two different momenta $k_{\parallel 1}$ and $k_{\parallel 2}$. The $n = \pm\frac{1}{2}$ states at $k_{\parallel 1}$ are positioned close to $k_\parallel = 0$, whilst the $n = \pm\frac{1}{2}$ states at $k_{\parallel 2}$ are positioned close to $k_\parallel = \frac{\pi}{2}$, i.e. the Brillouin zone boundary.

Subsequently, the states at $k_{\parallel 1}$ are situated towards the centre of the $n = \pm\frac{1}{2}$ cuts across the 2D surface Dirac cone (Fig.4.2**a**), close to the Dirac point. Given their relatively low energy (i.e. close to $E = 0$), the spin-polarization vector $\boldsymbol{P}$ (Eqn.4.6) along the associated constant energy contour is therefore aligned almost completely parallel to $-k_\parallel$ for the $n = +\frac{1}{2}$ state, and $+k_\parallel$ for the $n = -\frac{1}{2}$ state, with a negligible component aligned along $k_\perp$. The reversal of the alignment of $\boldsymbol{P}$ along $k_\parallel$ is a direct result of spin-momentum locking, since the $n = \pm\frac{1}{2}$ states have opposing $\pm k_\perp$ values, thus $\boldsymbol{P}$ undergoes a π rotation around the constant energy contour. This is reflected in the momentum-resolved local spin density $\boldsymbol{S}_i^n\left(k_\parallel, \boldsymbol{r}_i\right)$ (Eqn.4.8) of a given atom i in a 1D nanostructure. Specifically, $\boldsymbol{S}_i^n\left(k_\parallel, \boldsymbol{r}_i\right)$ has a large component aligned parallel to $k_\parallel$, which can be labelled $S_\parallel^n\left(k_\parallel, \boldsymbol{r}_i\right)$, and a negligible component parallel to $k_\perp$, which can be labelled $S_\perp^n\left(k_\parallel, \boldsymbol{r}_i\right)$. For the degenerate states $n = \pm\frac{1}{2}$ at $k_{\parallel 1}$, this is manifested in the $S_\parallel^{+\frac{1}{2}}$ and $S_\parallel^{-\frac{1}{2}}$ components, and hence $\boldsymbol{S}_i^{+\frac{1}{2}}$ and $\boldsymbol{S}_i^{-\frac{1}{2}}$, aligned almost parallel to the nanostructure axis, but in opposing directions. Collectively, considering all atoms together, this gives rise to spin textures at $k_{\parallel 1}$ that are oriented along opposing directions of the nanostructure axis for each $n = +\frac{1}{2}$ and $n = -\frac{1}{2}$ degenerate state, as shown schematically in Fig.4.2**c**.

The states at $k_{\parallel 2}$ are positioned along the same $n = \pm\frac{1}{2}$ cuts across the 2D surface Dirac cone (Fig.4.2**a**), however, they are markedly higher in energy. Consequently, due to spin-momentum locking, $\boldsymbol{P}$ has now undergone an almost $\frac{\pi}{2}$ rotation around the associated constant energy contour. An important consequence is that $\boldsymbol{P}$ is now aligned almost parallel to $-k_\perp$ for both $n = +\frac{1}{2}$ and $n = -\frac{1}{2}$ degenerate states. Moreover, $\boldsymbol{P}$ has a negligible component aligned parallel to $-k_\parallel$ and $+k_\parallel$ for the $n = +\frac{1}{2}$ and $n = -\frac{1}{2}$ state, respectively. This is the component that relates to $n = \pm\frac{1}{2}$ having opposing $\pm k_\perp$ values, and the consequent switch in alignment because of spin-momentum locking. For 1D nanostructures this is again reflected in the local spin density, with a negligible $S_\parallel^n$ component parallel to $k_\parallel$, and a large $S_\perp^n$ component parallel to $k_\perp$. For degenerate states $n = \pm\frac{1}{2}$ at $k_{\parallel 2}$, only the negligible $S_\parallel^{+\frac{1}{2}}$ and $S_\parallel^{-\frac{1}{2}}$ components have opposing spin orientations, respectively. However, the significant $S_\perp^{+\frac{1}{2}}$ and $S_\perp^{-\frac{1}{2}}$ components are both oriented in the same direction. Thus, the overall local spin density of an atom $\boldsymbol{S}_i^n$, should tend to orientate in the tangent plane to the nanostructure axis, following the perimeter. The direction of this orientation should be the same for both $n = \pm\frac{1}{2}$ degenerate states, as only the negligible $S_\parallel^{+\frac{1}{2}}$ and $S_\parallel^{-\frac{1}{2}}$ components switch directions. Considering all the atoms together, this should result in a spin texture with a 2π rotation of the local spin density around the nanostructure perimeter. Furthermore, the chirality of this rotation for both $n = \pm\frac{1}{2}$ degenerate states should be the same, as shown schematically in Fig.4.2**c**.

We now focus on the specific cases of the 1D Bi_2Se_3 NWs and NRs introduced above (Fig.4.1). For each case, we discuss how the dispersion of electronic spectrum is dictated by the respective morphologies, which is reflected in the differing behaviour of the perimeter dependence of the surface state gap. There will also be a detailed discussion of spin properties in reference to the model described above, with phenomena specific to each nanostructure again arising from their respective morphologies.

4.2.2 Nanowires

Band structures for the investigated range of NW models (8.2 nm $\leq P_{NW} \leq$ 30.4 nm) were computed using a realistic tight-binding model, as described in the Methodology above. The representative band structure computed for the largest NW model ($P_{NW} \sim$ 30.4 nm) is displayed in Fig.4.4. The band structure is characterized by the presence of discrete 1D subbands with a hyperbolic dispersion, as expected from the quantization along $k_\perp$ (Eqn.4.2) and Eqn.4.3, respectively. We find that a finite surface state gap (E_{NW}) and doubly degenerate bands characterize the electronic spectrum of all NWs. For wider NWs, with a large perimeter, the origin of the energy gap stems from the π Berry phase and the resulting half integer shift, which was described above. For smaller NWs, the hybridization between surface states localized at opposite surfaces of the NW may also contribute. In the absence of an applied magnetic flux, as E_{NW} approaches 0, this represents the perimeter of the NW being pushed towards the 2D limit, i.e. a surface. The band structure with a zero energy gap would be marked by a pair of linearly dispersing bands crossing at $k_\parallel = 0$. All of these factors pertain to the band structures of the investigated range of NR models too. However, specific differences in the dispersion of NR band structures and the perimeter dependence of the energy gap arise due to the distinctive NW and NR morphologies, as shall be discussed in further detail with respect to the NR case below.

The dependence of E_{NW} on P_{NW} is displayed in Fig.4.3. From the general model above, it is evident that as P_{NW} increases, the circumferential confinement around the NW perimeter is reduced. Specifically, as the inter-level spacing between quantized values of $k_{\perp}$ (Eqn.4.2), and therefore the 1D sub-bands, decreases. Clearly, E_{NW} also decreases, and one would expect the relationship $E_{NW} \sim P_{NW}^{-1}$ (Eqn.4.5). However, we find a relationship of $E_{NW} \sim P_{NW}^{-1.5}$ (Fig.4.3). We believe that the discrepancy in our finding may be connected to the perimeter range of the NWs under investigation (i.e. 8.2 nm $\leq P_{NW} \leq$ 30.4 nm). Namely, that due to the relatively small size of the NWs, particularly at the lower end of that range, the finite penetration depth of surface states may lead to a deviation from the ideal $E_{NW} \sim P_{NW}^{-1}$ scenario.

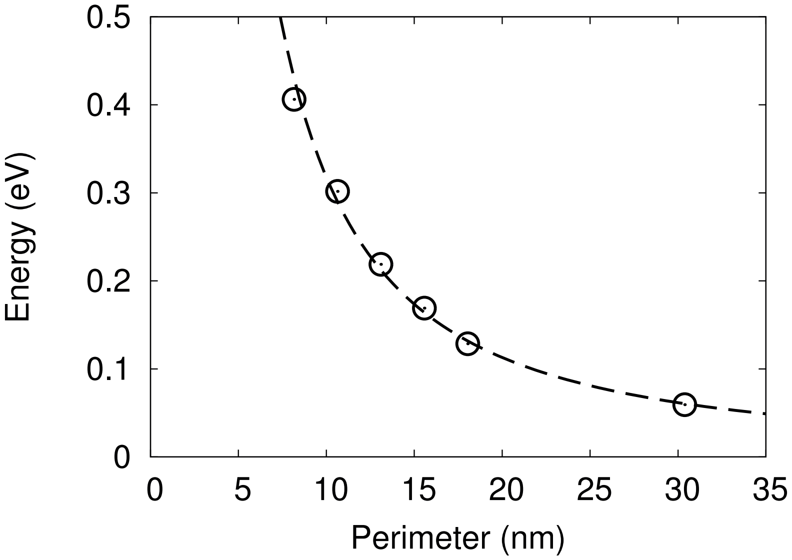

Figure 4.3 – Tight-binding results for NW surface state gap as a function of NW perimeter (P_{NW}) (black hollow circles). Numerical fit of $E_{NW} \sim P_{NW}^{-1.5}$ is given by black dashed curve.

For the NW ($P_{NW} \sim$ 30.4 nm) in Fig.4.4, we define a pair of $n = \pm\frac{1}{2}$ degenerate states, similarly to the general model above, at two different momenta, $k_{\parallel 1}$ and $k_{\parallel 2}$, close to Γ and Brillouin zone boundary, respectively. At both $k_{\parallel 1}$ and $k_{\parallel 2}$, for each $n = \pm\frac{1}{2}$ degenerate state we computed the momentum-resolved local spin density $\boldsymbol{S}_i^n$ (Eqn.4.8). A consequence of the cylindrical symmetry of both NW and NR morphologies is that the wave function for each $n = \pm\frac{1}{2}$ degenerate state, at either $k_{\parallel 1}$ or $k_{\parallel 2}$, is circularly localised on the surface of a nanostructure around its perimeter. This contrasts with calculations performed on a strictly 2D Bi_2Se_3 surface [139, 170], in slab geometries of sufficient thickness, where degenerate surface-states of opposite spin helicities are spatially separated, due to their localisation at opposite surfaces. Subsequently, to clearly resolve the real-space spin properties, we take the

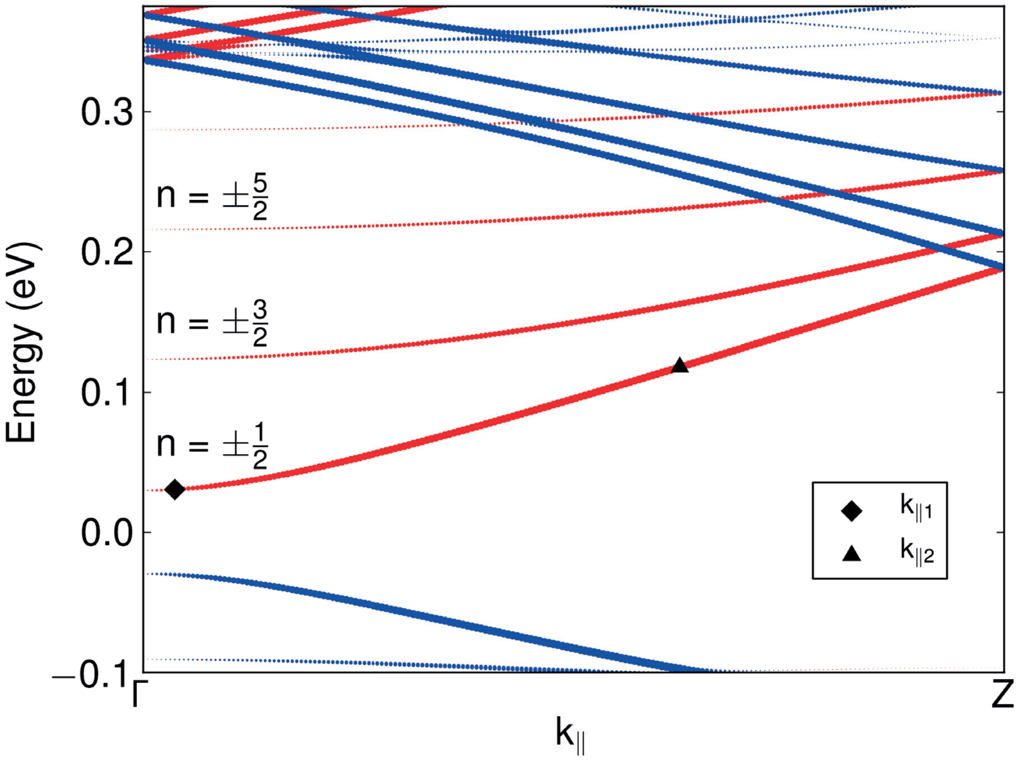

Figure 4.4 – Tight-binding band structure of a hexagonal NW with a perimeter of 30.2 nm. Size of points is proportional to the magnitude of h^n (see text and Eqn.4.10). Red and blue colours correspond to a left and right handed chirality of h^n, respectively. $k_{\parallel 1}$ and $k_{\parallel 2}$ define momenta for two pairs of $n = \pm\frac{1}{2}$ degenerate states close to the origin and Brillouin zone boundary, respectively.

sum, $\boldsymbol{S}_i^{tot}$, of the local spin densities, $\boldsymbol{S}_i^n$, for each $n = \pm\frac{1}{2}$ degenerate state

$$\boldsymbol{S}_i^{tot} = \boldsymbol{S}_i^{+\frac{1}{2}} + \boldsymbol{S}_i^{-\frac{1}{2}}. \tag{4.9}$$

This is plotted as function of atomic position $\boldsymbol{r}_i$ (Fig.4.5). The localisation of the total local spin density $\boldsymbol{S}_i^{tot}$, at both $k_{\parallel 1}$ (Fig.4.5**a**) and $k_{\parallel 2}$ (Fig.4.5**b**), around the NW perimeter is immediately evident, thereby confirming the surface state origin of the parent $n = \pm\frac{1}{2}$ states.

The difference in spin textures that arise from $\boldsymbol{S}_i^{tot}$ calculated at $k_{\parallel 1}$ (Fig.4.5**a**) and $k_{\parallel 2}$ (Fig.4.5**b**) shows that the spin-momentum locking properties of the 2D surface Dirac cone are manifested in the 1D hexagonal NW. A direct correspondence between the helicity of the spin polarization vector (Eqn.4.6) of the Dirac cone (red arrows Fig.4.2**a**) and the the real-space spin properties of the NW (Fig.4.5) is exhibited. We explain this below in reference to spin phenomena discussed in the general model above.

Close to Γ at $k_{\parallel 1}$, we find that for the degenerate $n = \pm\frac{1}{2}$ states, the significant component of $\boldsymbol{S}_i^n$ (Eqn.4.8) is the $S_\parallel^n$ component aligned along the NW axis. Importantly, $S_\parallel^{+\frac{1}{2}}$ and $S_\parallel^{-\frac{1}{2}}$ have an opposing alignment along the axis. This is a consequence of spin-momentum locking of the surface Dirac cone, as was detailed in the general model above. Conversely, the component around the NW perimeter $S_\perp^n$ is found to be negligible for both $n = \pm\frac{1}{2}$ states. For each $n = \pm\frac{1}{2}$ state at $k_{\parallel 1}$, this results in spin textures analogous to those schematically drawn in Fig.4.2**c**. Consequently, by calculating $\boldsymbol{S}_i^{tot}$ (Eqn.4.9) at $k_{\parallel 1}$, the opposing, and significant, $S_\parallel^{+\frac{1}{2}}$ and $S_\parallel^{-\frac{1}{2}}$ components cancel, and the component $S_\parallel^{tot}$ is zero. Conversely, the negligible $S_\perp^{+\frac{1}{2}}$ and $S_\perp^{-\frac{1}{2}}$ components, lying in the tangent plane to the NW axis, are aligned in the same direction around the NW perimeter and are summed together to give $S_\perp^{tot}$. Hence, at $k_{\parallel 1}$ this results in the spin texture shown in Fig.4.5**a**, where the total local spin density $\boldsymbol{S}_i^{tot}$ on an atom is extremely small, comprised of the negligible $S_\perp^{tot}$ component, which lies entirely in the tangent plane and follows the perimeter.

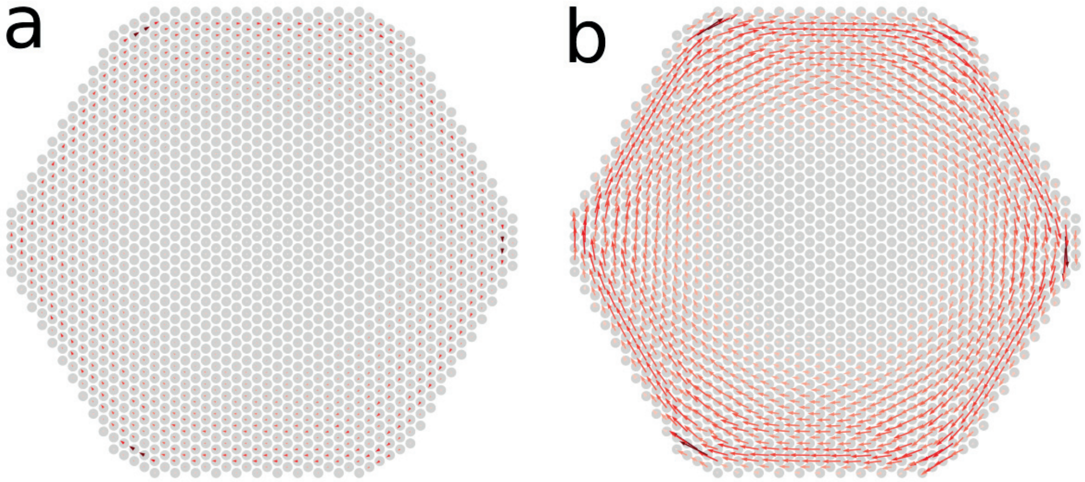

Figure 4.5 – Spin textures for a hexagonal Bi_2Se_3 NW (P_{NW} = 30.4 nm) at $k_{\parallel 1}$ (**a**) and $k_{\parallel 2}$ (**b**) (see Fig.4.4 and text). Red arrows denote total local spin density $\boldsymbol{S}_i^{tot}$ (Eqn.4.9), grey circles indicate the position of Bi and Se atoms. The view direction is equivalent to that shown in Fig.4.1**a**.

On the other hand, close to the Brillouin zone boundary at $k_{\parallel 2}$, we find the $S_\perp^n$ component of $\boldsymbol{S}_i^n$ to be significant, whilst the $S_\parallel^n$ component is negligible, as expected from the general model. Spin-momentum locking of the 2D surface Dirac cone is again manifested in $S_\parallel^{+\frac{1}{2}}$ and $S_\parallel^{-\frac{1}{2}}$ aligning in opposing directions along the NW axis. Furthermore, $S_\perp^{+\frac{1}{2}}$ and $S_\perp^{-\frac{1}{2}}$ are both aligned in the tangent plane to the NW axis and follow the same direction around the perimeter. Thus, on calculating $\boldsymbol{S}_i^{tot}$, the negligible $S_\parallel^{+\frac{1}{2}}$ and $S_\parallel^{-\frac{1}{2}}$ components cancel, and $S_\parallel^{tot}$ is zero. Conversely, the significant $S_\perp^{+\frac{1}{2}}$ and $S_\perp^{-\frac{1}{2}}$ components are summed giving $S_\perp^{tot}$, with a much larger magnitude to that at $k_{\parallel 1}$, resulting in the spin texture shown in Fig.4.5**b**. The spin is again aligned entirely in the tangent plane to the NW axis, however, the far larger magnitude of $\boldsymbol{S}_i^{tot}$ is clearly evident, due to the significant $S_\perp^{tot}$ component. The consequent spin texture (Fig.4.5**b**) has a pronounced 2π rotation of the total local spin density $\boldsymbol{S}_i^{tot}$ around the NW perimeter. Moreover, this rotation follows a clockwise rotation around the wire. The handedness of this rotation is equivalent to the left handed helicity observed for the 2D TI conduction band (CB) SS (red arrows Fig.4.2**a**). Since $\boldsymbol{S}_i^{tot}$ is also derived from CB states, this again highlights the direct correspondence between the spin helicity of the 2D surface Dirac cone and the quantized sub-bands of the 1D NW.

To quantify the 2π rotation of the local spin density around the NW perimeter, for a given state n, at a particular $k_\parallel$ and E, the following quantity can be calculated

$$h^n(k_\parallel) = \sum_i \left(\boldsymbol{S}_i^n \big(k_\parallel, \boldsymbol{r}_i\big) \times \frac{\boldsymbol{r}_i}{|r_i|} \right), \tag{4.10}$$

where $\boldsymbol{S}_i^n\big(k_\parallel, \boldsymbol{r}_i\big)$ is the momentum-resolved local spin density on a given atom i, as defined above (Eqn.4.8), whilst $\boldsymbol{r}_i$ is the atomic position vector from the 1D nanostructure axis.

The energy dependence of $h^n(k_\parallel)$ for the P_{NW} = 30.2 nm NW is plotted in Fig.4.4. Analysis of this dependence below provides further insight into the correspondence between the spin helicity of the 2D surface Dirac cone and the spin properties of the 1D NW. Moreover, we find that it gives rise to interesting transport properties, as we detail through the definition of a spin polarization density (Eqn.4.11).

An ideal 2π rotation of the local spin density $\boldsymbol{S}_i^n$ around the NW perimeter, with the spin aligned entirely in the tangent plane to the NW axis, i.e. with $S_\parallel^n = 0$ and $\boldsymbol{S}_i^n = S_\perp^n$, would be reflected in a maximum value of h^n. Under the assumption of a 100% spin polarization, this value would equal $h^n = \pm 1$ for a clockwise and anti-clockwise rotation, respectively. However, for the NW in Fig.4.4, the maximum possible value of h^n is reduced from ± 1, as spin polarization is less than 100% because of the strong SOI present in $\mathrm{Bi_2Se_3}$, as discussed above.

The behaviour of $h^n(E, k_\parallel)$ in Fig.4.4 stems from three primary factors. The first being that not only is $|h^n| < 1$, as just discussed, it is also reduced from its maximum possible value. This is because the half integer shift arising from the π Berry phase (Eqn.4.3) means that all the $\pm n$ sub-bands in the gapped spectrum in Fig.4.4 have $k_\perp \neq 0$ (Eqn.4.2). Thus, the finite $k_\perp$ value of each $\pm n$ sub-band entails that they do cut across the centre of the Dirac cone (Fig.4.2**a**), as this corresponds to $k_\perp = 0$. Consequently, there is always a finite $S_\parallel^n$ contribution to $\boldsymbol{S}_i^n$. For example, as was discussed in reference to the $n = \pm\frac{1}{2}$ sub-bands above. Physically, this represents the spin component on a given atom that aligns along the NW axis out of the tangent plane, thereby reducing the ideal in-plane 2π rotation of $\boldsymbol{S}_i^n$, and hence h^n from its maximum value.

Secondly, analysing the dependence of h^n with respect to $k_\parallel$ in Fig.4.4. It is clearly discernible that h^n is significantly larger at $k_{\parallel 2}$ close to the Brillouin zone boundary, than at $k_{\parallel 1}$ close to $k_\parallel = 0$. The general behaviour can be explained with respect to the $n = \pm\frac{1}{2}$ degenerate states, where quantitatively this is reflected in a value of $h^n = 0.64$ at $k_{\parallel 2}$ against that of $h^n = 0.14$ at $k_{\parallel 1}$. The pertaining reasons are as described previously. Namely, that the larger value of h^n at $k_{\parallel 2}$ is because $S_{\perp}^n$ is significant and $S_{\parallel}^n$ negligible, whilst at $k_{\parallel 1}$ the reverse holds, and hence h^n is reduced.

Thirdly, analysing the energy dependence of h^n. Evident from Fig.4.4 is that at $k_{\parallel}$ close to the Brillouin zone boundary (e.g. at $k_{\parallel 2}$) the magnitude of h^n is largest for the lowest energy $n = \pm\frac{1}{2}$ sub-bands, and gradually diminishes for higher energy $\pm n$ sub-bands (e.g $n = \pm\frac{3}{2}, \pm\frac{5}{2}, \ldots$). This is because the $n = \pm\frac{1}{2}$ sub-bands have the smallest value of $k_{\perp}$ (Eqn.4.2). Thus, seen as cuts across the 2D surface Dirac cone (Fig.4.2**a**), they cut across the cone closest to the centre at $k_{\perp} = 0$. Consequently, at $k_{\parallel 2}$ for $n = \pm\frac{1}{2}$, the spin polarization vector along the associated constant energy contour has the closest parallel alignment to $k_{\perp}$, relative to the higher energy ($n = \pm\frac{1}{2}, \pm\frac{3}{2}, \pm\frac{5}{2}, \ldots$) sub-bands. This leads to the largest values for the $S_{\perp}^n$ component and resultantly h^n. However, as $|n|$ increases, the corresponding magnitude of $|k_{\perp}|$ also increases, as evident from Eqn.4.2. The increasing values of $|k_{\perp}|$ correspond to cuts across the 2D surface Dirac cone (Fig.4.2**a**), and associated constant energy contours, at an increasing distance from the centre at $k_{\perp} = 0$. Consequently, due to spin-momentum locking the extent to which the spin polarization vector along the energy contours aligns parallel to $k_{\perp}$ diminishes with increasing $|n|$. Subsequently, as the energy of the ($n = \pm\frac{1}{2}, \pm\frac{3}{2}, \pm\frac{5}{2}, \ldots$) sub-bands increase, the contribution of the $S_{\perp}^n$ component to $\boldsymbol{S}_i^{tot}$ decreases, whilst that of $S_{\parallel}^n$ increases. Hence, the extent to which there is an ideal 2π rotation around the NW perimeter in the tangent plane also decreases, and therefore so does h^n, with increasing E.

A large value of h^n for a given state n, for example the $n = \pm\frac{1}{2}$ states at $k_{\parallel 2}$ (Fig.4.4), implies that the corresponding magnitude of the overall spin polarization vector (Eqn.4.6) $|\boldsymbol{P}(\boldsymbol{k})| \sim 0$. Primarily, as the close to ideal 2π rotation of $\boldsymbol{S}_i^n$ around the NW perimeter, means that the expectation value of the spin operators (Eqn.4.7) $\left\langle S_{x,y}(\boldsymbol{k}) \right\rangle \sim 0$ and $\left\langle S_z(\boldsymbol{k}) \right\rangle$ is negligible. For states with a smaller h^n, for example the $n = \pm\frac{1}{2}$ states at $k_{\parallel 1}$ (Fig.4.4), $|\boldsymbol{P}(\boldsymbol{k})|$ has a small finite value. This is mainly due to the finite value of $\left\langle S_z(\boldsymbol{k}) \right\rangle$, as $S_{\parallel}^n$ is the major component of $\boldsymbol{S}_i^n$, whilst $\left\langle S_{x,y}(\boldsymbol{k}) \right\rangle \sim 0$ as $S_{\perp}^n \sim 0$.

Thus, in order to explore potential spin-dependent transport properties, we define a spin polarization density as

$$H(E) = \frac{\int \sum_n h^n(k_{\parallel}) \delta(E - E_{n,k_{\parallel}}) dk_{\parallel}}{\sum_n \int \delta(E - E_{n,k_{\parallel}}) dk_{\parallel}}, \tag{4.11}$$

where h^n is as above (Eqn.4.10), the denominator defines the number of available transport channels at a given energy E, and the numerator the sum of h^n with respect to those available transport channels.

The clear-cut oscillatory dependence of $H(E)$ (Fig.4.6) reflects the quantization along $k_{\perp}$, and the variation of $h^n(E, k_{\parallel})$. At lower energies, there are a reduced number of available transport channels, however, for those channels, there is a strong 2π rotation of $\boldsymbol{S}_i^n$ around the NW perimeter. Conversely, as E increases, the number of available channels increase, yet the degree to which there is a clear $\boldsymbol{S}_i^n$ rotation around the NW perimeter decreases within those channels, for reasons that have been outlined. This behaviour could be exploited in potential device applications. For example, one could imagine harnessing the energy-dependent spin polarization density in Fig.4.6 to generate spin polarized charge carriers. Specifically, this might be achieved by locally contacting a section of a hexagonal NW and driving a charge current $\boldsymbol{J}$ along one direction of the NW axis. For a given $\boldsymbol{J}$, based on the behaviour in Fig.4.6, this would result in an injection of spin polarized charge carriers at the local contact. If such transport behaviour were to be observed in a Bi_2Se_3 NW, this could be exploited in future quantum devices in burgeoning technologies such as spintronics.

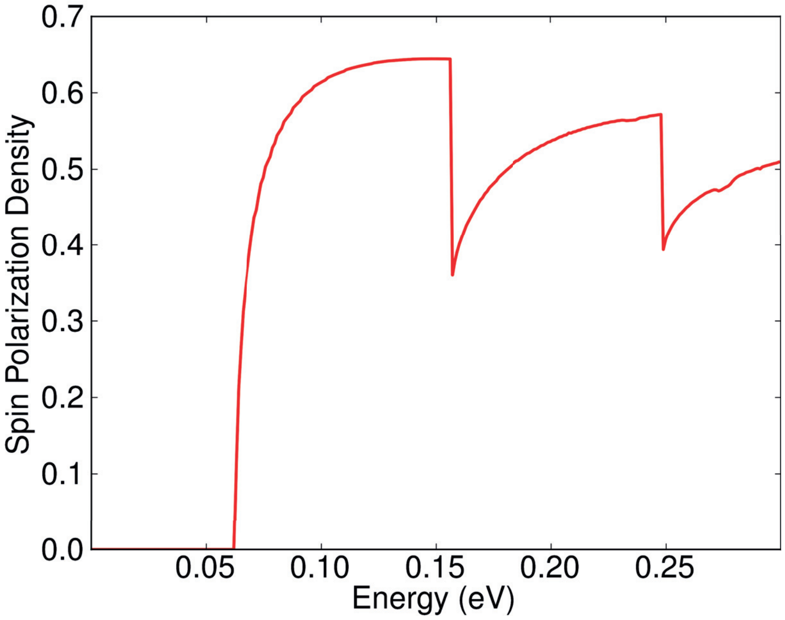

Figure 4.6 – Energy dependence of spin polarization density $H(E)$ (see text and Eqn.4.11).

4.2.3 Nanoribbons

As for NWs, band structures for the investigated range of NRs (23.8 nm $\leq P_{NR} \leq$ 59.2 nm) were computed using the same tight-binding method described in the Methodology. General trends observed for NWs are found for NRs too. Namely, the band structures of all investigated NRs exhibit a finite energy gap (E_{NR}), and that E_{NR} decreases with increasing P_{NR} (Fig.4.7), as one would expect from Eqn.4.5. Moreover, all the NR electronic spectra are characterised by a series of quantized degenerate 1D sub-bands as evident from the band structure (Fig.4.8) of the largest NR model ($P_{NR} \sim$ 59.2 nm).

However, the separate NR and NW morphologies result in distinct differences in, firstly, the perimeter P_{NR} dependence of the energy gap E_{NR} (Fig.4.7) for NRs relative to E_{NW} on P_{NW} for NWs (Fig.4.3). Secondly, in the general dispersion of their electronic spectra, as

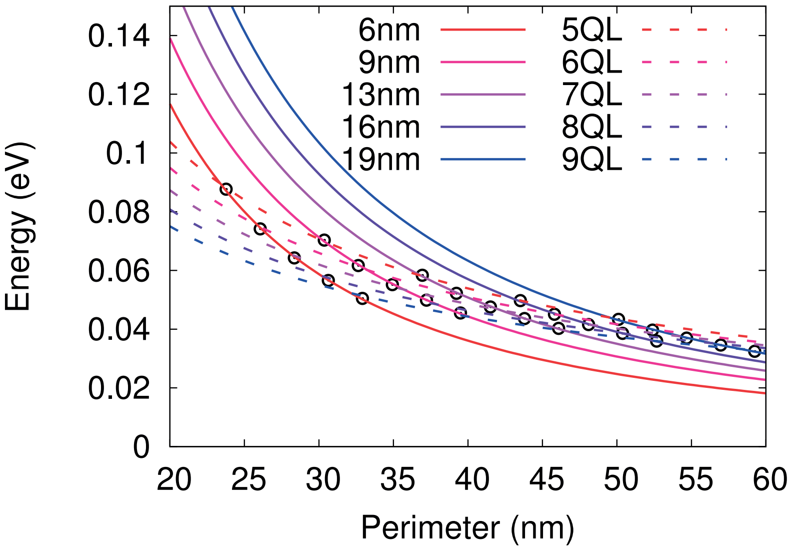

Figure 4.7 – Tight-binding results for NR surface state gap (E_{NR}) as a function of NR perimeter (E_{NR}). Numerical fits for $E_{NR}(P_{NR})$ for various NR widths in the range ~6 nm–19 nm (Red-Blue solid lines), and for various thicknesses in the range 5QL–9QL (Red-Blue dashed lines).

evident from a comparison of Fig.4.8 to Fig.4.4. The differences stem from the fact that the axial direction of NRs, which is parallel to the [11$\bar{2}$0] direction (a in Fig.4.1**c**), is normal to the QL stacking direction. Consequently, the NR morphology is defined by two structural degrees of freedom, one being the thickness, the other the width, as described in the Methodology of this chapter. Importantly, NRs are thus defined by two distinct sets of facets, the top and bottom (0001) facets parallel to the NR axis, and the other set the side facets aligned parallel to the (10$\bar{1}$0) surface.

Interestingly, the two structural degrees of freedom, represented by the two facet types, lead to two separate regimes for $E_{NR}(P_{NR})$ (Fig.4.7), one for each degree of freedom. Firstly, with respect to NR width (solid lines Fig.4.7), our calculations predict a relationship of $E_{NR} \sim P_{NR}^{-1.7}$, for all investigated widths, implying this dependence to be independent of NR width. This relationship is also similar to that found for NWs above (Fig.4.3). Conversely, with respect to thickness (dashed lines Fig.4.7), the sensitivity of E_{NR} to P_{NR} decreases as the thickness increases. This is reflected in an incremental reduction in the calculated power decay law describing $E_{NR}(P_{NR})$, from $E_{NR} \sim P_{NR}^{-0.95}$ for 5QL thick NRs (red dashed line Fig.4.7), to $E_{NR} \sim P_{NR}^{-0.75}$ for 9QL thick NRs (blue dashed line Fig.4.7).

The contrasting NW and NR morphologies are exemplified in the difference between the two respective band structures of the largest NW (Fig.4.4) and NR (Fig.4.8) systems investigated, particularly in the dispersion of the 1D sub-bands. Two primary factors contribute to the additional complexity of the NR dispersion. One being that NR morphologies exhibit two different facet types, and, secondly, the difference in periodicities between NR and NWs. With respect to the facet type, in the 2D limit, the top and bottom facets corresponds to the (0001)

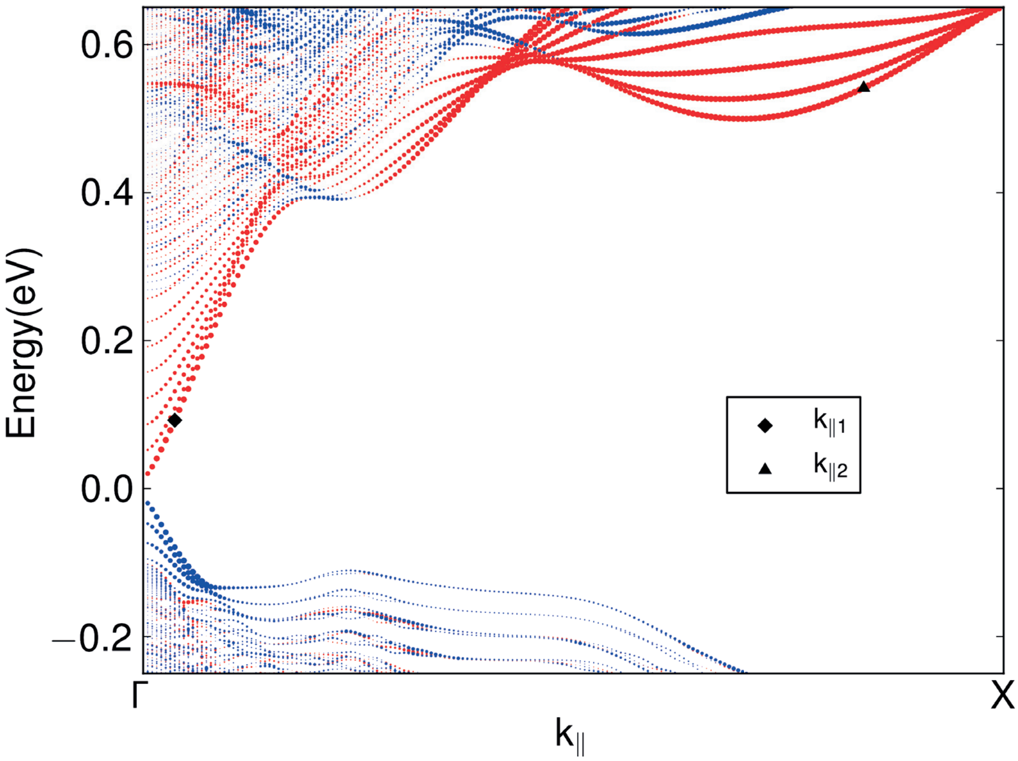

Figure 4.8 – Tight-binding band structure of a NR with a perimeter of 59.2 nm. Size of points reflects the magnitude of h^n (see text). Red and blue colours correspond to a left and right handed chirality of h^n, respectively. $k_{\|1}$ and $k_{\|2}$ define momenta for two pairs of $n = \pm\frac{1}{2}$ degenerate states close to the origin and Brillouin zone boundary, respectively.

surface, which is characterised by a symmetric Dirac cone centred around Γ, as was described in the Introductory chapter (Fig.1.6). The side facets are equivalent to that of the high-index surface, defined by the stoichiometric edge termination I and a stacking angle of $\theta = 57°$, discussed with respect to Fig.3.4**a** in the previous chapter. This surface is characterised by an anisotropic Dirac cone centred around Γ. Thus, in the 1D NRs there is a competition between two distinct facets which originate from surfaces with markedly different band dispersions, and hence corresponding properties of surface state charge carriers such as the Fermi velocity. Given that all facets of the NWs are identical, this is probably a decisive factor underpinning the observed dispersion in the more complex NR band structures.

As touched upon in the Methodology of this chapter, the NW axis is parallel to the *c* direction of the bulk hexagonal unit cell, and thus the NW models have a periodicity equivalent to the corresponding c (∼ 28.65 Å) lattice parameter. Conversely, the NR axis is parallel to the a direction, and hence NRs have a far smaller periodicity, equal to the a (∼ 4.11 Å) lattice parameter. Consequently, the 1D Brillouin zone for NRs is significantly larger, for example the maximum value of $k_{\|}$ for the NR in Fig.4.8 is 0.76 Å^{-1}. On the other hand, that for NWs is significantly smaller, for example the maximum value of $k_{\parallel}$ in for the NW in Fig.4.4 is 0.11 Å^{-1}. It is also worth mentioning the perimeter of the NR in Fig.4.8 (P_{NR} = 59.2 nm) is significantly larger than that of the NW in Fig.4.4 (P_{NW} = 30.4 nm). Thus, the simple general model above would predict that the inter-level spacing between the quantized 1D NR sub-bands, as reflected in a smaller $k_{\perp}$ (Eqn.4.2) value of a given sub-band, to be significantly less than that for NWs. This may explain the increased density of NR sub-bands (Fig.4.8) in a given energy range relative to the NW case (Fig.4.4).

The contrasting surface origins of both sets of NR facets is also reflected in more complex spin properties than was found for NWs. To analyse the spin behaviour in NRs, we again define two pairs of $n = \pm\frac{1}{2}$ degenerate states, one pair at momentum $k_{\parallel 1}$ and the other at $k_{\parallel 2}$ (Fig.4.8), close to the origin and Brillouin zone boundary, respectively. We also compute the local spin density for a given state $\boldsymbol{S}_i^n$ (Eqn.4.8). This is comprised of two components, $S_{\parallel}^n$ aligned parallel to the NR axis (i.e. a direction in Fig.4.1**c**), and $S_{\perp}^n$ aligned in the orthogonal direction in the tangent plane to the NR axis (i.e. cb plane in Fig.4.1**c**).

For each pair of $n = \pm\frac{1}{2}$ degenerate states, one pair at $k_{\parallel 1}$ and the other at $k_{\parallel 2}$, we also calculate the sum of the local spin densities $\boldsymbol{S}_i^{tot}$ (Eqn.4.9). As expected from the general model described above, the spin non-degeneracy for a given pair of $n = +\frac{1}{2}$ and $n = -\frac{1}{2}$ states, is only exhibited in opposing alignments of the $S_{\parallel}^{+\frac{1}{2}}$ and $S_{\parallel}^{-\frac{1}{2}}$ components, respectively. Conversely, the $S_{\perp}^{+\frac{1}{2}}$ and $S_{\perp}^{-\frac{1}{2}}$ components are aligned in the same direction. The pertaining reasons are exactly analogous to that described for NWs and in the general model above, and originate from spin-momentum locking of the 2D surface Dirac cone. Each pair of $n = \pm\frac{1}{2}$ states, at $k_{\parallel 1}$ and $k_{\parallel 2}$, belong to the lowest energy $n = \pm\frac{1}{2}$ sub-bands. Consequently, at $k_{\parallel 1}$ the major component to $\boldsymbol{S}_i^n$ is $S_{\parallel}^n$, whilst $S_{\perp}^n$ is negligible. On the other hand, at $k_{\parallel 2}$ the major component to $\boldsymbol{S}_i^n$ is $S_{\perp}^n$, whilst $S_{\parallel}^n$ is negligible. This is based on the same reasoning as for NWs. Namely, that the $n = \pm\frac{1}{2}$ sub-bands are the lowest in energy and have the lowest quantized values of $k_{\perp}$ (Eqn.4.2), and therefore they are the cuts closest to the centre of the 2D surface Dirac cone and associated constant energy contours (see general model for a detailed discussion). The calculation of $\boldsymbol{S}_n^{tot}$, at $k_{\parallel 1}$ and $k_{\parallel 2}$, subsequently leads to the spin textures shown in Fig.4.9.

The general features of the $k_{\parallel}$ dependency of $\boldsymbol{S}_i^{tot}$ for NRs, as evident from the spin textures at $k_{\parallel 1}$ (Fig.4.9**a**) and $k_{\parallel 2}$ (Fig.4.9**b**), resembles that for NWs. Similarly, this is a consequence of the spin-momentum locking properties of the 2D surface Dirac cone exhibited in the 1D sub-bands of the NR. At $k_{\parallel 1}$, the cancellation of the major $S_{\parallel}^{+\frac{1}{2}}$ and $S_{\parallel}^{-\frac{1}{2}}$ components means that $\boldsymbol{S}_i^{tot}$ has a small magnitude, comprised of the negligible $S_{\perp}^{+\frac{1}{2}}$ and $S_{\perp}^{-\frac{1}{2}}$ components. Conversely, at $k_{\parallel 2}$, the magnitude of $\boldsymbol{S}_i^{tot}$ is significantly larger, due to the summing of the major $S_{\perp}^{+\frac{1}{2}}$ and $S_{\perp}^{-\frac{1}{2}}$ components, whilst the negligible $S_{\parallel}^{+\frac{1}{2}}$ and $S_{\parallel}^{-\frac{1}{2}}$ components cancel. Thus, as for NWs, $\boldsymbol{S}_i^{tot}$ is aligned entirely in the tangent plane to the NR axis at $k_{\parallel 1}$ (Fig.4.9**a**) and $k_{\parallel 2}$ (Fig.4.9**b**).

In the case of NWs, $\boldsymbol{S}_i^{tot}$ was uniformly localised around the hexagonal perimeter of the

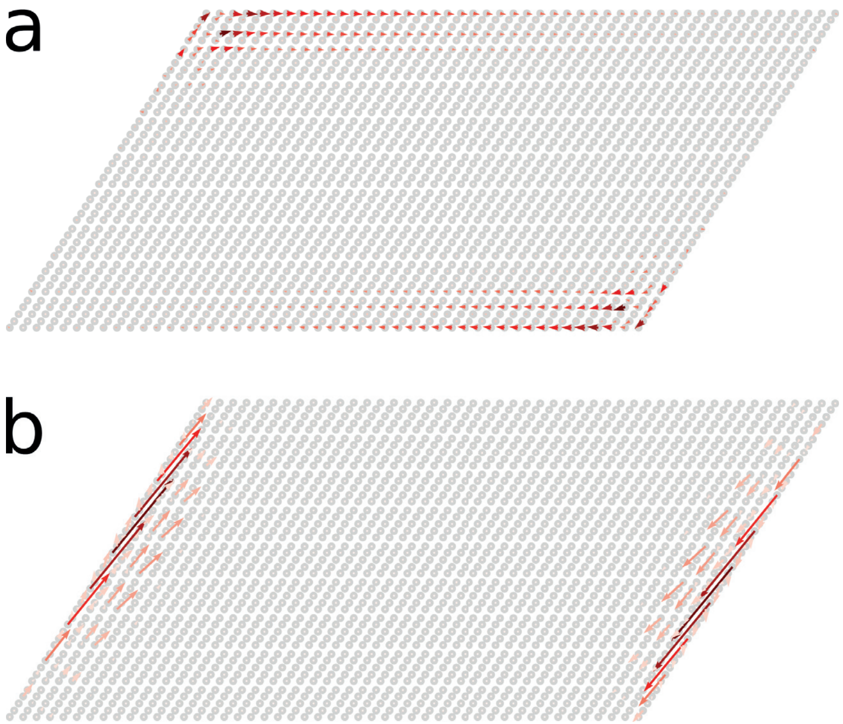

Figure 4.9 – Spin textures for a 19 nm wide and 9QL thick Bi_2Se_3 NR (i.e. P_{NR} = 59.2 nm) at $k_{\parallel 1}$ (**a**) and $k_{\parallel 2}$ (**b**) (see Fig.4.8 and text). Red arrows denote total local spin density $\boldsymbol{S}_i^{tot}$ (Eqn.4.9), grey circles indicate the position of Bi and Se atoms. The view direction is equivalent to that shown in Fig.4.1**c**.

NW at both $k_{\parallel 1}$ and $k_{\parallel 2}$ (Fig.4.5). Furthermore, at $k_{\parallel 2}$ this lead to a 2π rotation of $\boldsymbol{S}_i^{tot}$ around the NW perimeter (Fig.4.5**b**). However, the detailed spin texture behaviour for NRs is more complicated. Firstly, such a 2π rotation of $\boldsymbol{S}_i^{tot}$ around the NR perimeter is noticeably absent. Moreover, at $k_{\parallel 1}$ (i.e. close to $k_\parallel = 0$), we find that $\boldsymbol{S}_i^{tot}$ is confined to the top and bottom facets of the NR only, with an opposite alignment along each facet (Fig.4.9**a**). On the other hand, at $k_{\parallel 2}$ (i.e. close to the Brillouin zone boundary), $\boldsymbol{S}_i^{tot}$ is confined to the side facets of the NR, with an opposing alignment parallel to each respective side facet (Fig.4.9**b**). The fact that the spin localises on each distinctive NR facet, at $k_{\parallel 1}$ and $k_{\parallel 2}$, respectively, is suggestive that the underlying cause of the observed spin texture behaviour originates from the different surface origins of each set of facets. Where those respective surfaces have distinct electronic spectra, characterised by differing 2D surface Dirac cones and related properties, as described above.

This additional complexity in how the helicity of the surface Dirac cone is exhibited in the real space properties of the lowest energy $n = \pm\frac{1}{2}$ sub-bands is also apparent across the electronic spectrum of the NR. This can again be analysed by calculating h^n (Eqn.4.10), as was done previously for NWs, and observing the variation of $h^n(k_\parallel)$ (Fig.4.8). General trends are similar to that for NWs, namely that the lowest energy modes have the largest magnitude of h^n. Furthermore, for given value of $k_\parallel$, as E increases h^n decreases. Nonetheless, the evolution of h^n, with respect to E, and the $k_\parallel$ dependency, is not as clear-cut as for NWs. We believe that the more complex behaviour of $h^n(k_\parallel)$ (Fig.4.8) is again rooted in the presence of the two separate NR facet types and their differing surface origin.

4.3 Conclusions

In summary, a tight-binding formalism was applied to study finite-size effects, and the confinement of spin helical Dirac fermions, in 1D Bi_2Se_3 nanostructures of a nanowire and nanoribbon morphology. We find the electronic structure to be extremely sensitive to morphology. For NWs, this sensitivity is exhibited in the dependence of the band gap on NW dimensions deviating from the analytic prediction. Similarly for NRs, the presence of two distinct facet types gives rise to two regimes for the band gap dependence, with each related to a respective facet. Our calculations show the spin helicity of the 2D surface Dirac cone to be clearly manifested in the quantized NW sub-bands. Interestingly, we predict that the confinement of the topological surface states in a 1D NW results in a tunable spin polarization density, which could potentially be exploited in spin-based transport applications. In the case of NRs, the separate surface origins of each NR facet, with Dirac cones of differing dispersions, results in a more complex correspondence between the spin helicity of the 2D topological surface states and the spin properties of the 1D NR sub-bands.

5 One-dimensional Nanostructures of Topological Crystalline Insulators

Topological crystalline insulators (TCIs) represent a novel topological phase [21], where the non-trivial topology is governed by the underlying crystalline symmetry. This is in contrast to the Z_2 topological insulators (TIs) where the key ingredients are that of time-reversal symmetry combined with strong spin-orbit interactions (SOI). The TCI SnTe, introduced in the Introductory chapter, has a non-trivial topology that stems from the mirror symmetry of the rock-salt crystal structure (Fig.1.7) [24, 45].

An intriguing consequence of the topological protection in SnTe is that it is highly sensitive to parameters that control the mirror symmetry, such as the crystal structure or the application of external fields. This sensitivity is exemplified by the electronic structure of the mirror symmetry preserving $\{100\}$, $\{110\}$ and $\{111\}$ crystal surfaces all displaying different sets of topological surface states (SSs) [52, 54, 171, 172]. In the Introduction we discussed how the (001) surface possesses four Dirac cones, with two each lying at the $\bar{\Lambda}$ points on the two mirror symmetric $\bar{X}_{1,2} - \bar{\Gamma} - \bar{X}_{1,2}$ lines in the surface Brillouin zone (see Fig.1.7 and Fig.1.8 and related text). Recent work on this surface and associated thin films has emphasized the rich interplay between crystal symmetry and non-trivial topology in TCIs. For example, a gap opening at just two Dirac cones lying on one of the $\bar{X}_{1,2} - \bar{\Gamma} - \bar{X}_{1,2}$ lines was experimentally observed [53, 173], as a result of structural distortion breaking the crystal symmetry along one of the two mirror planes [174]. Another theoretical work predicted that (001) thin films with an odd number of layers realize an electrically tunable 2D TCI phase with spin-filtered edge states [97]. Both examples showcase the great potential in applying symmetry breaking perturbations to tune the TCI phase. On a more fundamental level, and of most relevance to work described in this chapter, was the discovery that (001) thin films composed of an even and odd number of layers are defined by separate topological invariants, based of their differing symmetry [96]. Intriguingly, this gives rise to distinct regimes of topological phase transitions.

Following these observations, and given the sensitivity of the TCI phase to crystal symmetry, it is of great interest to study its manifestation in lower dimensional nanostructures. Nanostructuring offers several advantages in relation to the enhancement of surface contributions and the ability to synthesize morphologies of clearly defined surfaces, as was discussed in the Introduction. However, the impact of crystal symmetry and finite-size effects upon the electronic structure of nanostructures is largely unexplored. Consequently, this forms the overarching theme of this chapter. Importantly, we seek to establish a direct correspondence between the crystal symmetry dependent topologically non-trivial phases of the 2D TCI (001) thin films [96] in corresponding nanostructures. We focus on studying one particular morphology, the $\{100\}$ nanowire [101, 102], described in the Introduction in reference to Fig.1.12, due to its simple morphology, as only one particular type of surface (i.e. the $\{100\}$ surfaces) is exposed.

Thus, in this chapter we initially review how (001) thin films of an odd or even layer thickness have distinct topological properties stemming from their differing crystal symmetries, which is discernible in the thickness dependency of the surface-state hybridized gap. Specifically, as the majority of these results were originally arrived at in [96], we reproduce them here such that we can relate the topological properties of 2D thin films with phenomena we explore for 1D NWs. Thus, we relate the aforementioned symmetry dependency to the surface-state hybridized gaps for corresponding cases in $\{100\}$ square cross-section NWs. Subsequently, we show that the topologically non-trivial phases of odd and even numbers of layers in 2D TCI (001) thin films are manifested in the surface states of 1D NWs. Intriguingly, we find that surface states of 1D NWs composed of an odd number of layers are robust, due to the symmetry dependent topology of the parent 2D TCI phase, and in stark contrast to the less robust NW surface states for an even number of layers

5.1 Methodology

The electronic structure of SnTe (001) thin films and $\{100\}$ NWs was investigated via the tight-binding (TB) approximation. The specific formalism of the TB method was described in the Methodology chapter, where Table.2.4 lists the SnTe TB parameters. Again the use of the TB method was somewhat imposed by the size of the systems being studied. This holds particularly true for NWs, as supercells are required, where the number of atoms makes first principles methods such as DFT, impractical or currently not feasible, depending on the system size. Confidence in the TB method is provided by the sufficiently accurate reproduction of the essential features of the DFT derived band structure, as was discussed in reference to Fig.2.6 in the Methodology chapter. One potential issue, as touched upon in the last chapter, with the utilised TB formalism is that surface and edge potential effects are not accounted for. However, given the rock-salt crystal symmetry of SnTe and the fact that all investigated surfaces are stoichiometric, we believe that surface and edge reconstruction effects would not have a significant impact on any conclusions drawn from the results described below.

Calculations were performed on SnTe (001) thin films modelled as two-dimensional slabs. The thickness of the slab is defined by the number of atomic monolayers (MLs) n stacked parallel to the [001] direction (Fig.5.1**a**), whilst periodic boundary conditions are imposed along the two orthogonal [010] and [100] directions, parallel to the slab surfaces (Fig.5.1**a**). An example of a thin film with $n = 5$, i.e. composed of an odd number of MLs, is shown in Fig.5.1**a**. SnTe (001) odd and even thin films have separate symmetries. The defining crystal symmetry for odd thin films is the (001) mirror symmetry, as they are symmetric under the reflection $z \rightarrow -z$ about the two-dimensional (xy) plane parallel to the middle atomic layer. For example, for the $n = 5$ odd thin film in Fig.5.1**a** this corresponds to the third atomic ML.Conversely, for an even numbers of layers, (001) mirror symmetry is absent and the defining symmetry is glide symmetry, which is reflection about a mirror plane followed by a translation parallel to that plane. Specifically, even thin films are symmetric under the reflection $z \rightarrow -z$ about a (xy) plane (Fig.5.1**a**) exactly in the middle of the slab between two MLs, followed by a translation of half a lattice vector parallel to that plane. The translation of half a lattice vector is crucial as it distinguishes even thin films as belonging to a non-symmorphic space group, since it involves a point group operation such as a reflection combined with a fractional lattice translation. Odd thin films conversely belong to a symmorphic space group, as there exists at least one point left invariant by all of the symmetries.

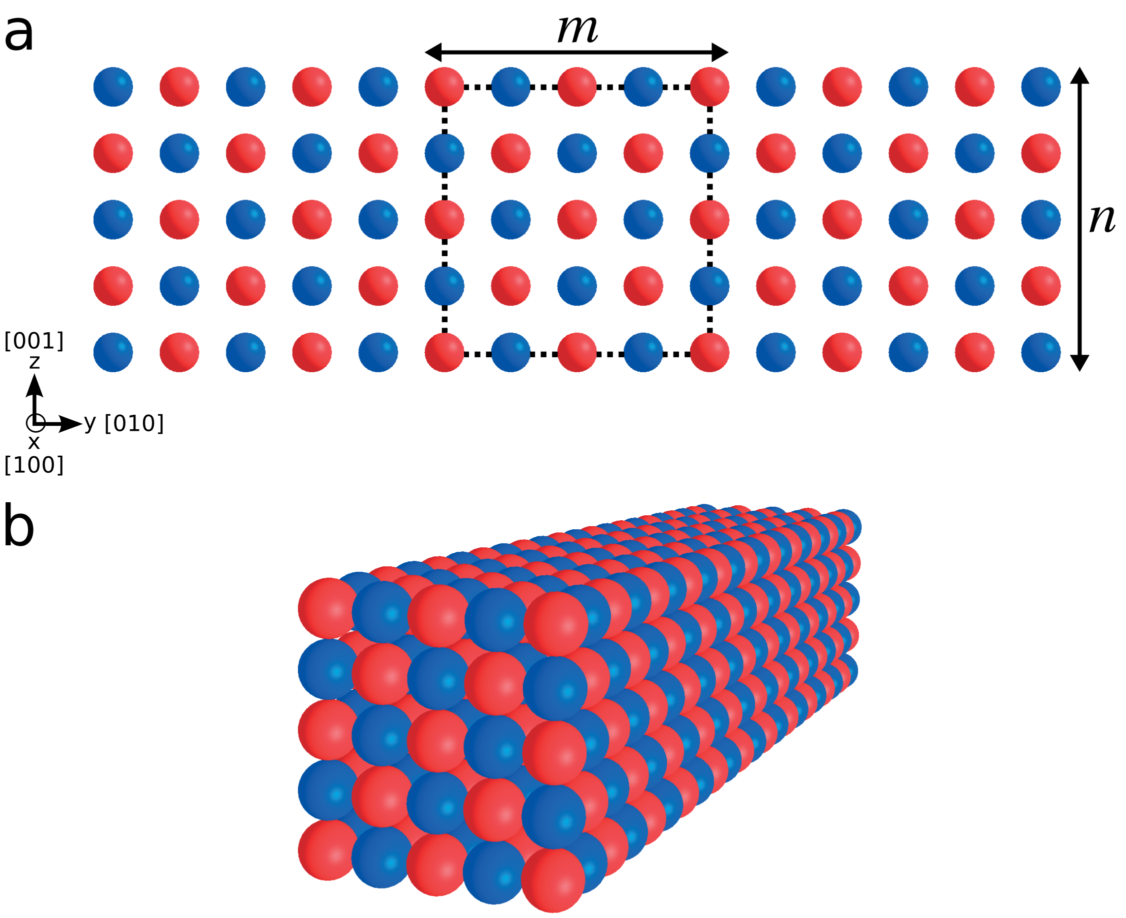

Figure 5.1 – Atomic models of a SnTe (001) thin film and $\{100\}$ NW. **a** SnTe (001) slab of thickness $n = 5$. Periodicity directions of the slab are along the [100] and [010] directions. m defines the width of a $n \times m$ NW. For example, the black dotted square in **a** outlines the cross-section of the 5×5 NW shown in the perspective view in **b**. The axial direction of the NW in **b** is equivalent to the [100] direction in **a**. In both figures red spheres represent Sn atoms, whilst blue Te atoms.

One dimensional SnTe {100} NWs were constructed by additionally constricting a slab along the [010] direction (Fig.5.1**a**), where the width of a NW is given by the number of atomic MLs m stacked parallel to [010]. Subsequently, periodic boundary conditions are imposed solely along the [100] direction. The structural correspondence between the investigated slab and NW models is shown in Fig.5.1**a**. If we define the dimensions of a given NW as the thickness × width (i.e. $n \times m$), two classes of NWs were studied. The first being square cross-section NWs where $n = m$, and both the thickness and the width were comprised of equivalent numbers of either odd or even MLs. Consequently, as $n = m$ for the discussion below we refer to square cross-section NWs as $n \times n$ NWs. For example, Fig.5.1**b** shows a 5×5 odd square cross-section NW. The second being rectangular cross-section NWs where $n \neq m$, and the thickness and width were composed of differing numbers of odd or even MLs. Rectangular cross-section NWs included odd-odd (n and m odd but $n \neq m$), odd-even (n odd and m even), even-odd (n even and m odd) and even-even (n and m even but $n \neq m$). For odd square cross-section NWs, and odd-odd rectangular NWs, the defining symmetry is again (001) mirror symmetry, as they are symmetric under the reflection $z \rightarrow -z$ about the plane parallel to the middle atomic ML, which can be seen in Fig.5.1**b**. Conversely, for all the other NW types, including even square cross-section, even-even, odd-even and even-odd rectangular NWs, the defining symmetry is a glide symmetry, i.e. a non-symmorphic operation, whereby the NWs are symmetric under the reflection $z \rightarrow -z$ about a plane in between two MLs, which splits the NW into two equal halves, followed by a translation of half a lattice vector parallel to that plane.

5.2 Results

5.2.1 Two-dimensional Thin Films

We begin by discussing the finite-size induced band gap in (001) thin films, followed by square cross-section NWs. We relate the observed behaviour in thin films to the two distinct 2D TCI phases present, and subsequently explore how these phases are manifested in the electronic structure of 1D NWs.

Tight-binding band structure calculations were performed on (001) thin films modelled as slabs, where the slab thickness n varied between $3 \leq n \leq 30$. The finite thickness of the slabs results in hybridization between surface states localized at opposite surfaces. As the decay length of the surface states into the bulk is on the same order of magnitude as the slab thickness, this leads to a spatial overlap of the wavefunctions of each surface, and consequently a gap opening. The thickness dependence of the induced energy gap is shown in Fig.5.2, clearly evident are two separate regimes depending on whether n is odd or even.

In the odd case, for thin films where $n \leq 11$ the fundamental band gap is located at $\bar{\mathrm{X}}$ in the surface Brillouin zone (Fig.1.7), as can be observed in the band structure of a thin film with $n = 5$ in Fig.5.3**a**. However, as the thickness increases the fundamental gap shifts away from

$\bar{\mathrm{X}}$, with the transition occurring at $n \sim 11$, and is located towards the $\bar{\Lambda}$ point on the mirror symmetric $\bar{\Gamma}-\bar{\mathrm{X}}-\bar{\Gamma}$ line in the surface Brillouin zone (Fig.1.7). As discussed in the Introduction chapter, in the 3D limit $\bar{\Lambda}$ is the momentum at which the Dirac point is located (Fig.1.7), since the crossing of the topologically protected TCI surface states results in a zero energy gap. A comparison of the band structure of a $n = 19$ (Fig.5.3**b**) film with that of $n = 5$ (Fig.5.3**a**) clearly shows the transition from $\bar{\mathrm{X}}$ to $\bar{\Lambda}$. Consequently, in Fig.5.2, for odd thin films where $n \leq 11$, the plotted band gap is that at $\bar{\mathrm{X}}$, whilst for $n \geq 11$ it is that at $\bar{\Lambda}$. In the even case, aside from very thin films where there is a slight indirect gap, the fundamental gap is located at $\bar{\Lambda}$, for example as in the band structures shown in Fig.5.5. Thus, for all even n the plotted band gap is that at $\bar{\Lambda}$.

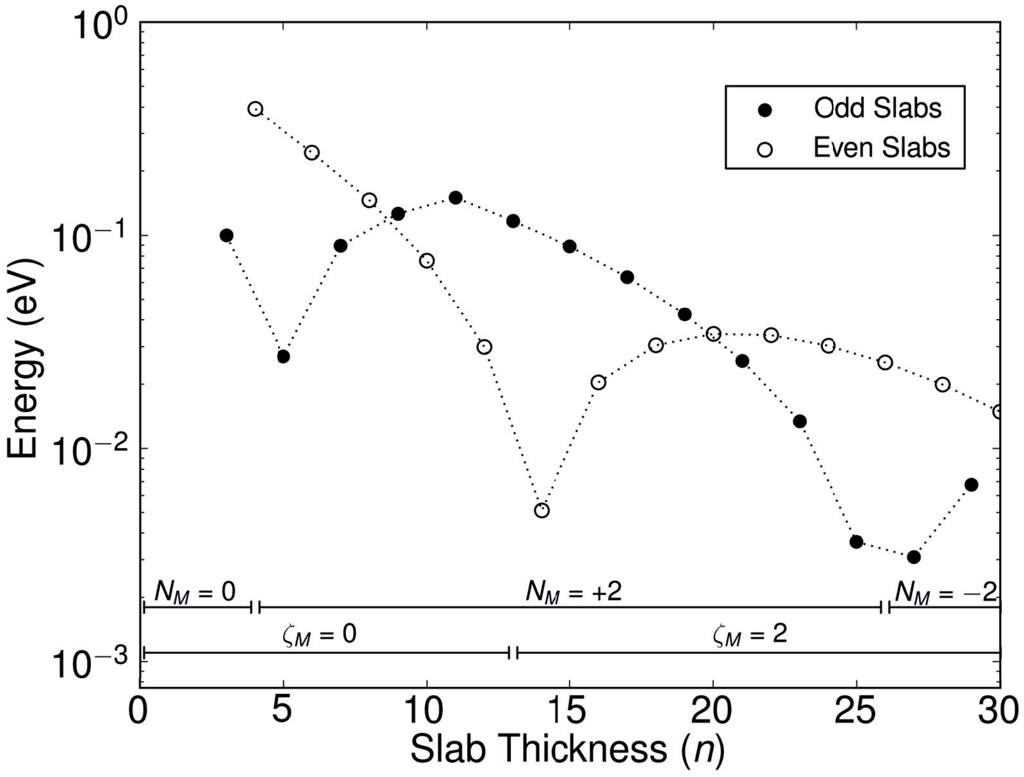

Figure 5.2 – Oscillations in the band gap of SnTe (001) slabs of odd and even thickness n. Filled (empty) circles display how the band gap varies as a function of thickness for odd (even) values of n. Oscillations in band gap are related to distinct topological phase transitions, as denoted by changes in the $N_M(\zeta_M)$ topological invariant for odd (even) thin films. It should be noted that this plot reproduces the results originally published in [96], as discussed previously.

The energy gap in Fig.5.2 for both odd and even cases is characterized by an oscillatory dependency on film thickness. Similar behaviour has been observed in Bi_2Se_3 thin films [154, 175, 176], where the oscillations are indicative of fluctuations from a topologically non-trivial quantum spin Hall phase to a trivial phase. Similarly, in the case of SnTe (001) thin films, the observed oscillations for odd and even cases stem from distinct topological phase transitions. The difference in behaviour between odd and even thin films arises from the fact that each has a topology defined by separate topological invariants, due to their respective crystal symmetries

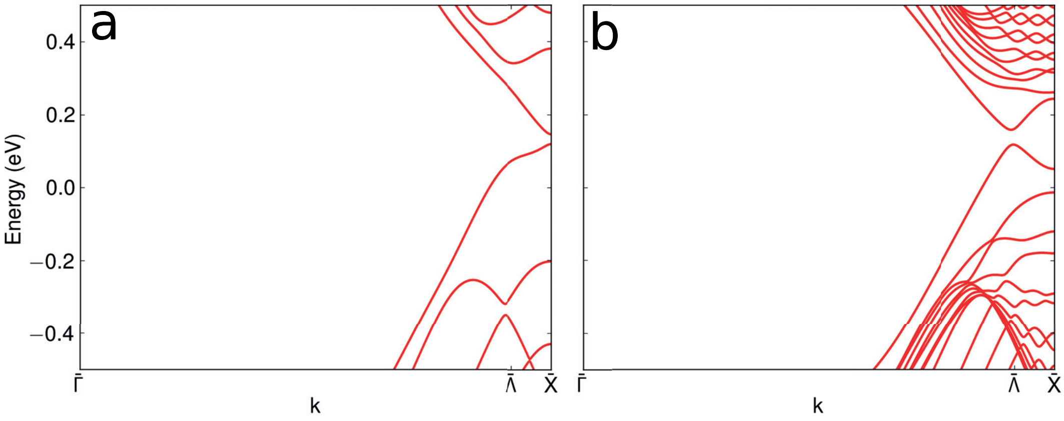

Figure 5.3 – Band structures for (**a**) $n = 5$ and (**b**) $n = 19$ slab showing the change of the fundamental band gap from $\bar{\mathrm{X}}$ to $\bar{\Lambda}$, respectively.

Odd thin films

For odd thin films, the defining symmetry is (001) mirror symmetry, as described in the Methodology. Consequently, as detailed in the Introduction, this allows the definition of the mirror Chern number (Eqn.1.18) [22], N_M, which serves as a topological invariant to define the non-trivial topology present in odd thin films.

A non-zero integer value of the mirror Chern number denotes a TCI with mirror symmetry [24]. Interestingly, SnTe (001) odd thin films have been found to have a non-trivial value of $|N_M| = 2$ [96, 97, 177], thus realizing a 2D TCI phase, for a wide range of n (Fig.5.2).

The oscillations in the calculated energy gaps in the odd case (Fig.5.2) coincide with clear variations in N_M, i.e. with distinct topological phase transitions. The first phase transition occurs close to when the computed band gap takes a minimal value at $n = 5$. This is a consequence of a band inversion at $\bar{\mathrm{X}}$ between $3 \leq n \leq 5$. For $n = 3$ the conduction (valence) band at $\bar{\mathrm{X}}$ is primarily comprised of states derived from Sn (Te) p orbitals (Fig.5.4**a**), whereas for $n = 5$ this ordering is inverted (Fig.5.4**b**), indicating a topologically non-trivial phase. Furthermore, as this implies the band gap at $\bar{\mathrm{X}}$ closing and then reopening between $3 \leq n \leq 5$, at $n = 5$ it has a minimal value. Confirmation of the topological phase transition is given by the mirror Chern number, where $N_M = 0$ for $n = 3$, and $N_M = +2$ for $n = 5$ [96, 97].

The second topological phase transition occurs in the vicinity of the second energy minimum at $n = 27$. The transition in this case is accompanied by the band gap closing

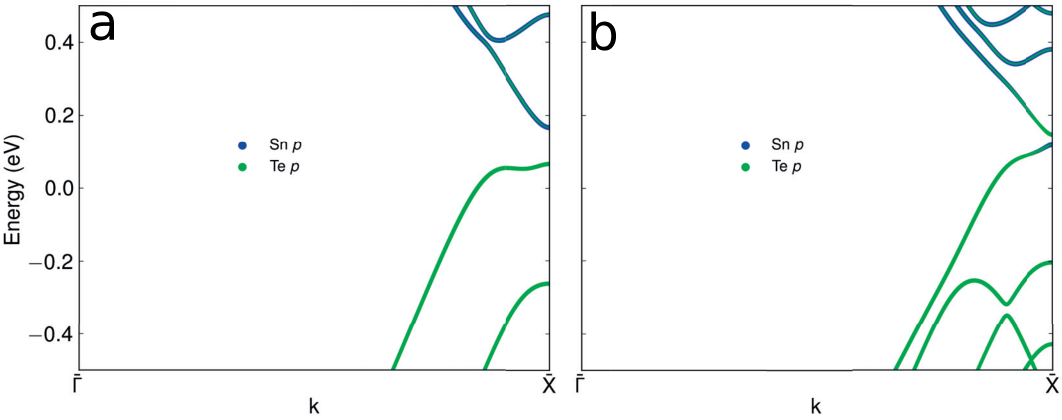

Figure 5.4 – Band inversion in SnTe (001) slabs. Band structures for (**a**) $n = 3$ and (**b**) $n = 5$ slabs, where magnitude of blue (green) circles represents Sn(Te) p orbital contribution to the weight of the electronic wavefunction. Orbital contribution for conduction and valence bands for $n = 5$ (**b**) thin film inverted with respect to $n = 3$ at $\bar{\mathrm{X}}$.

at the two $\bar{\Lambda}$ points, between $25 \le n \le 27$, on the mirror symmetric $\bar{\Gamma} - \bar{\mathrm{X}}_{1,2}$ lines in the surface Brillouin zone (Fig.1.7). This is reflected in a sign change in N_M, where $N_M = +2$ for $n = 25$, and $N_M = -2$ for $n = 27$ [96]. (001) SnTe thin films are predicted to possess spin filtered edge states [97], where edge states propagating in opposing directions having opposing $\pm i$ mirror eigenvalues. Given that the sign of the Chern invariants $\upsilon_{+i}(\upsilon_{-i})$ (Eqn.1.18) dictates the direction of propagation of edge states [22], this implies that a given edge state propagating in a given direction direction for $n = 25$ ($N_M = +2$) should have an opposing $\pm i$ mirror eigenvalue to that for $n = 27$ ($N_M = -2$), due to the difference in their mirror Chern invariants. Moreover, since the electron spin polarization in the z direction is proportional to the mirror eigenvalue [97], the sign difference in the respective mirror Chern numbers for $n = 25$ ($N_M = +2$) and $n = 27$ ($N_M = -2$) should be manifested in the spin polarization of their respective edge states.

Even thin films

The topological properties of even thin films are distinguished from that of odd due to crucial differences in their symmetry (see Methodology of this chapter). Firstly, in contrast to odd thin films, in even thin films (001) mirror symmetry is absent. Thus, as the definition of the mirror Chern number requires the presence of mirror symmetry [22, 24], it is therefore no longer a valid topological invariant. Moreover, as glide symmetry is the defining symmetry operation for even thin films, this necessitates the definition of a topological invariant protected by translational symmetry, alongside that of reflection and time reversal. As such, a glide-winding number, ζ_m, can be defined [96] as a topological invariant in 2D

$$\zeta_m = \frac{(\zeta_+ - \zeta_-)}{2}, \tag{5.1}$$

where $\zeta_\pm$ is the winding number of the Wannier centre

$$\zeta_\pm = \frac{1}{2\pi}\int_0^{2\pi}\left(\frac{\partial\theta_\pm(k_y)}{\partial k_y} - \frac{\theta_\pm(2\pi)-\theta_\pm(0)}{2\pi}\right)dk_y \in \mathbb{Z}, \tag{5.2}$$

and where the Wannier centre $\theta_\pm$ itself can be derived from the Wilson loop [178, 179].

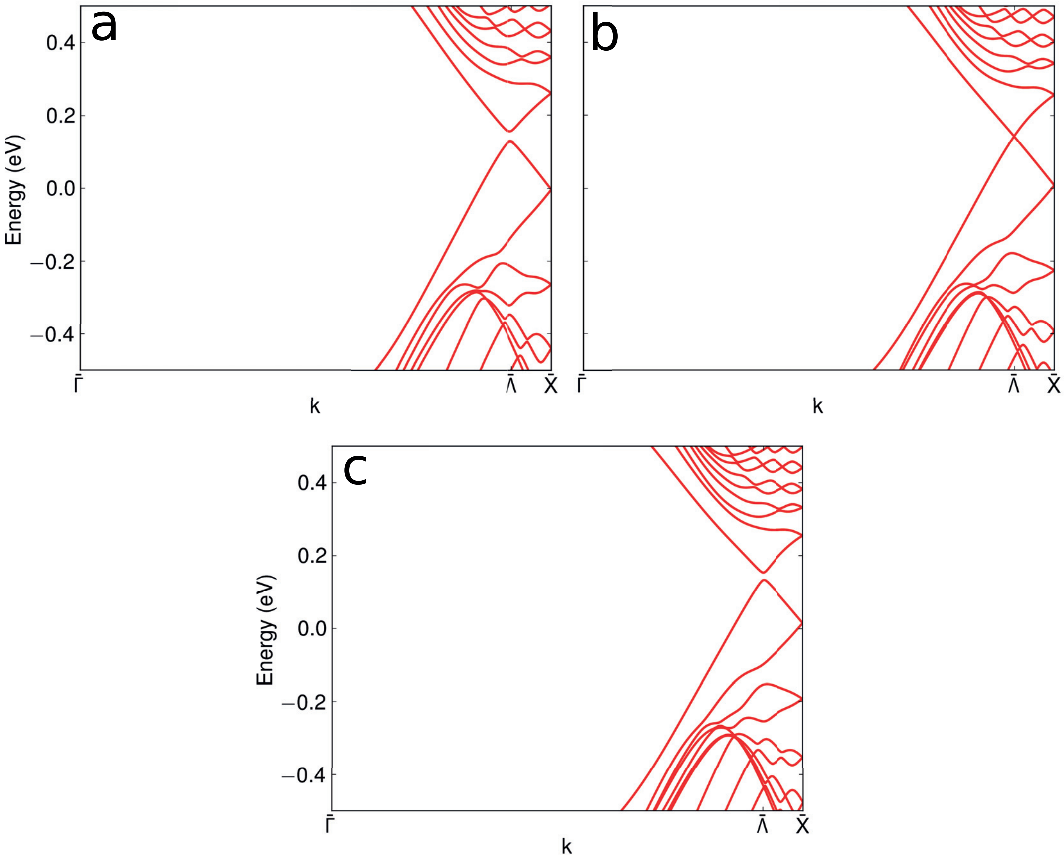

Figure 5.5 – Topological phase transition manifested in band structures of SnTe (001) even thin films. Band structures for (**a**) $n = 12$, (**b**) $n = 14$ and (**c**) $n = 16$ even thin films. Band gap at $\bar{\Lambda}$ vanishes between $12 \le n \le 14$, and reappears for $n \ge 14$.

The oscillatory thickness dependence of the band gap for even thin films is marked by one clear topological phase transition (Fig.5.2), compared to two observed in the odd case. The phase transition from topologically trivial $\zeta_M = 0$ to non-trivial $\zeta_M = 2$ coincides with the computed band gap having a minimal value at $n = 14$ (Fig.5.2). The phase transition is clearly demonstrated in the electronic structure of even thin films, where the band gap closes at the $\bar{\Lambda}$ points between $12 \le n \le 14$, as evident from the corresponding band structures for $n = 12$ (Fig.5.5**a**) and $n = 14$ (Fig.5.5**b**), and subsequently reopens for $n \ge 14$ (Fig.5.5**c**). This is similar to the second phase transition for odd thin films (i.e. from $N_M = +2$ to $N_M = -2$ at $25 \le n \le 27$). It should be noted that our computed values for the band gaps are in accordance with that of a similar study investigating finite-size effects in SnTe (001) thin films [96].

5.2.2 Square Cross-Section Nanowires

We now analyse the dimensionality dependence of the band gap of SnTe square cross-section $\{100\}$ NWs. Square cross-section $n \times n$ NWs have four equivalent $\{100\}$ surfaces due to the identical thickness and width along the [001] and [010] directions (Fig.5.1), respectively. For small enough dimensions of $n \times n$, confinement along both the [001] and [010] directions results in a finite-size induced energy gap. The dependence of the fundamental band gap on $n \times n$ NW dimensions is shown in Fig.5.6. Differing behaviour is again evident, depending on whether n is odd or even, as was the case for thin films above. However, unlike the case for thin films, as the dimensions $n \times n$ of the NW increase the band gap vanishes, and remains closed, as discussed for even and odd cases below.

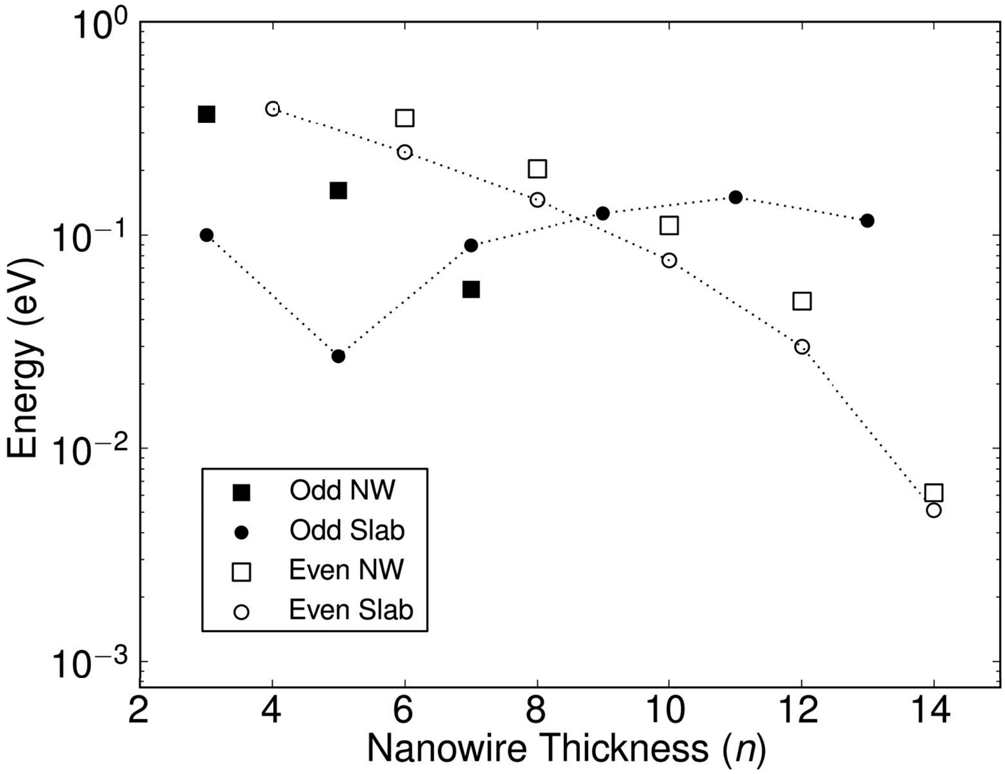

Figure 5.6 – Dependence of the SnTe $n \times n$ square cross-section NW band gap on dimensions. Filled (empty) squares show how the band gap varies as a function NW dimensions for odd (even) NWs. Filled (empty) circles show how the band gap varies as a function of slab thickness for odd (even) n.

The separate regimes are similarly due to the respective symmetries of the odd and even NWs, with odd NWs defined by (001) mirror symmetry, whilst even NWs by a glide symmetry (see Methodology of this chapter). It is well established that nonsymmorphic operations, such as glide symmetry, can have a marked effect on electronic structure, due to the phenomenon of bands "sticking together" and resulting in additional degeneracies [180]. Consequently, the presence of glide symmetry, alongside that of time reversal and inversion, leads to a fourfold degeneracy at the Brillouin zone boundary for even NWs. This degeneracy is clearly visible at $\bar{\mathrm{X}}$ in the band structures of the 8 × 8 and 16 × 16 NWs displayed in Fig.5.7**c** and Fig.5.7**d**, respectively. Conversely, as odd NWs are defined solely by reflection symmetry, i.e a point group operation, this fourfold degeneracy is absent at $\bar{\mathrm{X}}$, evident in the band structures of the 7 × 7 and 15 × 5 NWs displayed in Fig.5.7**a** and Fig.5.7**b**, respectively. These symmetry effects can subsequently explain the differing behaviour of odd and even NWs in Fig.5.6.

For odd NWs the absence of a fourfold degeneracy at $\bar{\mathrm{X}}$, means the valence band maximum (VBM) and the conduction band minimum (CBM) are both significantly higher and lower in energy (Fig.5.7**a**), respectively, than the same bands at $\bar{\mathrm{X}}$ for even NWs of similar dimensions (Fig.5.7**c**). Furthermore, the presence of a fourfold degeneracy at $\bar{\mathrm{X}}$ for even NWs means that the VBM and CBM are pinned to the next lowest and highest bands in energy, respectively. This results in a fundamental band gap located at $\bar{\mathrm{X}}$ for odd NWs (Fig.5.7**a**), and shifted slightly off $\bar{\mathrm{X}}$ for even NWs (Fig.5.7**c**). Moreover, this entails that the computed energy gaps for odd NWs decay significantly faster with increasing $n \times n$ dimensions relative to even NWs, as Fig.5.6 shows. For odd NWs the fundamental band gap vanishes after the dimensions of the NW exceed 7 × 7, whilst for even NWs gap closure occurs after they exceed 14 × 14. The minimum of the induced energy gap for even NWs (Fig.5.6), at NW dimensions of 14 × 14, coincides with that of even thin films, at a thickness of $n = 14$. It is interesting that this is concurrent with the even thin film topological phase transition from the trivial $\zeta_M = 0$ to the non-trivial $\zeta_M = 2$, at $12 \leq n \leq 14$, in Fig.5.2. For odd NWs the gap closure (Fig.5.6) takes place slightly after the $N_M = 0$ to $N_M = +2$ phase transition (Fig.5.2) that occurs for odd thin films at $3 \leq n \leq 5$.

For odd and even NWs of dimensions greater than 7 × 7 and 14 × 14, respectively, the vanishing of a band gap (Fig.5.6) results in the formation of gapless surface states (SS). Even and odd NWs show characteristic SS dispersions, as exhibited in the one-dimensional band structures for a 15 × 15 and a 16 × 16 NW in Fig.5.7**b** and Fig.5.7**d**, respectively. The distinctive SS can be seen as boundary states of the topologically non-trivial 2D TCI phases predicted in odd and even SnTe (001) thin films [96, 97, 177], which were described above.

Odd NW SS display a single distinct band crossing close to $\bar{\mathrm{X}}$ (Fig.5.7**b**), and are derived from the 2D TCI phase where a mirror Chern number of $|N_M| = 2$ defines the non-trivial topology. This 2D TCI phase is predicted to be robust due to the topological protection offered by the underlying symmetry of the crystal [96, 97, 177]. Consequently, as long as mirror symmetry is preserved, we predict this topological protection to be expressed in the robust 1D SS of odd NWs.

Conversely, even NW SS tend to exhibit a double band crossing close to $\bar{\mathrm{X}}$ (Fig.5.7**d**), and are derived from the 2D TCI phase where the glide-winding invariant $|\zeta_m| = 2$ denotes the non-trivial topology. Unlike N_M, the ζ_m invariant has no mirror symmetry protection, and instead is protected by a complex symmetry involving inversion symmetry [96]. It is therefore predicted to have no bulk-boundary correspondence, as inversion symmetry is preserved in the bulk but not at the boundary. Subsequently, the topological protection offered by the $|\zeta_m| = 2$ TCI phase is less robust in comparison to $|N_M| = 2$, which we predict to also be reflected in the 1D SS of even NWs. The manifestation of the 2D TCI phases in the 1D SS of the cubic NWs seems to originate from the equivalent symmetry operations underpinning odd (even) thin films and odd (even) cubic NWs. The correspondence between the 2D TCI phases and the 1D NW SS is explored in detail in the discussion on rectangular NWs below.

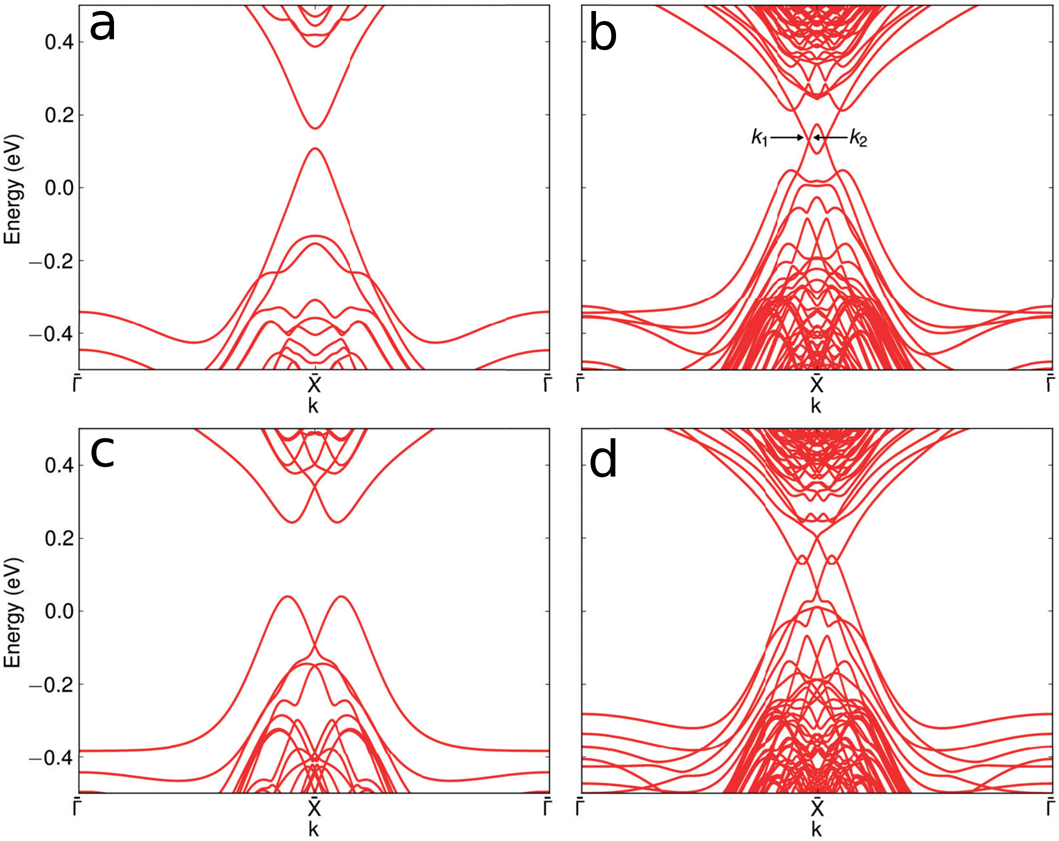

Figure 5.7 – Band structures for a series of odd (**a**,**b**) and even (**c**,**d**) $n \times n$ NWs. **a** 7 × 7 odd NW. **b** 15 × 15 odd NW, k_1 and k_2 define momenta for two pairs of $j = \pm 1$ degenerate states whose spin textures are shown in Fig.5.8. **c** 8 × 8 even NW. **d** 16 × 16 even NW.

We now explore spin properties of 1D NW SS, using the 15 × 15 odd NW as an exemplar, given that it derives from the 2D TCI phase with $|N_M| = 2$, and has a simple SS dispersion defined by a single crossing (Fig.5.7**b**), as described above. We focus on the real-space spin properties, and follow a similar procedure to that for the Bi_2Se_3 nanostructures in the previous chapter. We define two pairs of $j = \pm 1$ degenerate conduction band (CB) states, one pair at momentum k_1 and the other at k_2. The $j = \pm 1$ CB states at k_1 are situated just before, and those at k_2 just after, the SS crossing in Fig.5.7**b**.

Subsequently, as before, from the expectation value of the spin operators (Eqn.4.7), for a given state j we compute the local spin density $\boldsymbol{S}_i$ on an atom i via

$$\boldsymbol{S}_i^j(k_\parallel, \boldsymbol{r}_i) = \left(\frac{\hbar}{2}\right)\Big\langle \psi(k_\parallel)|\sigma_\alpha \otimes P_i|\psi(k_\parallel)\Big\rangle \quad (\alpha = x, y, z), \tag{5.3}$$

where P_i is a projector onto atom i, and is defined $P_i = \sum_{\lambda\sigma}|i\lambda\sigma\rangle\langle i\lambda\sigma|$, with λ the orbital index and σ the spin. The morphology of the 15×15 odd NW, equivalent to that in Fig.5.1**b**, again entails that the wavefunction for each degenerate $j = \pm 1$ state, at either k_1 or k_2, is localised around the perimeter. Thus, to clearly resolve the real-space spin properties, the sum, $\boldsymbol{S}_i^{tot}$, of the local spin densities, $\boldsymbol{S}_i^j$, for $j = \pm 1$ is calculated

$$\boldsymbol{S}_i^{tot} = \boldsymbol{S}_i^{+1} + \boldsymbol{S}_i^{-1}, \tag{5.4}$$

as was done previously for the Bi_2Se_3 nanostructures. This quantity is determined for each pair of states at k_1 and k_2 and plotted as a function of atomic position $\boldsymbol{r}_i$ in Fig.5.8**a** and Fig.5.8**b**, respectively.

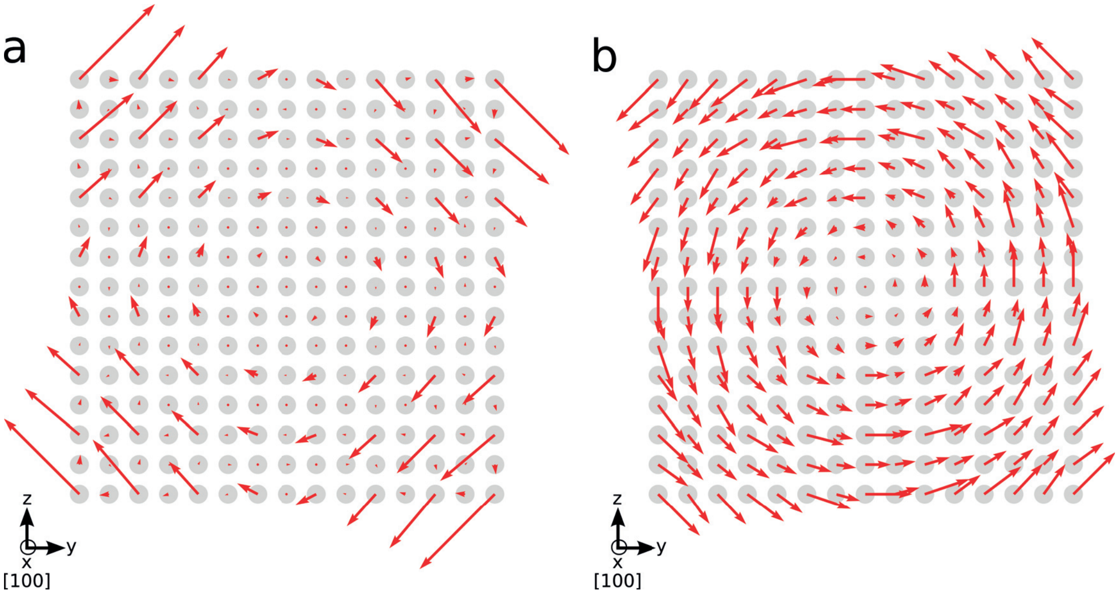

Figure 5.8 – Spin textures for conduction band surface states (SS) of a SnTe 15×15 odd NW. **a** and **b** correspond to SS positioned at momenta before (k_1) and after (k_2) the crossing in Fig.5.7**b**, respectively. Red arrows denote total local spin density $\boldsymbol{S}_i^{tot}$ (Eqn.4.9), grey circles indicate the position of Sn and Te atoms. [001] is the axial direction of the NW.

Confirmation of the SS origin of the states at k_1 (Fig.5.8**a**) and k_2 (Fig.5.8**b**) is given by the localisation of $\boldsymbol{S}_i^{tot}$ around the NW perimeter, and its increasing magnitude from the centre to the perimeter. Interestingly, the spin texture is aligned entirely in the tangent plane to the NW axis, and there is a clear 2π rotation of $\boldsymbol{S}_i^{tot}$ around the NW perimeter. However, the behaviour of $\boldsymbol{S}_i^{tot}$ for the states at k_1 belonging to one SS branch is distinct to that for the states at k_2 belonging to the other. Firstly, the spin texture at k_1 has a left-handed chirality, whilst that at k_2 is right-handed. This is simply a consequence of the fact that the conduction band states at k_1 and k_2 belong to opposite SS branches, with k_1 on one side of the SS crossing and k_2, as the SS crossing occurs away from a time-reversal invariant momentum point. Secondly, there is marked difference in the spin textures, with a more pronounced 2π rotation at k_2 in comparison to k_1. This stems from the different orbital contributions to the states belonging to each respective SS branch. The states at k_1 are primarily comprised of Sn p orbitals, whilst those at k_2 from Te p orbitals. This can be clearly observed in Fig.5.9 where the Sn p and Te p orbital contributions to the band structure in Fig.5.7**b** are plotted. The rotation of $\boldsymbol{S}_i^{tot}$ is similar to the behaviour predicted for hexagonal Bi_2Se_3 NWs in the previous chapter. In that case a clear correspondence between the real-space spin properties of the NW and the helicity of the 2D Dirac cone was established. However, it is less apparent whether a similar correspondence between the parent 2D TCI phase and the real space spin properties, as for example in Fig.5.8, of SnTe NWs can be made. One reason being that qualitatively equivalent behaviour to that in Fig.5.8 is observed for even square cross-section NWs of similar dimensions, implying that its origin is not rooted in the symmetry dependent topology of the parent 2D TCI phases. As Sn and Te are both elements with strong SOI, and given that Rashba-type spin-orbit splitting of SS [181, 182] could lead to similar behaviour to that in Fig.5.8, this may be an underlying cause for the observed phenomena.

The computed 1D dispersions of the NW band structures in Fig.5.7 stem from two primary factors, one being the non-trivial topology of the respective parent 2D TCI phase, and the other being quantum confinement effects due to the dimensions and morphology of the NWs. An interesting question is the extent to which the observed 1D NW SS, for example in Fig.5.7**c** and Fig.5.7**d**, are a manifestation of the parent 2D TCI phase, or simply a consequence of quantum confinement. To further explore this, we mimic quantum confinement effects, of the type present in 1D square cross-section NWs, in 2D thin films. In order to do so we calculate the thin film band structure along a series of equally spaced linear 1D cuts across the 2D projected Brillouin zone (Fig.5.9**a**). For computing the band structure along these 1D cuts the thin films are again modelled in a slab geometry. However, whereas the slab band structure calculations described above were performed on a unit cell in a two atom basis, for the purposes of the band structure calculations along the 1D cuts a four atom basis is used. As such, the area of the slab unit cell for the four atom basis is doubled relative to that of the two atom basis. Consequently, the area of the Brillouin zone for a slab in the four atom basis (denoted by black solid lines in Fig.5.9**a**) is halved with respect to that of a slab in the two atom basis (denoted by black dashed lines in Fig.5.9**a**).

The dimensions of the Brillouin zone (black solid lines Fig.5.9**a**) along which the cuts are taken are given by $-\frac{\pi}{2} \leq k_x, k_y \leq \frac{\pi}{2}$. As confinement for a $n \times n$ square cross-section NW is being mimicked in a thin film of thickness n, the number of cuts is thus equivalent to the width of the NW i.e. n. The cuts correspond to discrete lines across the Brillouin zone which are defined as

$$k_y = \frac{k}{n}\pi \quad k \in [0, n-1], \tag{5.5}$$

for integer values of n. Given the rotational symmetry of the Brillouin zone, band structures of the 1D cuts are calculated along $k_x \in [0, \frac{\pi}{2}]$ for cuts restricted to $0 \leq k_y \leq \frac{\pi}{2}$. Subsequently, again using a 15 × 15 odd NW as an example, confinement was mimicked in a $n = 15$ thin film, and band structure calculations were performed along the cuts denoted by the red dotted lines in Fig.5.9**a**. The collective electronic spectrum of these cuts for a $n = 15$ thin film is plotted with the band structure for a 15 × 15 NW in Fig.5.9**b**. The 1D NW SS clearly reside within the quantum confinement gap (~ 0.07eV), implying their origin in the 2D TCI phase ($|N_M| = 2$) of the corresponding thin film.

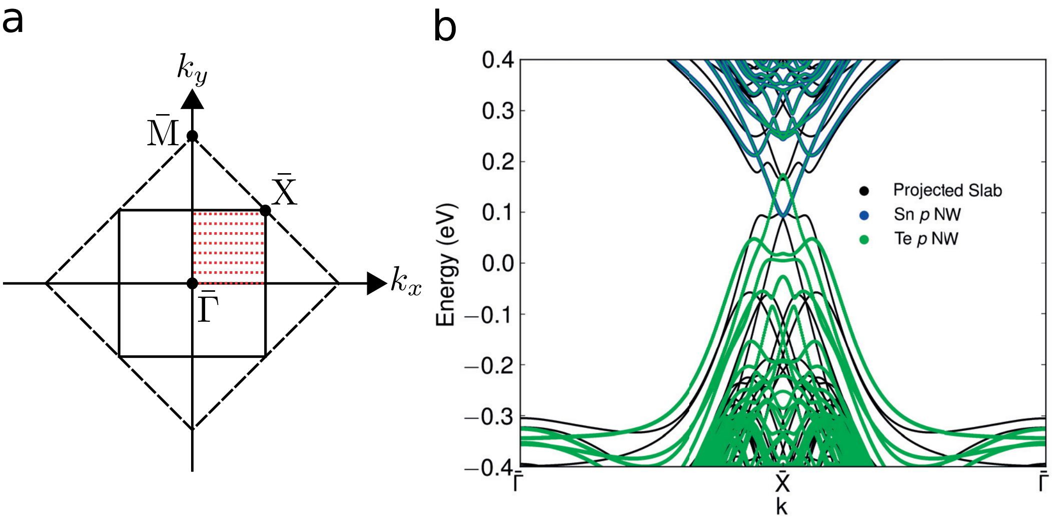

Figure 5.9 – SnTe 15 × 15 odd NW SS derived from the 2D TCI phase of a $n = 15$ thin film. **a** Schematic showing discrete 1D cuts (red dashed lines) in projected 2D Brillouin zone of a $n = 15$ thin film along which band structure calculations are performed. Cuts are taken through the projected Brillouin zone of slab with a unit cell in a four atom basis (black solid lines), as opposed to the Brillouin zone for an ordinary slab unit cell (black dashed lines) in a two atom basis, which is shown for the purposes of comparison. **b** Collective electronic spectrum for slab band structure calculations performed along cuts (red dashed lines) in **a** shown by black solid lines. Band structure for the 15 × 15 odd NW is shown by coloured circles, where the magnitude of blue (green) circles represents Sn(Te) p orbital contribution to the weight of the electronic wavefunction.

5.2.3 Rectangular Cross-Section Nanowires

To further explore the relationship between the 1D NW SSs and the respective parent 2D TCI phases we compute the band structure of a series of $n \times m$ rectangular cross-section NWs (Fig.5.10). The four types of investigated rectangular cross-section NWs were described in the Methodology of this chapter. They can be divided into two sets, for the first set n is odd, and includes an odd-odd 5 × 55 NW (Fig.5.10**a**) and an odd-even 5 × 50 NW (Fig.5.10**b**). For the second set n is even, and includes an even-even 14 × 54 NW (Fig.5.10**c**) and an even-odd

14×55 NW (Fig.5.10**d**). Given that the width m of all the $n \times m$ rectangular NWs is significantly larger than their thickness n, each system is effectively being pushed towards the 2D limit.

Of all the four cases, only for the odd-odd 5×55 NW is (001) mirror symmetry preserved. This is indicated by the absence of a fourfold band degeneracy at $\bar{X}$ (Fig.5.10**a**). Intriguingly, distinct SS are formed defined by a single band crossing close to $\bar{X}$. These SS seem exactly analogous to those observed in the case of the 15×15 odd NW discussed above (Fig.5.7**b**), and are in agreement with the SnTe (001) odd thin film edge states predicted in Ref. [96, 177]. Consequently, given the presence of (001) mirror symmetry, we conclude these are robust SS and are a 1D manifestation of the 2D TCI phase in (001) odd thin films where the non-trivial topology is protected by the mirror Chern number $|N_M| = 2$.

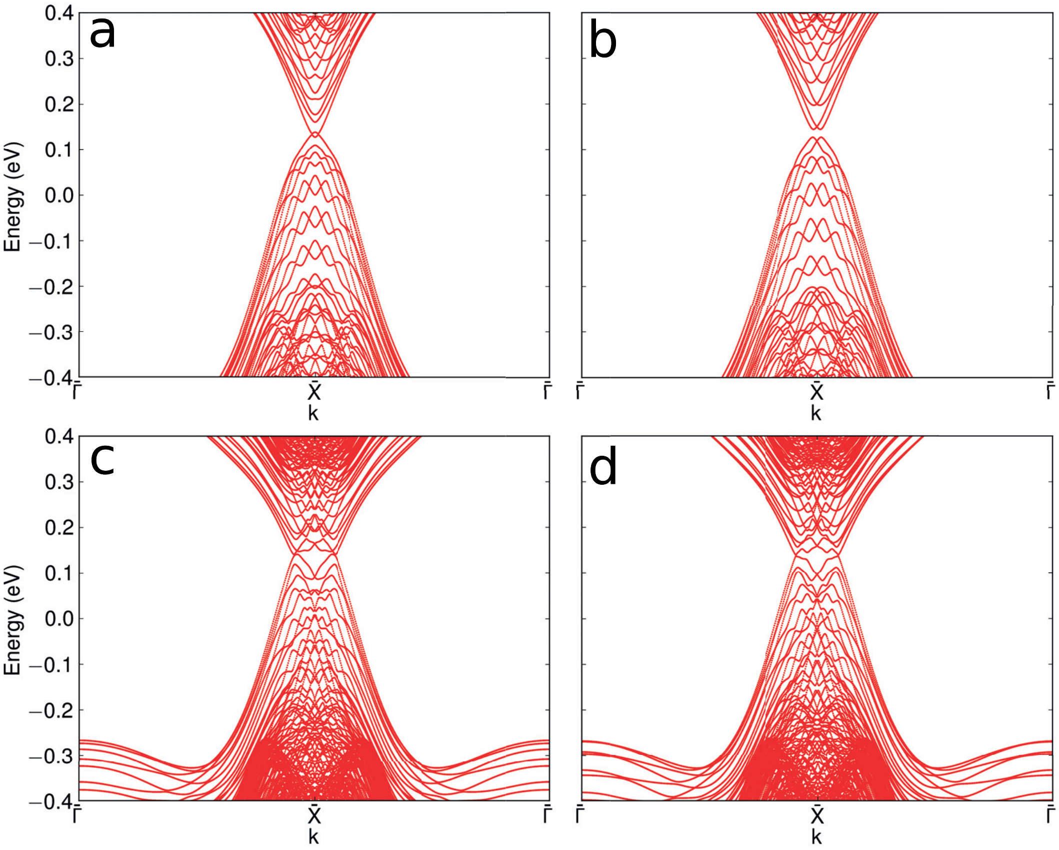

Figure 5.10 – Band structures for a series of rectangular cross-section $n \times m$ NWs. **a** 5×55 odd-odd NW. **b** 5×50 odd-even NW. **c** 14×54 even-even NW. **d** 14×55 even-odd NW.

A comparison with the band structure of the 5×50 odd-even NW (Fig.5.10**b**) strengthens this conclusion. As Fig.5.10**b** shows, there is no SS crossing and a clear band gap. Even though the 5×50 and 5×55 NWs are of similar dimensions, they have different symmetries. The primary symmetry operation defining the 5×50 NW is glide symmetry, confirmation of which is given by the fourfold band degeneracy at $\bar{X}$. Consequently, as there is no (001) mirror symmetry, the electronic spectrum is gapped, in stark contrast to the mirror symmetry protected robust SSs for the odd-odd rectangular NW case just described. The clear mirror symmetry dependency of the topologically derived SS in Fig.5.10**a** is further highlighted by the fact that aside from the absence of a SS crossing and the fourfold degeneracy at $\bar{\mathrm{X}}$, the band structures in Fig.5.10**a** and Fig.5.10**b** are qualitatively similar. Given the presence of glide symmetry, one might expect SS derived from the 2D TCI phase with $|\zeta_m| = 2$ in Fig.5.10**b**. However, the trivial behaviour of the spectrum in Fig.5.10**b** is perhaps unsurprising, as the dimensions of the 5×50 NW imply the system being pushed towards the 2D limit, and given its thickness of $n = 5$, the phase transition from trivial $|\zeta_m| = 0$ to non-trivial $|\zeta_m| = 2$ in (001) thin films occurs for a thin film thickness of $n \sim 14$ (Fig.5.2).

Conversely, the even-even 14×54 (Fig.5.10**c**) and the even-odd 14×55 (Fig.5.10**d**) NWs both have a thickness of $n = 14$, and in both cases glide symmetry is present, as confirmed by the fourfold degeneracy at $\bar{\mathrm{X}}$. However, aside from that, their electronic spectra are markedly different to that of the odd-even 5×50 NW (Fig.5.10**b**). The key difference is the dispersion of the SS of the 14×54 (Fig.5.10**c**) and the 14×55 (Fig.5.10**d**) NWs, which are similar to that of the even square cross-section NWs discussed above (Fig.5.7**d**), and the edge states of a 2D TCI (001) even thin film with $|\zeta_m| = 2$ in Ref. [96]. Thus, we infer that the observed SS dispersions are a 1D manifestation of the $|\zeta_m| = 2$ even thin film 2D TCI phase, based on the presence of glide symmetry and the thickness ($n = 14$) of the 14×54 and the 14×55 NWs. The extremely similar band structures in Fig.5.10**c** and Fig.5.10**d**, and the clear contrast with Fig.5.10**b**, seems to provide further evidence that their SS properties derive from a non-trivial 2D TCI phase with $|\zeta_m| = 2$, whilst the dispersion in Fig.5.10**b** originates from a trivial phase. It is important to note that unlike SS derived from a non-trivial topology of the $|N_M| = 2$ TCI phase, the $|\zeta_m| = 2$ derived SS are not robust. Specifically, two branches can merge and become gapped. A comparison of the dispersion of the SS for the square cross-section 16×16 NW (Fig.5.7**d**), and that of the rectangular cross-section NWs in Fig.5.10**c**, and Fig.5.10**d**, seems to provide tentative evidence of this. The less robust nature of the SS is a consequence of the fact that the ζ_m invariant has no bulk-boundary correspondence [96], as was described above.

5.3 Conclusions

To summarize, this chapter investigated, via the use of a tight-binding formalism, the connection between the crystal-symmetry-dependent 2D TCI phases of SnTe (001) thin films and the electronic structure of nanowires. Analogously to 2D thin films, we find that finite-size effects in 1D NWs are strictly governed by the pertaining crystal symmetry. This is demonstrated in the dimensionality dependence of the finite-size induced band gap, where square cross-section NWs defined by either mirror or glide symmetry exhibit two different regimes. We find this is further expressed in the dispersion of the NW electronic spectra. In particular, we find that the mirror or glide symmetry dependent 2D TCI phase are expressed in the surface states (SS) of square cross-section NWs defined by an equivalent symmetry. This is supported by our finding that the SSs do not originate from quantum confinement. Finally, by studying similar relations in rectangular cross-section NWs, we are able to relate the topological protection offered by each 2D TCI phase to the NW SS.

6 Outlook

Ever since the initial theoretical proposal of the Z_2 TI phase [9, 11] and subsequent experimental realizations [10, 26, 33, 34] the search for novel topological phases, and their materials realizations, has mushroomed. A somewhat modest snapshot is given by Fig.1.5, where the chronology of a selection of these discoveries is displayed. As such, this currently forms one of the most active and exciting branches of condensed matter physics. This work broadly focused on the Z_2 topological insulator (TI) and the topological crystalline insulator (TCI) phases. Relative to the numerous subsequent advances (Fig.1.5), Z_2 topological insulators represent a relatively mature sub-branch [8, 66] of the field, even though TCIs were discovered more recently, they are nonetheless well established [23].

Much of the initial work on Z_2 TIs and TCIs, understandably, involved the characterization of the topological surface states. In this respect, surface sensitive techniques such as angle-resolved photoemission spectroscopy (ARPES) and scanning tunneling microscopy proved to be enormously useful. Both in terms of imaging the Dirac cone and confirming its helical spin polarization, as was described in the Introduction. For the purposes of any practical applications seeking to exploit the unique properties of TSS, it is obviously necessary to first have the ability to directly access and manipulate them. With respect to the bulk crystal in Bi_2Se_3, Bi_2Te_3, and SnTe this has been hampered by material imperfections, as we detailed in the Introduction. Consequently, improving control over TSS via material improvements forms an active area of research, in both the bismuth chalcogenide TIs and the TCI SnTe. This was a primary motivation underlying this work, as nanostructuring overcomes many of those problems, as has been described. We specifically investigated the impact of nanoscale confinement on electronic structure, and properties of low-dimensional nanostructures derived from the bulk topological phase. Consequently, we would like to briefly place our results in perspective of some of the current work being done on TI and TCI nanostructures, and discuss possible future directions.

Our work on Bi_2Se_3 nanowires and nanoribbons in Chapter 4 showed that electronic structure and the spin-momentum locking properties of the 2D surface Dirac cone are highly sensitive to dimensionality reduction. This sensitivity implies the ability to have a degree of control over associated properties. An experimental example of this control was how the application of an applied magnetic flux enabled the observation of Aharonov-Bohm oscillations in magnetoconductance measurements of Bi_2Se_3 related nanowires [87, 92]. Crucially, these measurements were consistent with transport originating from the topological surface states. This can be seen as a promising first step in utilising Bi_2Se_3 NWs in future electronic technologies. For example, given that transport associated with helical surface states can be tuned into the ballistic regime [91], one could envisage Bi_2Se_3 NWs as dissipationless interconnects in electronic devices. Even more exciting is the prospect of harnessing the spin-momentum locking properties of TSS to electrically manipulate spin currents, with potential applications in spintronics. Substantial progress has been made with respect to Bi_2Se_3 thin films in this direction. For example, in Ref. [183] it was shown that Bi_2Se_3 thin films of thickness less than 6 QLs form spin split Rashba like surface states, with the inner and outer Rashba branches localised on opposite surfaces of the thin film, implying possible control over the spin branches. More directly, in Ref. [165] a Bi_2Se_3 thin film was shown to exert a TSS derived spin transfer torque on an adjacent ferromagnetic thin film. Furthermore, this is also the strongest spin transfer torque, per unit charge current density, measured thus far. In terms of lower dimensional nanostructures, in Chapter 4 we showed the direct correspondence between the spin helicity of the surface Dirac cone and the quantized 1D sub-bands of a Bi_2Se_3 NW. Moreover, we calculated that this gives rise to an energy dependent spin polarisation density, and hypothesized the potential to exploit this quantity to generate spin polarised charge carriers. Even though spin-based transport measurements in TI nanostructures are still lacking, the work in Ref. [87, 92] nonetheless provides a crucial first step in that direction.

In TCIs, the topological protection stems from spatial symmetries, for example in the case of SnTe from the mirror symmetry of the underlying crystal. This is in distinct contrast to Z_2 TIs where the topological protection originates from the nonspatial time-reversal symmetry. Consequently, the TSS in TCIs are far more sensitive, and thus tunable, to symmetry breaking perturbations. Our work on TCI NWs in Chapter 5 highlighted how the sensitivity of the 2D TCI phases in SnTe (001) thin films to crystal structure is exhibited in symmetry related NWs. This rich interplay between mirror-symmetry protected topology, crystal symmetry, and electronic structure has also been highlighted in the recent prediction of an electrically tunable quantum spin hall state in SnTe (111) thin films [98]. Consequently, based on this prediction, and our work on SnTe $\{100\}$ NWs, it would be of great interest to investigate SnTe nanostructures which expose two distinct surface types. For example, the nanostructures synthesized in Ref. [102], where both the (100) and (111) surfaces exposed. Specifically, to explore how the differing TSS present in the SnTe (001) and (111) thin films are manifested in the electronic spectrum of the nanostructure.

Bibliography

[1] K. Klitzing, G. Dorda, and M. Pepper, “New Method for High-Accuracy Determination of the Fine-Structure Constant Based on Quantized Hall Resistance,” *Physical Review Letters*, vol. 45, pp. 494–497, aug 1980.

[2] D. Thouless, M. Kohmoto, M. Nightingale, and M. den Nijs, “Quantized Hall Conductance in a Two-Dimensional Periodic Potential,” *Physical Review Letters*, vol. 49, pp. 405–408, aug 1982.

[3] N. W. Ashcroft and D. N. Mermin, *Solid State Physics.* Toronto: Thomson Learning, 1 ed., jan 1976.

[4] M. Nakahara, *Geometry, Topology and Physics, Second Edition.* CRC Press, 2003.

[5] M. V. Berry, “Quantal Phase Factors Accompanying Adiabatic Changes,” *Proceedings of the Royal Society A: Mathematical, Physical and Engineering Sciences*, vol. 392, pp. 45–57, mar 1984.

[6] B. I. Halperin, “Quantized Hall conductance, current-carrying edge states, and the existence of extended states in a two-dimensional disordered potential,” *Physical Review B*, vol. 25, pp. 2185–2190, feb 1982.

[7] F. D. M. Haldane, “Model for a Quantum Hall Effect without Landau Levels: Condensed-Matter Realization of the "Parity Anomaly",” *Physical Review Letters*, vol. 61, pp. 2015–2018, oct 1988.

[8] M. Z. Hasan and C. L. Kane, “Colloquium: Topological insulators,” *Reviews of Modern Physics*, vol. 82, pp. 3045–3067, nov 2010.

[9] C. L. Kane and E. J. Mele, “Quantum Spin Hall Effect in Graphene,” *Physical Review Letters*, vol. 95, p. 226801, nov 2005.

[10] B. A. Bernevig, T. L. Hughes, and S.-C. Zhang, “Quantum spin Hall effect and topological phase transition in HgTe quantum wells.,” *Science (New York, N.Y.)*, vol. 314, pp. 1757–61, dec 2006.

[11] C. L. Kane and E. J. Mele, “Z2 Topological Order and the Quantum Spin Hall Effect,” *Physical Review Letters*, vol. 95, p. 146802, sep 2005.

[12] L. Fu and C. Kane, “Time reversal polarization and a Z2 adiabatic spin pump,” *Physical Review B*, vol. 74, p. 195312, nov 2006.

[13] L. Fu and C. Kane, “Topological insulators with inversion symmetry,” *Physical Review B*, vol. 76, p. 045302, jul 2007.

[14] J. E. Moore and L. Balents, “Topological invariants of time-reversal-invariant band structures,” *Phys. Rev. B*, vol. 75, p. 121306, mar 2007.

[15] L. Fu, C. Kane, and E. Mele, “Topological Insulators in Three Dimensions,” *Physical Review Letters*, vol. 98, p. 106803, mar 2007.

[16] J. Moore and L. Balents, “Topological invariants of time-reversal-invariant band structures,” *Physical Review B*, vol. 75, p. 121306, mar 2007.

[17] R. Roy, “Topological phases and the quantum spin Hall effect in three dimensions,” *Physical Review B*, vol. 79, p. 195322, may 2009.

[18] A. Kitaev, V. Lebedev, and M. Feigel’man, “Periodic table for topological insulators and superconductors,” in *AIP Conference Proceedings*, vol. 1134, pp. 22–30, AIP, may 2009.

[19] A. Schnyder, S. Ryu, A. Furusaki, and A. Ludwig, “Classification of topological insulators and superconductors in three spatial dimensions,” *Physical Review B*, vol. 78, p. 195125, nov 2008.

[20] X.-L. Qi, T. L. Hughes, and S.-C. Zhang, “Topological field theory of time-reversal invariant insulators,” *Physical Review B*, vol. 78, p. 195424, nov 2008.

[21] L. Fu, “Topological Crystalline Insulators,” *Physical Review Letters*, vol. 106, p. 106802, mar 2011.

[22] J. Teo, L. Fu, and C. Kane, “Surface states and topological invariants in three-dimensional topological insulators: Application to Bi1-xSbx,” *Physical Review B*, vol. 78, p. 045426, jul 2008.

[23] Y. Ando and L. Fu, “Topological Crystalline Insulators and Topological Superconductors: From Concepts to Materials,” *Annual Review of Condensed Matter Physics*, vol. 6, pp. 361–381, mar 2015.

[24] T. H. Hsieh, H. Lin, J. Liu, W. Duan, A. Bansil, and L. Fu, “Topological crystalline insulators in the SnTe material class.,” *Nature Communications*, vol. 3, p. 982, jan 2012.

[25] M. König, S. Wiedmann, C. Brüne, A. Roth, H. Buhmann, L. W. Molenkamp, X.-L. Qi, and S.-C. Zhang, “Quantum spin hall insulator state in HgTe quantum wells.,” *Science (New York, N.Y.)*, vol. 318, pp. 766–70, nov 2007.

[26] D. Hsieh, D. Qian, L. Wray, Y. Xia, Y. S. Hor, R. J. Cava, and M. Z. Hasan, “A topological Dirac insulator in a quantum spin Hall phase.,” *Nature*, vol. 452, pp. 970–4, apr 2008.

[27] L. S. LERNER, K. F. CUFF, and L. R. WILLIAMS, “Energy-Band Parameters and Relative Band-Edge Motions in the Bi-Sb Alloy System near the Semimetal—Semiconductor Transition,” *Reviews of Modern Physics*, vol. 40, pp. 770–775, oct 1968.

[28] B. Lenoir, M. Cassart, J.-P. Michenaud, H. Scherrer, and S. Scherrer, “Transport properties of Bi-RICH Bi-Sb alloys,” *Journal of Physics and Chemistry of Solids*, vol. 57, pp. 89–99, jan 1996.

[29] S. Golin, “Band Model for Bismuth-Antimony Alloys,” *Physical Review*, vol. 176, pp. 830–832, dec 1968.

[30] D. Hsieh, Y. Xia, L. Wray, D. Qian, A. Pal, J. H. Dil, J. Osterwalder, F. Meier, G. Bihlmayer, C. L. Kane, Y. S. Hor, R. J. Cava, and M. Z. Hasan, “Observation of unconventional quantum spin textures in topological insulators.,” *Science (New York, N.Y.)*, vol. 323, pp. 919–22, feb 2009.

[31] S.-M. Huang, S.-Y. Xu, I. Belopolski, C.-C. Lee, G. Chang, B. Wang, N. Alidoust, G. Bian, M. Neupane, C. Zhang, S. Jia, A. Bansil, H. Lin, and M. Z. Hasan, “A Weyl Fermion semimetal with surface Fermi arcs in the transition metal monopnictide TaAs class.,” *Nature Communications*, vol. 6, p. 7373, jan 2015.

[32] H. Zhang, C.-X. Liu, X.-L. Qi, X. Dai, Z. Fang, and S.-C. Zhang, “Topological insulators in Bi2Se3, Bi2Te3 and Sb2Te3 with a single Dirac cone on the surface,” *Nature Physics*, vol. 5, pp. 438–442, may 2009.

[33] Y. Xia, D. Qian, D. Hsieh, L. Wray, A. Pal, H. Lin, A. Bansil, D. Grauer, Y. S. Hor, R. J. Cava, and M. Z. Hasan, “Observation of a large-gap topological-insulator class with a single Dirac cone on the surface,” *Nature Physics*, vol. 5, pp. 398–402, may 2009.

[34] D. Hsieh, Y. Xia, D. Qian, L. Wray, J. H. Dil, F. Meier, J. Osterwalder, L. Patthey, J. G. Checkelsky, N. P. Ong, A. V. Fedorov, H. Lin, A. Bansil, D. Grauer, Y. S. Hor, R. J. Cava, and M. Z. Hasan, “A tunable topological insulator in the spin helical Dirac transport regime.,” *Nature*, vol. 460, pp. 1101–5, aug 2009.

[35] T. Zhang, P. Cheng, X. Chen, J.-F. Jia, X. Ma, K. He, L. Wang, H. Zhang, X. Dai, Z. Fang, X. Xie, and Q.-K. Xue, “Experimental Demonstration of Topological Surface States Protected by Time-Reversal Symmetry,” *Physical Review Letters*, vol. 103, p. 266803, dec 2009.

[36] Z. Alpichshev, J. G. Analytis, J.-H. Chu, I. R. Fisher, Y. L. Chen, Z. X. Shen, A. Fang, and A. Kapitulnik, “STM Imaging of Electronic Waves on the Surface of Bi2Te3 : Topologically Protected Surface States and Hexagonal Warping Effects,” *Physical Review Letters*, vol. 104, p. 016401, jan 2010.

[37] J. Black, E. Conwell, L. Seigle, and C. Spencer, “Electrical and optical properties of some M_{2}^{V-B}N_{2}^{VI-b} semiconductors,” *Journal of Physics and Chemistry of Solids*, vol. 2, pp. 240–251, jan 1957.

[38] J. Navrátil, J. Horák, T. Plecháček, S. Kamba, P. Lošt'ák, J. Dyck, W. Chen, and C. Uher, "Conduction band splitting and transport properties of Bi2Se3," *Journal of Solid State Chemistry*, vol. 177, pp. 1704–1712, apr 2004.

[39] D. Kong, J. J. Cha, K. Lai, H. Peng, J. G. Analytis, S. Meister, Y. Chen, H.-J. Zhang, I. R. Fisher, Z.-X. Shen, and Y. Cui, "Rapid surface oxidation as a source of surface degradation factor for Bi2Se3.," *ACS Nano*, vol. 5, pp. 4698–703, jun 2011.

[40] D. Kim, S. Cho, N. P. Butch, P. Syers, K. Kirshenbaum, S. Adam, J. Paglione, and M. S. Fuhrer, "Surface conduction of topological Dirac electrons in bulk insulating Bi2Se3," *Nature Physics*, vol. 8, pp. 460–464, apr 2012.

[41] J. G. Analytis, R. D. McDonald, S. C. Riggs, J.-H. Chu, G. S. Boebinger, and I. R. Fisher, "Two-dimensional surface state in the quantum limit of a topological insulator," *Nature Physics*, vol. 6, pp. 960–964, nov 2010.

[42] J. G. Analytis, J.-H. Chu, Y. Chen, F. Corredor, R. D. McDonald, Z. X. Shen, and I. R. Fisher, "Bulk Fermi surface coexistence with Dirac surface state in Bi2Se3: A comparison of photoemission and Shubnikov–de Haas measurements," *Physical Review B*, vol. 81, p. 205407, may 2010.

[43] Y. S. Hor, A. Richardella, P. Roushan, Y. Xia, J. G. Checkelsky, A. Yazdani, M. Z. Hasan, N. P. Ong, and R. J. Cava, "p-type Bi2Se3 for topological insulator and low-temperature thermoelectric applications," *Physical Review B*, vol. 79, p. 195208, may 2009.

[44] J. G. Checkelsky, Y. S. Hor, M.-H. Liu, D.-X. Qu, R. J. Cava, and N. P. Ong, "Quantum Interference in Macroscopic Crystals of Nonmetallic Bi2Se3," *Physical Review Letters*, vol. 103, p. 246601, dec 2009.

[45] Y. Tanaka, Z. Ren, T. Sato, K. Nakayama, S. Souma, T. Takahashi, K. Segawa, and Y. Ando, "Experimental realization of a topological crystalline insulator in SnTe," *Nature Physics*, vol. 8, pp. 800–803, sep 2012.

[46] P. Dziawa, B. J. Kowalski, K. Dybko, R. Buczko, A. Szczerbakow, M. Szot, E. Łusakowska, T. Balasubramanian, B. M. Wojek, M. H. Berntsen, O. Tjernberg, and T. Story, "Topological crystalline insulator states in Pb(1-x)Sn(x)Se.," *Nature Materials*, vol. 11, pp. 1023–7, dec 2012.

[47] S.-Y. Xu, C. Liu, N. Alidoust, M. Neupane, D. Qian, I. Belopolski, J. D. Denlinger, Y. J. Wang, H. Lin, L. A. Wray, G. Landolt, B. Slomski, J. H. Dil, A. Marcinkova, E. Morosan, Q. Gibson, R. Sankar, F. C. Chou, R. J. Cava, A. Bansil, and M. Z. Hasan, "Observation of a topological crystalline insulator phase and topological phase transition in Pb(1-x)Sn(x)Te.," *Nature Communications*, vol. 3, p. 1192, jan 2012.

[48] K. Hummer, A. Grüneis, and G. Kresse, "Structural and electronic properties of lead chalcogenides from first principles," *Physical Review B*, vol. 75, p. 195211, may 2007.

[49] X. Gao and M. S. Daw, “Investigation of band inversion in (Pb,Sn)Te alloys using ab initio calculations,” *Physical Review B*, vol. 77, p. 033103, jan 2008.

[50] A. Svane, N. E. Christensen, M. Cardona, A. N. Chantis, M. van Schilfgaarde, and T. Kotani, “Quasiparticle self-consistent GW calculations for PbS, PbSe, and PbTe: Band structure and pressure coefficients,” *Physical Review B*, vol. 81, p. 245120, jun 2010.

[51] K. M. Rabe and J. D. Joannopoulos, “Ab initio relativistic pseudopotential study of the zero-temperature structural properties of SnTe and PbTe,” *Physical Review B*, vol. 32, pp. 2302–2314, aug 1985.

[52] S. Safaei, P. Kacman, and R. Buczko, “Topological crystalline insulator (Pb,Sn)Te: Surface states and their spin polarization,” *Physical Review B*, vol. 88, p. 045305, jul 2013.

[53] Y. Okada, M. Serbyn, H. Lin, D. Walkup, W. Zhou, C. Dhital, M. Neupane, S. Xu, Y. J. Wang, R. Sankar, F. Chou, A. Bansil, M. Z. Hasan, S. D. Wilson, L. Fu, and V. Madhavan, “Observation of Dirac node formation and mass acquisition in a topological crystalline insulator.,” *Science (New York, N.Y.)*, vol. 341, pp. 1496–9, sep 2013.

[54] J. Liu, W. Duan, and L. Fu, “Two types of surface states in topological crystalline insulators,” *Physical Review B*, vol. 88, p. 241303, dec 2013.

[55] P. B. Littlewood, B. Mihaila, R. K. Schulze, D. J. Safarik, J. E. Gubernatis, A. Bostwick, E. Rotenberg, C. P. Opeil, T. Durakiewicz, J. L. Smith, and J. C. Lashley, “Band Structure of SnTe Studied by Photoemission Spectroscopy,” *Physical Review Letters*, vol. 105, p. 086404, aug 2010.

[56] K. Lischka, “Deep level defects in narrow gap semiconductors,” *physica status solidi (b)*, vol. 133, pp. 17–46, jan 1986.

[57] J. R. Burke, R. S. Allgaier, B. B. Houston, J. Babiskin, and P. G. Siebenmann, “Shubnikov-de Haas Effect in SnTe,” *Physical Review Letters*, vol. 14, pp. 360–361, mar 1965.

[58] N. Wang, D. West, J. Liu, J. Li, Q. Yan, B.-L. Gu, S. B. Zhang, and W. Duan, “Microscopic origin of the p -type conductivity of the topological crystalline insulator SnTe and the effect of Pb alloying,” *Physical Review B*, vol. 89, p. 045142, jan 2014.

[59] J. G. Checkelsky, Y. S. Hor, R. J. Cava, and N. P. Ong, “Bulk Band Gap and Surface State Conduction Observed in Voltage-Tuned Crystals of the Topological Insulator Bi2Se3,” *Physical Review Letters*, vol. 106, p. 196801, may 2011.

[60] K. S. Novoselov, A. K. Geim, S. V. Morozov, D. Jiang, Y. Zhang, S. V. Dubonos, I. V. Grigorieva, and A. A. Firsov, “Electric field effect in atomically thin carbon films.,” *Science (New York, N.Y.)*, vol. 306, pp. 666–9, oct 2004.

[61] S. S. Hong, W. Kundhikanjana, J. J. Cha, K. Lai, D. Kong, S. Meister, M. A. Kelly, Z.-X. Shen, and Y. Cui, “Ultrathin topological insulator Bi2Se3 nanoribbons exfoliated by atomic force microscopy.,” *Nano Letters*, vol. 10, pp. 3118–22, aug 2010.

[62] J. N. Coleman, M. Lotya, A. O'Neill, S. D. Bergin, P. J. King, U. Khan, K. Young, A. Gaucher, S. De, R. J. Smith, I. V. Shvets, S. K. Arora, G. Stanton, H.-Y. Kim, K. Lee, G. T. Kim, G. S. Duesberg, T. Hallam, J. J. Boland, J. J. Wang, J. F. Donegan, J. C. Grunlan, G. Moriarty, A. Shmeliov, R. J. Nicholls, J. M. Perkins, E. M. Grieveson, K. Theuwissen, D. W. McComb, P. D. Nellist, and V. Nicolosi, "Two-dimensional nanosheets produced by liquid exfoliation of layered materials.," *Science (New York, N.Y.)*, vol. 331, pp. 568–71, feb 2011.

[63] R. S. Wagner and W. C. Ellis, "Vapor-Liquid-Solid mechanism of single crystal growth," *Applied Physics Letters*, vol. 4, p. 89, dec 1964.

[64] A. M. Morales, "A Laser Ablation Method for the Synthesis of Crystalline Semiconductor Nanowires," *Science*, vol. 279, pp. 208–211, jan 1998.

[65] D. Kong, J. C. Randel, H. Peng, J. J. Cha, S. Meister, K. Lai, Y. Chen, Z.-X. Shen, H. C. Manoharan, and Y. Cui, "Topological Insulator Nanowires and Nanoribbons," *Nano Letters*, vol. 10, pp. 329–333, dec 2009.

[66] Y. Ando, "Topological Insulator Materials," *Journal of the Physical Society of Japan*, vol. 82, p. 102001, oct 2013.

[67] H. Peng, K. Lai, D. Kong, S. Meister, Y. Chen, X.-L. Qi, S.-C. Zhang, Z.-X. Shen, and Y. Cui, "Aharonov-Bohm interference in topological insulator nanoribbons.," *Nature Materials*, vol. 9, pp. 225–9, mar 2010.

[68] D. Kong, W. Dang, J. J. Cha, H. Li, S. Meister, H. Peng, Z. Liu, and Y. Cui, "Few-Layer Nanoplates of Bi2Se3 and Bi2Te3 with Highly Tunable Chemical Potential," *Nano Letters*, vol. 10, pp. 2245–2250, may 2010.

[69] Y. Liu, Y. Y. Li, S. Rajput, D. Gilks, L. Lari, P. L. Galindo, M. Weinert, V. K. Lazarov, and L. Li, "Tuning Dirac states by strain in the topological insulator Bi2Se3," *Nature Physics*, vol. 10, pp. 294–299, mar 2014.

[70] Y. Wang, F. Xiu, L. Cheng, L. He, M. Lang, J. Tang, X. Kou, X. Yu, X. Jiang, Z. Chen, J. Zou, and K. L. Wang, "Gate-controlled surface conduction in Na-doped Bi2Te3 topological insulator nanoplates.," *Nano Letters*, vol. 12, pp. 1170–5, mar 2012.

[71] A. Koma, "Van der Waals epitaxy for highly lattice-mismatched systems," *Journal of Crystal Growth*, vol. 201-202, pp. 236–241, may 1999.

[72] H. Li, J. Cao, W. Zheng, Y. Chen, D. Wu, W. Dang, K. Wang, H. Peng, and Z. Liu, "Controlled synthesis of topological insulator nanoplate arrays on mica.," *Journal of the American Chemical Society*, vol. 134, pp. 6132–5, apr 2012.

[73] H. Peng, W. Dang, J. Cao, Y. Chen, D. Wu, W. Zheng, H. Li, Z.-X. Shen, and Z. Liu, "Topological insulator nanostructures for near-infrared transparent flexible electrodes.," *Nature Chemistry*, vol. 4, pp. 281–6, apr 2012.

[74] W. Zheng, T. Xie, Y. Zhou, Y. L. Chen, W. Jiang, S. Zhao, J. Wu, Y. Jing, Y. Wu, G. Chen, Y. Guo, J. Yin, S. Huang, H. Q. Xu, Z. Liu, and H. Peng, “Patterning two-dimensional chalcogenide crystals of Bi2Se3 and In2Se3 and efficient photodetectors.,” *Nature Communications*, vol. 6, p. 6972, jan 2015.

[75] F. Xiu, L. He, Y. Wang, L. Cheng, L.-T. Chang, M. Lang, G. Huang, X. Kou, Y. Zhou, X. Jiang, Z. Chen, J. Zou, A. Shailos, and K. L. Wang, “Manipulating surface states in topological insulator nanoribbons.,” *Nature Nanotechnology*, vol. 6, pp. 216–21, apr 2011.

[76] D. Kong, K. J. Koski, J. J. Cha, S. S. Hong, and Y. Cui, “Ambipolar field effect in Sb-doped Bi2Se3 nanoplates by solvothermal synthesis.,” *Nano Letters*, vol. 13, pp. 632–6, feb 2013.

[77] H. Steinberg, D. R. Gardner, Y. S. Lee, and P. Jarillo-Herrero, “Surface State Transport and Ambipolar Electric Field Effect in Bi2Se3 Nanodevices,” *Nano Letters*, vol. 10, pp. 5032–5036, dec 2010.

[78] D. Kong, Y. Chen, J. J. Cha, Q. Zhang, J. G. Analytis, K. Lai, Z. Liu, S. S. Hong, K. J. Koski, S.-K. Mo, Z. Hussain, I. R. Fisher, Z.-X. Shen, and Y. Cui, “Ambipolar field effect in the ternary topological insulator (Bi(x)Sb(1-x))2Te3 by composition tuning.,” *Nature Nanotechnology*, vol. 6, pp. 705–9, nov 2011.

[79] S. S. Hong, J. J. Cha, D. Kong, and Y. Cui, “Ultra-low carrier concentration and surface-dominant transport in antimony-doped Bi2Se3 topological insulator nanoribbons,” *Nature Communications*, vol. 3, p. 757, mar 2012.

[80] G. Hao, X. Qi, Y. Liu, Z. Huang, H. Li, K. Huang, J. Li, L. Yang, and J. Zhong, “Ambipolar charge injection and transport of few-layer topological insulator Bi2Te3 and Bi2Se3 nanoplates,” *Journal of Applied Physics*, vol. 111, p. 114312, jun 2012.

[81] A. A. Taskin, S. Sasaki, K. Segawa, and Y. Ando, “Manifestation of Topological Protection in Transport Properties of Epitaxial Bi2Se3 Thin Films,” *Physical Review Letters*, vol. 109, p. 066803, aug 2012.

[82] D.-X. Qu, Y. S. Hor, J. Xiong, R. J. Cava, and N. P. Ong, “Quantum oscillations and hall anomaly of surface states in the topological insulator Bi2Te3.,” *Science (New York, N.Y.)*, vol. 329, pp. 821–4, aug 2010.

[83] Y. Aharonov and D. Bohm, “Significance of Electromagnetic Potentials in the Quantum Theory,” *Physical Review*, vol. 115, pp. 485–491, aug 1959.

[84] S. Washburn and R. A. Webb, “Aharonov-Bohm effect in normal metal quantum coherence and transport,” *Advances in Physics*, vol. 35, pp. 375–422, jan 1986.

[85] A. G. Aronov and Y. V. Sharvin, “Magnetic flux effects in disordered conductors,” *Reviews of Modern Physics*, vol. 59, pp. 755–779, jul 1987.

[86] A. Bachtold, C. Strunk, J.-P. Salvetat, J.-M. Bonard, L. Forro, T. Nussbaumer, and C. Schonenberger, “Aharonov-Bohm oscillations in carbon nanotubes,” *Nature*, vol. 397, pp. 673–675, feb 1999.

[87] S. S. Hong, Y. Zhang, J. J. Cha, X.-L. Qi, and Y. Cui, “One-dimensional helical transport in topological insulator nanowire interferometers.,” *Nano Letters*, vol. 14, pp. 2815–21, may 2014.

[88] Z. Li, Y. Qin, F. Song, Q.-H. Wang, X. Wang, B. Wang, H. Ding, C. Van Haesondonck, J. Wan, Y. Zhang, and G. Wang, “Experimental evidence on the Altshuler-Aronov-Spivak interference of the topological surface states in the exfoliated Bi2Te3 nanoflakes,” *Applied Physics Letters*, vol. 100, p. 083107, feb 2012.

[89] J. H. Bardarson, P. W. Brouwer, and J. E. Moore, “Aharonov-Bohm Oscillations in Disordered Topological Insulator Nanowires,” *Physical Review Letters*, vol. 105, p. 156803, oct 2010.

[90] Y. Zhang and A. Vishwanath, “Anomalous Aharonov-Bohm Conductance Oscillations from Topological Insulator Surface States,” *Physical Review Letters*, vol. 105, p. 206601, nov 2010.

[91] J. H. Bardarson and J. E. Moore, “Quantum interference and Aharonov-Bohm oscillations in topological insulators.,” *Reports on progress in physics. Physical Society (Great Britain)*, vol. 76, p. 056501, may 2013.

[92] S. Cho, B. Dellabetta, R. Zhong, J. Schneeloch, T. Liu, G. Gu, M. J. Gilbert, and N. Mason, “Aharonov-Bohm oscillations in a quasi-ballistic three-dimensional topological insulator nanowire.,” *Nature Communications*, vol. 6, p. 7634, jan 2015.

[93] H. Guo, C.-H. Yan, J.-W. Liu, Z.-Y. Wang, R. Wu, Z.-D. Zhang, L.-L. Wang, K. He, X.-C. Ma, S.-H. Ji, W.-H. Duan, X. Chen, and Q.-K. Xue, “Topological crystalline insulator PbxSn1-xTe thin films on SrTiO3 (001) with tunable Fermi levels,” *APL Materials*, vol. 2, p. 056106, may 2014.

[94] C.-H. Yan, H. Guo, J. Wen, Z.-D. Zhang, L.-L. Wang, K. He, X.-C. Ma, S.-H. Ji, X. Chen, and Q.-K. Xue, “Growth of topological crystalline insulator SnTe thin films on Si(111) substrate by molecular beam epitaxy,” *Surface Science*, vol. 621, pp. 104–108, mar 2014.

[95] C. Zhang, Y. Liu, X. Yuan, W. Wang, S. Liang, and F. Xiu, “Highly tunable Berry phase and ambipolar field effect in topological crystalline insulator Pb(1-x)Sn(x)Se.,” *Nano Letters*, vol. 15, pp. 2161–7, mar 2015.

[96] H. Ozawa, A. Yamakage, M. Sato, and Y. Tanaka, “Topological phase transition in a topological crystalline insulator induced by finite-size effects,” *Physical Review B*, vol. 90, p. 045309, jul 2014.

[97] J. Liu, T. H. Hsieh, P. Wei, W. Duan, J. Moodera, and L. Fu, "Spin-filtered edge states with an electrically tunable gap in a two-dimensional topological crystalline insulator.," *Nature Materials*, vol. 13, pp. 178–83, feb 2014.

[98] J. Liu and L. Fu, "Electrically tunable quantum spin Hall state in topological crystalline insulator thin films," *Physical Review B*, vol. 91, p. 081407, feb 2015.

[99] S. Safaei, M. Galicka, P. Kacman, and R. Buczko, "Quantum spin Hall effect in IV-VI topological crystalline insulators," *New Journal of Physics*, vol. 17, p. 063041, jun 2015.

[100] J. Shen, Y. Jung, A. S. Disa, F. J. Walker, C. H. Ahn, and J. J. Cha, "Synthesis of SnTe nanoplates with {100} and {111} surfaces.," *Nano Letters*, vol. 14, pp. 4183–8, jul 2014.

[101] M. Safdar, Q. Wang, Z. Wang, X. Zhan, K. Xu, F. Wang, M. Mirza, and J. He, "Weak Antilocalization Effect of Topological Crystalline Insulator Pb1-xSnxTe Nanowires with Tunable Composition and Distinct {100} Facets.," *Nano Letters*, vol. 15, pp. 2485–90, apr 2015.

[102] Z. Li, S. Shao, N. Li, K. McCall, J. Wang, and S. X. Zhang, "Single crystalline nanostructures of topological crystalline insulator SnTe with distinct facets and morphologies.," *Nano Letters*, vol. 13, pp. 5443–8, jan 2013.

[103] M. Safdar, Q. Wang, M. Mirza, Z. Wang, and J. He, "Crystal Shape Engineering of Topological Crystalline Insulator SnTe Microcrystals and Nanowires with Huge Thermal Activation Energy Gap," *Crystal Growth & Design*, vol. 14, pp. 2502–2509, may 2014.

[104] M. Saghir, M. R. Lees, S. J. York, and G. Balakrishnan, "Synthesis and Characterization of Nanomaterials of the Topological Crystalline Insulator SnTe," *Crystal Growth & Design*, vol. 14, pp. 2009–2013, apr 2014.

[105] M. Safdar, Q. Wang, M. Mirza, Z. Wang, K. Xu, and J. He, "Topological surface transport properties of single-crystalline SnTe nanowire.," *Nano Letters*, vol. 13, pp. 5344–9, jan 2013.

[106] J. Shen, Y. Xie, and J. J. Cha, "Revealing Surface States in In-Doped SnTe Nanoplates with Low Bulk Mobility.," *Nano Letters*, vol. 15, pp. 3827–32, jun 2015.

[107] M. Born and R. Oppenheimer, "Zur Quantentheorie der Molekeln," *Annalen der Physik*, vol. 389, no. 20, pp. 457–484, 1927.

[108] P. Hohenberg, "Inhomogeneous Electron Gas," *Physical Review*, vol. 136, pp. B864–B871, nov 1964.

[109] W. Kohn and L. J. Sham, "Self-Consistent Equations Including Exchange and Correlation Effects," *Physical Review*, vol. 140, pp. A1133–A1138, nov 1965.

[110] D. Langreth and M. Mehl, "Beyond the local-density approximation in calculations of ground-state electronic properties," *Physical Review B*, vol. 28, pp. 1809–1834, aug 1983.

[111] D. M. Ceperley, “Ground State of the Electron Gas by a Stochastic Method,” *Physical Review Letters*, vol. 45, pp. 566–569, aug 1980.

[112] J. P. Perdew, “Self-interaction correction to density-functional approximations for many-electron systems,” *Physical Review B*, vol. 23, pp. 5048–5079, may 1981.

[113] J. P. Perdew, K. Burke, and M. Ernzerhof, “Generalized Gradient Approximation Made Simple,” *Physical Review Letters*, vol. 77, pp. 3865–3868, oct 1996.

[114] M. C. Payne, T. A. Arias, and J. D. Joannopoulos, “Iterative minimization techniques for ab initio total-energy calculations: molecular dynamics and conjugate gradients,” *Reviews of Modern Physics*, vol. 64, pp. 1045–1097, oct 1992.

[115] J. C. Phillips, “Energy-Band Interpolation Scheme Based on a Pseudopotential,” *Physical Review*, vol. 112, pp. 685–695, nov 1958.

[116] J. C. Phillips and L. Kleinman, “New Method for Calculating Wave Functions in Crystals and Molecules,” *Physical Review*, vol. 116, pp. 287–294, oct 1959.

[117] W. E. Pickett, “Pseudopotential methods in condensed matter applications,” *Computer Physics Reports*, vol. 9, pp. 115–197, apr 1989.

[118] D. Hamann, M. Schlüter, and C. Chiang, “Norm-Conserving Pseudopotentials,” *Physical Review Letters*, vol. 43, pp. 1494–1497, nov 1979.

[119] J. Ihm, A. Zunger, and M. L. Cohen, “Momentum-space formalism for the total energy of solids,” *Journal of Physics C: Solid State Physics*, vol. 12, pp. 4409–4422, nov 1979.

[120] P. J. H. Denteneer and W. van Haeringen, “The pseudopotential-density-functional method in momentum space: details and test cases,” *Journal of Physics C: Solid State Physics*, vol. 18, pp. 4127–4142, jul 1985.

[121] N. Troullier and J. L. Martins, “Efficient pseudopotentials for plane-wave calculations,” *Physical Review B*, vol. 43, pp. 1993–2006, jan 1991.

[122] D. Vanderbilt, “Soft self-consistent pseudopotentials in a generalized eigenvalue formalism,” *Physical Review B*, vol. 41, pp. 7892–7895, apr 1990.

[123] L. Kleinman, “Relativistic norm-conserving pseudopotential,” *Physical Review B*, vol. 21, pp. 2630–2631, mar 1980.

[124] G. B. Bachelet and M. Schlüter, “Relativistic norm-conserving pseudopotentials,” *Physical Review B*, vol. 25, pp. 2103–2108, feb 1982.

[125] M. J. Oliveira and F. Nogueira, “Generating relativistic pseudo-potentials with explicit incorporation of semi-core states using APE, the Atomic Pseudo-potentials Engine,” *Computer Physics Communications*, vol. 178, pp. 524–534, apr 2008.

[126] M. J. Verstraete, M. Torrent, F. Jollet, G. Zérah, and X. Gonze, “Density functional perturbation theory with spin-orbit coupling: Phonon band structure of lead,” *Physical Review B*, vol. 78, p. 045119, jul 2008.

[127] A. D. Corso and A. M. Conte, “Spin-orbit coupling with ultrasoft pseudopotentials: Application to Au and Pt,” *Physical Review B*, vol. 71, p. 115106, mar 2005.

[128] Y. L. Chen, J. G. Analytis, J.-H. Chu, Z. K. Liu, S.-K. Mo, X. L. Qi, H. J. Zhang, D. H. Lu, X. Dai, Z. Fang, S. C. Zhang, I. R. Fisher, Z. Hussain, and Z.-X. Shen, “Experimental realization of a three-dimensional topological insulator, Bi2Te3.,” *Science (New York, N.Y.)*, vol. 325, pp. 178–81, jul 2009.

[129] D. Hsieh, Y. Xia, D. Qian, L. Wray, F. Meier, J. Dil, J. Osterwalder, L. Patthey, A. Fedorov, H. Lin, A. Bansil, D. Grauer, Y. Hor, R. Cava, and M. Hasan, “Observation of Time-Reversal-Protected Single-Dirac-Cone Topological-Insulator States in Bi2Te3 and Sb2Te3,” *Physical Review Letters*, vol. 103, p. 146401, sep 2009.

[130] L. Nordström and D. J. Singh, “Noncollinear Intra-atomic Magnetism,” *Physical Review Letters*, vol. 76, pp. 4420–4423, jun 1996.

[131] T. Oda, A. Pasquarello, and R. Car, “Fully Unconstrained Approach to Noncollinear Magnetism: Application to Small Fe Clusters,” *Physical Review Letters*, vol. 80, pp. 3622–3625, apr 1998.

[132] R. Gebauer, S. Serra, G. L. Chiarotti, S. Scandolo, S. Baroni, and E. Tosatti, “Noncolinear spin polarization from frustrated antiferromagnetism: A possible scenario for molecular oxygen at high pressure,” *Physical Review B*, vol. 61, pp. 6145–6149, mar 2000.

[133] H. J. Monkhorst and J. D. Pack, “Special points for Brillouin-zone integrations,” *Physical Review B*, vol. 13, pp. 5188–5192, jun 1976.

[134] P. Giannozzi, S. Baroni, N. Bonini, M. Calandra, R. Car, C. Cavazzoni, D. Ceresoli, G. L. Chiarotti, M. Cococcioni, I. Dabo, A. Dal Corso, S. de Gironcoli, S. Fabris, G. Fratesi, R. Gebauer, U. Gerstmann, C. Gougoussis, A. Kokalj, M. Lazzeri, L. Martin-Samos, N. Marzari, F. Mauri, R. Mazzarello, S. Paolini, A. Pasquarello, L. Paulatto, C. Sbraccia, S. Scandolo, G. Sclauzero, A. P. Seitsonen, A. Smogunov, P. Umari, and R. M. Wentzcovitch, “QUANTUM ESPRESSO: a modular and open-source software project for quantum simulations of materials.,” *Journal of physics. Condensed matter : an Institute of Physics journal*, vol. 21, p. 395502, sep 2009.

[135] R. Wyckoff, *Crystal structures.* New York: Interscience Publishers, 1963.

[136] E. Kioupakis, M. L. Tiago, and S. G. Louie, “Quasiparticle electronic structure of bismuth telluride in the G W approximation,” *Physical Review B*, vol. 82, p. 245203, dec 2010.

[137] K. Wittel and R. Manne, “Atomic spin-orbit interaction parameters from spectral data for 19 elements,” *Theoretica Chimica Acta*, vol. 33, no. 4, pp. 347–349, 1974.

[138] M. L. Cohen, M. Schlüter, J. R. Chelikowsky, and S. G. Louie, “Self-consistent pseudopotential method for localized configurations: Molecules,” *Physical Review B*, vol. 12, pp. 5575–5579, dec 1975.

[139] O. V. Yazyev, J. E. Moore, and S. G. Louie, “Spin Polarization and Transport of Surface States in the Topological Insulators Bi2Se3 and Bi2Te3 from First Principles,” *Physical Review Letters*, vol. 105, p. 266806, dec 2010.

[140] J. C. Slater and G. F. Koster, “Simplified LCAO Method for the Periodic Potential Problem,” *Physical Review*, vol. 94, pp. 1498–1524, jun 1954.

[141] K. Kobayashi, “Electron transmission through atomic steps of Bi2Se3 and Bi2Te3 surfaces,” *Physical Review B*, vol. 84, p. 205424, nov 2011.

[142] C. S. Lent, M. A. Bowen, J. D. Dow, R. S. Allgaier, O. F. Sankey, and E. S. Ho, “Relativistic empirical tight-binding theory of the energy bands of GeTe, SnTe, PbTe, PbSe, PbS, and their alloys,” *Superlattices and Microstructures*, vol. 2, pp. 491–499, jan 1986.

[143] S. Nakajima, “The crystal structure of Bi2Te3-xSex,” *Journal of Physics and Chemistry of Solids*, vol. 24, pp. 479–485, mar 1963.

[144] G. Wulff, “XXV. Zur Frage der Geschwindigkeit des Wachsthums und der Auflösung der Krystallflächen,” *Zeitschrift für Kristallographie - Crystalline Materials*, vol. 34, jan 1901.

[145] E. Ringe, R. P. Van Duyne, and L. D. Marks, “Kinetic and Thermodynamic Modified Wulff Constructions for Twinned Nanoparticles,” *The Journal of Physical Chemistry C*, vol. 117, pp. 15859–15870, aug 2013.

[146] C. Herring, “Some Theorems on the Free Energies of Crystal Surfaces,” *Physical Review*, vol. 82, pp. 87–93, apr 1951.

[147] T. Björkman, A. Gulans, A. V. Krasheninnikov, and R. M. Nieminen, “van der Waals Bonding in Layered Compounds from Advanced Density-Functional First-Principles Calculations,” *Physical Review Letters*, vol. 108, p. 235502, jun 2012.

[148] L. Cheng, H. J. Liu, J. Zhang, J. Wei, J. H. Liang, J. Shi, and X. F. Tang, “Effects of van der Waals interactions and quasiparticle corrections on the electronic and transport properties of Bi2Te3,” *Physical Review B*, vol. 90, p. 085118, aug 2014.

[149] L. D. Alegria, M. D. Schroer, A. Chatterjee, G. R. Poirier, M. Pretko, S. K. Patel, and J. R. Petta, “Structural and electrical characterization of Bi2Se3 nanostructures grown by metal-organic chemical vapor deposition.,” *Nano Letters*, vol. 12, pp. 4711–4, sep 2012.

[150] Y. Zou, Z.-G. Chen, Y. Huang, L. Yang, J. Drennan, and J. Zou, “Anisotropic Electrical Properties from Vapor–Solid–Solid Grown Bi2Se3 Nanoribbons and Nanowires,” *The Journal of Physical Chemistry C*, vol. 118, pp. 20620–20626, sep 2014.

[151] C.-X. Liu, H. Zhang, B. Yan, X.-L. Qi, T. Frauenheim, X. Dai, Z. Fang, and S.-C. Zhang, “Oscillatory crossover from two-dimensional to three-dimensional topological insulators,” *Physical Review B*, vol. 81, p. 041307, jan 2010.

[152] K. He, Y. Zhang, C.-Z. Chang, C.-L. Song, L.-L. Wang, X. Chen, J.-F. Jia, Z. Fang, X. Dai, W.-Y. Shan, S.-Q. Shen, Q. Niu, X.-L. Qi, S.-C. Zhang, X.-C. Ma, and Q.-K. Xue, “Crossover of the three-dimensional topological insulator Bi2Se3 to the two-dimensional limit,” *Nature Physics*, vol. 6, pp. 584–588, jun 2010.

[153] O. V. Yazyev, E. Kioupakis, J. E. Moore, and S. G. Louie, “Quasiparticle effects in the bulk and surface-state bands of Bi2Se3 and Bi2Te3 topological insulators,” *Physical Review B*, vol. 85, p. 161101, apr 2012.

[154] H.-Z. Lu, W.-Y. Shan, W. Yao, Q. Niu, and S.-Q. Shen, “Massive Dirac fermions and spin physics in an ultrathin film of topological insulator,” *Physical Review B*, vol. 81, p. 115407, mar 2010.

[155] C.-Y. Moon, J. Han, H. Lee, and H. J. Choi, “Low-velocity anisotropic Dirac fermions on the side surface of topological insulators,” *Physical Review B*, vol. 84, p. 195425, nov 2011.

[156] Z. Xu, X. Guo, M. Yao, H. He, L. Miao, L. Jiao, H. Liu, J. Wang, D. Qian, J. Jia, W. Ho, and M. Xie, “Anisotropic topological surface states on high-index Bi2Se3 films.,” *Advanced materials (Deerfield Beach, Fla.)*, vol. 25, pp. 1557–62, mar 2013.

[157] H. T. He, H. C. Liu, B. K. Li, X. Guo, Z. J. Xu, M. H. Xie, and J. N. Wang, “Disorder-induced linear magnetoresistance in (221) topological insulator Bi2Se3 films,” *Applied Physics Letters*, vol. 103, p. 031606, jul 2013.

[158] F. Zhang, C. L. Kane, and E. J. Mele, “Surface states of topological insulators,” *Physical Review B*, vol. 86, p. 81303, aug 2012.

[159] F. Zhang, C. L. Kane, and E. J. Mele, “Surface State Magnetization and Chiral Edge States on Topological Insulators,” *Physical Review Letters*, vol. 110, p. 046404, jan 2013.

[160] S. Roy, K. Saha, and S. Das, “Probing surface states exposed by crystal terminations at arbitrary orientations of three-dimensional topological insulators,” *Physical Review B*, vol. 91, p. 195415, may 2015.

[161] D. Soriano, F. Ortmann, and S. Roche, “Three-Dimensional Models of Topological Insulators: Engineering of Dirac Cones and Robustness of the Spin Texture,” *Physical Review Letters*, vol. 109, p. 266805, dec 2012.

[162] X.-L. Qi and S.-C. Zhang, “Topological insulators and superconductors,” *Reviews of Modern Physics*, vol. 83, pp. 1057–1110, oct 2011.

[163] C. Nowka, L. Veyrat, S. Gorantla, U. Steiner, B. Eichler, O. G. Schmidt, H. Funke, J. Dufouleur, B. Büchner, R. Giraud, and S. Hampel, “Catalyst-free Growth of Single Crystalline Bi2Se3 Nanostructures for Quantum Transport Studies,” *Crystal Growth & Design*, vol. 15, pp. 4272–4278, sep 2015.

[164] D. Pesin and A. H. MacDonald, “Spintronics and pseudospintronics in graphene and topological insulators.,” *Nature Materials*, vol. 11, pp. 409–16, may 2012.

[165] A. R. Mellnik, J. S. Lee, A. Richardella, J. L. Grab, P. J. Mintun, M. H. Fischer, A. Vaezi, A. Manchon, E.-A. Kim, N. Samarth, and D. C. Ralph, “Spin-transfer torque generated by a topological insulator,” *Nature*, vol. 511, pp. 449–451, jul 2014.

[166] C. H. Li, O. M. J. van ’t Erve, J. T. Robinson, Y. Liu, L. Li, and B. T. Jonker, “Electrical detection of charge-current-induced spin polarization due to spin-momentum locking in Bi2Se3.,” *Nature Nanotechnology*, vol. 9, pp. 218–24, mar 2014.

[167] A. Stern and N. H. Lindner, “Topological quantum computation–from basic concepts to first experiments.,” *Science (New York, N.Y.)*, vol. 339, pp. 1179–84, mar 2013.

[168] L. He, F. Xiu, X. Yu, M. Teague, W. Jiang, Y. Fan, X. Kou, M. Lang, Y. Wang, G. Huang, N.-C. Yeh, and K. L. Wang, “Surface-dominated conduction in a 6 nm thick Bi2Se3 thin film.,” *Nano Letters*, vol. 12, pp. 1486–90, mar 2012.

[169] C.-X. Liu, X.-L. Qi, H. Zhang, X. Dai, Z. Fang, and S.-C. Zhang, “Model Hamiltonian for topological insulators,” *Physical Review B*, vol. 82, p. 045122, jul 2010.

[170] W. Zhang, R. Yu, H.-J. Zhang, X. Dai, and Z. Fang, “First-principles studies of the three-dimensional strong topological insulators Bi2Te3, Bi2Se3 and Sb2Te3,” *New Journal of Physics*, vol. 12, p. 065013, jun 2010.

[171] C. Yan, J. Liu, Y. Zang, J. Wang, Z. Wang, P. Wang, Z.-D. Zhang, L. Wang, X. Ma, S. Ji, K. He, L. Fu, W. Duan, Q.-K. Xue, and X. Chen, “Experimental Observation of Dirac-like Surface States and Topological Phase Transition in Pb1-xSnxTe (111) Films,” *Physical Review Letters*, vol. 112, p. 186801, may 2014.

[172] Y. Tanaka, T. Shoman, K. Nakayama, S. Souma, T. Sato, T. Takahashi, M. Novak, K. Segawa, and Y. Ando, “Two types of Dirac-cone surface states on the (111) surface of the topological crystalline insulator SnTe,” *Physical Review B*, vol. 88, p. 235126, dec 2013.

[173] I. Zeljkovic, Y. Okada, M. Serbyn, R. Sankar, D. Walkup, W. Zhou, J. Liu, G. Chang, Y. J. Wang, M. Z. Hasan, F. Chou, H. Lin, A. Bansil, L. Fu, and V. Madhavan, “Dirac mass generation from crystal symmetry breaking on the surfaces of topological crystalline insulators.,” *Nature Materials*, vol. 14, pp. 318–24, mar 2015.

[174] M. Serbyn and L. Fu, “Symmetry breaking and Landau quantization in topological crystalline insulators,” *Physical Review B*, vol. 90, p. 035402, jul 2014.

[175] W. Dang, H. Peng, H. Li, P. Wang, and Z. Liu, “Epitaxial Heterostructures of Ultrathin Topological Insulator Nanoplate and Graphene,” *Nano Letters*, vol. 10, pp. 2870–2876, jul 2010.

[176] J. Linder, T. Yokoyama, and A. Sudbø, “Anomalous finite size effects on surface states in the topological insulator Bi2Se3,” *Physical Review B*, vol. 80, p. 205401, nov 2009.

[177] J. Liu, X. Qian, and L. Fu, “Crystal field effect induced topological crystalline insulators in monolayer IV-VI semiconductors.,” *Nano Letters*, vol. 15, pp. 2657–61, apr 2015.

[178] R. Yu, X. L. Qi, A. Bernevig, Z. Fang, and X. Dai, “Equivalent expression of Z2 topological invariant for band insulators using the non-Abelian Berry connection,” *Physical Review B*, vol. 84, p. 075119, aug 2011.

[179] A. Alexandradinata, X. Dai, and B. A. Bernevig, “Wilson-loop characterization of inversion-symmetric topological insulators,” *Physical Review B*, vol. 89, p. 155114, apr 2014.

[180] *Group Theory*. Berlin, Heidelberg: Springer Berlin Heidelberg, 2008.

[181] I. Barke, F. Zheng, T. K. Rügheimer, and F. J. Himpsel, “Experimental Evidence for Spin-Split Bands in a One-Dimensional Chain Structure,” *Physical Review Letters*, vol. 97, p. 226405, dec 2006.

[182] L. V. Bondarenko, D. V. Gruznev, A. A. Yakovlev, A. Y. Tupchaya, D. Usachov, O. Vilkov, A. Fedorov, D. V. Vyalikh, S. V. Eremeev, E. V. Chulkov, A. V. Zotov, and A. A. Saranin, “Large spin splitting of metallic surface-state bands at adsorbate-modified gold/silicon surfaces.,” *Scientific Reports*, vol. 3, p. 1826, jan 2013.

[183] G. Landolt, S. Schreyeck, S. V. Eremeev, B. Slomski, S. Muff, J. Osterwalder, E. V. Chulkov, C. Gould, G. Karczewski, K. Brunner, H. Buhmann, L. W. Molenkamp, and J. H. Dil, “Spin Texture of Bi2Se3 Thin Films in the Quantum Tunneling Limit,” *Physical Review Letters*, vol. 112, p. 057601, feb 2014.

Naunidh Singh Virk

Rue de la Borde 3C, Lausanne, Vaud, 1018, Switzerland
Email: naunidh.virk@gmail.com. Skype username: naunivirk
British

Education

Oct 2011- Present	**École Polytechnique Fédérale de Lausanne**-PhD Theoretical Physics Supervisor: **Professor Oleg Yazyev**
Oct 2009- Oct 2010	**Imperial College London**-MRes Nanomaterials**-Distinction** Supervisors: **Professor Nicholas. M. Harrison** and **Dr Barbara Montanari**
Oct 2006- July 2009	**University of Bristol**-BSc Chemistry Hons Supervisor: **Professor Neil Allan**
2001 - 2006	**Bancroft's School, Woodford Green.** **3 A levels**: Chemistry (B), Maths (B), History (B), **1 AS Level**: Biology (B) **9 GCSEs** (6A*, 2A, 1B)

Achievements

i. Publications

- Crepaldi, L. Moreschini, G. Autes, C. Tournier-Colletta, S. Moser, N. Virk, H. Berger, Ph. Bugnon, Y. J. Chang, K. Kern, A. Bostwick, E. Rotenberg, O.V. Yazyev and M. Grioni, "Giant ambipolar Rashba effect in a semiconductor: BiTeI", Phys. Rev. Lett. 109, 096803 (2012).

- F. Gargiulo, G. Autès, N. Virk, S. Barthel, M. Rösner, L. R. M. Toller, T. O. Wehling, and O. V. Yazyev, "Electronic transport in graphene with aggregated hydrogen adatoms", Phys. Rev. Lett. (2014).

- N. Virk and O. V. Yazyev, "Dirac fermions at high-index surfaces of bismuth chalcogenide topological insulator nanostructures", under review, Nat. Sci. Reports.

- N. Virk, G. Autès, O. V. Yazyev, "One-dimensional nanostructures of Bi_2Se_3 topological insulators", in preparation.

- N. Virk, G. Autès, H. Lee, O. V. Yazyev, "One-dimensional nanostructures of the topological crystalline insulator SnTe", in preparation.

ii. Posters

- "First-Principles Exploration of High-Energy Facets of Bismuth Chalcogenide Nanocrystals", 31st International Conference on the Physics of Semiconductors, Zurich, Switzerland, July 29th- August 3rd 2012.

- "First-Principles Exploration of High-Energy Facets of Bismuth Chalcogenide Nanocrystals", Topological Materials, University of Bremen, Bremen, Germany, August 13th-17th 2012.

- "First-Principles Exploration of High-Energy Facets of Bismuth Chalcogenide Nanocrystals", 16th International Workshop on Computational Physics and Materials Science: Total Energy and Force Methods, ICTP, Trieste, Italy, January 10-12th 2013.

- “First-Principles Exploration of High-Energy Facets of Bismuth Chalcogenide Nanocrystals” PASC HP2C/PASC Materials Simulation Junior Retreat, Boldern, Mannedorf, Zurich, Switzer- land, July 9th-12th 2013.

- “First-Principles Exploration of High-Energy Facets of Bismuth Chalcogenide Nanocrystals” International Workshop on Computational Physics and Materials science ("Total Energy and Force methods"), CECAM HQ EPFL, Lausanne, Switzerland, January 9th-11th, 2014.

- “Nanostructures of Bismuth Chalcogenide Topological Insulators: A Computational Study”, International Winter School on the Electronic Properties of Novel Materials (IWEPNM) 2015, Kirchberg in Tirol, March 7th-March 14th 2015.